Analysis of test beam data using a technological prototype of a highly granular calorimeter and study of light quark production at a future linear collider

Yuichi Okugawa

To cite this version:

Yuichi Okugawa. Analysis of test beam data using a technological prototype of a highly granular calorimeter and study of light quark production at a future linear collider. High Energy Physics - Experiment [hep-ex]. Université Paris-Saclay; Tōhoku Daigaku (Sendai, Japon), 2024. English. NNT : 2024UPASP008 . tel-04505588

HAL Id: tel-04505588
https://theses.hal.science/tel-04505588

Submitted on 15 Mar 2024

Analysis of test beam data using a technological prototype of a highly granular calorimeter and study of light quark production at a future linear collider

Analyse des données d'un test en faisceau avec un prototype technologique d'un calorimètre hautement granulaire et étude de la production de quarks légers dans un futur collisionneur linéaire

Thèse de doctorat de l'université Paris-Saclay
et du Tohoku University

École doctorale n°576 Particules, hadrons, énergie et noyau : instrumentation, imagerie, cosmos et simulation (PHENIICS)
Spécialité de doctorat : Physique des particules
Graduate School : Physique
Référent : Faculté des sciences d'Orsay

Thèse préparée dans les unités de recherche **IJCLab** (Université Paris-Saclay, CNRS)
et **département de physique** (Tohoku University),
sous la direction de **Roman PÖSCHL**, Directeur de thèse,
et la co-direction de **Tomoyuki SANUKI**, Professeur

Thèse soutenue à Paris-Saclay, le 07 Février 2024, par

Yuichi OKUGAWA

Composition du jury

Membres du jury avec voix délibérative

Achille STOCCHI Professeur, Université Paris-Saclay, IJCLab (Orsay, France)	Président
Shoji ASAI Professeur, Tokyo University (Tokyo, Japon)	Rapporteur & Examinateur
Juan FUSTER Professeur, Instituto de Fìsica Corpuscular (Paterna, Espagne)	Rapporteur & Examinateur
Jenny LIST Professeur, DESY (Hamburg, Allemagne)	Examinatrice
Yukinari SUMINO Professeur, Tohoku University (Sendai, Japon)	Examinateur

THESE DE DOCTORAT

NNT : 2024UPASP008

Ph.D. Thesis

Analysis of Test Beam Data Using a Technological Prototype of a Highly Granular Calorimeter and Study of Light Quark Production at a Future Linear Collider

（高精細カロリメータ試作機を用いたテストビームデータの解析及び将来のリニアコライダーにおける軽クォーク生成の研究）

東北大学・パリサクレー大学

奥川　悠元

令和５年

Titre: Analyse des données d'un test en faisceau avec un prototype technologique d'un calorimètre hautement granulaire et étude de la production de quarks légers dans un futur collisionneur linéaire

Mots clés: Calorimètre, physique des particules, interactions électrofaibles, quark léger, ILC, CALICE

Résumé: Cette thèse présente deux études principales concernant le collisionneur linéaire international (ILC), le futur collisionneur linéaire électron-positron fonctionnant à une énergie de centre de masse de $\sqrt{s} = 250\,\mathrm{GeV}$, avec une extension potentielle à $\sqrt{s} = 1\,\mathrm{TeV}$.

La première étude porte sur l'analyse des données enregistrées avec un prototype dùun calorimètre électromagnétique silicium-tungstène (SiW-ECAL). Les calorimètres à haute granularité font partie de tous les concepts de détecteurs des projets actuels et futurs de la physique des particules. Ce type de calorimètre permet de reconstruire précisément l'énergie du jet avec une haute résolution à l'aide des algorithmes dits "Particle Flow Algorithms (PFA)". Pour vérifier la faisabilité de SiW-ECAL, 15 couches comprenant en total $15,360$ pixels de silicium, ont été assemblées. Après la chaîne complète de mise en service et leur étalonnage, le prototype fut testé en faisceau de test au SPS du CERN. L'étude analyse des donées energistrées avec un faisceau d'électrons d'une énergie de 10 GeV. Les donées sont comparées avec une simulation du prototype basé sur le logiciel de simulation GEANT4. La résolution de l'énergie électromagnétique à 10 GeV a été mesurée à $12.5 \pm 0.2\%$ et s'est avérée compatible avec le résultat simulé de $13.6 \pm 0.3\%$.

La seconde étude porte sur la mesure des sections efficaces différentielles de la production de quarks légers dans le processus en $e^{+}e^{-} \rightarrow q\bar{q}$ à $\sqrt{s} = 250\,\mathrm{GeV}$ avec $q\bar{q}$ étant u, d ou s. La section efficace différentielle est mesurée par rapport au cosinus de l'angle polaire du quark diffusé. La mesure précise peut permettre d'extraire les constantes de couplage électrofaible avec le photon ou Z du modèle standard. Ces couplages électrofaibles dépendent de l'hélicité du fermion. Par conséquent, cette mesure profite grandement de la polarisation des faisceaux d'électrons et de positrons. Afin d'extraire le processus dur original, nous sélectionnons l'objet chargé avec la plus grande impulsion d'un jet, qui représente l'empreinte du processus dur. Pour ce faire, une méthode précise d'identification des particules est nécessaire, ce qui est réalisé par l'utilisation des informations dE/dx fournies par la chambre à projection temporelle (TPC) de l'ILD. La précision obtenue sur l'asymétrie avant-arrière A_{FB} pour les états finaux $u\bar{u}$ et $d\bar{d}$ se situe entre 3.1% et 9.5% y compris l'erreur systematique. Pour l'état final $s\bar{s}$ la précision sur A_{FB} est entre 0.2% et 1.5%.

université
PARIS-SACLAY

ÉCOLE DOCTORALE
Particules, hadrons, énergie et noyau :
instrumentation, imagerie, cosmos
et simulation (PHENIICS)

Title: Analysis of test beam data using a technological prototype of a highly granular calorimeter and study of light quark production at a future linear collider

Keywords: Calorimeter, particle physics, electroweak interactions, light quark, ILC, CALICE

Abstract: This thesis presents two main studies regarding the International Linear Collider (ILC), the future electron-positron linear collider operating at center of mass energy of $\sqrt{s} = 250\,\mathrm{GeV}$, with the potential extension to $\sqrt{s} = 1\,\mathrm{TeV}$.

The first study is the analysis of data recorded with the silicon-tungsten electromagnetic calorimeter (SiW-ECAL) prototype. Highly granular calorimeters are part of all detector concepts of current and future particle physics projects, to precisely reconstruct the jet energy with high resolution using Particle Flow Algorithm. To verify the feasibility of a SiW-ECAL, 15 layers of a technological prototypes, comprising $15,360$ silicon pixels, were assembled. After the full chain of commissioning, the prototypes were tested in beam at the SPS at CERN. The study analyzes one of the 10 GeV electron beam runs, and compare the result with the GEANT4 simulation using the same setup. The electromagnetic energy resolution for the 10 GeV run was measured to be $12.5 \pm 0.2\%$ and found to be compatible with simulated result of $13.6 \pm 0.3\%$.

The second study is the measurement of the differential cross sections of light quark production in the process in $e^+e^- \to q\bar{q}$ at $\sqrt{s} = 250\,\mathrm{GeV}$ with $q\bar{q}$ being u, d or s. The differential cross section is measured with respect to the cosine of the polar angle of the scattered quark. The precise measurement may allow for the extraction of electroweak coupling constants to the Standard Model photon or Z. These electroweak couplings depend on the fermion helicity. Therefore, this measurement is greatly supported by the polarization of electron and positron beams. In order to extract the underlying hard process, we select the charged Particle Flow Object (PFO) with the largest momentum within a jet. To accomplish this, a precise particle identification method is required. We use the dE/dx information provided by the Time Projection Chamber (TPC) of ILD. The obtained precision for the forward-backward asymmetry, A_{FB}, for the $u\bar{u}$ and $d\bar{d}$ channels including the systematic error ranges between 3.1% and 9.5% at the time of the submission of thesis. For $s\bar{s}$, A_{FB} can be measured with systematic uncertainty as small as 0.2% and 1.5%.

“It doesn’t matter how beautiful your theory is, it doesn’t matter how smart you are. If it doesn’t agree with experiment, it’s wrong.”

Richard P. Feynman

Acknowledgements

This PhD thesis project was undertaken as part of the joint degree program between the University Paris-Saclay, France and Tohoku University, Japan. I had the privilege of being the first student in this program, and I am deeply grateful for the substantial support I received from numerous people. First and foremost, I express my deepest gratitude to my supervisor, Prof. Roman Pöschl. He has been a pillar of support since 2018, guiding me through both my master's and PhD studies. Despite the challenges posed by the COVID crisis and administrative differences between the two countries, he played a crucial role in sustaining the momentum of the thesis study. This involved hosting of weekly group meetings and engaging in scientific discussions during lunch (almost everyday!). Moreover, I express my sincere gratitude to Prof. Hitoshi Yamamoto for his unwavering support throughout my PhD program. He was also my supervisor during my master's studies at Tohoku University, and he continued to provide valuable guidance even after his retirement there, actively participating in our weekly meetings and sharing his exceptional insights with the project. I extend my deepest appreciation to Prof. Francois Richard for his contributions to the theoretical and experimental aspects of the project. Many of the analysis techniques and ideas were profoundly influenced by his expertise, proving to be essential to the success of the project. Special thanks go to Adrian Irles from IFIC, whose assistance with technical analysis problems and introduction to various data-taking tools proved invaluable. I also acknowledge Prof. Tomoyuki Sanuki for his ongoing support in facilitating collaboration between the two universities. The dedicated support of our team's engineers and technicians (Jihane, Dominique, Stephan, Alice, Alexandre, and many others) was indispensable to the realization of the beam test. Last but not least, my heartfelt appreciation goes to my family and friends who consistently demonstrated interest and provided unwavering support throughout my thesis studies. Without the support of everyone, this thesis would not have come to fruition.

Contents

List of Figures

List of Tables

Abbreviations

AB	**A**haronov-**B**ohm
ADC	**A**nalog-to-**D**igital **C**onverter
ASIC	**A**pplication **S**pecific **I**integrated **C**ircuit
ASU	**A**ctive **S**ensor **U**nit
BCID	**B**unch **C**rossing **ID**
BDT	**B**oosted **D**ecision **T**ree
BGA	**B**all **G**rid **A**rray
BSM	**B**eyond **S**tandard **M**odel
CALICE	**CA**orimeter for a **LI**near **C**ollider **E**xperiment
CCC	**C**lock & **C**ontrol **C**ard
COB	**C**hip-**O**n-**B**oard
CORE	**CO**ntrol & **RE**adout
CPS	**C**MOS **P**ixel **S**ensor
DAC	**D**igital-to-**A**nalog **C**onverter
DAQ	**D**ata **A**c**Q**uisition
DEPFET	**DEP**leted **F**ield **E**ffect **T**ransistor sensor
ECAL	**E**lectromagnetic **CAL**orimeter
EM	**E**lectro**M**agnetic
ETD	**E**ndplate of the **T**PC **D**etector
EW	**E**lectro**W**eak
FEV	**F**ront **E**nd board **V**ersion
FPCCD	**F**ine **P**ixel **CCD**
FSR	**F**inal **S**tate **R**adiation
FTD	**F**orward **T**racking **D**etector
FWHM	**F**ull **W**idth **H**alf **M**aximum

GEM	**G**as **E**lectron **M**ultiplier
GHU	**G**auge-**H**iggs **U**nification
HCAL	**H**adronic **CAL**orimeter
IDR	**I**LD **D**esign **R**eport
IDR	**I**nterim **D**esign **R**eport
ILC	**I**nternational **L**inear **C**ollider
ILD	**I**nternational **L**arge **D**etector
ISR	**I**nitial **S**tate **R**adiation
KK	**K**aluza **K**lein
LEP	**L**arge **E**lectron **P**ositron collider
LHC	**L**arge **H**adron **C**ollider
LO	**L**eading **O**rder
LPFO	**L**eading **P**article **F**low **O**bject
MC	**M**onte **C**arlo
MIP	**M**inimum **I**onization **P**article
OPAL	**O**mni-**P**urpose **A**pparatus at **L**EP
PCB	**P**rinted **C**ircuit **B**oard
PFA	**P**article **F**low **A**lgorithm
PFO	**P**article **F**low **O**bject
PID	**P**article **ID**entification
PV	**P**rimary **V**ertex
QCD	**Q**uantum **C**hromo **D**ynamics
QED	**Q**uantum **E**lectro **D**ynamics
QFT	**Q**uantum **F**ield **T**heory
RMS	**R**oot **M**ean **S**quare
SCA	**S**witch **C**apacitor **A**rray
SET	**S**ilicon **E**xternal **T**racker
SiD	**Si**licon **D**etector
SiPM	**Si**licon **P**hoto **M**ultiplier
SIT	**S**ilicon **I**nner **T**racker
SKIROC	**S**ilicon-pin **K**alorimeter **I**ntegrated **R**ead**O**ut **C**hip
SLC	**S**tanford **L**inear **C**ollider
SM	**S**tandard **M**odel

SNR	**S**ignal-to-**N**oise **R**atio
SPFO	**S**econdary **P**article **F**low **O**bject
SPS	**S**uper **P**roton **S**ynchrotron
SV	**S**econdary **V**ertex
TDR	**T**echnical **D**esign **R**eport
TMVA	**T**oolkit for **M**ulti**V**ariate Data **A**nalysis
TPC	**T**ime **P**rojection **C**hamber
VEV	**V**acuum **E**xpectation **V**alue
VTX	**V**er**T**e**X** Detector

Synthèse en Français

Introduction

Le Modèle Standard de la physique des particules est un cadre théorique visant à expliquer les propriétés des particules élémentaires et de leurs interactions. Il est connu pour prédire des observables physiques avec une précision significativement élevée. Le Modèle Standard comprend des fermions, des particules de spin demi-entier qui constituent la matière, et des bosons de spin entier agissant comme des porteurs de force. Actuellement, le Modèle Standard décrit les interactions entre particules qui impliquent trois forces fondamentales : la force forte, la force faible et la force électromagnétique. La force gravitationnelle est hors du champ d'application du Modèle Standard en raison de son couplage significativement faible avec la matière, ainsi que de son incapacité à être quantifiée de manière à être compatible avec la relativité générale.

Malgré le succès du Modèle Standard pour prédire des phénomènes en physique des particules à un niveau extrêmement précis, de nombreuses questions ouvertes et problèmes restent à expliquer. L'un d'entre eux est l'explication du *problème de hiérarchie.* La rupture de symétrie électrofaible est déclenchée par le mécanisme de Higgs. Alors que la dynamique des bosons de jauge est régie par la symétrie de jauge, il n'existe aucune symétrie qui puisse protéger le couplage du Higgs aux fermions, ainsi que son auto-couplage. La masse effective du boson de Higgs observée au LHC, avec m_H =125 GeV, est après les corrections quantiques quadratiques, qui s'annulent délicatement avec sa masse nue. Cela signifie que si l'on se déplace vers l'échelle de Planck, une correction de l'ordre du carré de la masse de Planck ($\sim 10^{19}$ GeV) est nécessaire. Ce réglage fin étrange est souvent appelé naturalité ou problème de hiérarchie. Une façon de stabiliser la masse du Higgs contre de grandes corrections quantiques est de considérer le boson de Higgs comme faisant partie d'une composante de dimension supplémentaire des potentiels de jauge. Ce modèle est appelé modèle de Unification Gauge-Higgs (GHU) [13, 15].

Dans le GHU, la symétrie de jauge est dynamiquement brisée avec une phase Aharonov-Bohm (AB) θ_H dans la cinquième dimension. Cela signifie que la dimension supplémentaire offre la possibilité pour les différentes saveurs de fermions d'étendre leur fonction d'onde à la dimension supplémentaire. De plus, les fermions de chiralité différente peuvent avoir une dépendance de leur fonction d'onde envers cette dimension supplémentaire. En conséquence, le boson de Higgs apparaît comme un mode de fluctuation de θ_H. Les phénomènes physiques du GHU sont très similaires au SM en dessous de l'échelle EW. Le GHU permet des couplages de jauge de quarks et de leptons de s'écarter du SM de moins de 0.1% pour $\theta_H \simeq 0.1$ sur l'échelle de masse de Kaluza-Klein (KK) [16]. Le modèle GHU présente également un boson Z' avec un fort couplage à la composante de fermions à droite, qui sont les modes KK de Z, γ et Z_R. Cela a été fortement contraint par l'expérience LHC lors de la recherche de bosons Z' et W' à $\sqrt{s}$ =13 TeV avec des données collectées jusqu'à 140fb^{-1} [17].

International Linear Collider

Le Collisionneur Linéaire International (ILC) est le futur collisionneur linéaire électron-positron qui fonctionne à une énergie dans le centre de masse de $\sqrt{s} = 250$ GeV, avec une extension potentielle à $\sqrt{s} = 1$ TeV. La Figure 1 montre la vue schématique de l'ILC. Il a une longueur totale de 20.5 km dans le cas de $\sqrt{s} = 250$ GeV, et de 40 km pour 1 TeV. L'ILC fonctionne avec un agencement structuré de faisceaux, organisé en trains et en paquets. Cette configuration permet aux détecteurs d'utiliser un mode de "puissance pulsée", où le courant de polarisation des détecteurs est éteint entre les trains, réduisant ainsi efficacement la consommation totale d'énergie du complexe de détecteurs. Chaque train comprimé est composé de 2,625 paquets et se produit à une fréquence de 5 Hz,

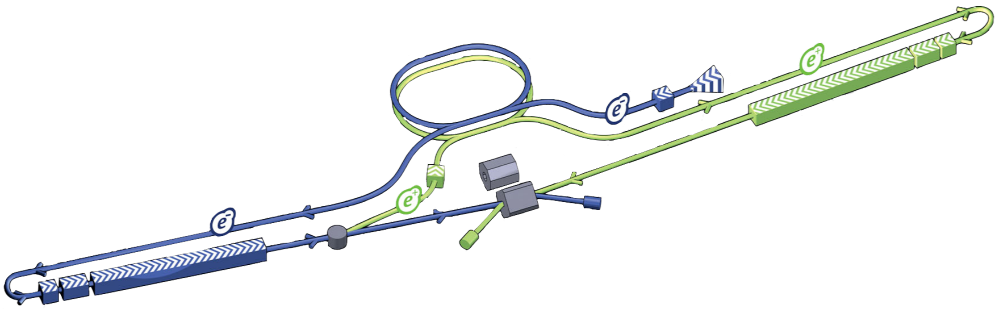

FIGURE 1: Schematic view of the ILC

chaque paquet étant séparé par 366 ns. La mise en œuvre réussie du mode de puissance pulsée nécessite une synchronisation entre l'électronique du détecteur et la fréquence du faisceau.

Collider circulaire, comme le Large Hadron Collider (LHC) au CERN, est fortement limité par la perte d'énergie due au rayonnement synchrotron. L'ILC présente de nombreux avantages par rapport aux collisionneurs hadroniques, tels que l'état initial bien connu des particules en collision grâce à la polarisation du faisceau et des arrière-plans de la chromodynamique quantique (QCD) comparativement petits et bien calculables. L'un des objectifs substantiels à atteindre par l'ILC est la mesure précise des propriétés des particules. L'ILC facilite la recherche indépendante du modèle des paramètres électrofaibles.

International Large Detector

International Large Detector (ILD) est la conception de détecteur proposée pour l'ILC. La vue en coupe transversale de l'ILD est illustrée dans la Figure 2. L'ILD est le

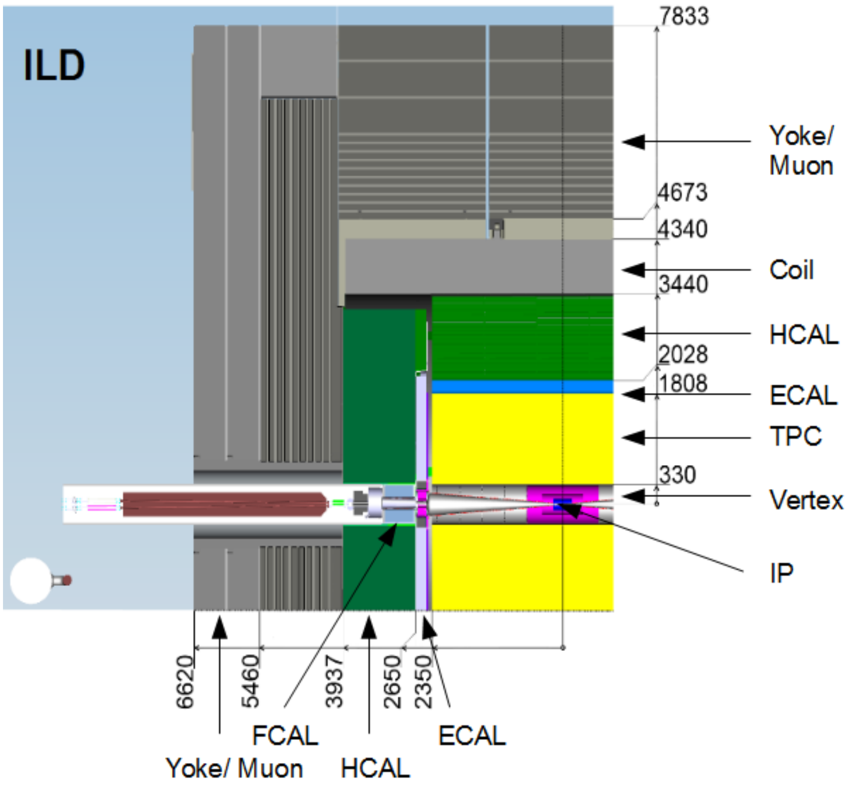

FIGURE 2: Vue en coupe transversale de l'ILD. La distance est mesurée en mm.

détecteur en forme de tonneau 4π d'une longueur de 13.240 m et d'un rayon de 7.833 m. Les particules vont hadroniser ou traverser l'ensemble du détecteur en fonction de leur type, comme le montre la Figure 3. Ci-dessous sont les descriptions succinctes de chaque sous-détecteur dans l'ILD :

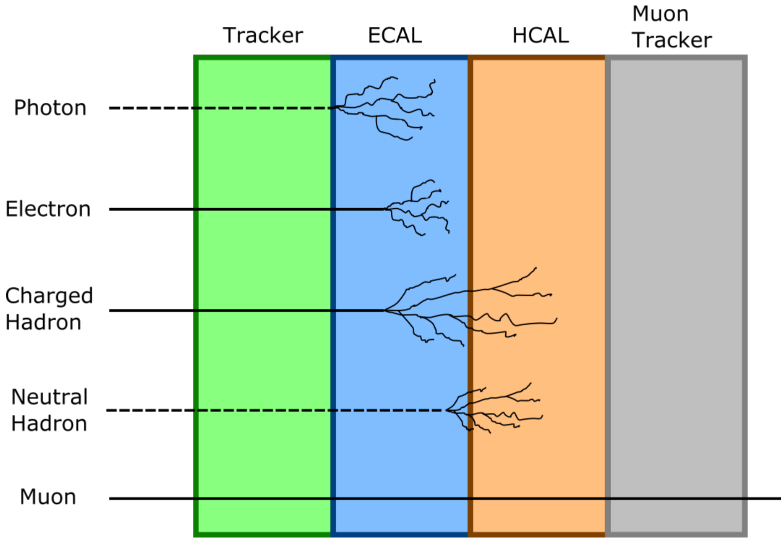

FIGURE 3: L'image montre différents types de particules s'arrêtant ou hadronisant à différents points dans le détecteur.

- **Détecteur de Vertex (VTX)**
  VTX est un détecteur pixel multicouche, spécialisé dans l'identification des vertices. Il constitue la couche la plus interne dans l'ILD, le sous-détecteur le plus proche du point d'interaction. Le détecteur est optimisé pour une résolution spatiale élevée et a une épaisseur minimale afin d'effectuer des mesures de précision de la position du vertex.
- **Traqueur Interne en Silicium (SIT)**
  SIT est une série de bandes de silicium qui entourent le VTX. Le but est d'assister les données du VTX en couvrant un plus grand angle polaire.
- **Disque de Suivi Avant (FTD)**
  FTD capture les particules émises dans la région avant. Il est composé de cinq disques de bandes de silicium, qui entourent le tube à faisceau.
- **Chambre à Projection Temporelle (TPC)**
  TPC est le détecteur gazeux dans l'ILD conçu pour effectuer une reconstruction tridimensionnelle des traces de particules chargées. Il peut enregistrer jusqu'à 224 points par trace et permet également les mesures de dE/dx.

- **Calorimètre Électromagnétique (ECAL)**
  ECAL est le calorimètre pour mesurer les énergies des particules chargées. Il est composé d'une unité d'absorbeur, qui crée le gerbe électromagnétique, et d'une unité de capteur, qui capture ces gerbes. Pour ces matériaux, le tungstène est choisi comme absorbeur, tandis que le silicium ou le scintillateur sont considérés comme des alternatives techniques pour les capteurs.
- **Calorimètre Hadronique (HCAL)**
  HCAL joue un rôle central dans la séparation des hadrons neutres et chargés. Les capteurs fortement segmentés à l'intérieur du HCAL facilitent les mesures précises de l'énergie.
- **Yoke à Muons**
  Le Yoke à Muons sert à l'identification des muons au-dessus de quelques GeV.

La acquisition de données globale dans l'ILC n'opère pas sur un déclencheur externe, maximisant la sensibilité physique.

L'ILD est optimisé pour l'algorithme Particle Flow (PFA) afin d'obtenir une résolution élevée de l'énergie des jets. Parmi l'énergie totale du jet, 65% provient de particules chargées, 25% de photons et 10% d'hadrons neutres. La calorimétrie traditionnelle mesure l'énergie du jet à partir de la somme des énergies contenues dans l'ECAL et le HCAL (Figure 4, à gauche). Cette méthode signifie que 75% de l'énergie du jet est mesurée dans le HCAL, ce qui limite la résolution de l'énergie du jet. De plus, les informations de suivi de haute qualité proviennent du traqueur, qui n'est pas adopté par cette méthode.

Dans l'approche PFA, on tente de mesurer les énergies individuelles des particules (Figure 4, à droite). Ici, les hadrons chargés et neutres sont distingués par la présence de la trace. L'énergie des particules chargées est mesurée dans le traqueur, celle des photons dans l'ECAL et celle des hadrons neutres dans le HCAL. L'avantage de cela est que 65% de l'énergie du jet est désormais mesurée dans le traqueur, qui offre une meilleure précision par rapport aux calorimètres. La calorimétrie PFA nécessite deux points : une granularité élevée à la fois de l'ECAL et du HCAL, et un algorithme optimisé pour mieux distinguer les particules à l'intérieur du calorimètre. La collaboration CALICE (CAlorimeter for a LInear Collider Experiment), une collaboration mondiale de R&D, vise à développer de nouveaux détecteurs performants pour les collisionneurs électron-positron. Un des objectifs principaux de la collaboration CALICE est de développer et tester des calorimètres électromagnétiques et hadroniques hautement granulaires, en vue des futurs collisionneurs linéaires.

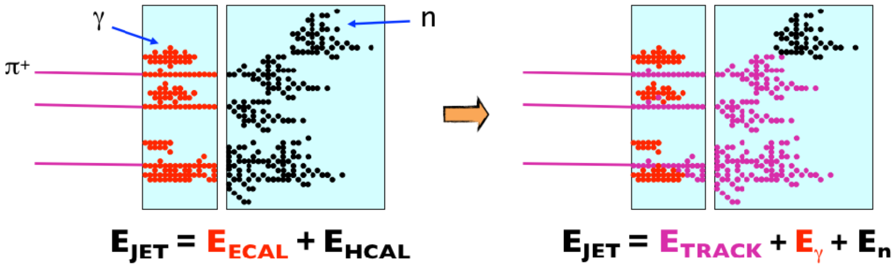

Figure 4: La différence entre l'approche traditionnelle et l'approche PFA dans le calcul de l'énergie des jets est illustrée ici. Dans l'approche traditionnelle (à gauche), l'énergie du jet est la somme des énergies contenues dans l'ECAL et le HCAL. Avec l'approche PFA (à droite), l'énergie du jet est calculée comme la somme des énergies dans la trace, les photons et les hadrons neutres.

Le Calorimètre Électromagnétique en Silicium-Tungstène

Le calorimètre en silicium-tungstène (SiW-ECAL) est l'une des alternatives techniques conçues pour le ECAL dans l'ILD. Le SiW-ECAL utilise le silicium comme matériau actif et le tungstène comme absorbeur. Comme le PFA nécessite une granularité élevée dans les calorimètres, le SiW-ECAL convient bien à cette fin car le silicium peut être segmenté en petits pixels. De plus, tous les calorimètres doivent s'insérer à l'intérieur de l'aimant de l'ILD, et le ECAL doit s'insérer dans un espace d'une épaisseur de 20 cm. Par conséquent, le tungstène a été choisi comme absorbeur, car il a une longueur de radiation de $X_0 = 3.5\,\text{mm}$ et un rayon de Molière de $R_M = 9\,\text{mm}$. De plus, le tungstène a une longueur d'interaction de $\lambda_I = 96\,\text{mm}$, ce qui permet de bien séparer les photons et les hadrons.

Le SiW-ECAL Prototype

Avant de construire des expériences de collisionneur, il est nécessaire de vérifier la faisabilité des candidats potentiels pour les calorimètres en testant leur réponse aux divers faisceaux, ainsi que la validation en comparant les résultats avec ceux produits par la simulation Monte Carlo. Depuis 2011, un prototype technologique pour le SiW-ECAL a été développé pour tester sa faisabilité pour l'ILD. Le prototype est composé d'un capteur en silicium, d'un circuit intégré spécifique à une application (ASIC), d'une carte de circuit imprimé (PCB) et d'une plaque de tungstène, comme illustré dans la Figure 5. Les capteurs en silicium du prototype sont segmentés en pixels de $5,5 \times 5.5\,\text{mm}^2$ et chaque pad de capteur a $8 \times 8 = 16$ pixels. Chaque pad de capteur est collé à l'arrière du

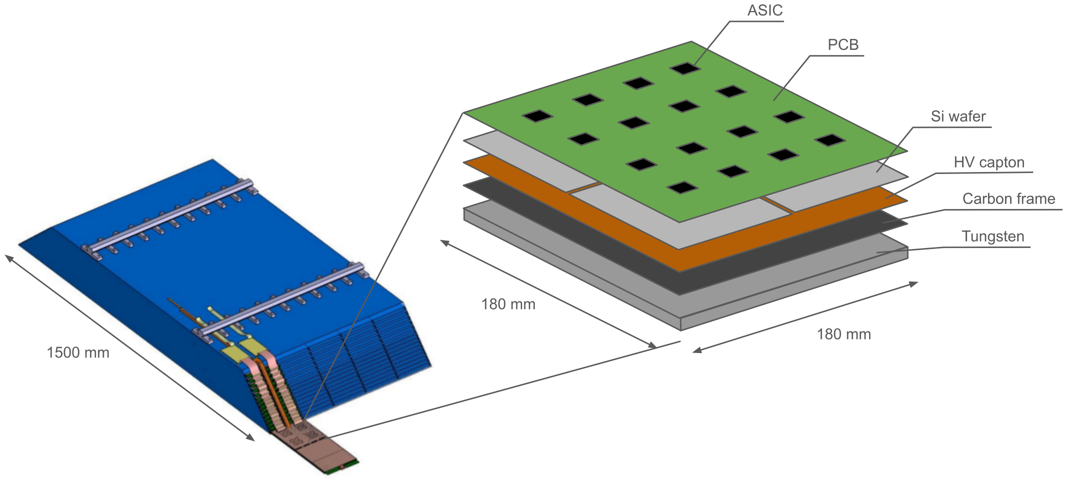

FIGURE 5: Module de barillet de l'ECAL (à gauche) et unité individuelle de SiW-ECAL avec ses principaux composants (à droite).

circuit imprimé (PCB), avec une tension de polarisation constante de 150 V appliquée sur la tranche. Pour l'unité ASIC, la technologie SKIROC (Silicon-pin Kalorimeter Integrated ReadOut Chip) en SiGe 0.35 µm de chez AMS, d'une taille de $7,2\times 8.6\,\mathrm{mm}^2$, est utilisée. SKIROC peut être configuré en mode d'impulsion de puissance, afin de synchroniser la fenêtre d'acquisition avec la structure de paquets de l'ILC. En raison de la faible consommation d'énergie en mode d'impulsion de puissance, SKIROC ne nécessite pas de système de refroidissement actif. Les cartes Front-End désignées comme Version 10 à 12 (FEV10-12) représentent des itérations de l'ASU développées depuis 2014. En 2022, des types supplémentaires de FEV ont été développés : le Chip-on-Board (COB) et le FEV 13. Les COBs sont une conception alternative de PCB où les ASIC sont directement soudés par fil sur le substrat à l'intérieur de cavités dédiées. Le FEV 13 présente une configuration distincte par rapport au FEV10-12.

Beam Test Experiment

Entre 2017 et 2020, un système compact de lecture numérique a été développé, permettant la lecture simultanée de 15 couches. Les tests en faisceau réalisés en 2021 et 2022 constituaient un test pour le nouveau système de lecture. Afin de compléter les 15 couches, toutes les couches produites depuis 2015 ont été utilisées pour la configuration. Cela comprenait différentes variantes de la carte d'interface, voir ci-dessous, ainsi que des couches qui ont révélé des problèmes comme cela sera évident ci-dessous. Par conséquent, les tests en faisceau doivent être compris plutôt comme des tests techniques, y compris la synchronisation avec le calorimètre analogique CALICE HCAL (AHCAL) lors de l'exécution combinée au CERN en juin 2022. Néanmoins, la configuration a permis d'enregistrer pour la première fois des gerbes de particules de haute énergie avec le prototype technologique. Alors qu'une analyse des données enregistrées à DESY en 2021 a été publiée dans [18], cette thèse se concentre sur la prise de données au CERN en juin 2022. Cependant, à des énergies supérieures à 10 GeV, des effets collectifs ont été observés qui doivent encore être compris. C'est pourquoi les analyses présentées ici se concentreront sur la prise de données à 10 GeV. Les sections suivantes présenteront également la chaîne complète de mise en service et d'étalonnage à laquelle j'ai contribué au cours de ma thèse.

Résultats du Test en Faisceau

Les données du test en faisceau ont été comparées à la simulation Monte Carlo à l'aide du logiciel de simulation `GEANT4`. Deux résultats principaux ont été obtenus grâce au test en faisceau d'électrons de 10 GeV. Premièrement, le nombre de coups enregistrés dans chaque couche a été comparé et tracé dans la Figure 6. Les deux distributions concordent sauf pour le nombre de coups aux extrémités haute et basse. Cette disparité peut être due à des incertitudes liées à la taille du faisceau et à sa position dans la simulation, qui diffèrent légèrement des paramètres de la simulation.

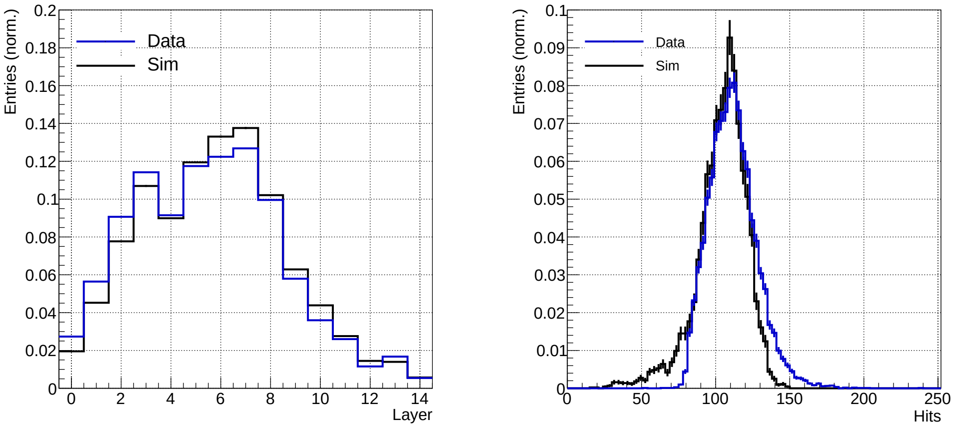

(a) Hits per layer

(b) Total number of hits

FIGURE 6: Comparaison du nombre de coups entre les données et la simulation. (a) Nombre total de coups par couche. (b) Nombre total de coups sur l'ensemble des 15 couches.

Deuxièmement, le dépôt d'énergie total dans le calorimètre a été comparé et ajusté avec la courbe gaussienne dans la Figure 7. Les résolutions énergétiques finales observées

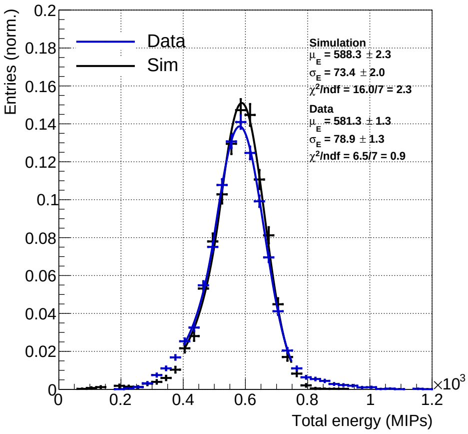

FIGURE 7: Comparaison du dépôt total d'énergie simulé et reconstruit à partir des 15 couches. Les distributions des données et de la simulation sont toutes deux normalisées à 1. En haut à gauche, on présente le résultat ajusté à l'aide de la fonction gaussienne, avec une plage d'ajustement entre 400 et 750 MIP (Minimum Ionizing Particle).

pour la simulation et la reconstruction sont les suivantes:

$$\begin{aligned} \frac{\sigma_{E_{sim}}}{E_{sim}} &= 12.5 \pm 0.3 \text{ (stat.) } \% \\ \frac{\sigma_{E_{reco}}}{E_{reco}} &= 13.6 \pm 0.2 \text{ (stat.) } \% \end{aligned} \tag{1}$$

Conclusion de l'Analyse du SiW-ECAL

Des tests techniques du prototype SiW-ECAL ont été réalisés. Pour le test en faisceau, nous avons assemblé 15 couches de prototypes SiW-ECAL, comprenant plusieurs variantes de PCB et plusieurs épaisseurs de capteurs. Le test a été effectué avec divers types de faisceaux, notamment des électrons, des muons et des pions, avec une énergie de faisceau de 10 GeV–200 GeV, tandis que cette analyse pilote s'est concentrée sur l'une des courses de faisceau d'électrons de 10 GeV. Pour préparer le test en faisceau, une chaîne complète de procédures de mise en service a été réalisée. Malgré les problèmes de délamination des capteurs, nos résultats de masquage ont démontré que plus de 80% des cellules pouvaient être utilisées pour les mesures. Les résultats de la reconstruction ont révélé que la résolution en énergie des gerbes électromagnétiques pouvait être mesurée jusqu'à 13,6% ± 0,2% (stat.). Cette valeur a été comparée à la simulation GEANT4 avec la même configuration de détecteur, montrant 12,5% ± 0,3% (stat.), démontrant une large concordance avec la reconstruction.

Production de Paires de Quarks Légers

Pour la deuxième partie de cette thèse, le processus de production de paires de quarks légers à l'ILC avec une énergie de centre de masse $\sqrt{s} = 250\,\mathrm{GeV}$ a été analysé, en utilisant la simulation complète du détecteur ILD. Comme décrit dans l'introduction, le Modèle Standard comporte des questions ouvertes encore à élucider. L'une d'entre elles est le problème de hiérarchie, et les théories au-delà du Modèle Standard peuvent être vérifiées par la mesure du couplage entre une paire de fermions et Z^0/γ. Dans cette thèse, nous avons analysé cela à travers le processus de production de paires de quarks légers, en particulier avec $e^+e^- \to Z^0/\gamma \to q_L\bar{q}L$ où qL représente les quarks légers avec $L = u, d, s$.

Asymétrie Avant-Arrière

Le couplage a été extrait à travers l'observable "Asymétrie Avant-Arrière". Il est défini comme le rapport des sections efficaces différentielles pour l'émission du fermion dans la direction avant ou arrière par rapport au faisceau d'électrons, représenté dans (2).

$$A_{FB} \equiv \frac{\sigma(\cos\theta > 0) - \sigma(\cos\theta < 0)}{\sigma(\cos\theta > 0) + \sigma(\cos\theta < 0)} \tag{2}$$

où $\sigma(\cos\theta > 0)$ ($\sigma(\cos\theta < 0)$) est la section efficace totale dans laquelle les fermions sont dispersés vers la direction avant (arrière).

Stratégie de Reconstruction

Les processus $e^+e^- \to q\bar{q}$ à $250\,\mathrm{GeV}$ résultent en deux états finals de jet. La mesure précise de l'observable A_{FB} comme décrite dans (2) nécessite l'identification précise à la fois de la charge et des propriétés angulaires de ces deux jets. Pour distinguer q de $\bar{q}$, les charges portées par le jet ou l'objet PFO doivent être comparées pour les deux hémisphères. Chaque état final avec une saveur différente a une propriété unique :

- $s\bar{s}$: Le quark étrange se hadronise principalement en kaon avec une probabilité de 23.9% [19]. Par conséquent, les kaons peuvent être utilisés comme empreinte du processus dur.
- $u\bar{u}$: Contrairement au quark étrange, le quark u se hadronisera principalement en pions avec une probabilité de 38.3%, avec une probabilité mineure de 12.2% de

se hadroniser en kaons [19]. Par conséquent, les pions peuvent être utilisés comme empreinte du processus dur.

- $d\bar{d}$: De manière similaire au quark u, le quark d se hadronisera également principalement en pions avec 38.7% [19]. Ainsi, les pions peuvent également être utilisés comme empreinte du processus dur. Notez qu'il peut également se hadroniser en kaon (6.17%), via $d \to K^{*0} \to K^{+}\pi^{-}$, tandis que la charge semble être inversée par rapport au quark d'origine.

Toute la quantité de mouvement du processus dur est transportée par la particule primaire, qui forme des hadrons durs. Par conséquent, pour calculer la section efficace différentielle à partir du processus dur, nous utilisons les PFO avec la plus grande quantité de mouvement dans chaque jet, appelée Leading PFO (LPFO). Les quarks u et d se hadronisant principalement en pion, il est difficile de démêler chaque événement. D'autre part, le quark s se hadronise principalement en kaons, permettant de le distinguer des événements u et d. Par conséquent, nous avons choisi de calculer A_{FB} pour les spectres combinés u/d et individuellement seulement pour le quark s. De plus, comme u et d se hadronisent également en kaons, il est nécessaire d'estimer la contribution du bruit de fond de ces processus. Par conséquent, la stratégie est la suivante :

1. Reconstruire les événements $q\bar{q}$ en utilisant le pion comme empreinte. Cette distribution sera interprétée comme l'empreinte des processus durs $e^{+}e^{-} \to u\bar{u}/d\bar{d}$.
2. Mesurer la section efficace différentielle et comparer le résultat avec le MC.
3. Reconstruire les événements $q\bar{q}$ en utilisant le kaon comme empreinte.
4. En supposant que les kaons des processus $u\bar{u}$ et $d\bar{d}$ suivent le MS, soustraire sa distribution des événements totaux.
5. Calculer la section efficace et A_{FB} après soustraction du bruit de fond. Cette distribution sera l'empreinte du processus dur des événements $s\bar{s}$.

Identification des Particules Chargées

La mesure de la section efficace différentielle telle qu'elle est pertinente pour cette analyse repose fortement sur une identification correcte des particules. Dans l'ILD, le TPC permet l'identification des particules via le dE/dx et la formule de Bethe-Bloch. Chaque type de particule suit une courbe distincte dans la formule de Bethe-Bloch lorsqu'on trace sa perte d'énergie dans le milieu (dE/dx) par rapport à son élan. Cela peut être utilisé pour distinguer les particules passant à travers le détecteur. La Figure 8a montre la distribution dE/dx par rapport à l'élan de la trace, chaque couleur correspondant à un type de particule comme indiqué dans la légende. Les distributions dans chaque bin représentent le nombre d'entrées dans des plages d'élan individuelles, avec le kaon, le pion et le proton dominant la majorité de la distribution. Cette séparation et cette dominance deviennent plus prononcées lorsqu'elles sont projetées sur l'axe dE/dx, comme le montre la Figure 8b. Pour l'identification des kaons chargés, une approche de sélection différente a été adoptée. Dans le cas de l'identification des pions, elle peut tirer profit du fait qu'il existe une région exempte de bruit dans la partie supérieure de la distribution de dE/dx, alors que pour les kaons, elle est contaminée à la fois par les limites supérieure et inférieure des pions et des protons, respectivement. Afin d'optimiser la sélection des kaons, la distance dE/dx $\Delta_{dE/dx-i}$ est définie comme suit [20]:

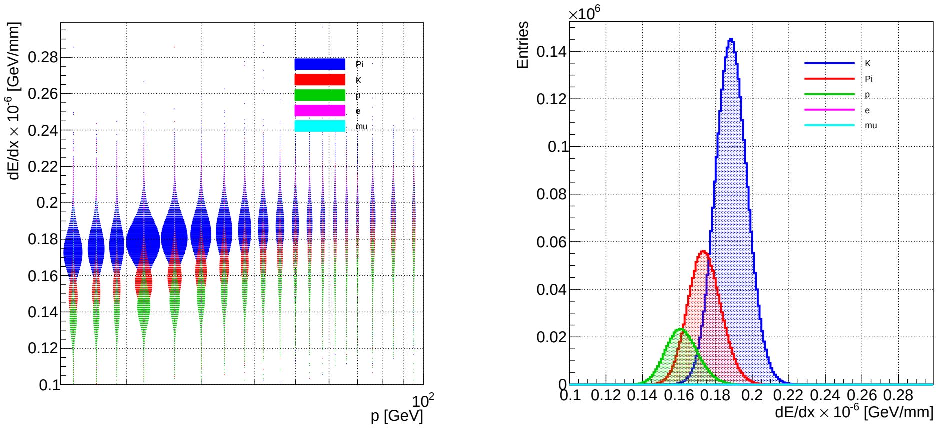

(a) (b)

FIGURE 8: Distribution du dE/dx pour des traces individuelles dans les échantillons $q_L\bar{q}_L$. (a) dE/dx par rapport à l'élan de la trace et (b) sa projection sur dE/dx.

$$\Delta_{dE/dx-i} = \left(\frac{dE/dx_{exp} - dE/dx_{i,BB}}{\Delta dE/dx_{exp}} \right) \tag{3}$$

où dE/dx_{exp} est la valeur mesurée de dE/dx, $dE/d_{i,BB}$ est la valeur théorique de dE/dx attendue à partir de la formule de Bethe-Bloch pour la particule i, et $\Delta dE/dx_{exp}$ est l'incertitude expérimentale attendue pour la mesure de dE/dx.

Résultat de l'analyse

Tout d'abord, les distributions des angles polaires pour les échantillons générés $u\bar{u}$ et $d\bar{d}$ avec une luminosité intégrée de $\mathcal{L}_{int} = 4.2$ ab^{-1} ont été analysées. Pour les processus de fond, le rayonnement en état initial et les processus de production de dibosons ont été considérés comme prédominants par rapport à l'analyse de la production de paires légères. Après le rejet des bruits de fond, la distribution des angles polaires des pions pour les polarisations des faisceaux d'électrons gauches et droits est représentée dans la Figure 9. La section efficace différentielle a été ajustée avec la fonction suivante :

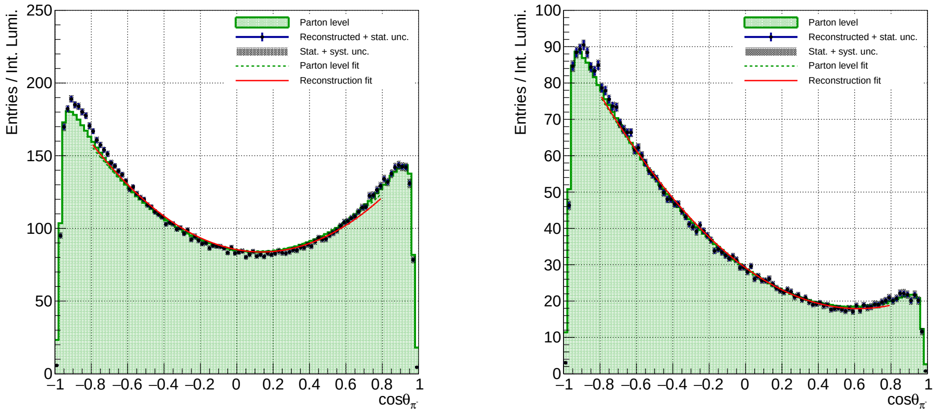

(a) (b)

Figure 9: Les distributions des angles polaires des processus de fond ($s\bar{s}$ et processus de diboson) sont soustraites du processus signal ($u\bar{u}$, $d\bar{d}$) dans (a) les échantillons de polarisation e^-Le^+R et (b) les échantillons de polarisation e^-Re^+L. La ligne verte en pointillés représente la courbe de l'ajustement pour la distribution au niveau des partons, tandis que la ligne rouge montre la courbe de l'ajustement pour la reconstruction.

$$\frac{d\sigma}{d\cos\theta} = S(1+\cos^2\theta) + A\cos\theta \tag{4}$$

où S et A sont les paramètres d'ajustement. Les résultats de l'ajustement de la Figure 9 sont résumés dans le Tableau 2.

		S	$\sigma_\mathbf{S}$	**A**	$\sigma_\mathbf{A}$
$\mathbf{e^-_L e^+_R}$	**Gen**	85.7	0.026	-20.2	0.073
	Reco	85.4	0.175	-23.4	0.495
$\mathbf{e^-_R e^+_L}$	**Gen**	29.2	0.015	-35.5	0.040
	Reco	29.2	0.088	-36.2	0.246

Table 2: Résultat de l'ajustement pour la région d'angle polaire $|\cos\theta| < 0.8$.

Deuxièmement, la distribution de l'angle polaire des échantillons générés $s\bar{s}$ est analysée. Les Kaons chargés sont utilisés pour mesurer la section efficace $e^+e^- \to s\bar{s}$. Après les soustractions de fond, la distribution de l'angle polaire pour le Kaon chargé est représentée dans la Figure 10. Les paramètres obtenus à partir de l'ajustement sont présentés avec les incertitudes statistiques et systématiques combinées dans le tableau 5.15.

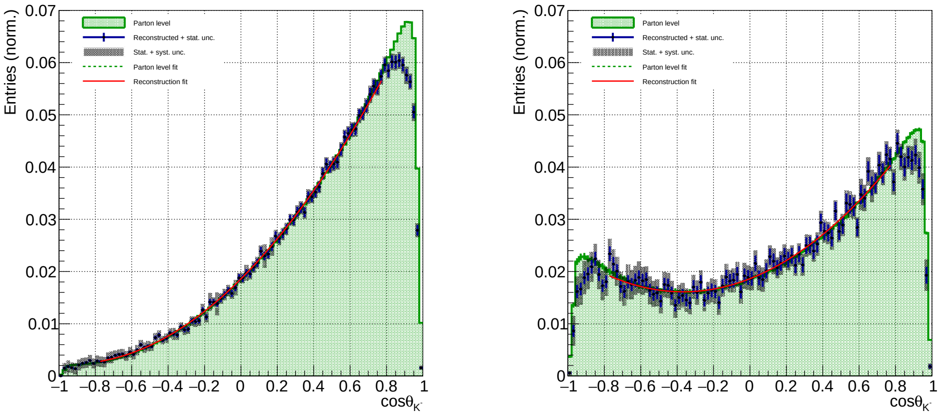

(a) (b)

FIGURE 10: Les distributions de l'angle polaire des processus de fond ($u\bar{u}$, $d\bar{d}$ et processus di-boson) sont soustraites du processus signal ($s\bar{s}$) dans (a) les échantillons de polarisation e^-Le^+R et (b) les échantillons de polarisation e^-Re^+L. La ligne pointillée verte représente la courbe d'ajustement pour la distribution au niveau des partons, tandis que la ligne rouge montre la courbe d'ajustement pour la reconstruction.

		S	$\sigma_\mathbf{S}$	**A**	$\sigma_\mathbf{A}$
$\mathbf{e_L^-e_R^+}$	**Gen**	1.86e-2	1.54e-5	3.51e-2	4.35e-5
	Reco	1.85e-2	1.06e-4	3.48e-2	2.89e-4
$\mathbf{e_R^-e_L^+}$	**Gen**	1.86e-2	4.00e-5	1.35e-2	1.10e-4
	Reco	1.86e-2	2.20e-4	1.37e-2	6.16e-4

TABLE 3: Le résultat des ajustements à la distribution de l'angle polaire dans l'échantillon $s\bar{s}$ pour les deux polarisations est résumé dans ce tableau. La région d'ajustement a été choisie pour $|\cos\theta| < 0.8$ afin de ne pas tenir compte de l'effet d'acceptation.

Conclusion de l'Analyse de la Production de Paires de Quarks Légers

Cette analyse a effectué la première mesure de la section efficace et de A_{FB} du processus de production de paires de quarks légers avec Z^0/γ à l'ILC, avec une énergie au centre de masse de $\sqrt{s} = 250\,\mathrm{GeV}$, en utilisant la simulation complète du détecteur de l'ILD. Pour mesurer la section efficace différentielle du processus de production de paires de quarks légers, les PFO de premier plan ont été utilisés comme empreinte du processus dur. Afin de distinguer les événements de quarks légers, des identifications de Pion et de Kaon ont été effectuées pour les PFO de premier plan. Pour l'identification des PID, nous avons utilisé les informations de dE/dx du TPC. Nous avons utilisé une coupure conservatrice sur la valeur de dE/dx pour l'identification des Pions, afin de maximiser la pureté finale. Pour l'identification des Kaons, une distance dE/dx a été définie pour contrer la contamination par les Pions et les protons. Les Pions ont été utilisés pour l'identification des $u\bar{u}$ et $d\bar{d}$, tandis que les Kaons ont été utilisés pour l'identification des $s\bar{s}$. Le résultat final de la mesure de la section efficace pour les événements $s\bar{s}$ a montré une précision de 0,340% pour la polarisation à gauche et de 0,694% pour la polarisation à droite. Pour les événements $u\bar{u}$ et $d\bar{d}$, le résultat de la mesure de A_{FB} a montré un accord avec les valeurs générées et reconstruites dans sa précision pour les deux polarisations, bien qu'elles souffrent encore des incertitudes systématiques. Pour les événements $s\bar{s}$, la mesure de A_{FB} a non seulement montré son accord entre la génération et la reconstruction, mais a également montré qu'elle pouvait atteindre une précision jusqu'au niveau de quelques pourcents.

L'analyse a principalement souffert d'une perte significative d'efficacité lors de l'identification des PID, car la méthode d'identification par dE/dx a réduit l'efficacité de 70% pour les Pions et de 88% pour les Kaons. Bien que cette analyse ait été réalisée en utilisant la technique de mesure conventionnelle de dE/dx, des recherches récentes [3] ont révélé que passer à la méthode de comptage de clusters améliorera encore la séparation avec une résolution de dE/dx jusqu'à 3,5%.

Chapter 1

The Standard Model

In this section, thorough introduction to the Standard Model and its open questions are being discussed.

1.1 History

In the field of physics, understanding the fundamental building blocks of the universe has always been the primary interest to many people. The current theoretical framework to understand such question was shaped by the 1970s, yet its formation has started in the early 20th century. Along the course of understanding the atomic stucture, J.J.Thomson has first introduced the “Plum pudding model” in 1904 [21], in an attempt to explain the structure of nucleus in any matter. In this model, the atomic nucleus is composed of negatively charged particle enclosed in a sphere of uniform positively charged particle. With this prevailing theory, Ernest Rutherford has conducted gold foil experiment between 1908 and 1913 [22]. The experiment was to emit the alpha particles towards the thin gold foil to observe the amount of which it gets scattered. Thomson’s model predicted that its electric fields of the atoms are not strong enough to scatter alpha particle backwards, thus most of them will be found at the front. The discovery was that the gold foil could scatter some alpha particles in all direction, which is beyond the reach where a simple Coulomb force could explain. The result has led Rutherford to conclude that the atom has largely empty structure, and negatively charged particles, later known to be electrons, are orbiting around the positively charged core nucleus, which are later discovered to be a combination of protons and neutrons.

In mid-20th century, Quantum Field Theory (QFT) was developed to explain that both elementary particles and force carriers can be expressed in terms of quantum fields. Moreover, spin-statistics theorem categorized particles in either a boson (which follows the Bose-Einstein statistics) or a fermion (which follows the Fermi-Dirac statistics), depending on their spin quantity. Such foundation allowed Standard Model to further classify particles into quark, lepton and bosons, which contributed to their discoveries at various high energy accelerators. In July 2012, CERN has announce the discovery of Higgs boson, which was long theorized missing piece in the Standard Model.

1.2 Fundamental Particles

The Standard Model (SM) of the particle physics, is a theoretical framework to explain the properties of elementary particles and their interactions. Figure 1.1 shows the table of Standard Model particles and their categories. SM is known for predicting physical observable with significantly high precision. For example, a g-2 experiment they have measured the fine structure constant in Quantum Electrodynamics (QED) that is consistent with the theory up to 0.37 parts per billion [23]. Currently, Standard Model describes particle interactions which involve in three fundamental forces: strong, weak and electromagnetic force. Gravitational force is out of scope of Standard Model framework due to its significantly weak coupling to the matter, as well as its inability to be quantized in order to be consistent with general relativity. Therefore, description of gravitational force in this thesis has been omitted. The Standard Model is founded upon the $SU(3)_C \times SU(2)_L \times U(1)_Y$ symmetry framework, which is intricately linked to the principles of gauge theory (see Section 1.2.1 and 1.2.2). Furthermore, it incorporates the Higgs mechanism, providing a comprehensive explanation for the spontaneous symmetry breaking. (see Section 1.4) Particles are classified in two different categories: boson and fermion. The description and the differences in their physical properties are introduced in the following sections.

1.2.1 Fermions

Fermions constitute the elementary particles of matter. They possess a half-integer spin and are categorized into three generations. Within the framework of the Standard Model, fermions are further distinguished into two primary sub-categories: quarks and leptons, with each category comprising six distinct members. Quarks are subject to strong, weak, and electromagnetic forces, whereas leptons engage solely in weak

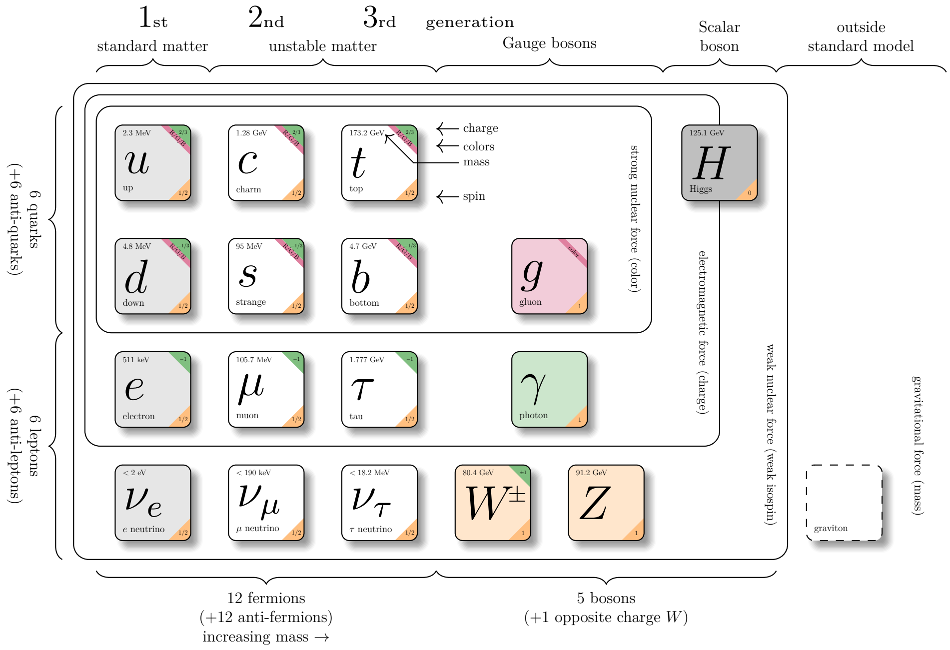

FIGURE 1.1: The Standard Model table

and electromagnetic interactions. The electroweak gauge symmetry group, denoted as $SU(2)_L \times U(1)_Y$, exhibits chirality, where a notable distinction emerges between left-handed and right-handed fermions, manifesting in distinct multiplet formations. Here, Y represents the weak hypercharge, with left-handed fermions forming doublets and right-handed fermions constituting singlets. The emergence of electric charge, denoted as Q, is a consequence of electroweak symmetry breaking, wherein the electroweak gauge group undergoes a transition to yield the familiar electromagnetism, $U(1)_{EM}$ ($SU(2)_L \times U(1)_Y \mapsto U(1)_{EM}$). This electric charge can be expressed as a linear combination involving both the third component of $SU(2)_L$ isospin (I_3^L) and the weak hypercharge.

$$Q = I_3^L + \frac{1}{2}Y \tag{1.1}$$

The strong interaction operates within the framework of the $SU(3)_C$ group, where C represents the color charge. Quarks are characterized as color triplets under the $SU(3)_C$ group, signifying their possession of color charge, whereas leptons, by contrast, are identified as color singlets, indicating their lack of color charge.

In summary, the gauge groups $SU(3)_C \times SU(2)_L \times U(1)_Y$ serves as a comprehensive representation for both strong and electroweak interactions, with $SU(3)_C$ indicating the strong interactions, while $SU(2)_L \times U(1)_Y$ characterizes the electroweak interactions. The quantum numbers of each fermions are summarized in table 1.1.

	I	II	III	I_3^L	Y	Q	C
Leptons	e_L	μ_L	τ_L	-1/2	-1	-1	0
	ν_{eL}	$\nu_{\mu L}$	$\nu_{\tau L}$	+1/2	-1	0	0
	e_R	μ_R	τ_R	0	-2	-1	0
	ν_{eR}	$\nu_{\mu R}$	$\nu_{\tau R}$	0	0	0	0
Quarks	u_L	c_L	t_L	+1/2	+1/3	+2/3	1
	d_L	s_L	b_L	-1/2	+1/3	-1/3	1
	u_R	c_R	t_R	0	+4/3	+2/3	1
	d_R	s_R	b_R	0	-2/3	-1/3	1

Table 1.1: Hyper charge and isospins of fermions. I, II, III shows the generations of the fermions.

1.2.2 Bosons

Bosons are a class of particles of integer spin. Within this category, gauge bosons play a central role as mediators of the fundamental forces. Gauge bosons with a spin of 1, encompassing particles such as photons, gluons, and the W and Z bosons, are formally categorized as vector bosons. In contrast, bosons with a spin of 0 are referred to as scalar bosons, which corresponds to the Higgs boson. The multiplicity of vector bosons participating in each interaction is linked to the number of generators within the respective gauge groups: the $U(1)$ group, characterized by a solitary generator corresponding to the photon; the $SU(2)$ group, marked by three generators corresponding to the $W^{\pm}$ and Z bosons; and the $SU(3)$ group, distinguished by eight generators corresponding to the eight distinct gluons. Original gauge theory requires the vector bosons to be massless, since the mass term in the Lagrangian introduces extra terms after the gauge transformation, which violates the gauge symmetry. Consequently, particles such as photons and gluons remain massless, in agreement with experimental observation. In contrast, the acquisition of mass by gauge bosons like the W and Z bosons is achieved through the Higgs mechanism, which is introduced in Section 1.4.

1.3 Interactions

1.3.1 Electromagnetic Interaction

The classical description of electromagnetism is encapsulated by Maxwell's equations, a foundational framework in classical electromagnetism. Quantum Electrodynamics (QED), an extension of this classical theory, delves into the quantum field theory realm by establishing the gauge group $U(1)_{EM}$ to characterize electromagnetic interactions at the quantum level. The equation of the motion is described using Lagrangian density, $\mathcal{L}$, and two fermions fields $\psi(x)$ are defined as below:

$$\mathcal{L} = i\bar{\psi}(x)\gamma^{\mu}\partial_{\mu}\psi(x) - m\bar{\psi}(x)\psi(x) \tag{1.2}$$

where the γ^{μ} are the gamma matrices and m is the mass of the fermion. The theory should be invariant under local U(1) gauge transformation $e^{i\theta}\psi$

$$\psi(x) \to e^{i\theta(x)}\psi(x) \tag{1.3}$$

This would cause no difference in the mass term. Kinetic term, on the other hand, changes the Lagrangian density and becomes:

$$i\bar{\psi}(x)\gamma^{\mu}\partial_{\mu}\psi(x) \to i\bar{\psi}(x)\gamma^{\mu}\partial_{\mu}\psi(x) - \bar{\psi}(x)\gamma^{\mu}\psi(x)\partial_{\mu}\theta(x) \tag{1.4}$$

where we are left with extra second term. In order to preserve the local gauge symmetry, vector field A_{μ}, which is also known as photon field, is introduced as following:

$$-eA_{\mu}(x)\bar{\psi}(x)\gamma^{\mu}\psi(x) \tag{1.5}$$

where the local gauge transformation is done by

$$A_{\mu}(x) \to A_{\mu}(x) - \frac{1}{e}\partial^{\mu}\theta(x) \tag{1.6}$$

The (1.5) will then transformed as:

$$-eA_{\mu}(x)\bar{\psi}(x)\gamma^{\mu}\psi(x) \to -eA_{\mu}(x)\bar{\psi}(x)\gamma^{\mu}\psi(x) + \bar{\psi}(x)\gamma^{\mu}\psi(x)\partial_{\mu}\theta(x) \tag{1.7}$$

which cancels the second term in the (1.4). After introducing covariant derivative operator as

$$\partial_{\mu} \to D_{\mu} = \partial_{\mu} - ieA_{\mu} \tag{1.8}$$

the the final local gauge invariant Lagrangian density can be written as:

$$\mathcal{L} = \bar{\psi}(x)(i\gamma^{\mu}D_{\mu} - m)\psi(x) - \frac{1}{4}F_{\mu\nu}F^{\mu\nu} \tag{1.9}$$

where

$$F_{\mu\nu} = \partial_{\mu}A_{\nu} - \partial_{\nu}A_{\mu} \tag{1.10}$$

is the strength tensor for the photon field. The Lagrangian presented in (1.9) is gauge invariant under the $U(1)_{em}$ gauge transformation defined in (1.3).

1.3.2 Electroweak Interaction

Weak interactions can usually be observed through the phenomena e.g. beta decay ($n \to pe^{-}\bar{\nu}_e$), muon decay ($n \to e^{-}\nu_{\mu}\bar{\nu}_e$) or $\nu_e e^{-}$ scattering. When Fermi first theorized the weak interactions, the process was characterized by four fermions interacting at a single point without mediators. This coupling strength is described by the Fermi coupling constant.

$$G_F/(\hbar c)^3 = 1.1663787(6) \times 10^{-5}\ \text{GeV}^{-2} \tag{1.11}$$

However, Fermi's theory of weak interactions won't hold at the high energies. For example, dimensional analysis of the Fermi constant tells that the cross section of simple $\nu_e e^{-}$ scattering is proportional to the energy squared.

$$\sigma(\nu_e e^{-} \to \nu_e e^{-}) \propto G_F p^2, \quad p = p_{\nu_e} + p_{e^{-}} \tag{1.12}$$

Such huge dependence on the energy will eventually face the problem of the violation of the unitarity. In the 1960's, followed by the discovery of the parity violation in the weak interaction in Chien-Shiung Wu's experiment [24], Sheldon Glashow, Abdus Salam and Steven Weinberg proposed the new electroweak unification model which predicted the existence of the neutral current [25–27]. The model states that the parity is maximally violated in the weak interaction, and weak current interaction is expressed as a projection operator for the left-handed helicity P_L, defined as:

$$P_L \equiv \frac{1-\gamma_5}{2}, \quad \gamma_5 = \begin{pmatrix} 1 & 0 \\ 0 & -1 \end{pmatrix} \tag{1.13}$$

Therefore current-current interactions can be written as:

$$\bar{\psi}\gamma P_L\psi = \bar{\psi}\gamma\left(\frac{1-\gamma_5}{2}\right)\psi = \frac{1}{2}(\bar{\psi}\gamma^{\mu}\psi - \bar{\psi}\gamma^{\mu}\gamma_5\psi) \tag{1.14}$$

At the last term in (1.14), notice it includes the difference between vector and axial vector currents, which is known as $V-A$ structure (in $V-A$ theory). In electroweak unification model, we start by considering the electroweak gauge group $SU(2)_L \times U(1)_Y$. Each of these gauge groups is characterized by a number of vector fields equal to the number of their respective generators n^2-1.

$$W_{\mu}^{1}, \quad W_{\mu}^{2}, \quad W_{\mu}^{3}, \quad B_{\mu} \tag{1.15}$$

$SU(2)_L$ has three vector fields W_{μ}^{i} $(i=1,2,3)$, which couples the left-handed fermions to the weak isospin I^i and $U(1)_Y$ has the vector field B_{μ}, which has hypercharge Y. $SU(2)_L$ and $U(1)_Y$ have independent coupling constants g and g', respectively. They are not necessarily equal, and the ratio g'/g has key role in the theory. W_{μ}^{1} and W_{μ}^{2} can be combined to express the mass eigenstate of $W^{\pm}$

$$W_{\mu}^{\pm} = \frac{1}{\sqrt{2}}(W_{\mu}^{1} \mp iW_{\mu}^{2}) \tag{1.16}$$

We now know that vector fields W_{μ}^{1} and W_{μ}^{2} are responsible for forming $W^{\pm}$ bosons from (1.16). Spontaneous symmetry breaking results in the transformation of the W_{μ}^{3} and B_{μ} bosons into distinct physical bosons and these can be expressed in terms of the Weinberg angle θ_W

$$\begin{pmatrix} Z_{\mu} \\ A_{\mu} \end{pmatrix} = \begin{pmatrix} -\sin\theta_W & \cos\theta_W \\ \cos\theta_W & \sin\theta_W \end{pmatrix} \begin{pmatrix} B_{\mu} \\ W_{\mu}^{3} \end{pmatrix} \tag{1.17}$$

Here, the vector fields Z_{μ} and A_{μ} correspond to the Z^0 boson and γ, respectively. Covariant derivative of the electroweak interaction is:

$$D_{\mu} = \partial_{\mu} - igW_{\mu}^{i}I^{i} - ig'B_{\mu}Y \tag{1.18}$$

Therefore, the coupling between gauge fields (W_{μ}^{i} and B_{μ}) to any fermions can be expressed as follow.

$$D_{\mu}\psi = (\partial_{\mu} - igW_{\mu}^{i}I^{i} - ig'B_{\mu}Y)\psi \tag{1.19}$$

Note that since the symmetry of $U(1)$ gauge group is unbroken, W_{μ}^{3} remains massless. The broken symmetry of $SU(2)_L \times U(1)_Y$ requires to have massive spin boson, while there needs to be a theoretical framework for them to acquire mass. This mechanism is introduced in the Section 1.4.

1.3.3 Strong Interaction

Strong interaction is described by the Quantum Chromodynamics (QCD) of gauge theory. Its structure is based on the $SU(3)_C$ non-abelian gauge group, with three generators corresponding to three distinct charges, often defined as red, blue and green. Within the Standard Model framework, quarks and gluons would strongly interact with each other. Quark form one color triplet with one color degrees of freedom. Conversely, anti-quark have a anti-color triplet. Gluons come with the adjoint representation of $SU(3)_C$, meaning that it comes with a pair of color and anti-color combination. This signifies that gluons not only act as a mediator but also interact with each other via gluon-gluon interactions. In principle, $SU(3)_C$ gauge symmetry can allow 9 species of gluons with color octet ($\mathbf{8}$) and color singlet ($\mathbf{1}$) forming $\mathbf{8} \oplus \mathbf{1}$. However, singlet gluon signifies the existence color neutral strongly interacting gauge boson with infinite range, similarly to photons. Such long-ranged strong interactions are yet to be observed, thus the current QCD model only includes octet gluons. Lagrangian density of quark (ψ_i) and gluon ($\mathcal{A}^a_\mu$) interaction is described as following:

$$\mathcal{L} = \bar{\psi}_i(i\gamma^\mu (D_\mu)_{ij} - m\delta_{ij})\psi_j - \frac{1}{4}G^a_{\mu\nu}G^{\mu\nu}_a \tag{1.20}$$

where i and j represent color charge of field ψ which run from 1 to 3, m is the mass of the quark, and δ_{ij} is the Kronecker symbol. D_μ is the covariant derivative represented by

$$(D_\mu)_{ij} = \partial_\mu \delta_{ij} - ig(T_a)_{ij}\mathcal{A}^a_\mu \tag{1.21}$$

g is the strong coupling constant, T_a is the $SU(3)$ generators with $a = 1...8$. The $G^a_{\mu\nu}$ is the gauge invariant gluon field strength tensor, analogous to $F_{\mu\nu}$ in QED, represented by:

$$G^a_{\mu\nu} = \partial_\mu \mathcal{A}^a_\nu - \partial_\nu \mathcal{A}^a_\mu - g f_{abc}\mathcal{A}^b_\mu \mathcal{A}^c_\nu \tag{1.22}$$

where a, b and c indices again run from 1 to 8, as it is adjoint representation of $SU(3)$. The f_{abc} are the fine structure constants of this group.

1.4 Spontaneous Symmetry Breaking

In the Section 1.3.1, we have seen from the (1.3) that the unbroken symmetry of $U(1)_{EM}$ gauge group under the $U(1)$ gauge transformation prevents its spin-1 gauge boson (γ) from acquiring mass. However, vector bosons such as Z^0 and $W^{\pm}$ boson were experimentally observed to have individual masses at 91.2 GeV [28] and 80.4 GeV [29], respectively. These are called the “massive gauge bosons" and they acquire their mass via the *spontaneous symmetry breaking*, which is the broken symmetry of the $SU(2) \times U(1)$ gauge group.

1.4.1 Higgs Mechanism

The scalar field Lagrangian can be written in the following form:

$$\mathcal{L}_{Higgs} = |D_\mu \phi|^2 - V(\phi) \tag{1.23}$$

where the complex scalar field ϕ can be represented as

$$\phi = \begin{pmatrix} \phi^+ \\ \phi^0 \end{pmatrix} = \frac{1}{\sqrt{2}} \begin{pmatrix} \phi_1 - i\phi_2 \\ \phi_3 - i\phi_4 \end{pmatrix} \tag{1.24}$$

and is invariant under the local phase transformation. $V(\phi)$ in (1.23) is the potential for the Higgs field, which is given by

$$V(\phi) = -\mu^2 |\phi|^2 + \lambda(|\phi|^2)^2 \tag{1.25}$$

The term λ describes the self-interactions among the scalar fields and the vacuum

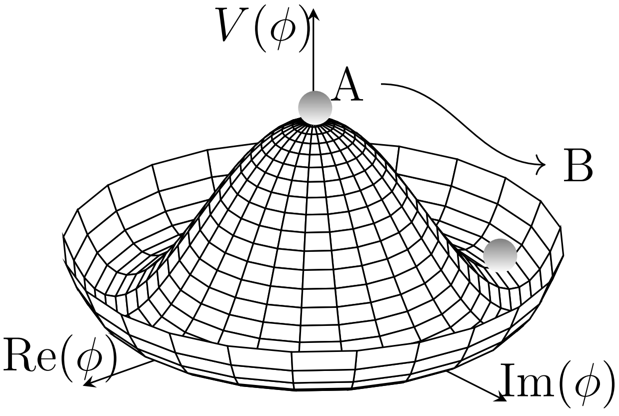

FIGURE 1.2: The Higgs potential $V(\phi)$

stability requires $\lambda > 0$. The minimum value that can be taken by this potential is called the Vacuum Expectation Value (VEV). One can take the derivative of (1.25) to search the potential's minima.

$$0 = -2\mu^2\mu^2\phi + 4\lambda\phi|\phi|^2 \tag{1.26}$$

and the minimum is

$$|\phi|^2 = |\phi^+|^2 + |\phi^0|^2 = \frac{\nu^2}{2} \tag{1.27}$$

where we defined

$$\nu \equiv \frac{\mu}{\sqrt{\lambda}} \tag{1.28}$$

as the VEV, and this spontaneously breaks the $SU(2) \times U(1)$ gauge symmetry. The vacuum state $\langle\phi\rangle$ is then

$$\langle\phi\rangle = \frac{1}{\sqrt{2}}\begin{pmatrix} 0 \\ \nu \end{pmatrix} \tag{1.29}$$

Expanding this around the vacuum state, we can express the complex scalar field as in (1.24)

$$\phi = \frac{1}{\sqrt{2}}\begin{pmatrix} \pi_1(x) - i\pi_2(x) \\ \nu + h(x) - i\pi_3(x) \end{pmatrix} = \begin{pmatrix} \pi^+(x) \\ \frac{1}{\sqrt{2}}(\nu + h(x) - i\pi_3(x)) \end{pmatrix} \tag{1.30}$$

The fields represented as π^+ and π_3 are Goldstone bosons, and can be set to zero by the $SU(2)$ gauge transformation, leaving one real component of the scalar field ϕ. The $h(x)$ is the fluctuation of the state around the VEV, and is called *Higgs boson*. Now, just as we saw in (1.19), let us apply covariant derivative on the Higgs field.

$$D_\mu\phi = (\partial_\mu - igW^i_\mu I^i - ig'B_\mu Y)\phi \tag{1.31}$$

Since we are interested in the contribution the gauge bosons acquire their masses, we will omit the $h(x)$ mix terms. Weak isospin and hypercharge for left-handed doublets is

$$\begin{aligned} I^i &= \frac{\sigma^i}{2} \quad (\sigma^i\text{: Pauli matrices}) \\ Y &= -\frac{1}{2} \end{aligned} \tag{1.32}$$

Then the first term in (1.23) becomes

$$
\begin{aligned}
|D_\mu\phi|^2 &= \left|\left(\partial_\mu + \frac{i}{2}g\sigma^i W_\mu^i + \frac{i}{2}g' B_\mu\right)\frac{1}{\sqrt{2}}\begin{pmatrix}0\\ \nu\end{pmatrix}\right|^2 \\
&= \frac{\nu^2}{2}\left(\frac{1}{2}\right)^2\left|\left(g\sigma^i W_\mu^i + g' B_\mu\right)\begin{pmatrix}0\\ 1\end{pmatrix}\right|^2 \\
&= \frac{\nu^2}{8}\left|\begin{pmatrix} gW_\mu^1 - ig' W_\mu^2 \\ -gW_\mu^3 + g' B_\mu\end{pmatrix}\right|^2 \\
&= \frac{\nu^2}{8}\left\{g^2\left(\left(W_\mu^1\right)^2 + \left(W_\mu^2\right)^2\right) + \left(gW_\mu^3 - g' B_\mu\right)^2\right\}
\end{aligned}
\tag{1.33}
$$

By using the $W^\pm$ field defined in (1.16), the g^2 term in (1.33) becomes

$$
\frac{1}{2}\left(\frac{g\nu}{2}\right)^2 W_\mu^+ W^{\mu-}
\tag{1.34}
$$

yielding the $W^\pm$ mass m_W

$$
m_W = \frac{g\nu}{2}
\tag{1.35}
$$

It is convenient to express the ratio of the coupling g and g' using the Weinberg angle we have seen in (1.17)

$$
\tan\theta_W = \frac{g'}{g}, \quad \cos\theta_W = \frac{g}{\sqrt{g^2 + g'^2}}, \quad \sin\theta_W = \frac{g'}{\sqrt{g^2 + g'^2}}
\tag{1.36}
$$

Then the remaining two neutral gauge bosons, Z and A can have masses:

$$
Z_\mu = \frac{1}{\sqrt{g^2 + g'^2}}(gW_\mu^3 - g' B_\mu) \quad \rightarrow \quad m_Z = \frac{\nu}{2}\sqrt{g^2 + g'^2}
\tag{1.37}
$$

$$
A_\mu = \frac{1}{\sqrt{g^2 + g'^2}}(g' W_\mu^3 + gB_\mu) \quad \rightarrow \quad m_A = 0
\tag{1.38}
$$

To put this in perspective, one can count the degrees of freedom (d.f.) before and after the spontaneous symmetry breaking. Before the Higgs mechanism, complex doublet scalar field ϕ had 4 d.f., three $SU(2)_L$ gauge bosons W_μ^i had 2 d.f. each, making it 6 d.f., and $U(1)_Y$ gauge boson B_μ had 2 d.f., which made it total of 12 d.f. After the symmetry breaking, the real scalar Higgs field yields one d.f., with three massive gauge bosons $W^\pm$ and Z with 3 d.f. each, making it 9 d.f., and a massless photon with 2 d.f. making it 12 d.f in total as well. One can argue that the gauge bosons $W^\pm$ and Z acquired longitudinal component of d.f. which caused them to bare masses.

1.4.2 Fermion Mass and Higgs Boson

In the original Standard Model, i.e. without the Higgs Mechanism, all fermions (as well as all gauge bosons) were considered massless. In Section 1.4.1, we explained that massive gauge bosons in $SU(2)_L \times U(1)_Y$ gauge acquire their mass via interacting with the Higgs field. Fermions acquire their mass through the Yukawa interaction, which is the interaction between the Higgs field ϕ and the Dirac field ψ. The Lagrangian of such interactions can generally be written as following format:

$$-\mathcal{L}_{Yukawa} = \sum_{i,j=1}^{3} \left(\sum_{a=u,\ell_\nu} Y_{ij}^{a} \bar{\psi}_{L,i}^{a} \tilde{\phi} \psi_{R,j}^{a} + \sum_{b=d,\ell_e} Y_{ij}^{b} \bar{\psi}_{L,i}^{b} \phi \psi_{R,j}^{b} \right) + h.c. \tag{1.39}$$

with $\tilde{\phi} = i\sigma_2 \phi^*$. $\psi_{L,R}$ corresponds to fermions with left and right-handed helicity. u, d (ℓ_ν, ℓ_e), and i, j represents that the particle is up or down type in i and jth generation. Y_{ij}^{a} is the Yukawa coupling matrix. If we substitute Higgs fields in (1.39) by its vacuum state in (1.29),

$$-\mathcal{L}_{Yukawa} = \sum_{i,j=1}^{3} \left(\sum_{a=u,\ell_\nu} \frac{Y_{ij}^{a} \nu}{\sqrt{2}} \bar{\psi}_{L,i}^{a} \psi_{R,j}^{a} + \sum_{b=d,\ell_e} \frac{Y_{ij}^{b} \nu}{\sqrt{2}} \bar{\psi}_{L,i}^{b} \psi_{R,j}^{b} \right) + h.c. \tag{1.40}$$

Then we can characterize each terms involving Yukawa coupling as mass for each fermion m_f:

$$m_f = \frac{Y_f \nu}{\sqrt{2}} \tag{1.41}$$

1.5 Quark Pair Production at ILC

At e^+e^- colliders such as ILC (see Chapter 2), fermion pair production happens through the Z/γ exchange, as shown in Figure 1.3. Fermion pair and Z/γ bosons are coupled with electroweak interactions via $V-A$ structure as shown in the Section 1.3.2. Consider a vertex where Z^0 and γ couples. The vertex can be written as a funtion of form factors F shown in (1.42).

$$\Gamma_{\mu}^{f\bar{f}X}(k^2, q, \bar{q}) = ie \left[\gamma_\mu \left(F_{1V}^{X}(k^2) + \gamma_5 F_{1A}^{X}(k^2) \right) + \frac{\sigma_{\mu\nu}}{2m_f} (q - \bar{q})^\nu \left(iF_{2V}^{X}(k^2) + \gamma_5 F_{2A}^{X}(k^2) \right) \right] \tag{1.42}$$

where $k^2 = (q + \bar{q})^2$ is the four momentum squared for the exchanged vector bosons. q and $\bar{q}$ are the four momenta of interacting fermion and anti-fermion, respectively.

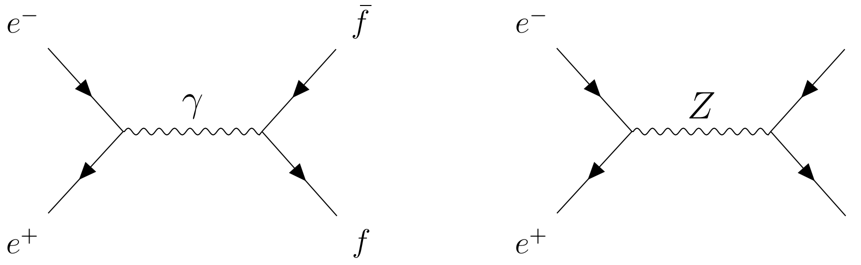

(a) γ process (b) Z exchange

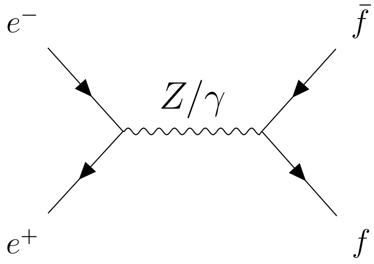

(c) Z/γ interference

FIGURE 1.3: The s-channel Feynman diagrams for the $e^+e^- \to f\bar{f}$ process through (a) γ and (b) Z exchange, as well as the (c) Z/γ interference.

$\sigma_{\mu\nu} = i\frac{1}{2}(\gamma_\mu\gamma_\nu - \gamma_\nu\gamma_\mu)$. At the tree level, Standard Model gives the form factors F_i^X as:

$$\begin{aligned} F_{1V}^{f\gamma} &= Q^f \\ F_{1A}^{f\gamma} &= 0 \\ F_{1V}^{fZ} &= \frac{I^f - 2Q^f \sin^2\theta_W}{2\cos\theta_W \sin\theta_W} \\ F_{1A}^{fZ} &= -\frac{I^f}{2\cos\theta_W \sin\theta_W} \end{aligned} \tag{1.43}$$

and

$$F_{2V}^{f\gamma} = F_{2A}^{f\gamma} = F_{2V}^{fZ} = F_{2A}^{fZ} = 0 \tag{1.44}$$

I^f is the same weak isospin defined in (1.32). Q^f is the electric charges of the fermions. In this thesis, our primary focus is on the production of light quark pairs through the e^+e^- process. Specifically, we center our attention on the couplings between vector bosons and dd, uu, and ss quark pairs. This interaction encompasses both up-type and down-type quarks. Consequently, we provide a detailed exposition of the couplings for $Zf\bar{f}$ in Equation (1.46) for both left-handed and right-handed helicity states for both quark types.

$$\begin{aligned} g_L^Z &= \frac{I^f - Q^f \sin^2\theta_W}{\sin\theta_W \cos\theta_W} \\ g_R^Z &= -\frac{Q^f \sin^2\theta_W}{\sin\theta_W \cos\theta_W} \end{aligned} \tag{1.45}$$

and thus the form factors for each polarizations writes:

$$\begin{aligned} \mathcal{F}_{ij}^L &= -F_{ij}^\gamma + \frac{-1/2 + \sin^2\theta_W}{\cos\theta_W \sin\theta_W} \frac{s}{s - m_Z^2 + i\Gamma_Z m_Z} F_{ij}^Z \\ \mathcal{F}_{ij}^R &= -F_{ij}^\gamma + \frac{\sin^2\theta_W}{\cos\theta_W \sin\theta_W} \frac{s}{s - m_Z^2 + i\Gamma_Z m_Z} F_{ij}^Z \end{aligned} \tag{1.46}$$

where m_Z and Γ_Z are the mass and decay width of Z bosons, respectively. In the electroweak theory, Born-level differential cross section for $e^+e^- \to f\bar{f}$ using the electron beam polarization $I = L, R$, produced at the angle θ is predicted as:

$$\begin{aligned} \left(\frac{d\sigma^I}{d\cos\theta}\right)_f = \frac{3}{4}\mathcal{A}N_c\beta \Bigg[& (1+\cos^2\theta)\{(\mathcal{F}_{1V}^I + \mathcal{F}_{1V}^I)^2 + (\beta\mathcal{F}_{1A}^I)^2\} \\ & - 4\cos\theta(\mathcal{F}_{1V}^I + \mathcal{F}_{2V}^I)\beta\mathcal{F}_{1A}^I \\ & + \sin^2\theta \left(\frac{\mathcal{F}_{1V}^I + \gamma^2\mathcal{F}_{2V}^I}{\gamma}\right)^2 \Bigg] \end{aligned} \tag{1.47}$$

where

$$\mathcal{A} = \frac{4\pi\alpha^2}{3s} \tag{1.48}$$

with α being the electromagnetic coupling constant, s is the center of mass energy. N_c in (1.47) is the number of colors of fermions, β and γ are the velocity and the Lorentz factor of the fermion f, respectively. Integrating over all scattering angle yields the total cross section as:

$$\begin{aligned} \sigma_{tot}^I &= \int_{-1}^{1} d\cos\theta \left(\frac{d\sigma^I}{d\cos\theta}\right)_f \\ &= 2\mathcal{A}N_c\beta\left[\left(1 + \frac{1}{2\gamma^2}\right)(\mathcal{F}_{1V}^I)^2 + (\beta\mathcal{F}_{1A}^I)^2 + 3\mathcal{F}_{1V}^I\mathcal{F}_{2V}^I + \left(1 + \frac{\gamma^2}{2}\right)(\mathcal{F}_{2V}^I)^2\right] \end{aligned} \tag{1.49}$$

It is worth noting that (1.49) is valid for polarized incoming beam, which is achievable in the ILC. Without the polarization condition, one can only extract the sum of all polarization states of the outgoing fermions.

1.6 Open Questions to New Physics

Despite the success of the Standard Model for predicting phenomena in particle physics to extremely precise level, there are many open questions and issues yet to be explained. One of them is the explanation for *hierarchy problem*. As mentioned in Section 1.4, the electroweak symmetry breaking is triggered by the Higgs mechanism. While the dynamics of gauge bosons are govern by the gauge symmetry, there is no symmetry that can protect Higgs coupling to fermions, as well as its self-coupling. The effective mass of the Higgs boson that was observed at the LHC, with $m_H = 125\,\text{GeV}$, is after the quadratic quantum corrections, which delicately cancels out with its bare mass. This signifies that if we move on to the Plank scale, correction with the order of square of Plank mass ($\sim 10^{19}\,\text{GeV}$) is necessary. This bizarre fine tuning often referred to as naturalness or hierarchy problem. One way to stabilize the Higgs mass against large quantum correction, is to consider Higgs boson as a part of extra-dimensional component of gauge potentials. This model is referred to as the Gauge-Higgs Unification (GHU) model [13, 15].

In GHU, gauge symmetry is dynamically broken with Aharonov-Bohm (AB) phase θ_H in the fifth dimension. This signifies that the extra dimension offers possibility for the different flavor fermions to extend its wave function to the extra dimension. Moreover, fermions with different chirality may have dependence in their wave function towards this extra dimension. As a result, Higgs boson appears as a fluctuation mode of the θ_H. Physical phenomena of the GHU is very similar to the SM below the EW scale. GHU permits gauge couplings of quarks and leptons to deviate from the SM with less than 0.1% for $\theta_H \simeq 0.1$ on the Kaluza-Klein (KK) mass scale [16]. The GHU model also features a Z' boson with large coupling to the right-handed component of fermions, which are the KK modes of Z, γ and Z_R. This was strongly constrained by the LHC experiment for searching Z' and W' bosons at $\sqrt{s} = 13\,\text{TeV}$ with data collected up to $140\ \text{fb}^{-1}$ [17].

In the future e^+e^- experiments, particularly at the ILC, it is possible to probe the region over tens of TeV in KK mass scale. Through the $e^+e^- \to f\bar{f}$ process, which includes the interference of Z', Z^0 and γ, substantial deviation from the SM is expected even when those Z' may be as heavy as $10\,\text{TeV}$. A study [13] has shown that fermion coupling to the neutral vector boson and Z' can be determined to be the values listed in Table 1.2, when $\theta_H = 0.10$ and KK mass scale of $m_{KK} = 13\,\text{TeV}$. If the ILC can precisely measure these couplings, we can distinguish GHU from the other BSM theories to determine whether they are consistent with the observation or not. This motivates us to study the Z/γ coupling to the fermion pair, which is presented in Chapter 5.

f	g^L_{Zf}	g^R_{Zf}	$g^L_{Z^{(1)}f}$	$g^R_{Z^{(1)}f}$	$g^L_{Z_R^{(1)}f}$	$g^R_{Z_R^{(1)}f}$	$g^L_{\gamma_R^{(1)}f}$	$g^R_{\gamma_R^{(1)}f}$
ν_e	0.5687	0	3.2774	0	1.0322	0	0	0
ν_μ	0.5687	0	3.1207	0	0.9852	0	0	0
ν_τ	0.5687	0	3.0165	0	0.9852	0	0	0
e	0.3058	0.2629	1.7621	0.0584	1.0444	0	2.7587	0.1071
μ	0.3058	0.2629	1.6778	0.0584	0.9969	0	2.6268	0.1071
τ	0.3058	0.2629	1.6218	0.0584	0.9652	0.0001	2.5391	0.1070
u	0.3934	0.1753	2.1951	0.0390	0.3415	0	1.7807	0.0714
c	0.3934	0.1753	2.1147	0.0389	0.3296	0	1.7154	0.0714
t	0.3938	0.1749	1.7406	0.3269	0.2740	-0.7395	1.4121	0.6017
d	-0.4811	0.0876	2.6842	0.1162	0.3297	0.1801	0.8904	0.2113
s	-0.4811	0.0876	2.5858	0.1460	0.3182	0.2197	0.8577	0.2657
b	-0.4811	0.0876	2.1284	0.2900	0.2646	0.4096	0.7059	0.5279

TABLE 1.2: List of coupling constants between neutral vector bosons, Z' to the fermion pair in the units of $g_w = e/\sin\theta_W$ when $\theta_H = 0.10$ and $m_{KK} = 13\,\text{TeV}$ [13].

Chapter 2

International Linear Collider

2.1 Introduction to ILC

In the course of particle physics history, particle accelerators played a huge role in the discovery and understanding of new physics and particles. There are two types of colliders: lepton and hadron colliders. The Large Hadron Collider (LHC) is a proton-proton collider situated near the France-Switzerland border, close to Geneva, with a circumference of 27 km. It is currently operational with a center-of-mass energy of 13.0 TeV. The discovery of a scalar particle with features as expected for the Standard Model Higgs Boson can be considered as the completion of the Standard Model. The large range of centre-of-mass energies swept over by the LHC allows for scanning the LHC data for signals of new physics, such as new resonances or intriguing signals with missing mass. The new scalar particle has to be examined with higher precision than available at LHC. The absence of clear signals for new physics calls for a closer look at the quantum fluctuations. Both call arguments for high precision measurements as they are available by lepton colliders and in particular by e^+e^- colliders. Lepton collider has multiple advantages over hadron colliders, such as well-known initial state of colliding particles and comparatively small and well calculable QCD backgrounds. Circular colliders are heavily limited by energy loss due to synchrotron radiation. The energy loss per turn is

$$E_{rad} \propto \frac{E^4}{m^4 r} \tag{2.1}$$

where E is energy, m is the particle mass and r is the curvature. As shown in eq. 2.1, radiated energy due to synchrotron radiation, E_{rad} is particularly significant when dealing with lighter particles as electrons. The International Linear Collider (ILC) [30] is

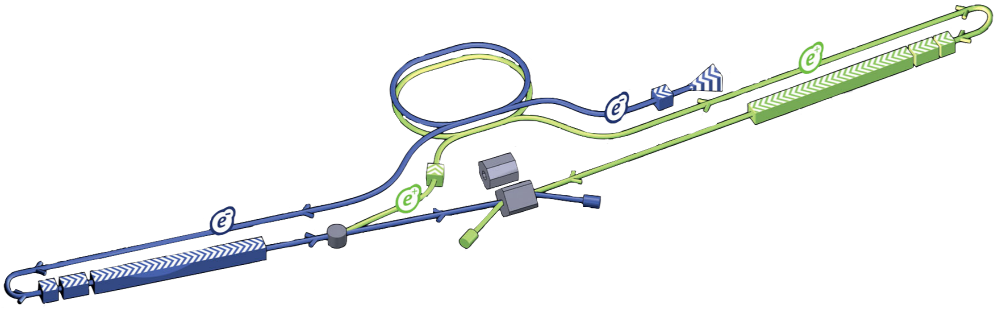

Figure 2.1: Layout of the ILC

a proposal for a linear electron-positron collider. It does not suffer from the synchrotron radiation and initial states of electron and positron beams can be controlled.

2.2 Physics Case of the ILC

One of the substantial goals to be achieved by ILC is the precision measurements of particle properties. ILC facilitates the model independent search of the electroweak parameters. Table 2.1 summarizes key physics processes at different centre-of-mass energies available with the ILC

Energy	Reaction	Objective
91 GeV	$e^+e^- \to Z^0$	Z^0 physics
160 GeV	$e^+e^- \to WW$	$W^\pm$ mass precision
250 GeV	$e^+e^- \to Z^0H$	Precision Higgs coupling
350 GeV	$e^+e^- \to t\bar{t}$	Top mass precision
	$e^+e^- \to \nu\bar{\nu}H$	Precision Higgs coupling
500 GeV	$e^+e^- \to t\bar{t}$	Top coupling
	$e^+e^- \to t\bar{t}H$	Top Higgs coupling
	$e^+e^- \to Z^0HH$	Higgs self coupling
1 TeV	$e^+e^- \to \nu\bar{\nu}t\bar{t}$	Composite Higgs and Top

Table 2.1: Main physical process that is expected to be seen at the ILC

At the initial energy of 250 GeV, where the cross section of the Higgs-strahlung process is the largest, it is expected to measure the Higgs boson mass with high precision by calculating the recoil mass. Higgs couplings to Standard Model fermions and the Z can be determined at the 1% level. The recoil technique opens also sensitivity to invisible Higgs decays. Studies of the Higgs boson are extended to the higher energies for the Higgs self-coupling and the coupling with the top quark, also known as top Yukawa coupling. Investigation of top quarks also plays a crucial role for the ILC project. A scan at the $t\bar{t}$ threshold around 350 GeV allows for extracting a theoretically well defined value of the top quark mass to a precision of at least 50 MeV. The coupling between gauge boson and top quark is particularly sensitive to the new physics and these processes motivate the studies presented in this thesis.

2.3 The Accelerator Apparatus

2.3.1 Electron Source

Polarized electron beam, which can satisfy the requirements for the bunch train, must be produced at electron source. At the ILC, the beam is produced by laser illuminating the GaAs photocathode inside the direct current (DC) gun. When polarized photons are incident upon the photocathode, polarized photoelectrons will be emitted due to the photoelectric effect and it is expected to have maximum of 80% polarization. These photoelectrons will form a polarized electron bunch, which will be delivered to the normal conducting structure, accelerating up to 76 MeV. It will then go through superconducting linac while longitudinally aligning the electrons' spin directions and accelerating them to 5 GeV. Finally, the bunch will be injected to the Damping Ring.

2.3.2 Positron Source

Electron beam that passed the main linac will go through superconducting helical undulator which let the electron beam oscillating around the main orbit, emitting in form of circularly polarized photons as a result. These photons with energy ranging between 10 MeV–30 MeV will hit the rim of the rotating titanium alloy target, pair producing e^+e^- as a result. After hitting the target, positrons are separated from electrons and photons by applying magnetic field at the end of the RF cavities. Similar to the electrons, positrons will also go through normal conducting and superconducting linac to

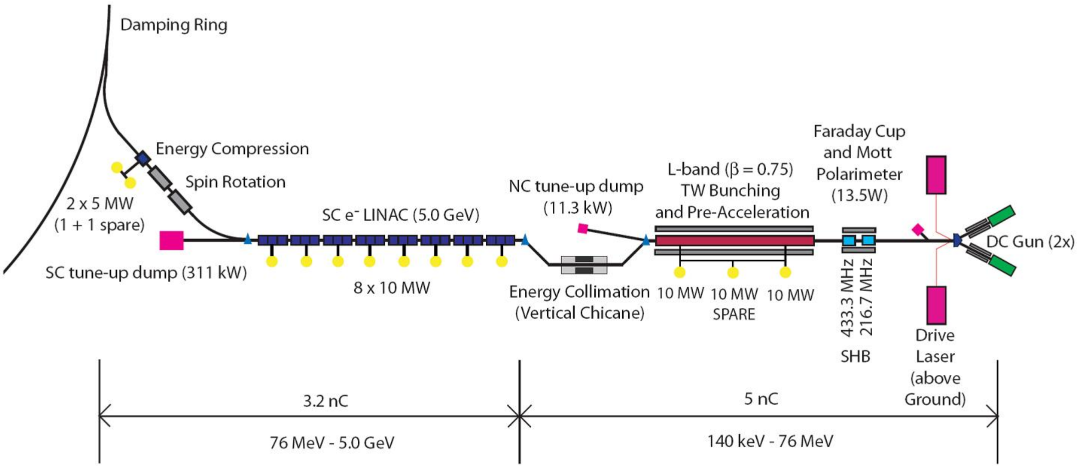

FIGURE 2.2: Sketch of electron source instruments.

be accelerated from 125 MeV to 5 GeV. With this method, positrons will inherit the polarization of the photon, obtaining at least 30% polarization through the process.

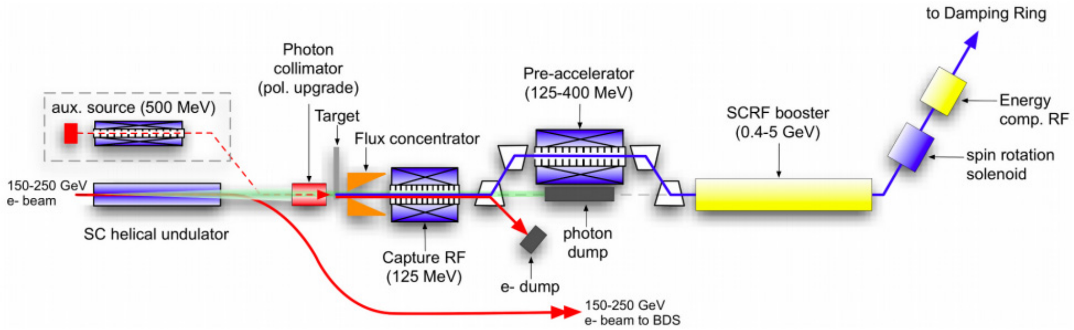

Figure 3.4. Overall Layout of the Positron Source, located at the end of the electron Main Linac.

FIGURE 2.3: Positron source layout.

2.3.3 Damping Ring

Electron and positron beam passes through a damping ring with 3.2 km circumference size, each operating at the beam energy of 5 GeV. Due to its physical structure, ILC relies on each single bunch crossing, unlike LHC which circulates bunches until they collide. Hence, optimizing the collision probability in each bunch crossing necessitates the minimization of beam emittance. The beam emittance, a function of the position relative to the nominal beam orbit and its derivative with respect to this orbit, varies with different momenta, leading to distinct orbits. Damping ring contributes to this by minimizing the phase space of the beam. When the beam circulates inside the damping ring, the one with higher momentum loses its energy due to the emission of synchrotron radiation, while the lower one obtains the energy by the acceleration provided by the ring. Damping ring layout is shown in the Fig. 2.4.

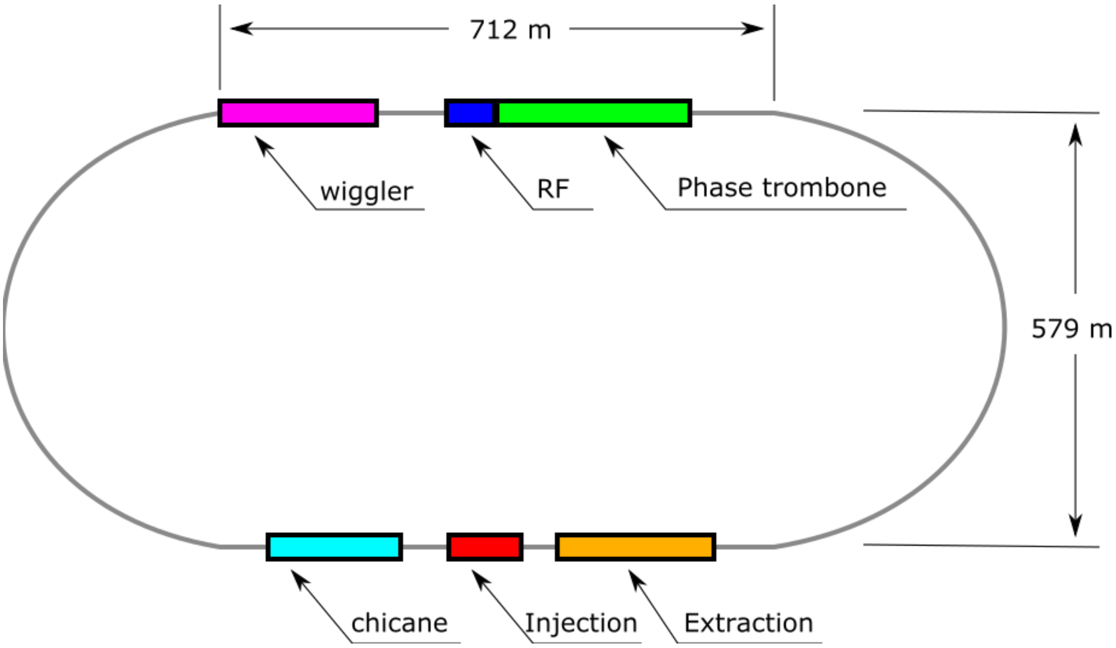

Figure 2.4: Layout of the damping ring.

2.3.4 Main Linac

There are two main linacs located at the both sides of the ILC, each accelerates electron and positron beams. Both of which are 11 km long, containing 7,400 of 1.3 GHz superconducting nine-cell niobium cavities, operating at 2 K (Fig. 2.5). These cavities accelerate beams from 15 GeV to 250 GeV at maximum, with average acceleration gradient of 31.5 MeV/m.

2.3.5 Beam Delivery System

Beam delivery system governs the work of delivering the beam from the electron and positron source, while converging the beam at the collision point. After the collision, it will deliver the spent beam to the beam dump.

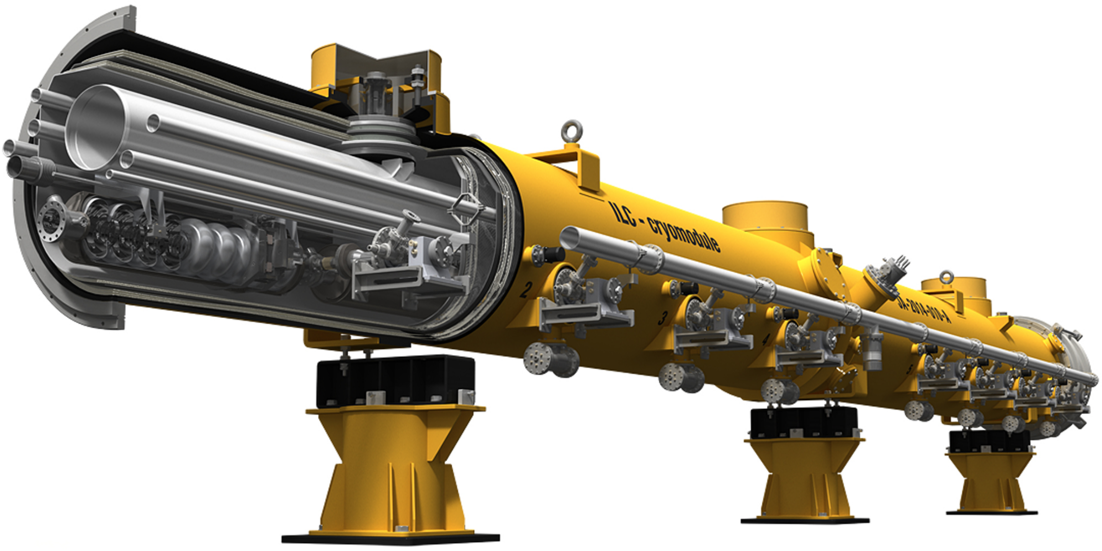

Figure 2.5: Cryomodule that is planned to implement niobium cavities.

2.4 Bunch Structure

The ILC operates with a structured beam arrangement, organized into trains and bunches. This configuration enables detectors to utilize a “power pulsing” mode, where the bias current of the detectors is turned off between trains, effectively reducing the overall power consumption of the detector complex. Each compressed train consists of 2,625 bunches and occurs at a frequency of 5 Hz, with each bunch separated by 366 ns. Successful implementation of the power pulsing mode requires synchronization between the detector electronics and the beam frequency. Power pulsing mode is considered for the SiW-ECAL analysis, as detailed in Section 4.3.5.

Chapter 3

International Large Detector

3.1 Introduction

In the proposed configuration of the ILC, two detector concepts are designated for placement at the interaction point: the Silicon Detector (SiD) and the International Large Detector (ILD). SiD functions as a multi-purpose detector, incorporating a 5-Tesla magnet and a silicon tracking system. ILD, another multi-purpose detector, employs a large-volume gas detector as a tracker, as detailed in Section 3.3.2. To enhance sensitivity to potential new physics phenomena, both detectors are equipped with multiple sub-detectors featuring high spatial and temporal resolution. Both SiD and ILD detectors will alternate their data taking by taking turns, also known as “push-and-pull" mechanism.

Figure 3.1 shows the schematic view of ILD. It has the 4π barrel structure with 13.240 m length and 7.833 m radius. Particles will hadronize or pass through the entire detector depending on their type as illustrated in Figure 3.2. Below are the brief description about each sub-detector in the ILD:

- **Vertex Detector (VTX)**
  VTX is a multi-layer pixel detector, specialized for the vertex identification. The detector is the inner most layer in the ILD, the closest sub-detector to the interaction point. The detector is optimized for high spatial resolution and it has the minimal thickness in order to conduct the precision measurements in the vertex position.

- **Silicon Inner Tracker (SIT)**
  SIT is a series of silicon strips that surround the VTX. The purpose is to assist the VTX data by covering the larger polar angle.

- **Forward Tracking Disk (FTD)**
  FTD captures the particle emitted in the forward region. It is composed of five silicon strip disks, which surround the beam pipe.

- **Time Projection Chamber (TPC)**
  TPC is the gaseous detector in the ILD designed to perform 3-dimensional reconstruction on charged particle tracks. It can register up to 224 hits per track and it also allows the dE/dx measurements.

- **Electromagnetic Calorimeter (ECAL)**
  ECAL is the calorimeter to measure the energies of the charged particles. It is comprised of absorber unit, which creates the electromagnetic shower, and the sensor unit, which captures those showers. For those materials, Tungsten is chosen to be the absorber, while silicon or scintillator are considered as the technical alternatives for the sensors.

- **Hadronic Calorimeter (HCAL)**
  HCAL plays a central role in separating neutral and charged hadrons. The highly segmented sensors inside the HCAL facilitates the precise energy measurements.

- **Muon Yoke**
  Muon Yoke serves for the identification of muons above few GeV.

Overall data acquisition in ILC does not operate on external trigger, maximizing the physical sensitivity.

3.2 Particle Flow Algorithm

Since the ILC is a lepton collider, final states of the collision have lower rate of QCD backgrounds compared to those of hadron colliders. Thus, in a clean environment where there are low radiation levels, the ILC motivates the reconstruction of individual particles produced inside the detector, which provides the ideal premises for the application for the Particle Flow Algorithm (PFA). PFA aims to reconstruct individual particles by taking available detector measurements for each given type. Figure 3.3 shows the detector measurements for different particle types:

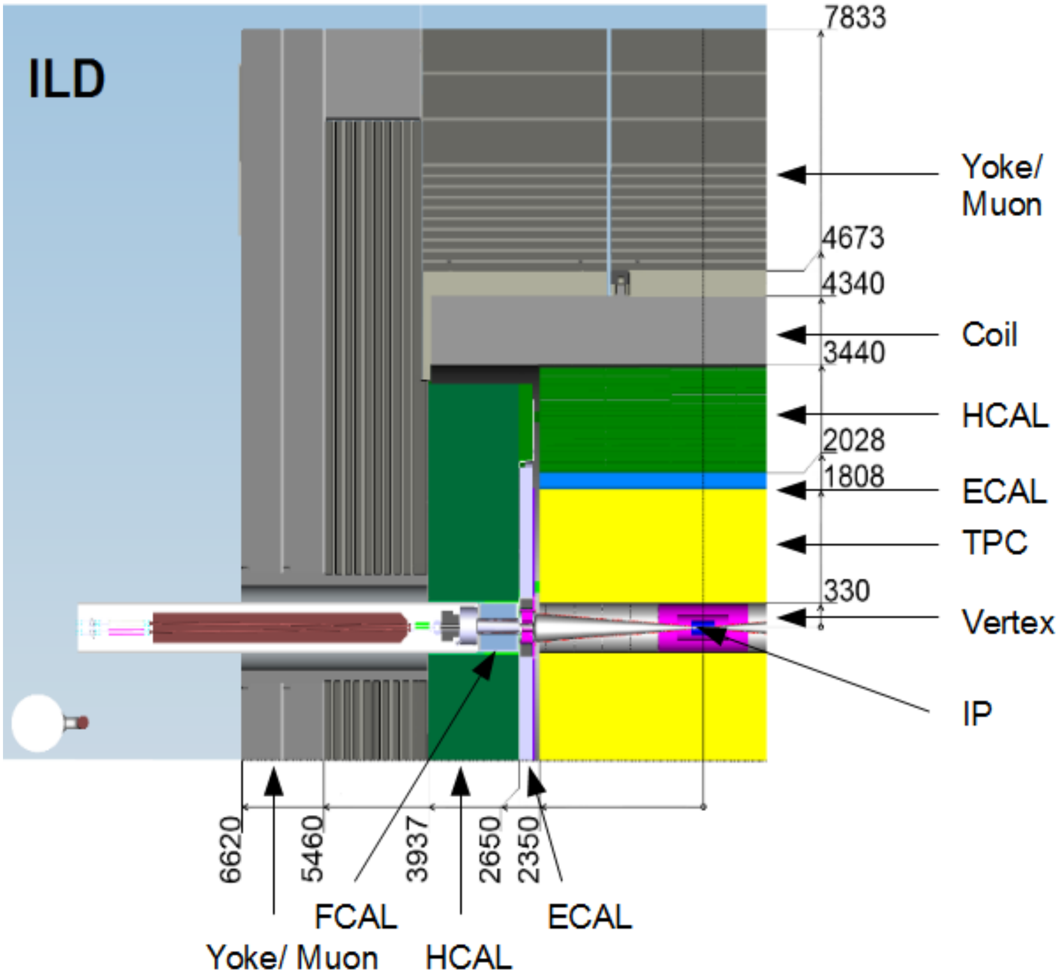

FIGURE 3.1: Cross sectional view of a quadrant of the ILD detector. The distance measures in mm.

- Photons only leave cluster in ECAL.
- Electrons will leave track in TPC and cluster in ECAL.
- Charged hadrons such as $\pi^{\pm}$, $K^{\pm}$ and protons will leave track in both TPC and ECAL, along with cluster in HCAL.
- Neutral hadrons such as π^0, K^0 and neutrons will leave cluster in HCAL, without any connected track.
- Muons will leave track in all TPC, ECAL, HCAL and Muon Yoke.

The design goal of the ILD is to achieve the jet energy resolution in order of 3-4% over the entire jet energy range. This is supposed to be achieved with PFA which has the goal to measure each individual particle's final states. The jet energy is shared, 65% comes

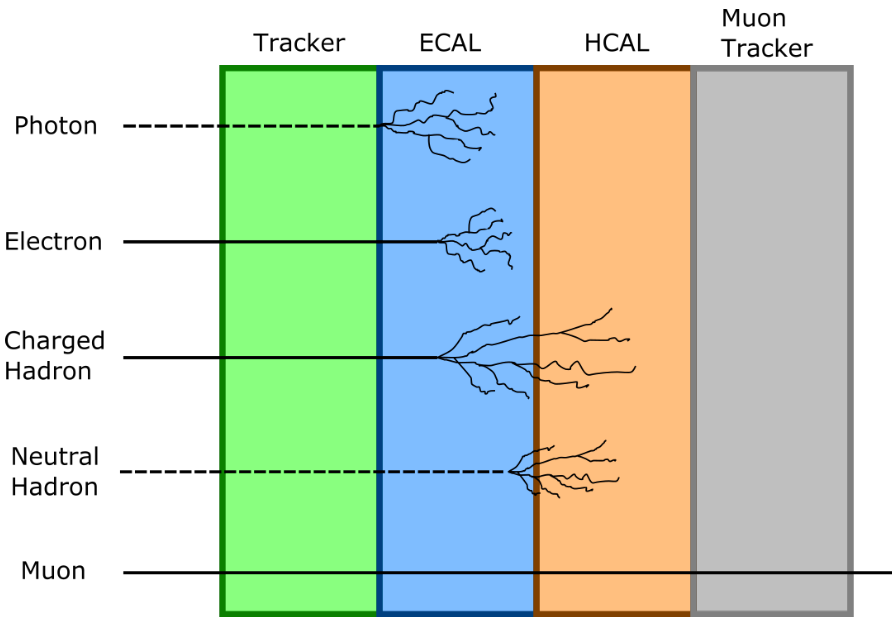

FIGURE 3.2: The image shows different particle types being stopped or hadronized at different points in the detector.

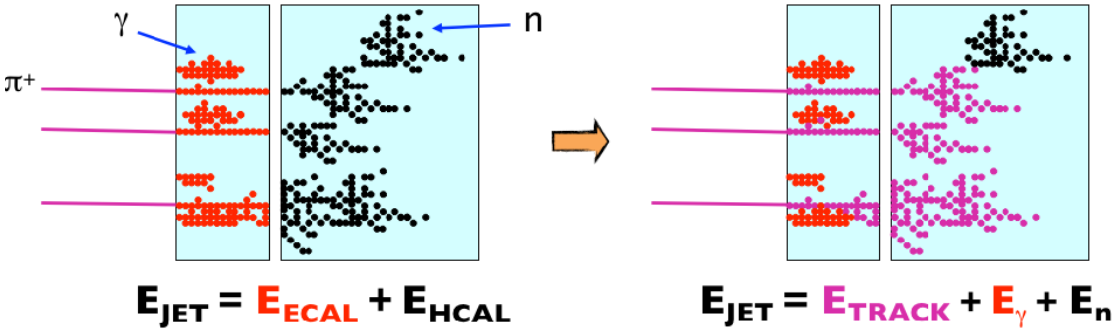

FIGURE 3.3: Difference in traditional and PFA approach in jet energy computation is shown here. In the traditional approach (left) jet energy is the sum of energies contained in ECAL and HCAL. With the PFA approach (right), jet energy is calculated as a sum of energies in track, gamma and neutral hadrons. [1]

from charged particles, 27% from photons, 10% from neutral hadrons, and 1% from neutrinos. Furthermore, for particle momenta up to approximately 100 GeV–150 GeV, tracking systems generally exhibit a higher precision in momentum resolution compared to calorimeters. This superiority is attributed to the tracking system's combination of high spatial resolution and its size. Therefore, for the calculation of the jet energy, PFA uses the tracker information for the charged particles while using the calorimeter information for the others.

The reduction of pixel size in calorimeters supports PFA to distinguish individual particles. An optimization study (using the *PandoraPFA*) [1] has shown the relation between the jet energy resolution (expressed as rms_{90}, the Root Mean Square of the central 90%

of the energy) and the transverse pixel size of ECAL and HCAL, for various jet energies (Figure 3.4). In such reconstruction scheme, the ECAL transverse segmentation should have at least as fine as $10{\times}10\,\mathrm{mm}^2$, in order to meet the ILD jet energy resolution requirement of 3-4%. Therefore, it is evident that the calorimeters for the ILD have to have highly granular sensors.

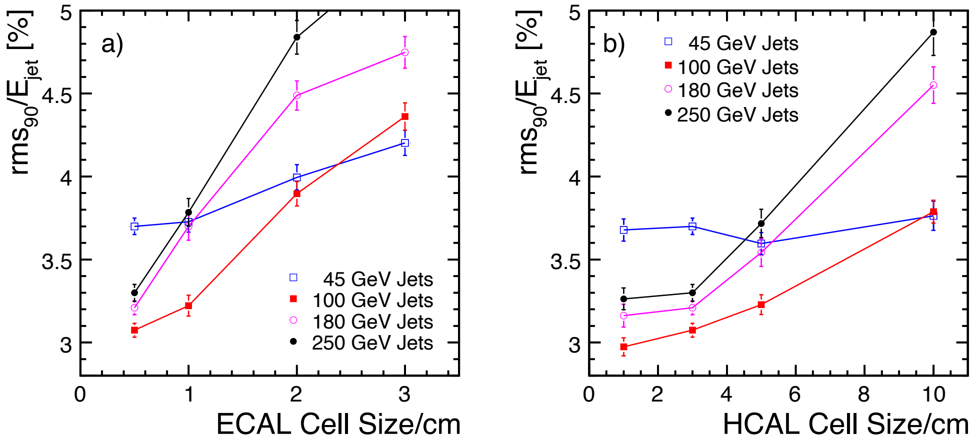

FIGURE 3.4: The dependence of the jet energy resolution on the transverse pixel segmentation for ECAL (left) and HCAL (right). [1]

3.3 Sub-detectors

3.3.1 Vertex Detector

Vertex detector is used for the precise vertex position measurements, aimed to identify primary vertex (PV) and secondary vertex (SV) positions. Primary vertex is the point where electron and positron collide. Quarks such as b and c quarks hadronize into B and D mesons with the life-time of about 1.5 ps [31, 32] until the decay giving rise to secondary vertices, which is displaced from the PV. This distance between PV and SV helps us distinguish b and c jets, from light quark jets (u, d and s). Therefore, precision measurement of PV and SV position plays a central role for jet flavor identification.

The ability to reconstruct vertices depends on the impact parameter resolution. In fact, the main performance goal of the ILD vertexing system is to reach the track impact parameter of $\sigma_b < 5 \oplus \frac{10}{p \sin^{3/2}\theta}$ µm. To satisfy this requirement, the VTX should fulfill following criteria:

- A spatial resolution near IP better than 3 µm.

- A material budget below 0.15% X_0/layer.
- A pixel occupancy not exceeding a few %.
- The first layer located at a radius of ∼1.6 cm.

Current design of VTX has a barrel structure with three cylindrical layers of double-sided ladder (Figure 3.5). Each layer is equipped with pixel sensors that are ∼2 mm apart from each other. The radius of each layer ranges from 16 to 60 mm from the beam line. The standard for both readout time and spatial resolution for the inner layers is higher than the those for the outer layer since they are closer to the IP. Therefore, the inner layer covers about 10% of the entire active detector surface of VTX, in order to optimise for single point resolution and short readout time.

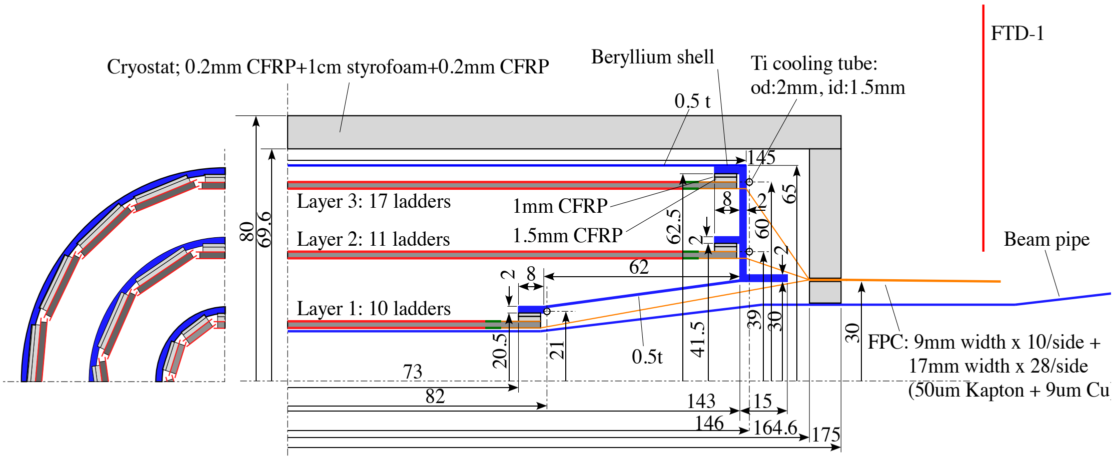

Figure 3.5: Cross sectional view of the VTX.

Currently, there are three technological alternatives for the VTX that are being considered: CMOS Pixel Sensors (CPS), Fine Pixel CCD (FPCCD) [33], and Depleted Field Effect Transistor sensors(DEPFET). They are:

- CPS is a 50 µm thick sensor produced with 0.35 µm CMOS process, which gives the spatial resolution of 3 µm with readout time of 10 µs. The detector is cost effective and suited for low-mass detector.
- FPCCD is a highly granular CCD consists of 5×5 μm^2 pixel sensors. It has 15 µm sensitive layer, resulting in less charge spread. The detector has high spatial resolution and the readout is performed between the bunch trains.
- DEPFET is a pixel detector combined with detector-grade silicon sensor. It has pixel size of 25×25 μm^2 with readout time of 25 µs.

The baseline design of the VTX is summarized in the Table 3.1.

	R (mm)	$\lvert z\rvert$ (mm)	$\lvert\cos\theta\rvert$	σ (µm)	Readout time (µs)
Layer 1	16	62.5	0.97	2.8	50
Layer 2	18	62.5	0.96	6	10
Layer 3	37	125	0.96	4	100
Layer 4	39	125	0.95	4	100
Layer 5	58	125	0.91	4	100
Layer 6	60	125	0.90	4	100

TABLE 3.1: Baseline design for the individual layer in the VTX. The spatial resolution and readout time listed here are based on the CMOS type detector option.

3.3.2 Time Projection Chamber

The time Projection chamber is the central tracker of the ILD. TPC offers two main measurements: three-dimensional track tracing and the energy loss per particle track length dE/dx.

The schematic view of the TPC is shown in the Figure 3.6. The TPC consists of a gas-filled field-cage in an electric field with two endplates that cap the gas volume. It has the radius of $330\,\text{mm} < r < 1770\,\text{mm}$ and the height of 2350 mm, covering the solid angle within $|\cos\theta| < 0.98$ region. The volume is filled with a stable gas, and currently T2K gas mixture Ar:CF$_4$:iC$_4$H$_{10}$ (95:3:2) is consider to minimize the transverse diffusion and maximize the drift velocity [34]. The endplate has 220 pad rows with each pad size $1{\times}6\,\text{mm}^2$, making it 10^6 pads in total. The resolution parameters are listed in the table 3.2.

Direction	σ_{point} (zero drift)	σ_{point} (full drift)	σ_{2hit}
$r\phi$	60 µm	100 µm	2 mm
rz	0.4 mm	1.4 mm	6 mm

TABLE 3.2: Resolution parameters expected for the TPC.

Currently, there are two technical options for the gas amplification system: Micromegas [35] and Gas Electron Multiplier (GEM) [36]. Micromegas has excellent spatial resolution of 12 µm with time resolution of 650 ps [37]. GEM detector has the excellent time resolution of 25 ps [38] with spatial resolution of 100 µm [39].

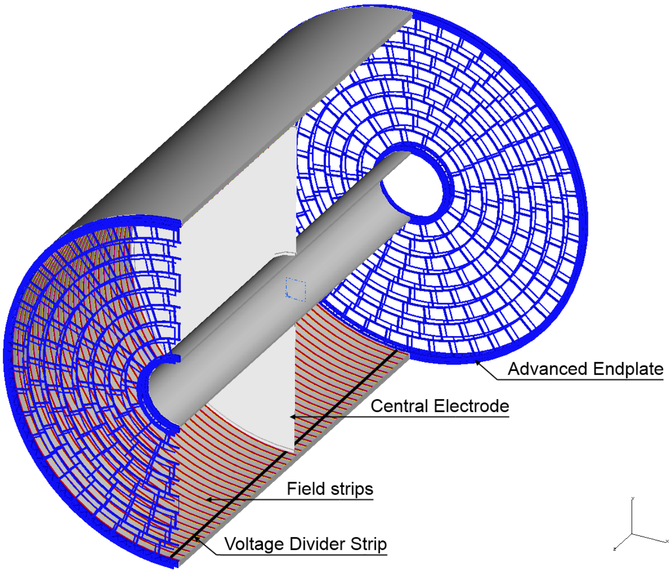

FIGURE 3.6: Cross sectional view of the TPC.

When a charged particle crosses the TPC, it will ionize the gas molecules along its path. Due to the electric field applied along the beam axis, those ionized particles will drift to the endplate at the edge of the detector. Based on the measurements from the pads on the endplate and the drift time, TPC can reconstruct the three-dimensional track of charged particles. The mechanism is depicted in Figure 3.7.

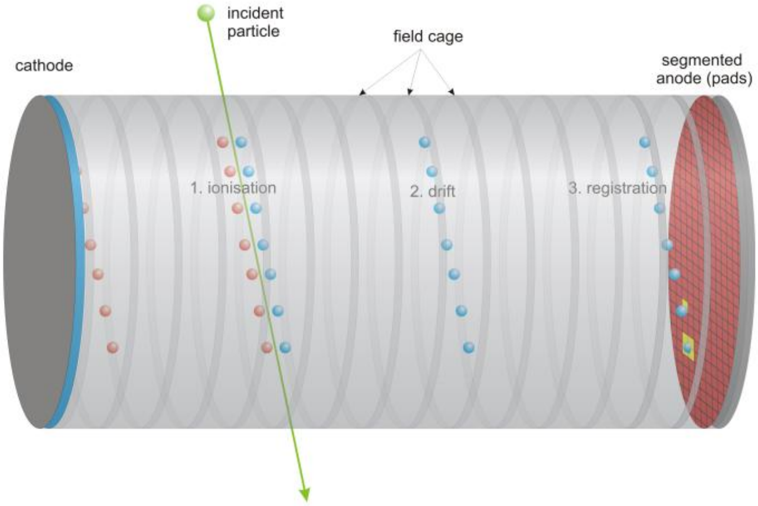

FIGURE 3.7: Principle of charged track measurement in TPC [2].

Another critical role of the TPC is the dE/dx determination. dE/dx is a parameter unique to different types of particles, which is used for the PID (see Section 5.6.5). The dE/dx value is conventionally calculated based on the deposited charge (Q_{hit}), obtained by summing all electrons generated from the ionization caused by the incident particle, shown in (3.1).

$$\left(\frac{dE}{dx}\right)_{hit} = \frac{Q_{hit}}{\Delta s} \tag{3.1}$$

where Δs is the length of the track segment The dE/dx of the track is calculated by taking the average of the dE/dx for each hit. The number of hits throughout the dE/dx distribution is shown in the Figure 3.8. The number of generated electron from the ionization follows the Landau distribution. The distribution has a large broad peak, which is mostly caused by the small energy transfer such as soft collisions. The tail represents the large energy transfer from the hard collisions. Such distribution with relatively large width will be the potential source of inaccurate dE/dx and momentum measurements. On the other hand, the number of ionizing interactions of the incident particle follows a Poissionian distribution, which has a significantly narrower width compared to the Landau distribution. It is, therefore, advantageous to count the number ionizing interactions, instead of summing all charges of the generated electrons. At the DESY test beam, the dE/dx resolution of $(4.2 \pm 0.1)\%$ was reported using the GEM based system [3], which complies with ILD TPC objective of 5%.

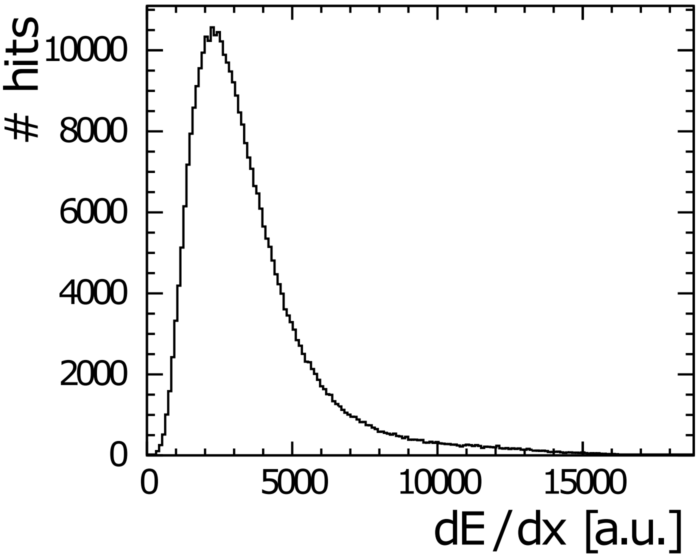

FIGURE 3.8: The dE/dx distribution of hits. The number of hits follows the Landau distribution [3].

3.3.3 Electromagnetic Calorimeter

PFA plays the central role in event reconstruction at the ILD. In order for the algorithm to work, each particles needs to be individually reconstructed, which implies the necessity for highly granular calorimeters.

The ECAL surrounds the TPC, and measures the energy of electrons, photons and charged hadrons. A key requirement for the ECAL is to be able to distinguish the overlapping showers, in order to realize the individual particle reconstruction. Therefore, the high three-dimensional granularity is requested for the ECALs. Moreover, both ECAL and HCAL have to be as compact as possible in order to fit inside the magnetic coils placed around them.

In the current baseline design, ECAL will be composed of 8 trapezoidal plates in order to form a cylindrical structure (Figure 3.9). Each plate contains 30 layers within the thickness of 20 cm, and each layer has an absorber material on one surface and an active material on the other side. These layers together will be inserted into the barrel module, indicated in Figure 3.10. As a result, the entire detector will have a distinct sandwich structure as shown in Figure 3.11.

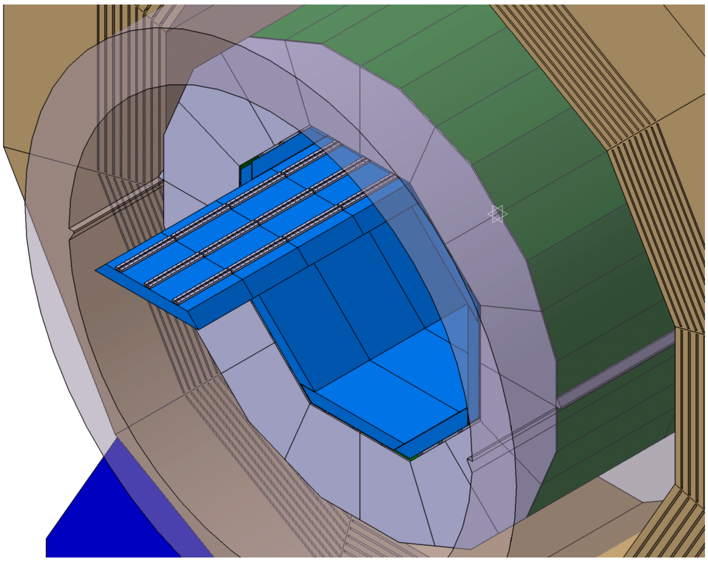

FIGURE 3.9: Cross sectional view of ILD with focus on the technical implementation to the ECAL.

Tungsten is chosen as an absorber material in order to satisfy the following requirements from the PFA: The radiation length X_0 is requested to be 3.5 mm in order to contain electromagnetic showers inside the ECAL. Half of the hadronic showers start from the ECAL, thus the Molière radius and the interaction length are requested to be R_M =9 mm and λ_I =96 mm, respectively, in order to distinguish the electromagnetic showers from the hadronic ones.

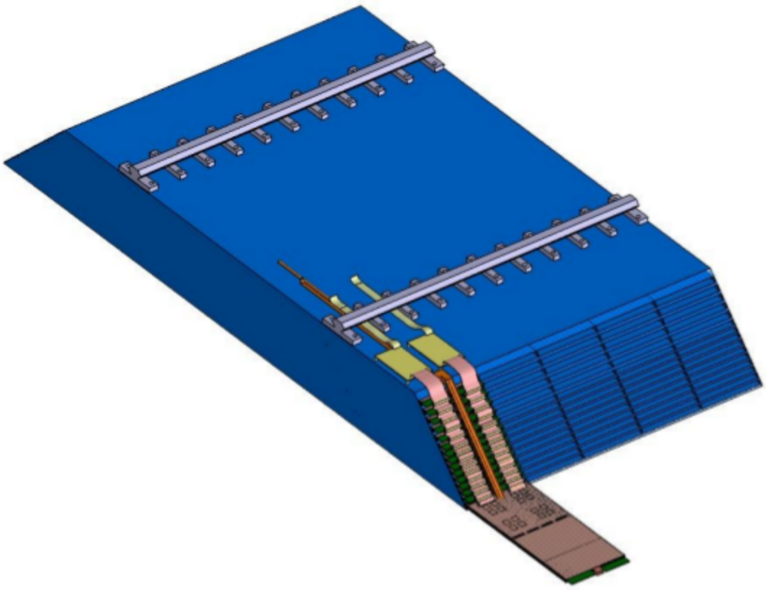

FIGURE 3.10: Drawing of an alveolar structure of a barrel module. Slab at the bottom is being inserted into aveoli inside the module.

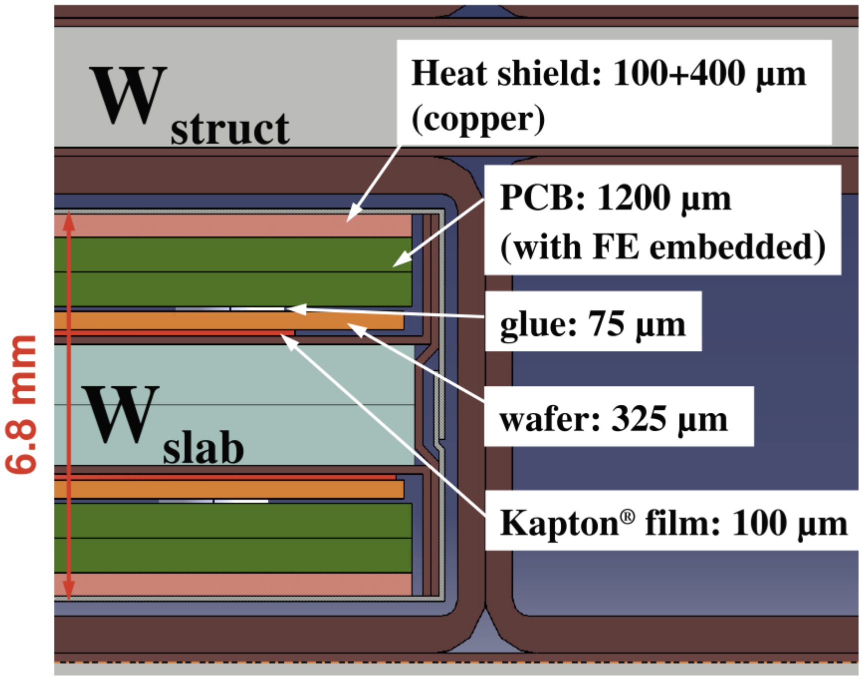

FIGURE 3.11: Sandwich structure of the ECAL.

One of the technological alternatives for the ILD ECAL is the Silicon Tungsten ECAL (SiW-ECAL), and this uses the silicon as an active medium. There are two main advantages of using silicon: First, silicon allows pixelization of the sensor. With a current set of technology, it is relatively easy to manufacture the silicon pin diodes for a pad size of 5×5 mm^2. Secondly, silicon supports a compact design owing to its relatively high X_0. Moreover, it exhibits robustness, implying that once the calibration constants are configured, there is no need for a sophisticated calibration system. The signal-to-noise ratio (SNR) is expected to be as high as 12.8 for a silicon wafer with thickness of 325 µm [40]. The value would allow for setting the trigger threshold below the single Minimum Ionization Particle (MIP) level with high efficiency. The detailed description on SiW-ECAL is discussed in Chapter 4.

Scintillator ECAL (Sc-ECAL) is another technological option for the ILD ECAL and it uses plastic scintillator for the active material. The structure of the Sc-ECAL is based on plastic scintillator strips, which are readout by the silicon photo multiplier (SiPM).

3.3.4 Hadronic Calorimeter

The role of HCAL is to measure the energies of neutral and charged hadrons, and separate individual particles in order to achieve jet energy resolution as high as 3-4%/$\sqrt{E}$ for the jets of 100 GeV [41] in which allows the clean separation of W and Z boson decays. Just as the ECAL, HCAL needs to be contained within the magnetic field, thus the detector needs to be as compact as possible. HCAL has a barrel structure and it is subdivided into 16 modules. Each module consists of 48 absorber plates with 16 mm thick each, and active layers with 5.5 mm thickness will be inserted in between. The detailed structure is shown in the Figure 3.12.

HCAL uses stainless steel as the absorber material for the reasons of cost and mechanical rigidity. Moreover, steel with moderate ratio of a hadronic interaction length of λ_I =17 cm to electromagnetic radiation length of X_0 =1.8 cm allows fine samplings in terms of X_0.

One of the technical alternatives to the HCAL is the Analog HCAL (AHCAL). AHCAL uses plastic scintillator as an active material. These scintillators are segmented into 3×3 cm^2 tiles with 3 mm thickness, which is then readout by the multi-pixel Geiger mode silicon photo-diodes (SiPM) (Figure 3.13). The size of pixel was decided based on the PFA performance study for AHCAL with various cell size, which is mentioned in the section 3.2. Figure 3.4 (right) shows that finer pixelization below 3×3 cm^2 does not provide substantial advantages toward improvement in jet energy resolution.

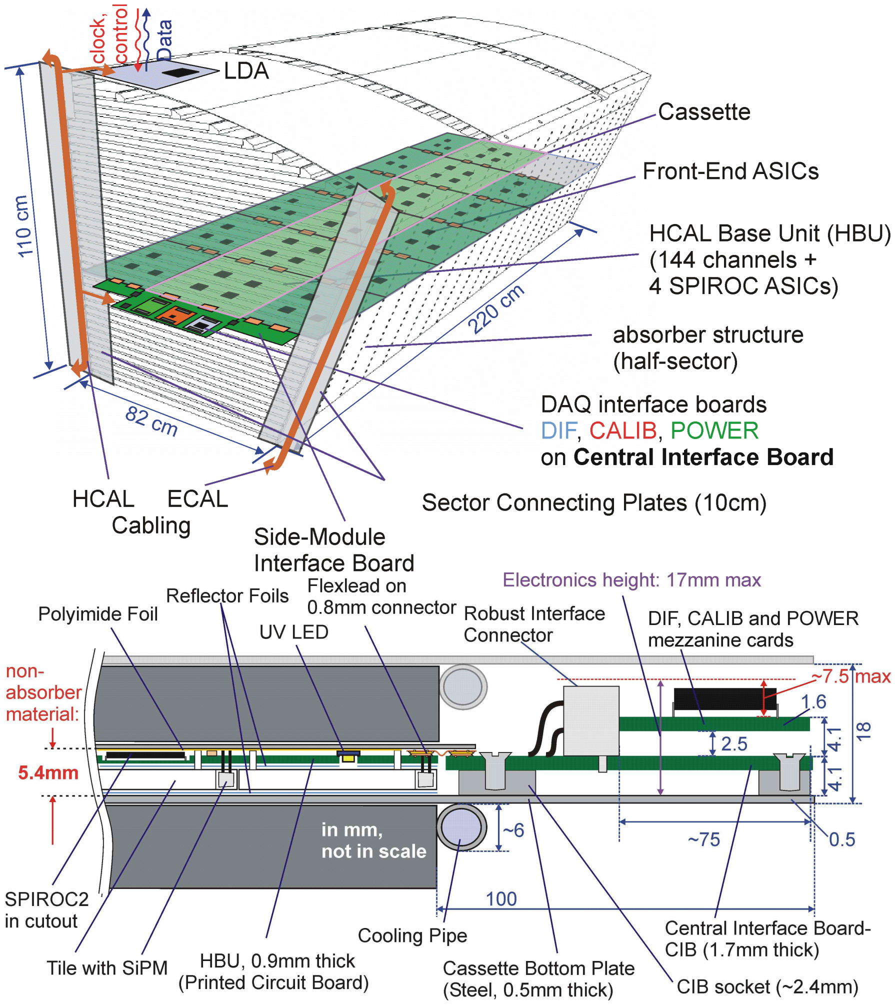

Figure 3.12: Cross sectional view of AHCAL.

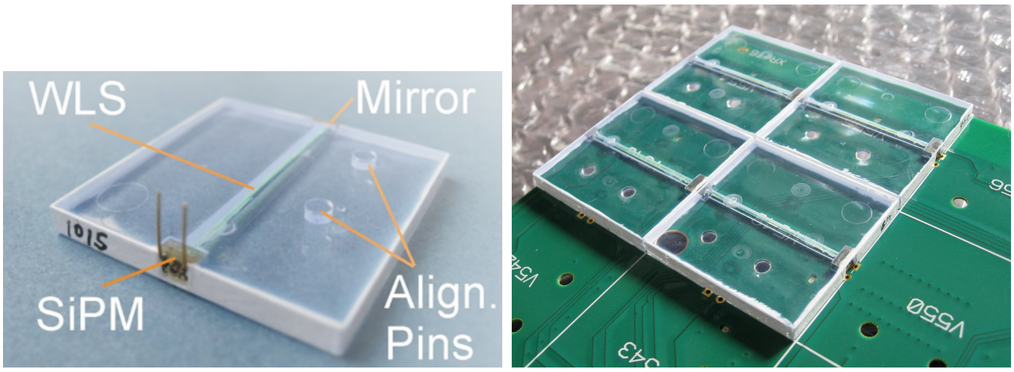

Figure 3.13: Scintillator tiles with embedded SiPMs.

Chapter 4

SiW-ECAL

4.1 Introduction

In section 3.3.3, the SiW-ECAL was introduced as one of the technological alternatives for the electromagnetic calorimeter of ILD. It is optimized for PFA. The R&D for this type of calorimeters is conducted by the CALICE (CAlorimeter for a LInear Collider Experiment) collaboration, a world-wide R&D collaboration, aiming at developing new and high performance detectors for electron-positron colliders. CALICE has conducted two beam tests at DESY on November 2021 and March 2022. Another beam test was done at CERN on June 2022.

4.2 Interaction of Particles with Matter

4.2.1 Energy loss by photons

A photon interacts with matter in following four primary mechanisms: ionization, photoelectric effect, Compton scattering and pair production. The probability of which these mechanism appears depends on the material and the energy of the incident particle. In Figure 4.1, the absorption cross section of photons inside tungsten are shown as a function of the incident photon energy. Ionization process takes place at low energies when photon looses its energy by ionizing an atom inside the matter. The cross section is maximum for ionization energies that correspond to the M, L, and K absorption edges of the material (tungsten in case of Figure 4.1). This absorption process starts to get dominated by coherent and incoherent Compton scattering. When the photon energy exceeds twice the mass of the electron, photon will start to pair produce electrons and positrons.

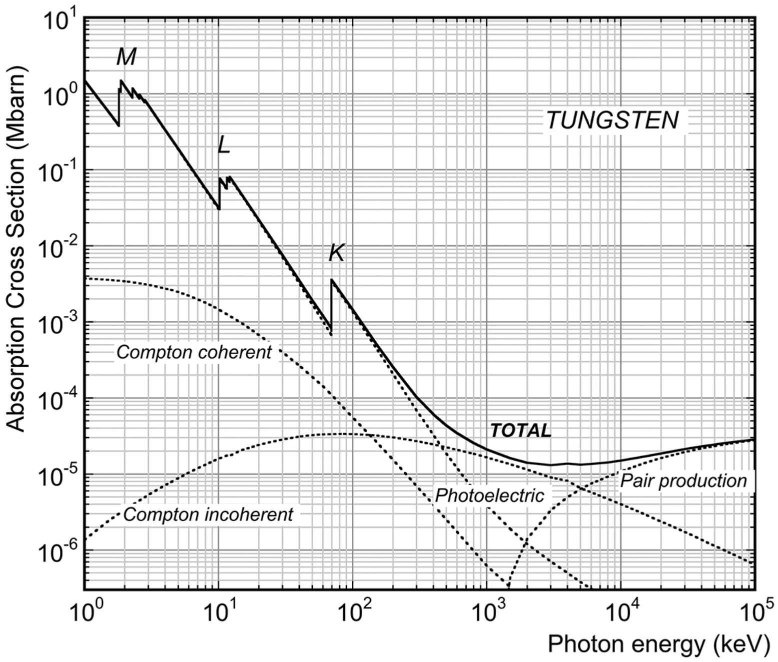

FIGURE 4.1: Photon absorption cross section for tungsten. [4]

4.2.2 Energy loss by charged particles

Any charged particle will lose its energy by interacting with matter via the Coulomb force with the atomic electron or nucleus. The energy deposition of a charged particle to an interacting material can be described by the Bethe-Bloch formula in Equation 4.1 [5], the mean energy loss per distance travelled by the charged particle that is both massive ($m \gg m_e$) and relativistic ($0.01 < \beta\gamma < 1000$).

$$\left\langle -\frac{dE}{dx} \right\rangle = Kz^2 \frac{Z}{A} \frac{1}{\beta^2} \left[\frac{1}{2} \ln \left(\frac{2m_e c^2 \beta^2 \gamma^2 W_{max}}{I^2} \right) - \beta^2 - \frac{\delta(\beta\gamma)}{2} \right] \tag{4.1}$$

The list of variable definitions are presented in table 4.1. Bethe-Bloch formula indicates that the stopping power of a charged particle depends on its momentum, mass and charge, which are introduced through W_{max}. Moreover, the property of the medium also plays the significant role since terms such as I, mean excitation energy of the material, affects the dE/dx.

As an example, Bethe-Bloch formula for muons in copper medium is plotted as a function of incident muon momentum in Figure 4.2. When the momentum of a particle

Symbol	Definition
dE/dx	Average energy loss in $\mathrm{MeV\,cm^2/g}$
N_A	Avogadro's number
r_e	Classical electron radius
m_e	Electron mass
z	Charge of the incident particle
M	Mass of the incident particle
Z	Atomic number of the medium
A	Atomic mass of the medium
I	Mean excitation energy of the medium
$\delta(\beta\gamma)$	Density effect correction to the ionization energy loss.
$W_{max} = \frac{2m_ec^2\beta^2\gamma^2}{1+2\gamma m_e/M+(m_e/M)^2}$	Maximum energy transfer in a single collision.
$K = 4\pi N_A e_e^2 m_e c^2$	Coefficient for dE/dx

TABLE 4.1: List of definition of variables used in Bethe-Bloch formula.

reaches minimum dE/dx value in the Bethe-Bloch curve ($\beta\gamma \simeq 3 \sim 4$ for the muons in the copper medium), this is called *Minimum Ionization Particle* (MIP). Particles with lower momentum will lose its energy with $1/\beta^2$ dependence since the slower particles are exposed to the atomic electrons for longer time. On the other hand, particles with higher momentum will also lose more energy as momentum gets higher, since the transverse component of its electric field gets larger due to the Lorenz transformation, thus increasing the interaction cross section. This effect is called relativistic rise.

4.2.3 Electromagnetic shower

When an energetic charged particle is incident on ECAL, undergoes a cascade of bremsstrahlung and pair creation processes. Electrons emit photon through bremsstrahlung process when they propagate through the detector medium. These photons will then pair create electron and positron pairs, which undergo further bremsstrahlung process. This continues until the electron eventually reaches below the minimum energy to ionize atomic nucleus, also known as critical energy (E_c). The product of the set of these processes is called electromagnetic shower. ECAL is required to contain the shower in its volume, as well as to collect the deposited energy. Therefore, the absorber material for the ECAL must have characteristic of stimulating electromagnetic shower, while stopping

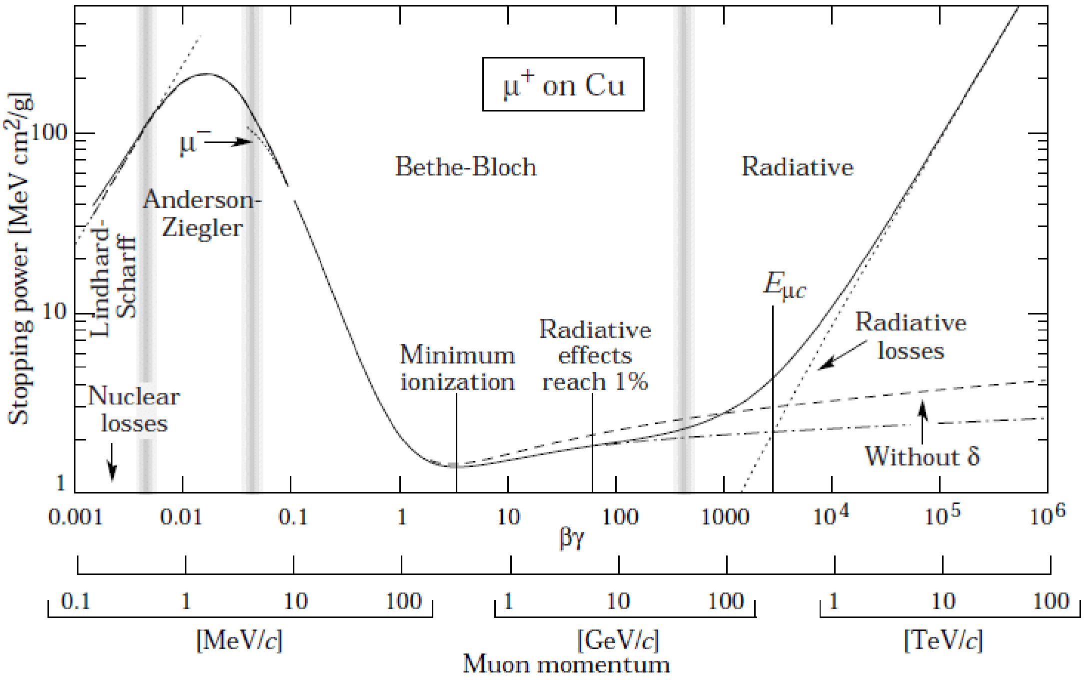

FIGURE 4.2: Stopping power (dE/dx) for muon in copper material as a function of muon momentum. [5]

it before its penetration. Radiation length X_0 is defined as the mean distance at which an electron drifts through the material before reaching $1/e$ of its energy.

4.2.4 Hadronic shower

The physical process of hadronic shower development occurs with completely different mechanism as oppose to the electromagnetic shower process. The hadronic shower is first initiated by the hard collision between the incident hadron and core nucleus. Then two physical processes can happen:

- When the collision is elastic, two objects will undergo strong interaction by exchanging gluons. This will excite and de-excite the nucleus, emitting photons as a result.
- When the collision is inelastic, it can create heavy hadrons such as $\pi^{\pm}$, π^0 and η.

There are stable hadrons with long life-time, such as proton, neutron and pion, which can escape the collision region. As a result, the deposited energy as a result of hadronic showers can fluctuate. Similarly to the electromagnetic interactions the material can be characterized by the interaction length λ_I, which is defined as the mean material depth that can be traveled by hadrons before reducing by the factor of $1/e$.

4.2.5 Detection by Silicon

One of the materials that is commonly used for ECAL is semiconductor silicon. When a charged particle or photon is incident to the p-n junction diode (with bias voltage applied across the detector), it will create a series of ionizing electron and hole pair in depletion zone along its track, as shown in Figure 4.3. Silicon crystals have specific density about $2.33\,\mathrm{g\,cm^{-3}}$, thus each MIP will leave about 80 electron hole pairs per µm, which corresponds to about 40 fC [42]. For a silicon sensor with thickness of 300 µm, for example, this will correspond to 42,000 electron hole pairs per MIP. Detail design for the silicon sensor we used for the beam test presented in this thesis, is introduced in Section 4.3.2.1.

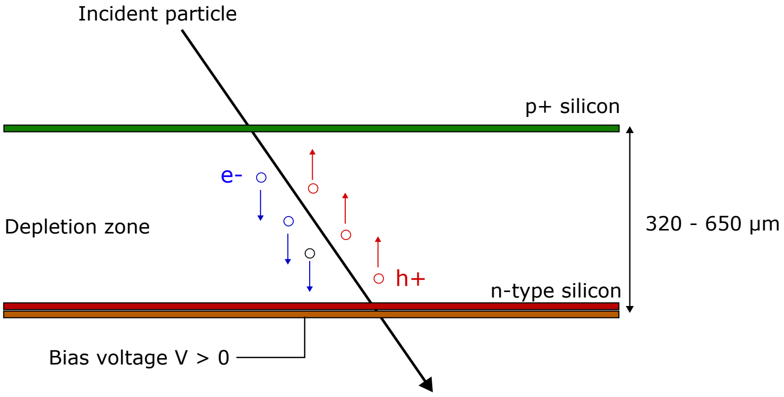

FIGURE 4.3: Illustration of photon and charge particle detection mechanism of silicon. Bias voltage of 150 V–200 V is applied across the detector.

4.3 Detector Prototype

In this section, the basic structure of the silicon-tungsten ECAL (SiW-ECAL) prototype is introduced. As it was introduced in section 3.2, the high granularity of the detector is an essential premise for a successful application of Particle Flow. One of the prime objectives of the CALICE collaboration is to develop and test the highly granular electromagnetic and hadronic calorimeters, which aim toward the future linear colliders. Before constructing any collider experiments, one needs to verify the feasibility of the potential candidates for the calorimeters by testing its calorimeter response to the various beams, as well as the validation by comparing with the results produced by the Monte Carlo simulation. The first physics prototype of the SiW-ECAL was tested between 2005 and 2011 at DESY, CERN and FNAL [43–45]. Each active layer was consisted of 3×3 silicon sensors with 500 µm thickness. Moreover, each silicon sensor was segmented into 6×6 pixels, with the size of 10 mm^2 each. The overall experiment demonstrated its capability to measure the beam energy with the resolution of $(16.51 \pm 0.35)\%/\sqrt{E}$ GeV.

After the proof of principle with the physics prototype, the development of the technological prototype commenced in 2011. One of the key differences between these two prototypes is the placement of the readout electronics. In case of the physics prototype, the ASICs were placed outside the detector volume, while they are incorporated in the detector volume in case of the technological prototype. First test beams were conducted with seven layers at MIP level (1 GeV–6 GeV) [46]. Between 2017 and 2020 and compact digital readout system has been developed that allows for the simultaneous readout of 15 layers. The beam tests carried out in 2021 and 2022 constituted a test for the new readout system. In order to complete 15 layers, all layers that have been produced since 2015 have been used for the setup. These comprised different variants of the interface board, see below, as well as layers that revealed problems as will become obvious as well below. Therefore, the beam tests are to be understood rather as technical tests including the synchronisation with the CALICE analogue HCAL (AHCAL) during the combined running at CERN in June 2022. Still, the setup allowed for the first to record high energy particle showers with the technological prototype. While an analysis of data recorded at DESY in 2021 has been published in [18] this thesis concentrates on the data taking at CERN in June 2022. However, at energies above 10 GeV collective effects have been observed that still have to be understood. That is why the analyses presented here will concentrate on the data taking at 10 GeV. The following sections will also outline the full commissioning and calibration chain to which I have contributed during my thesis.

4.3.1 SiW-ECAL structure

The prototype is equipped with silicon as an active material, and tungsten as an absorber. It is a sampling calorimeter, with active and absorber layer are placed in alternating positions, yielding an alveolar structure. Figure 4.4 illustrates the barrel module of ECAL on the left, and a single SiW-ECAL unit, referred to as Active Sensor Unit (ASU), introduced in Section 4.3.2. The layers of the final calorimeter consist of e.g. 30×5 slabs composed of chains of up to 8 ASUs. The SiW-ECAL is composed of following main components: Application Specific Integrated Circuit (ASIC) and Printed

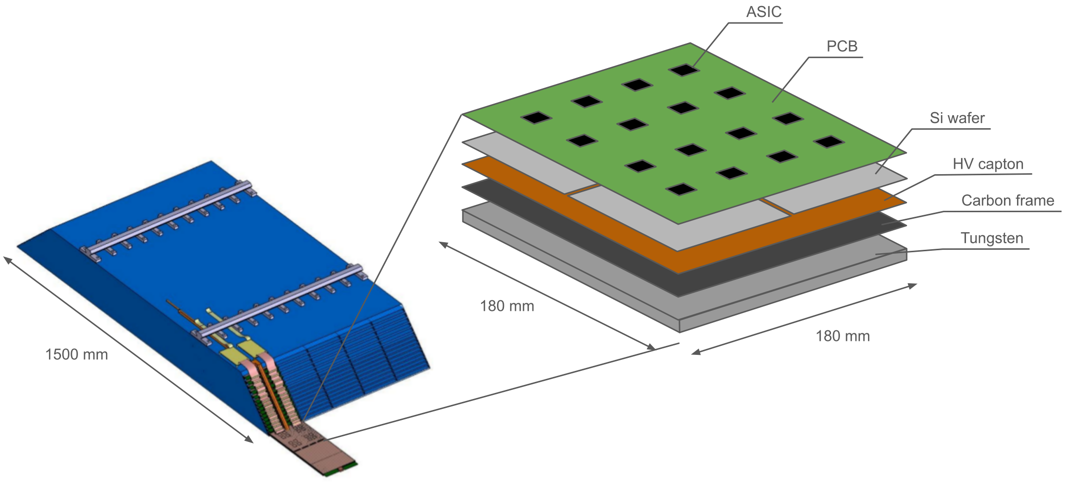

FIGURE 4.4: Barrel module of ECAL (left) and single SiW-ECAL unit and its main components (right).

Circuit Board (PCB), Si sensors and Tungsten (W). Each layer is equipped with four square Si sensor, with active area of $180 \times 180\,\text{mm}^2$ in total. Si sensors are segmented into 5.5×5.5 mm^2 pixel, giving 1024 pixels per layer (see Section 4.3.2.1). These pixels are read out by $4 \times 4 = 16$ ASICs placed on top of PCB for each layer, and each ASIC reads from $8 \times 8 = 64$ Si pixels (see Section 4.3.2). Tungsten plate is placed under the Si sensor. Between the active part and tungsten layer, there exists a carbon frame to support both structures.

4.3.2 The Active Sensor Unit

ASU is composed of a set of detector parts: Silicon sensor, ASIC and PCB. PCB with densely wired circuits is called Front End Board (FEV).

4.3.2.1 Silicon Sensors

Silicon sensors we used are made of p-on-n type with the crystal orientations of <100> or <111> [47]. Sensors are segmented into 5.5×5.5 mm^2 pixel and each pad has 256 pixels (Figure 4.5a), manufactured and developed by Hamamatsu Photonics. There are four silicon sensor pads are glued to the back of PCB using the conductive adhesive EPOTEK-4110 [48]. Four silicon sensors after the gluing are shown in the Figure 4.5b. Each sensor has the resistivity of $5\,\text{k}\Omega\,\text{cm}$. In the test beam campaign, we have tested sensors with thicknesses of 320, 500 and 650 µm. During the data taking, bias voltage of 150 V is applied across the entire sensors through the high voltage kapton. Electron

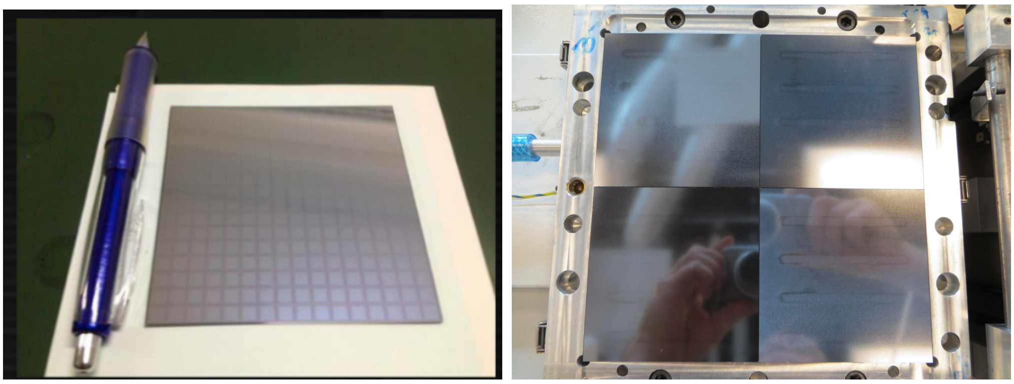

(a) Single sensor pad [47] (b) Four sensors glued on back of PCB

FIGURE 4.5: (a) Single sensor with dimension 9×9 cm^2. Each matrix corresponds to 5.5×5.5 mm^2 pixel. (b) Four sensors are attached behind the PCB.

holes resulted from the incident particle will propagate in form of electric pulse, which is registered by the pre-amplifier of the ASIC.

4.3.2.2 ASIC

The ASIC used for this beam test, is based on the SiGe 0.35 µm AMS technology with the size of $7.5{\times}8.7\,\mathrm{mm}^2$ [47]. The 16 ASICs are placed on top of PCB, each responsible for reading out data from 64 cells in their back. The product type of these ASICs are called the SKIROC [6] (Silicon-pin Kalorimeter Integrated ReadOut Chip) which are designed to readout from the silicon pin diodes. The schematic circuit diagram is shown in Figure 4.6. The signal acquisition chain is mainly categorized into four parts: pre-amplification, charge measurement, trigger decision and digitization/readout. Each channel input corresponds to the signal received from an individual cell in the sensor. These channels are equipped with a low-noise charge preamplifier featuring variable gain, controllable by adjusting the feedback capacitance C_f (Green box in Figure 4.6). The gain from this capacitance inversely proportional as $1/C_f$. Due to the expected high signal from the high energy beam (10 GeV–150 GeV) at SPS, the feedback capacitance was set to 6 pF to limit the gain. After the pre-amplification, the signal goes through the charge measurement by slow shaper and trigger determination by fast shaper, each depicted in blue and orange box in Figure 4.6, respectively.

Slow shaper is responsible for processing charge measurements. It is comprised of two gain modes, low and high gain, to cover the dynamic range of signals. These gains are represented by G1 and G10 in Figure 4.6, with respective capacitors. Following the trigger event, the charge of the triggered channel is retained for a fixed duration

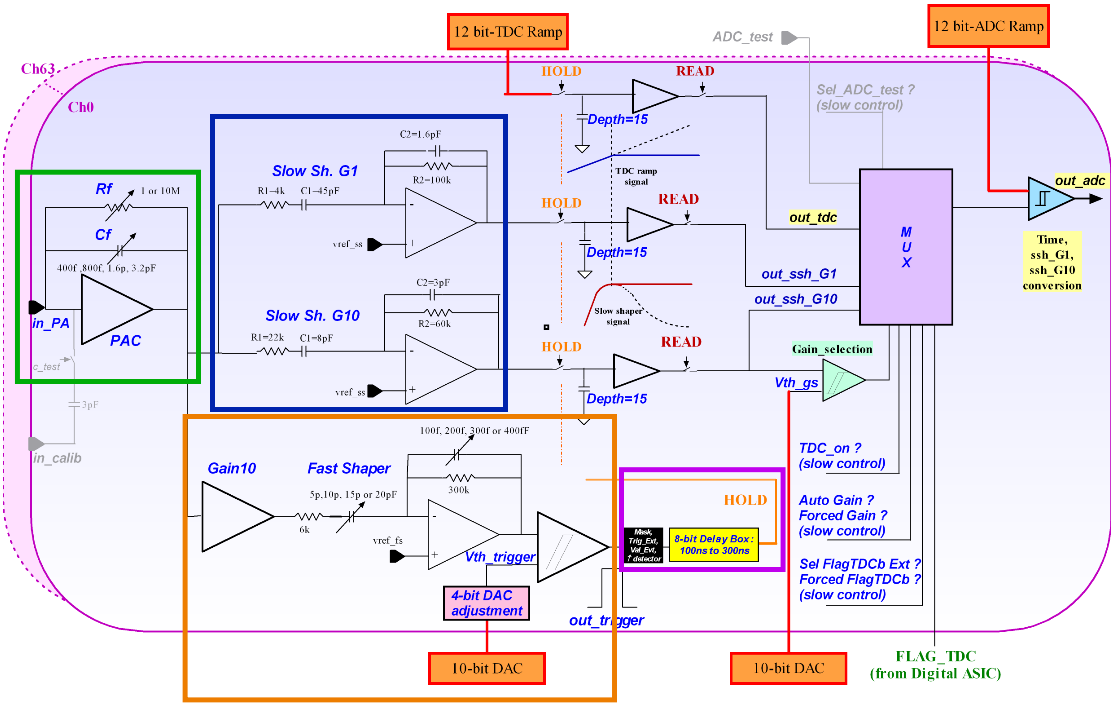

FIGURE 4.6: Circuit diagram of the SKIROC2 [6]. Each box with different color indicates main components of SKIROC. Green box is the pre-amplifier, blue box is the slow shaper, orange box processes the fast shaper and purple box takes care of delay for hold. The role of each component is described in the text.

before being stored in one of the memory cells within the 15-cell-deep physical switched capacitor array, referred to as SCA. When the SCA is saturated, indicating that all 15 memory slots are filled, the detector ceases processing triggers until it clears the entirety of its memory cells to the DAQ. Finally, the signal is digitized by the Analog to Digital Converter (ADC). Subsequently, this digitized signal is tagged along with cells that triggered and those did not trigger.

The fast shaper yields trigger decisions based on user-defined threshold values. Since ILC will not operate on external trigger, ASICs need to record all the signals acquired from the measurements. This means all the signals which passed the trigger threshold will be recorded by the data acquisition system (DAQ). In order to ensure signals as low as 1 MIP, the trigger thresholds were targeted to be as low as 0.5 MIP or above signal. As a reminder we note that in 500 µm Si, 0.5 MIP corresponds to around 20,000 electrons. First threshold is determined for each chip using the 10-bit DAC (Digital-to-Analog Converter) value ranging from 0 to 1024, which is referred to as common threshold. The second threshold is the fine tuning of the individual channel trigger, supplied by 4-bit DAC. SKIROC2 can only adjust common threshold while its newer variant SKIROC2a is capable of adjusting channel threshold.

Following the trigger, fast shaper will wait for slow shaper to measure the maximum charge provided by the signal. This delay for hold is processed in purple box in Figure 4.6. This delay time is unique to individual ASIC, which is calibrated in Section 4.6.6.

Another feature of the SKIROC is that it enables the charge injection for the calibration purpose. This signal is injected before the preamplifier, providing an ability to imitate a signal with controllable DAC input.

The maps for ASICs numbering is provided in Figure 4.7, facing the beam direction. The numbering of each channel in each ASIC is provided in Appendix A. The ASICs is labeled with numbers from 0-15, and channels are labeled from 0-63 for each ASIC.

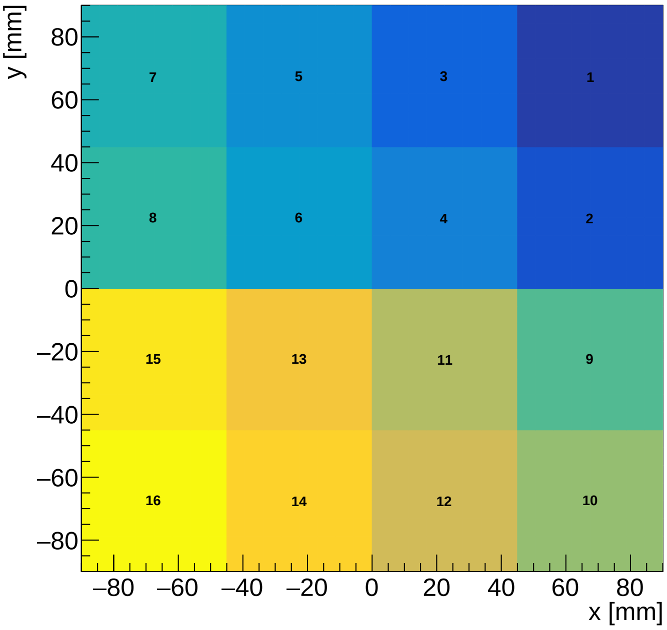

Figure 4.7: The ASU repartition for an ASU is presented. The placement for the ASUs are identical between FEVs and COBs.

4.3.2.3 Front-End Board

The Front-End boards designated as Version 10 to 12 (FEV10-12) represent iterations of the ASU developed since 2014 (see Figure 4.8). The digital readout card inserted from the right hand side of the picture is SLab digital interface Board (SL Board), which is introduced in Section 4.3.3.1. Each successive version of the FEV introduced incremental modifications to the internal circuitry of the ASU, resulting in improved

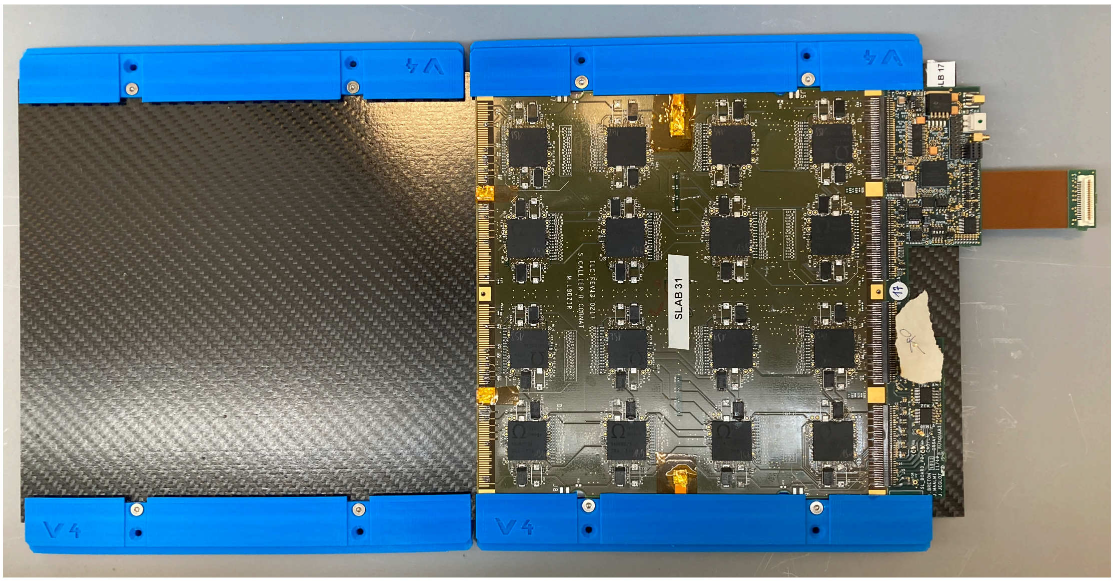

Figure 4.8: Front view of a FEV12 with SL board inserted to the right.

attenuation of electronic cross-talk between the wires. The most recent iteration at the time of the CERN beam test was the FEV13, which featured distinct circuitry compared to FEV10-12 (see Figure 4.9). In contrast to FEV10-12, FEV13 necessitates the use of an external connection card bonded with three flat wires for connectivity with the SL board.

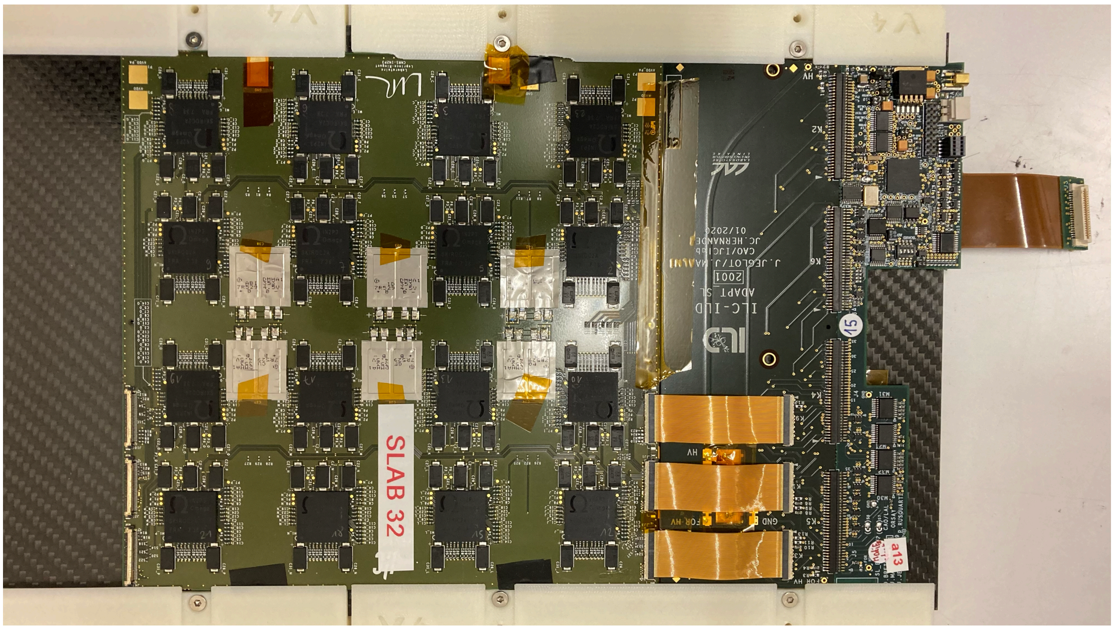

Figure 4.9: Front view of a FEV13 with SL board inserted to the right.

4.3.2.4 Chip on Board

The PCB has to support the compact design of the SiW-ECAL. This has motivated the development of a Chip-on-Board (COB) variant of the PCB. COBs are an alternative PCB design where ASICs are directly wire-bonded onto the substrate within dedicated cavities (Figure 4.10). Instead of Ball Grid Array (BGA) employed in FEVs, the ASICs on COBs are encapsulated using transparent plastic resins. The total thickness of COBs by itself is designed to be ∼1.2 mm, which is thinner compared with overall 3 mm of the BGA design. The design of the COB does not foresee decoupling capacitances next to the ASICs as the BGA variant. Therefore, it is more vulnerable to noise. In a future version decoupling capacitances could be integrated into the cavities. In order to understand how much decoupling is needed, some decoupling capacitances have been placed at the extremities of the COBs.

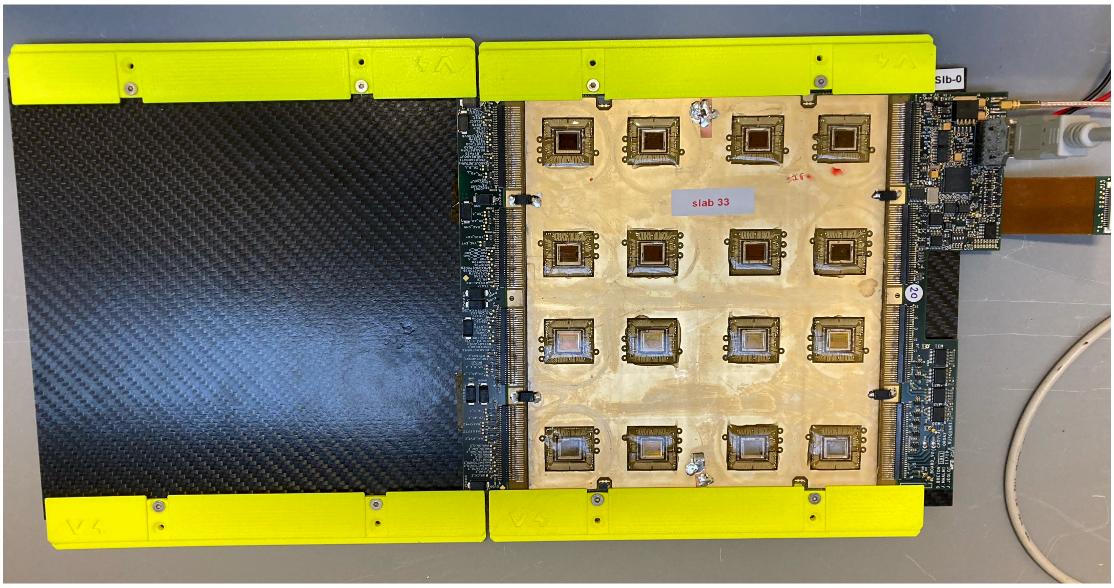

FIGURE 4.10: Front view of a COB with SL board inserted to the right.

4.3.3 Digital Readout System

4.3.3.1 SL-Board

The readout of the digitised signal from the SKIROC is realised by the SL-Board, which is inserted at one end of the ASU (Figure 4.11). The SL-Board functions as the detector interface for the SiW-ECAL, with the capability to process all the digitized signals from up to 15 parallel-connected ASUs in each layer. In the regular case that the system contains multiple SL Boards, data are propagated via the short flex cable to the CORE module, which is introduced in Section 4.3.3.2. In case when the system only features a single SL Board (e.g. for testing purpose), the acquisition can happen via an USB cable. SL board also has an input for both low and high voltage supplies. Furthermore, firmware updates of the SL-Board can be performed through an 8-pin connector located next to the flat cable.

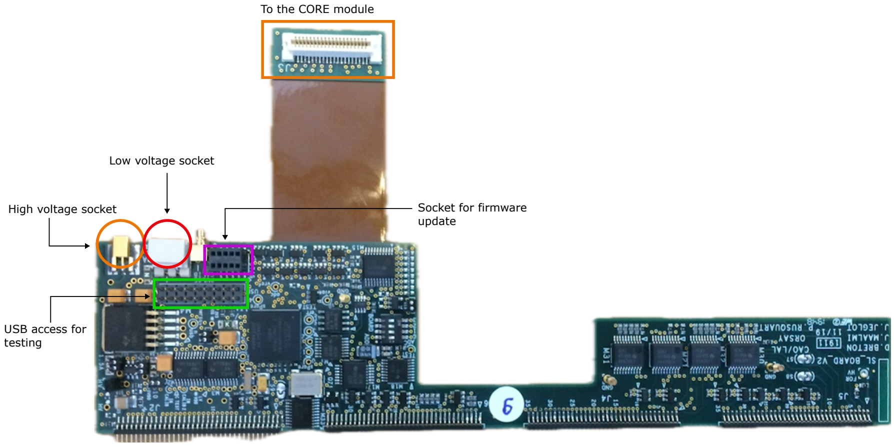

FIGURE 4.11: Picture of SL board with indication to each components described in the text.

4.3.3.2 CORE Module

The CORE module comprises the “CORE Mother” and “CORE Daughter”. The CORE Mother transmits common clocks and fast signals to the CORE Daughter to maintain system synchronization. The CORE Daughter serves as the interface between the CORE Mother and the Kapton and is based on a Cyclone IV FPGA [49]. The flat Kapton cable is connected to the CORE Daughter to initially aggregate signals from all 15 layers. During the CERN test beam the external 40 MHz clock was provided to both AHCAL and SiW ECAL by a so-called Clock and Control Card (CCC). As previously mentioned in Section 3.3.3, each barrel module will consist of a total of 30 layers. One CORE Daughter can serve up to 15 layers. The other 15 layers will be managed by another set of SL-Board and Kapton cable, subsequently connected to a second CORE Daughter (Figure 4.13). In addition to its hardware capabilities, the CORE module is capable of programming and upgrading the individual firmware on the SL-Board for each layer, employing the JTAG adaptor board. It is worth highlighting that the CORE module also provides the DAQ software system which is explained in Section 4.3.4.

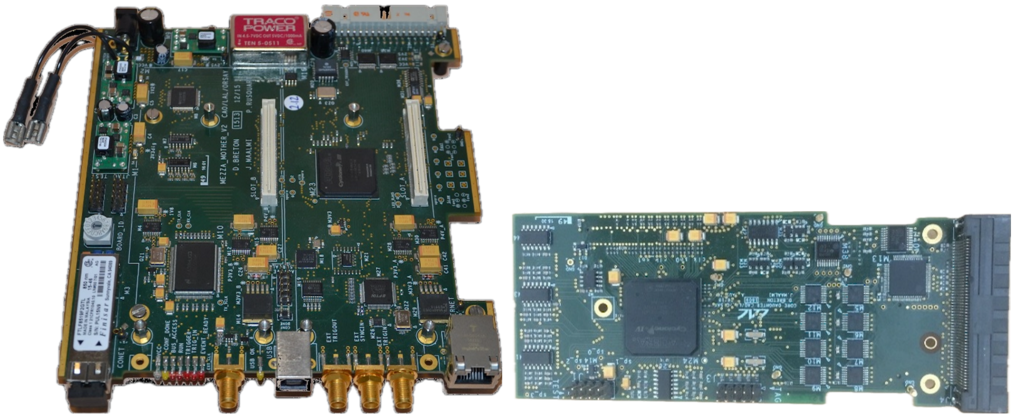

(a) CORE Mother (b) CORE Daughter

(c) Combined CORE module

FIGURE 4.12: Pictures of (a) CORE Mother, (b) CORE Daughter and (c) Combined CORE module.

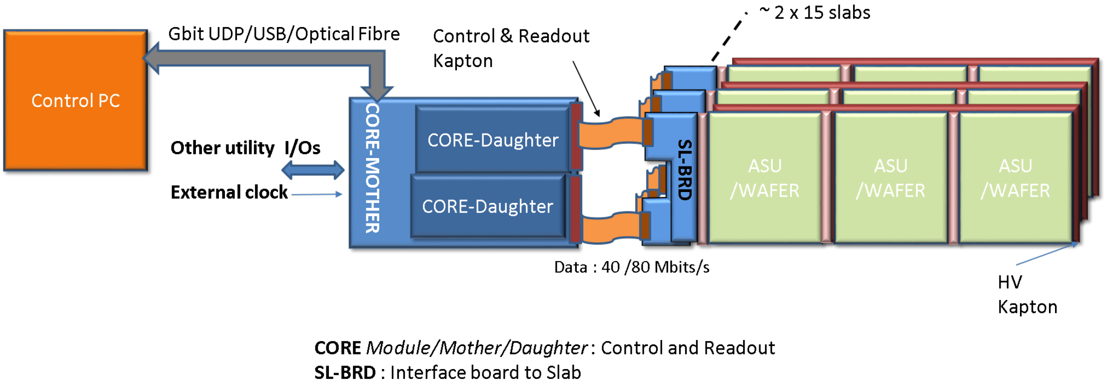

FIGURE 4.13: Simplified schematics of digital readout system and its connections. [7]

4.3.4 DAQ System

The Data Acquisition framework (DAQ) [50] serves as the tool designed for consolidating data readout and acquisition within a centralized system. A DAQ firmware specific to the SiWECAL is installed in the CORE module, enabling the manipulation of parameters such as individual masking switches, trigger thresholds, preamplifier settings, feedback capacitance, acquisition windows, and more. Figure 4.14 depicts the screen of DAQ interface. The online monitoring feature facilitates users to monitor the following

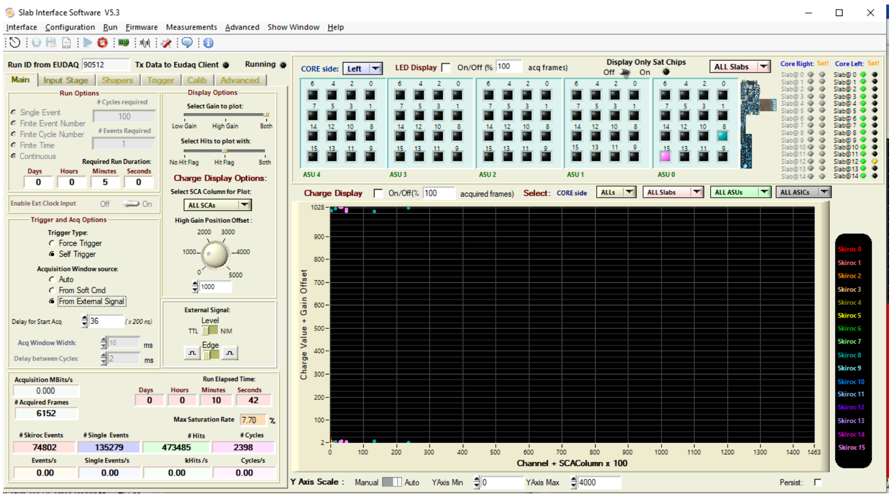

Run ID from EUDAQ: 90512
Tx Data to Eudaq Client ●
Running ●

Run Options: ○ Single Event ○ Finite Event Number ○ Finite Cycle Number ○ Finite Time ● Continuous
Cycles required: 100
Events Required: 1
Required Run Duration: Days 0, Hours 0, Minutes 5, Seconds 0
Enable Ext Clock Input: Off / On

Trigger Type: ○ Force Trigger ● Self Trigger
Acquisition Window source: ○ Auto ○ From Soft Cmd ● From External Signal
Delay for Start Acq: 36 (x 200 ns)
Acq Window Width: 10 ms
Delay between Cycles: 2 ms

Select Gain to plot: Low Gain / High Gain / Both
Select Hits to plot with: No Hit Flag / Hit Flag / Both
Charge Display Options:
Select SCA Column for Plot: ALL SCAs
High Gain Position Offset: 1000

Acquisition MBits/s: 0.000
Acquired Frames: 6152
Run Elapsed Time: Days 0, Hours 0, Minutes 10, Seconds 42
Max Saturation Rate: 7.70 %

# Skiroc Events	# Single Events	# Hits	# Cycles
74802	135279	473485	2398
Events/s	Single Events/s	kHits /s	Cycles/s
0.00	0.00	0.00	0.00

CORE side: Left
LED Display ☐ On/Off (% 100 acq frames)
Display Only Sat Chips: Off / On
ALL Slabs
Charge Display ☐ On/Off(% 100 acquired frames)
Select: CORE side: ALLs, ALL Slabs, ALL ASUs, ALL ASICs
Y Axis Scale: Manual / Auto
YAxis Min: 0
YAxis Max: 4000
Persist: ☐

FIGURE 4.14: An example interface screen of the DAQ software used during the test beam. On the left, it shows the lever arm adjustable parameters described in the text. Right hand side of the screen provides information on triggered cell and its charge value in real-time.

parameters in real-time:

- Hit map
- Hits per layer, chip and channel
- Number of filled SCAs
- Detector temperature
- AVDD and DVDD value

Another significant facet of this DAQ software is its capacity to support commissioning. The software is proficient in measuring the pedestal, representing the constant electronic noise superimposed on the trigger signal. The results of these pedestal measurements facilitate the subtraction of this noise from the DAC units displayed in the online monitor. Moreover, following pedestal subtraction, the DAQ software framework expedites the MIP (Minimum Ionizing Particle) calibration for individual cells, smoothing the commissioning process.

4.3.5 Power Pulsing

As outlined in Section 2.4, one of the key features of the ILC is its bunch structure (Figure 4.15). Each short 1 ms train has a bunch period of 366 ns, and each train occurs with a period of 200 ms. To minimize overall power consumption and heat dissipation

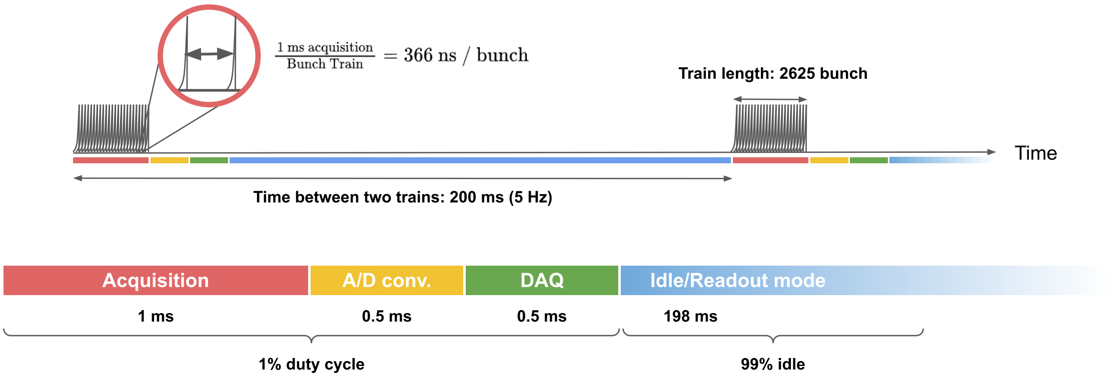

FIGURE 4.15: Bunch structure of the ILC electron and positron beams.

from the detector, SiW-ECAL employs this bunch structure by operating in power pulsing mode. The detector captures data during a 1 ms acquisition window when a train arrives. Subsequently, there is a 0.5 ms period dedicated to analog-to-digital conversion, followed by the DAQ. During the remaining time until the next train arrives, the bias current for the pre-amplifier is switched off while it continues to process data readout. SKIROC has an internal clock of 5 MHz, providing the timestamp known as the Bunch Crossing Identifier (BCID) for each trigger. This timestamp aligns within the 40 MHz clock from the CCC to synchronize with AHCAL. Each BCID is reset after each acquisition period, incrementing the acquisition number. Thus, one can uniquely identify each event using the acquisition number and BCID. The detailed description on event identification is introduced in Section 4.8. The current operational prototype of SiW-ECAL indeed possesses the capability to implement a power pulsing mode. However, due to non-synchronization between the bunch train from the SPS beam and the SiW-ECAL prototype, this feature was not used during the beam test. Nonetheless, we have effectively applied the similar feature by providing 1 ms of acquisition window during the data taking.

4.4 Detector Layer Setup

Figure 4.16 illustrates the structure of the SiW-ECAL prototype, featuring the ASUs, tungsten slabs and the supporting frames. All layers are supported by the $62.0 \times 30.0 \times 25.0\ \text{cm}^3$ metallic support with rails, in order to store all heavy weight tungsten slabs and delicate ASUs. Due to the tight spatial constraints, there are no room for the cooling systems to be inserted between the layers. Hence two fans were placed at the side of the frame, which ran constantly throughout the data taking. The layer setup for the SiW-ECAL during the test beam is presented in Table 4.2. The first layer is where the beam hits first. The side view of the detector is presented in Figure 4.17.

Figure 4.16: Exploded-view of the SiW-ECAL. [8]

The layers are separated by a distance of 15 mm. Note that in the TDR [51], ILD will be equipped with 30 layers within the same overall size of 22 cm. This signifies that in the real ILD, the active part of ECAL is twice as dense as our prototype. Therefore the the prototype under test has a different sampling fraction than the SiW-ECAL in ILD. This fact needs to be taken into account when comparing the energy resolution from the prototype to the one in the technical design. All the layers are mounted on a 2 mm Carbon Fiber Reinforced Polymer plate, which is equipped with 3D-printed rails for attachment to the supporting frame. Tungsten is mounted on one side, and the ASU is mounted on the other.

4.5 Beam Setup

The analysis focuses on the data taken during the test beam at CERN SPS in June 2022. Figure 4.18 illustrates the schematics of the accelerator complex at the CERN. The beam test was conducted at the H2 beam line. Users can choose the beam type between e^-, μ^- and $\pi^\pm$ with energy between 10 GeV–200 GeV. During the experiment, following energy levels were chosen:

- e^- : 10, 20, 40, 60, 80, 100, 150 GeV

Layer	ASU type	Sensor (µm)	W (mm)	X_0 cumulative
0	FEV13	650	4.2	1.2
1	FEV13	650	4.2	2.4
2	FEV13	650	4.2	3.6
3	FEV13	500	4.2	4.8
4	FEV13	650	4.2	6.0
5	FEV13	500	4.2	7.2
6	COB	500	4.2	8.4
7	FEV12	500	4.2	9.6
8	COB	500	4.2	10.8
9	FEV12	500	5.6	12.4
10	FEV11	320	5.6	14.0
11	FEV11	320	5.6	15.6
12	FEV10	320	5.6	17.2
13	FEV13	320	5.6	18.8
14	FEV11	320	5.6	20.4

TABLE 4.2: Detector composition.

- μ^- : 50, 150 GeV
- $\pi^\pm$: 10, 20, 70, 100, 150, 200 GeV

The SiW-ECAL was placed 17 cm in front of the AHCAL, as shown in the Figure 4.19.

4.6 Commissioning

Commissioning was performed for preparing detector for data taking. There are six steps to complete this calibration:

1. Masking
2. Noise threshold determination
3. Pedestal calibration

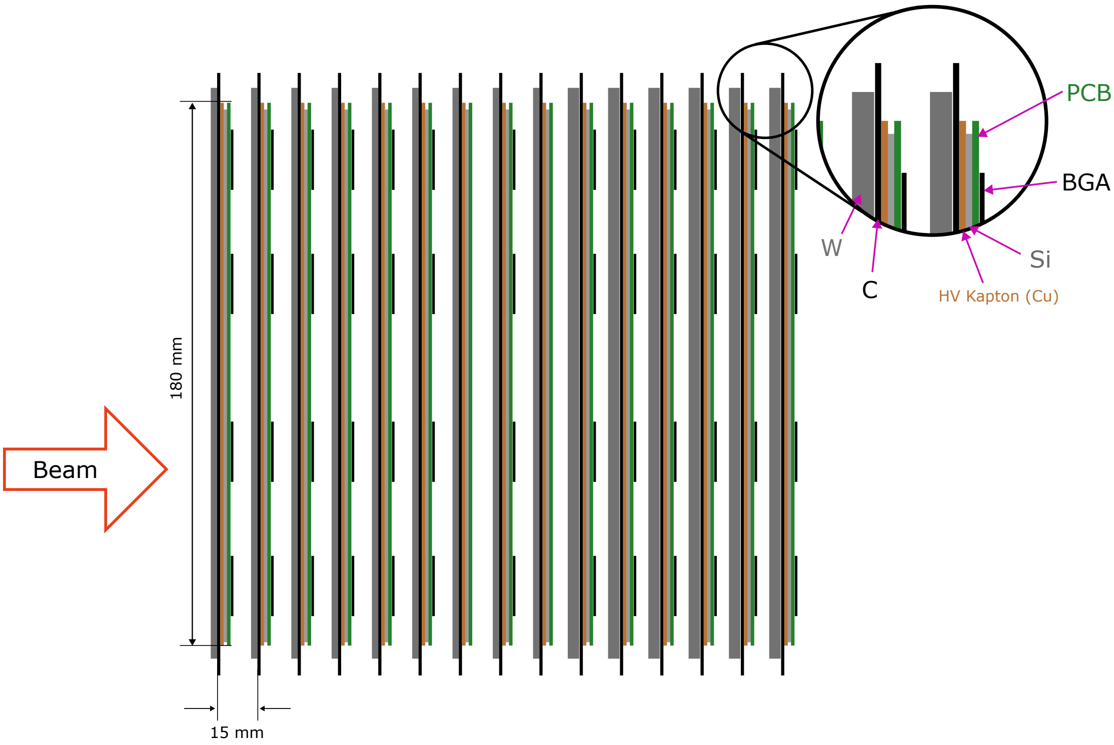

FIGURE 4.17: The side view of the detector with layer composition during the CERN June 2022 test beam is displayed. The first 9 layers are equipped with 4.2 mm thick tungsten, while the latter 6 layers feature 5.6 mm thick tungsten. The layers without BGA are the COB layers.

4. MIP calibration
5. Trigger threshold determination
6. Hold scan

4.6.1 Masking

Very noisy channels is identified in this part of commissioning. In this process, we required relatively high threshold in each step and progressively lowered its value, ranging from 350-275 DAC values. At these values that correspond to 1 MIP or more, one of the cells should trigger. The noisy cell is defined as the cell with trigger larger than the mean trigger throughout the entire active cells. Following the procedure, the noisy cells were masked in the DAQ software, and their pre-amplifiers were turned off to prevent cross talks to the neighboring cells. The masking result for Layer 1 is shown in Figure 4.20. First, one can notice the constant masking in one of the cells, represented as straight line in Figure 4.20a. This is due to electric cross-talk between the internal circuitry of the PCB and the pre-amplifier of that cell. This results in certain cells to exhibit higher

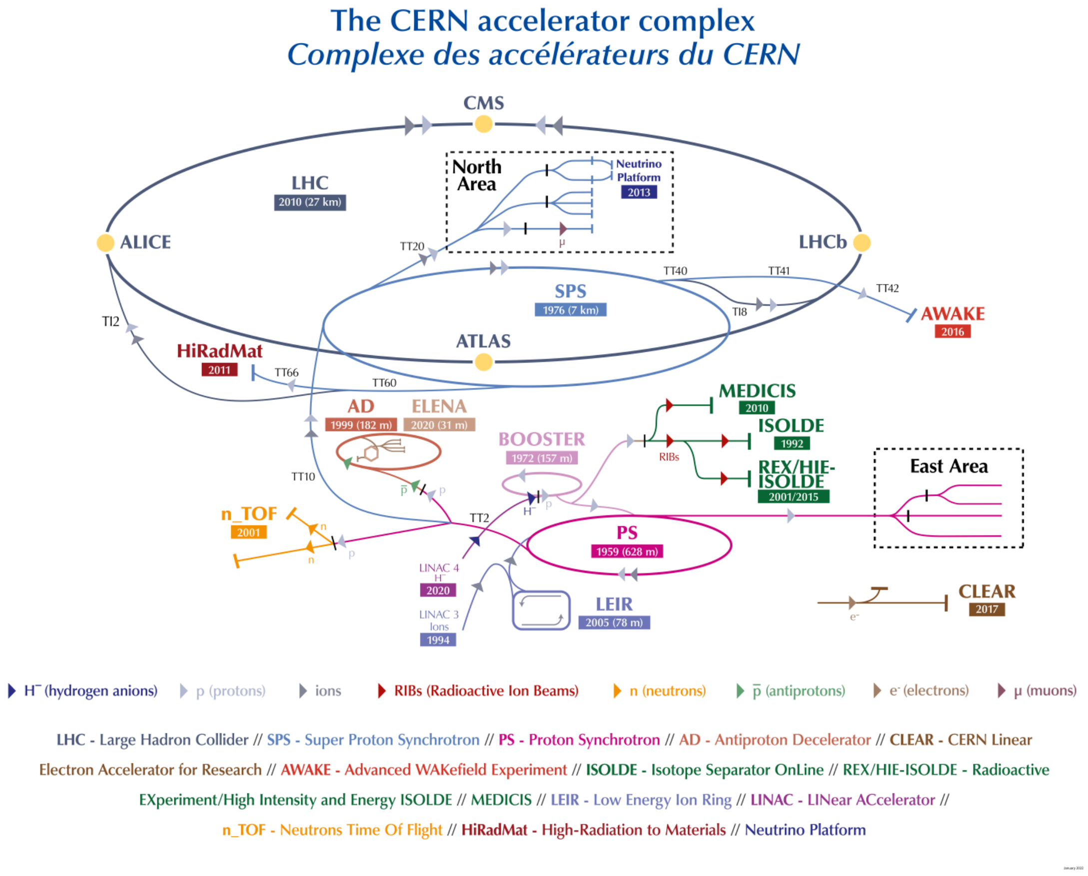

FIGURE 4.18: The illustration of the CERN accelerator complex as of 2022. [9]

FIGURE 4.19: Picture of the detector set up and beam pipe. ECAL is placed in front of the AHCAL prototype.

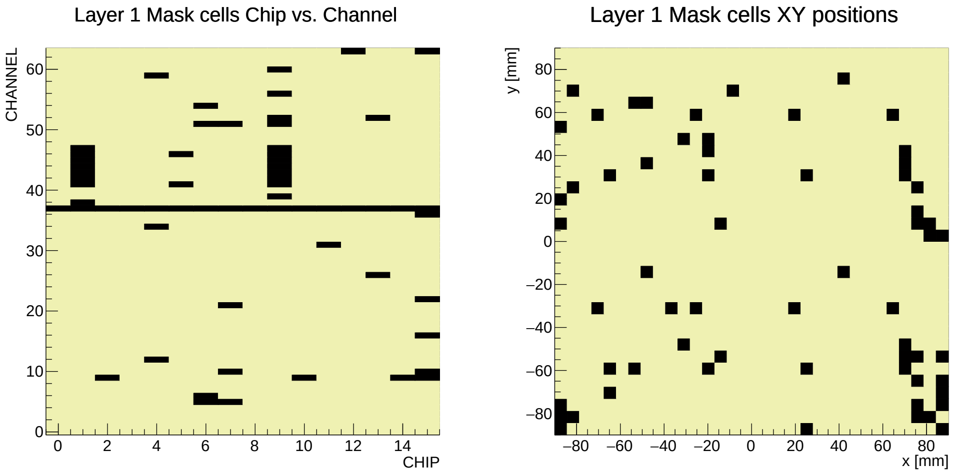

(a) Mask channel vs. chip

(b) Mask XY position

Figure 4.20: The mask map is shown for the Layer 1. Black spots represent the masked cell. (a): Channel vs chip distribution. (b): XY position.

noise level compared to others. The effect was already been reported in previous test beams [52]. This effect, however, is no longer present in COBs due to the optimized circuit wiring in the latest iteration of its PCB. This is depicted in Figure 4.21. The rest

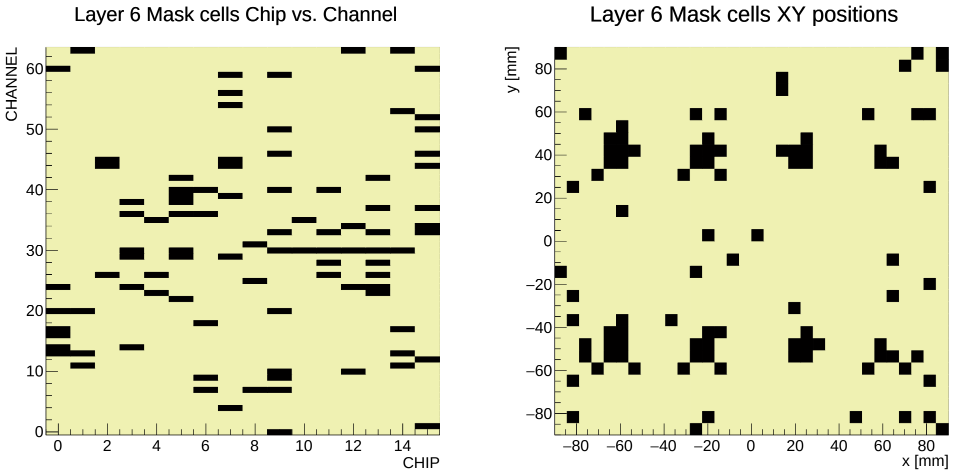

(a) Mask channel vs. chip

(b) Mask XY position

Figure 4.21: The mask map is shown for the COBs (Layer 6). Black spots represent the masked cell. (a): Channel vs chip distribution. (b): XY position.

of mask map for other layers are presented in Appendix B. Overall masking information for the entire layers is summarized in Figure 4.22. Figure 4.22a again reveals the issue of repetitive cell masking throughout all layers but the ones equipped with COBs. Despite the necessity of extensive masking for specific cells, we managed to preserve active cells predominantly in the region where x [mm] $<$ 0 and y [mm] $<$ 0. Figure 4.22b illustrates

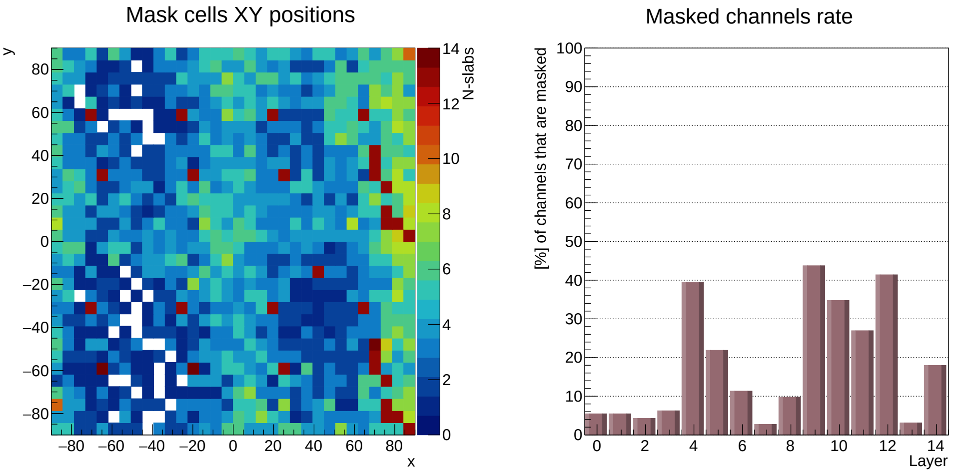

(a) (b)

Figure 4.22: (a) XY positions for the masked cells, with frequency for layers in z-axis. White cells are the channels which are not masked by all layers. (b) Percentage of masking in chip 12-15, where the beam hits.

the percentage of masking in this region. During the data taking the beam has been preferably directed to this position, in order to maximize the acceptance and capture the entire EM shower. Newer layers, such as FEV13 and COBs, maintain over 90% of their active cells, while older layers, like FEV11 and those below it, exhibit a higher fraction of masked cells, which will be introduced in Section 4.7. Nonetheless, the overall mask ratio for all cells averages 18.3%, which does not adversely impact our measurements during the beam test.

4.6.2 Noise Threshold

After the masking of noisy cells, noise thresholds were determined for individual channels before proceeding to pedestal determination and MIP calibration. In order to estimate the noise threshold, a threshold scan was performed by recording the number of hits per varying thresholds, as shown in Figure 4.23. Each color represents data points from first 8 channels in layer 7, ASIC 12. When the threshold is low (below 190 DAC for this particular ASIC), the chip gets saturated with noise hits. For the higher DAC value (above 210 DAC), the ASICs no longer records hits. In order to quantitatively determine this threshold, error function was fitted to the distribution. The fit function is defined as following:

$$f(x) = p_0 \cdot erfc\left(\frac{x - p_1}{p_2}\right) \tag{4.2}$$

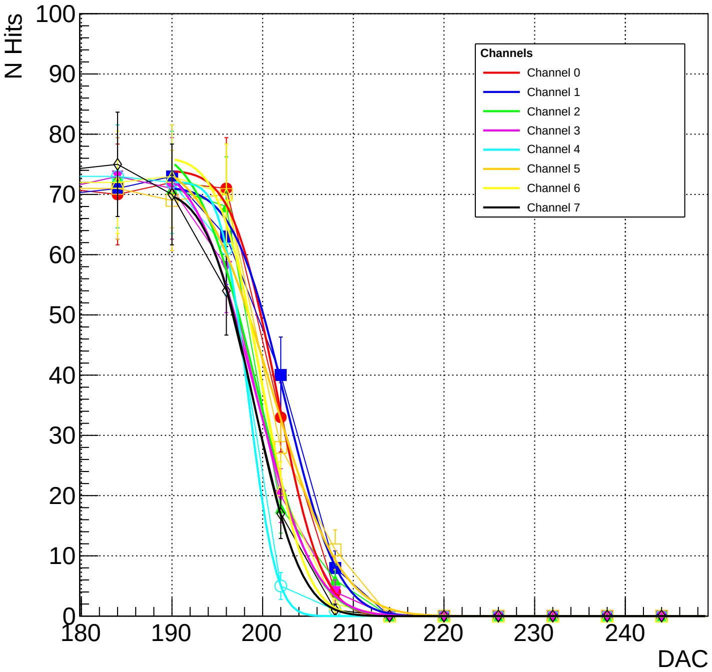

FIGURE 4.23: Threshold scan for layer 7, ASIC 12 with high gain setting. Channels from 0 to 7 is shown here for the display. Error bars represents the statistical uncertainty. The fitted line is the error function defined in (4.2).

where the error function $erfc(z)$ is defined as:

$$erfc(z) = \frac{2}{\sqrt{\pi}} \int_{z}^{\infty} e^{-t^2} dt \tag{4.3}$$

x is a DAC value, p_0 is a half of normalization, p_1 is the value in which FWHM occurs, p_2 is the width of the error function. The fit results are overlayed to the data points in Figure 4.23. From these fit parameters, the threshold was determined with p_1 parameter. The mean noise threshold for the entire active channels is set as a common noise threshold for individual ASIC. These threshold values are summarized in Figure 4.24. For SKIROC2a, the thresholds are fine tuned to the individual cell. The full list of threshold variables are displayed in Appendix C. The “noise thresholds” determined here is to prepare for pedestal and MIP calibration in coming sections. In order to ensure the threshold to be at 0.5 MIP, additional step is required to determine the “trigger thresholds” and this is described in Section 4.6.5.

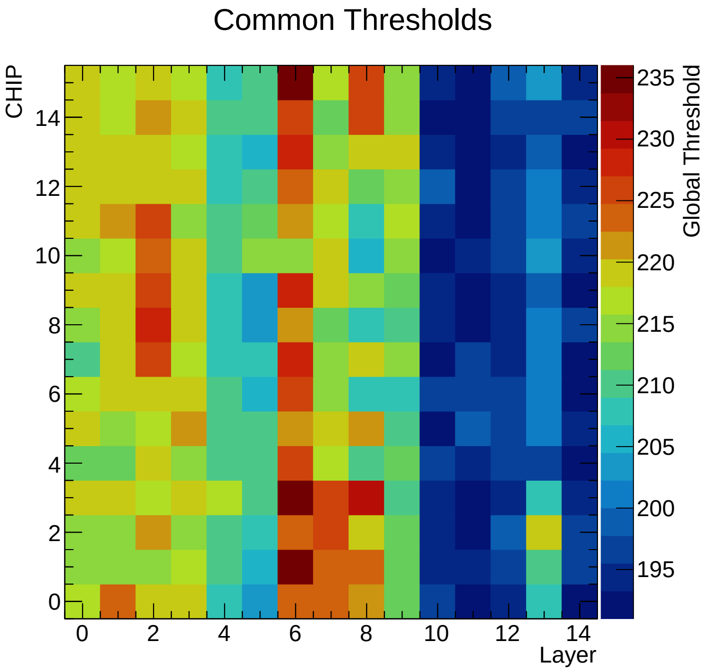

Figure 4.24: Common threshold that was determined from the threshold scan in a view of chip vs. layer.

4.6.3 Pedestals

The pedestal is defined as the mean of the ADC values for all channels without any triggers. The width that is associated to the pedestal is the attributed noise generated from the circuit electronics and the capacitance of the connected cell. The pedestal takes unique value for each layer, each chip, each channel and each SCA. One needs to subtract pedestal from the ADC values before proceeding to the charge measurements for the MIPs. To obtain the pedestal values in each SCA, non-triggered hit information was used. The pedestal distribution was fitted using the Gaussian function. The mean and standard deviation extracted from the fit correspond to pedestal and its width, respectively. Pedestal and pedestal width values for the first SCA in layer 7 is presented in Figure 4.25. Figure 4.25a shows the pedestal values with corresponding channel placed in XY map. This tells us that each ASIC has relatively uniform pedestal values throughout the channels. Pedestal width distribution in Figure 4.25b also displays uniformity throughout the layer. Complete pedestal and pedestal width values for all layers, all SCAs are summarized in Appendix D.

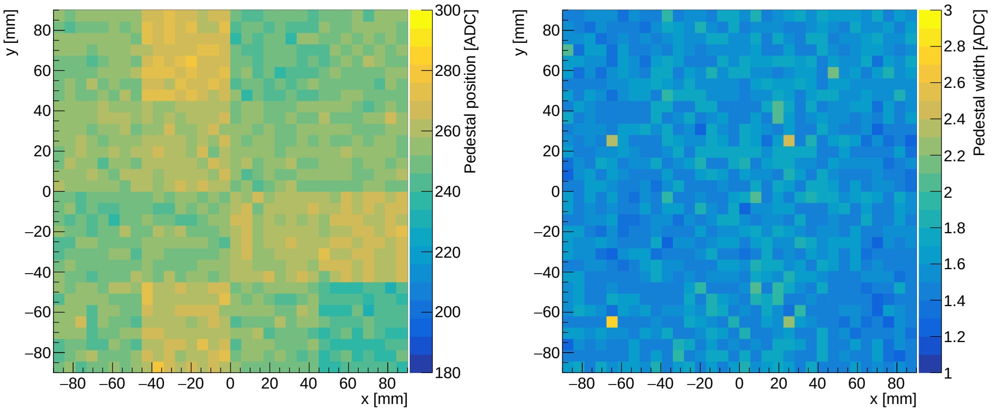

(a) Pedestals

(b) Pedestal width

FIGURE 4.25: Fitted pedestal information for the first SCA of the layer 7 with high gain setting is shown. (a): Fitted pedestal value and (b): width of the pedestal fit for each channel in all 15 layers.

4.6.4 MIP Calibration

Following pedestal determination, MIP calibration was executed for all detector cells. In the initial phase of this calibration, the detector was subjected to a muon beam with an energy of 150 GeV. Muons are the good approximation to the MIPs. Therefore, a signal distribution that can be approximated by at Gauss-Landau convolution function. The most probable value of the Landau distribution is defined as the energy deposition corresponding to 1 MIP. Conversely, the Gaussian portion of the distribution characterizes the uncertainty in the detector response attributed to noise. The resulting charge distribution and its corresponding fit for layer 7, ASIC 6 using high gain are depicted in Figure 4.26. For the complete set of MIP spectrum and its fits, refer to the Appendix E. The calibration constants were determined by extracting the mean and width values from the fit. MIP values and widths for layer 7 with high gain setting is shown in Figure 4.27. Both MIP value and width are confirmed to be consistent throughout this layer. This was also true for the other layers, which is presented in Appendix D.

4.6.5 Trigger Threshold

As described in Section 4.6.2, the noise threshold was established to set a minimum requirement for both pedestal and MIP calibration. However, our objective is to achieve a 0.5 MIP. Since SKIROC allows user to manually inject signal from the DAQ software, this feature was used to calibrate the trigger threshold. Using the ADC values obtained

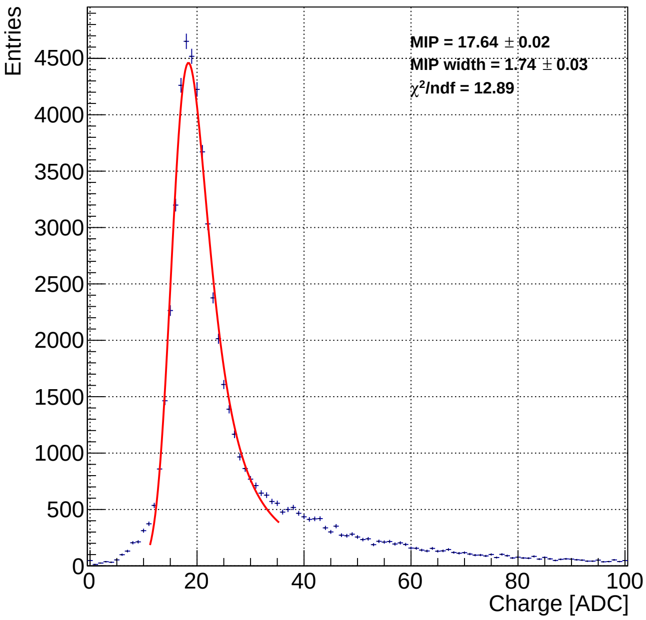

FIGURE 4.26: Charge measurement result after the pedestal subtraction for layer 7, ASIC 6, using high gain. The red line is the Landau-Gaussian convoluted fit function and the mean ADC value corresponds to 1 MIP.

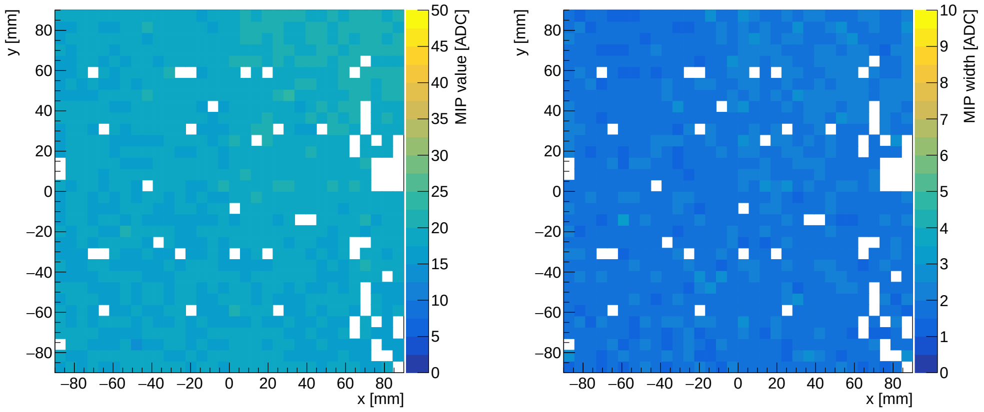

(a) Mean MIP values (b) MIP widths

FIGURE 4.27: MIP measurement results for layer 7 with high gain setting. (a) MIP values and (b) MIP width are shown in the z-axis.

from the MIP calibration, we injected a signal with a DAC value that yields an ADC output comparable to 1 MIP. The injection was varied around that value. The linear correspondence between the amplitude and the DAC values allow for extrapolating the DAC values to 0.5 MIP which hence defines the threshold of a given channel. The results for layer 7 with first 8 channels are shown in Figure 4.28. Each color represents

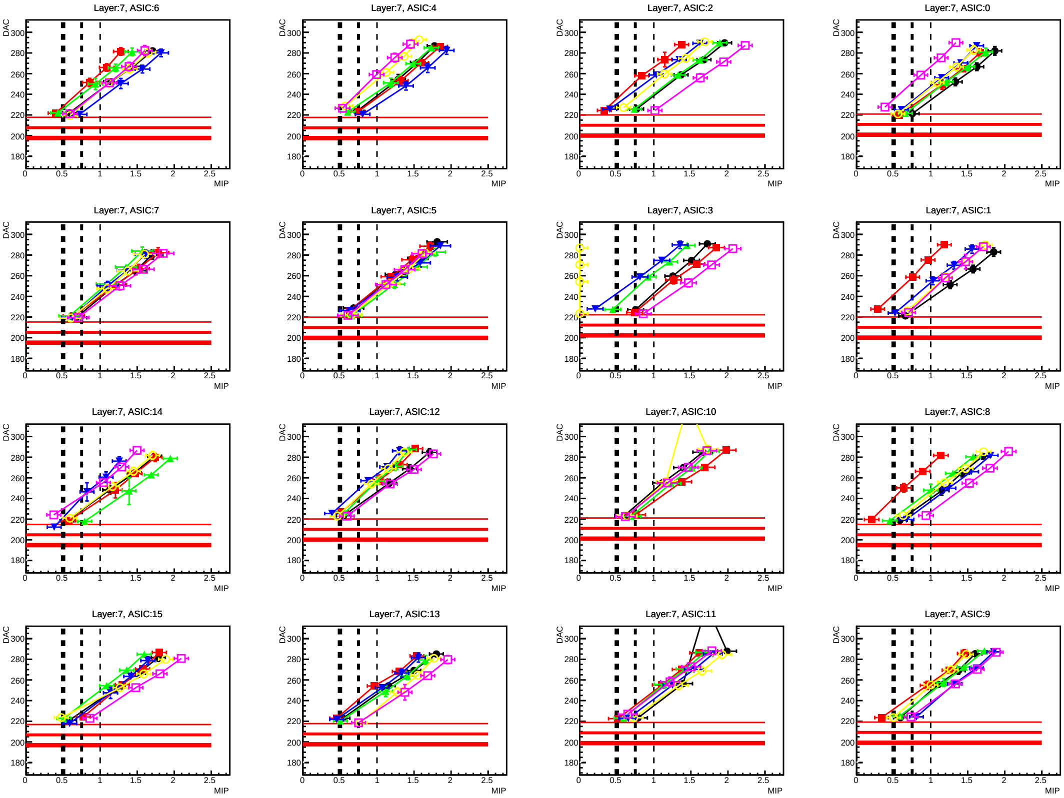

FIGURE 4.28: MIP injection results for layer 7 with first 8 channels on high gain setting are shown. Y-axis represents the injected pulse in DAC and x-axis shows its charge measurement divided by MIP value obtained from the MIP calibration. Red horizontal Lines (from thicker to thinner) correspond to: noise threshold, same with + 10, and + 20. Black Vertical Lines (from thicker to thinner) correspond to: 0.5 MIP, 0.75 MIP, and 1 MIP.

different channel. The data points on the line signifies an injected signal with DAC value equivalent to 0.5 MIP, 0.75 MIP, 1.0 MIP and 2.0 MIP. As we can see, the data displays linearity with increasing DAC inputs. Moreover, most of noise thresholds set for each ASIC is 20 DAC below the 0.5 MIP point on average. The rest of injection test results are presented in Appendix F.

4.6.6 Hold Scan

The fast shaper for triggering and the slow shaper for the actual charge measurements have different time constants, of 90 ns and 200 ns, respectively. The signal is to sampled at the maximum of the slow shaper signal. The time between the moment of triggering by the fast shaper and the actual readout of the slow shaper signal is determined by the hold value. The optimal time depends on the trigger threshold of the individual cell, and one needs to measure the time of which the charge readout it maximized, shown in

Figure 4.29. For this measurement, charge measurements were performed for individual channel with varying hold values. In Figure 4.30, maximum ADC charge readouts from 16 ASICs in layer 9 (FEV12) is plotted as a function of 8 different delay for hold values. The determined optimal hold value for this layer is between 80-100 DAC units, which corresponds to 160 ns–200 ns.

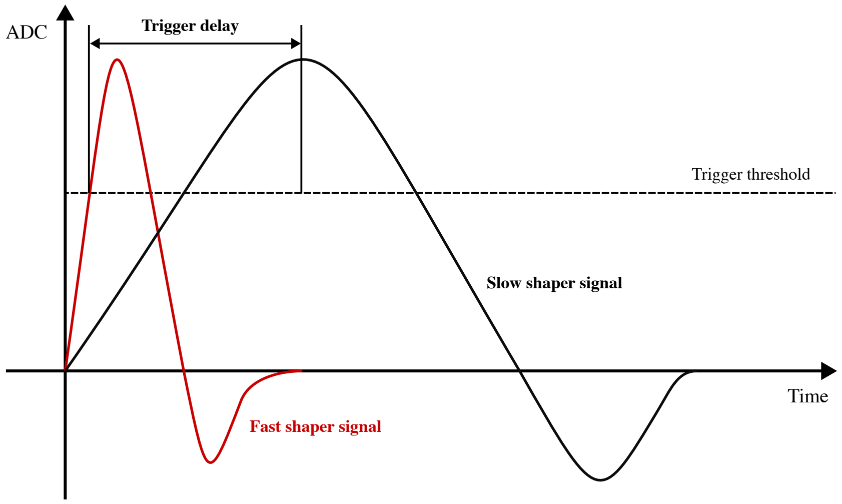

FIGURE 4.29: The value of the hold and of the trigger threshold with respect to the integrated signal.

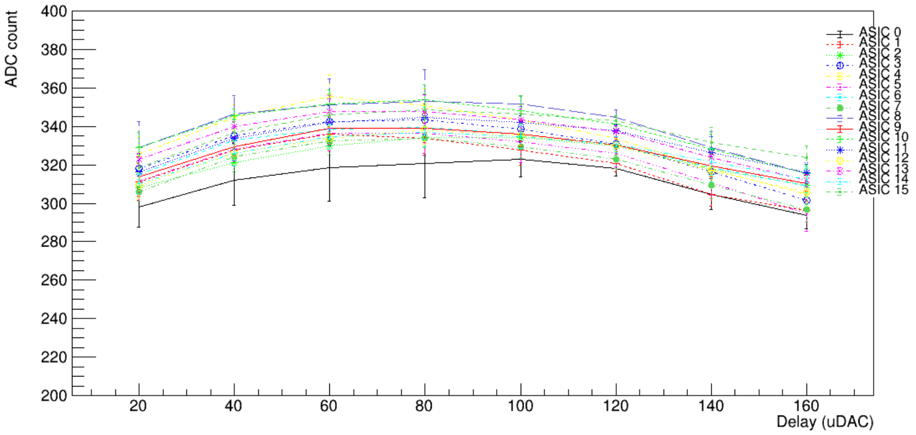

FIGURE 4.30: Maximum pedestal readout is measured with varying hold values from 20 to 160 DAC unit. The plot shows for the layer 9, FEV 12. The ADC readout maximizes at delay of 80.

4.7 Sensor Delamination

As outlined in Section 4.3.2.1, four silicon sensor pads are glued on back of each PCB. After the commissioning, we have discovered that some of these pads were partially or completely unrecognized by the DAQ, yielding, for example, a square pattern on the map, as seen in Figure 4.31. The cause of this delamination is suspected to be

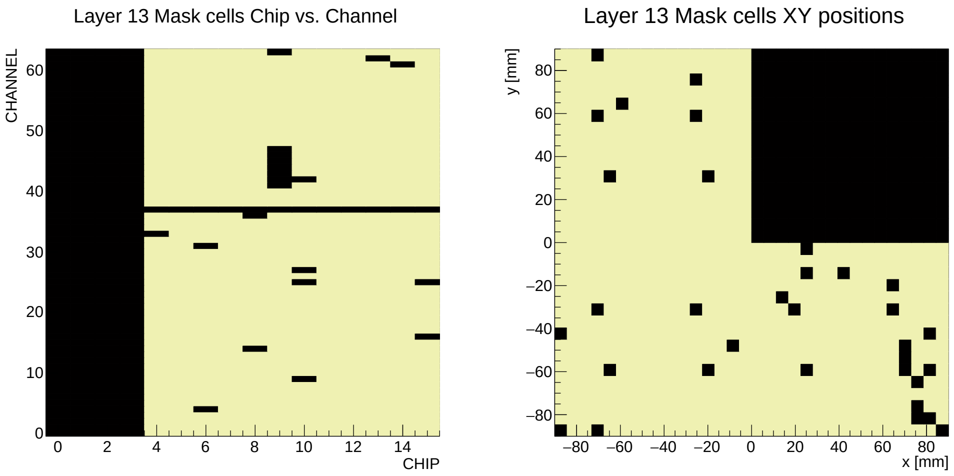

(a) Mask channel vs. chip

(b) Mask XY position

FIGURE 4.31: The mask map is shown for the Layer 13. (a): Channel vs chip distribution. (b): XY position. The black square region corresponds to ASICs which reads signal from the silicon sensor on upper right, which is seen as a sensor delamination effect.

the bending of PCB due to the environmental effects (e.g. temperature or humidity) or inhomogeneous mixing of adhesives used for the gluing, while these points remain speculative. In order to have comprehensive study on this delamination effect, series of mechanical tests need to be addressed, which has already been initiated at IFIC and IJCLab. Throughout the beam test, cells without DAQ response were masked, and their pre-amplifiers were deactivated to prevent interference with neighboring cells. Additionally, the beam position was adjusted to avoid the delaminated sensors, with particularly to the region where $x < 0\,\mathrm{mm}$ and $0 < 0\,\mathrm{mm}$ in the map.

4.8 Event Building and BCID

Once the beam data is taken with proper calibration setup, event building is performed. As described in Section 4.3.2.2, each trigger is recorded with BCID assigned by ASICs. The event building process gathers trigger information with the same BCID to construct an event which occurred in coincidence. The logic diagram for the BCID tagging is depicted in Figure 4.32. The top waveform represents the 5 MHz clock generated by the ASIC. when a signal hits the channel, the OR64 signal transmits an instruction to record the event, which is then stacked on top of the SCAs. Note that the OR64 signal exhibits a delay width of approximately 60 ns for SKIROC2 and 10 ns for SKIROC2a

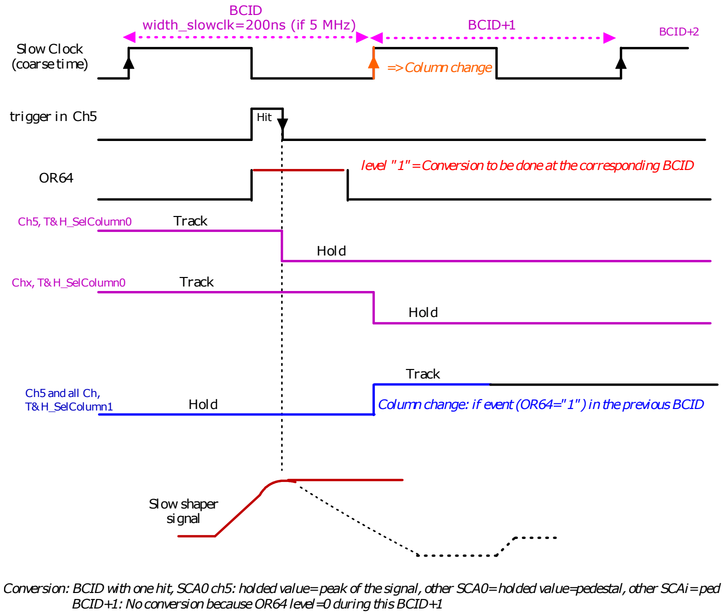

FIGURE 4.32: Illustration of the logic diagram for BCID tagging. Events are validated and stored by an ASIC, with hits and BCIDs correctly aligned [10].

when subjected to an input of 10 MIPs. The two purple signals transmit the timing information, indicating when the trigger is lowered and the subsequent clock has been raised. In previous studies [10], it was revealed that there are BCIDs without registered hit information. This is due to the fact that there exist some cases where the OR64 signal remains in the rising state when the subsequent slow clock rises, caused by its inherent delay. As a result, this event will also register a hit in subsequent BCID, without any registered hit. The frequency of occurrence for such phenomenon is

$$\text{Probability of empty BCID} = \frac{\text{OR64 delay width}}{\text{Slow clock width}} \tag{4.4}$$

The 5 MHz clock in ASIC yields a clock width of 200 ns. Consequently, the probability of encountering an empty BCID is 30% for SKIROC2 and 5% for SKIROC2a. In the event building process, two nearby BCIDs are merged into the original BCID (BCID-1, BCID, BCID+1) to alleviate the occurrence of empty BCIDs. Finally, this issue arises due to the asynchronous nature of the beam frequency in relation to the ASICs' clock. This is in contrast to the ILC, where the beam and detectors are synchronized.

4.9 Simulation

For the Monte Carlo simulations, the `Geant4` toolkit [53] was used with geometrical parameters provided by the `DD4HEP` framework [54]. The SiW-ECAL shown in Figure

4.17 has been implemented into the simulation. The simulation used for this analysis, this beam starts on the surface of the Tungsten plate of the first layer. Further the beam position and its width were iteratively adjusted according to their values during the beam test. This information was extracted from the hit map. The map is depicted in Figure 4.33. In order to quantify the beam position and width, a two dimensional Gaussian fit was performed for the first three layers, which were selected as the references. The X and Y projection of the hit map for these layers, along with their fit curves are presented in Figure 4.34. For the determination of beam position and width, we took the average of Gaussian mean and width from the three layers. Based on the fit results, the beam position was set to $(x, y) = (-53.43\,\mathrm{mm}, -41.73\,\mathrm{mm})$ with a width of $(\sigma_x, \sigma_y) = (23.5\,\mathrm{mm}, 29.7\,\mathrm{mm})$.

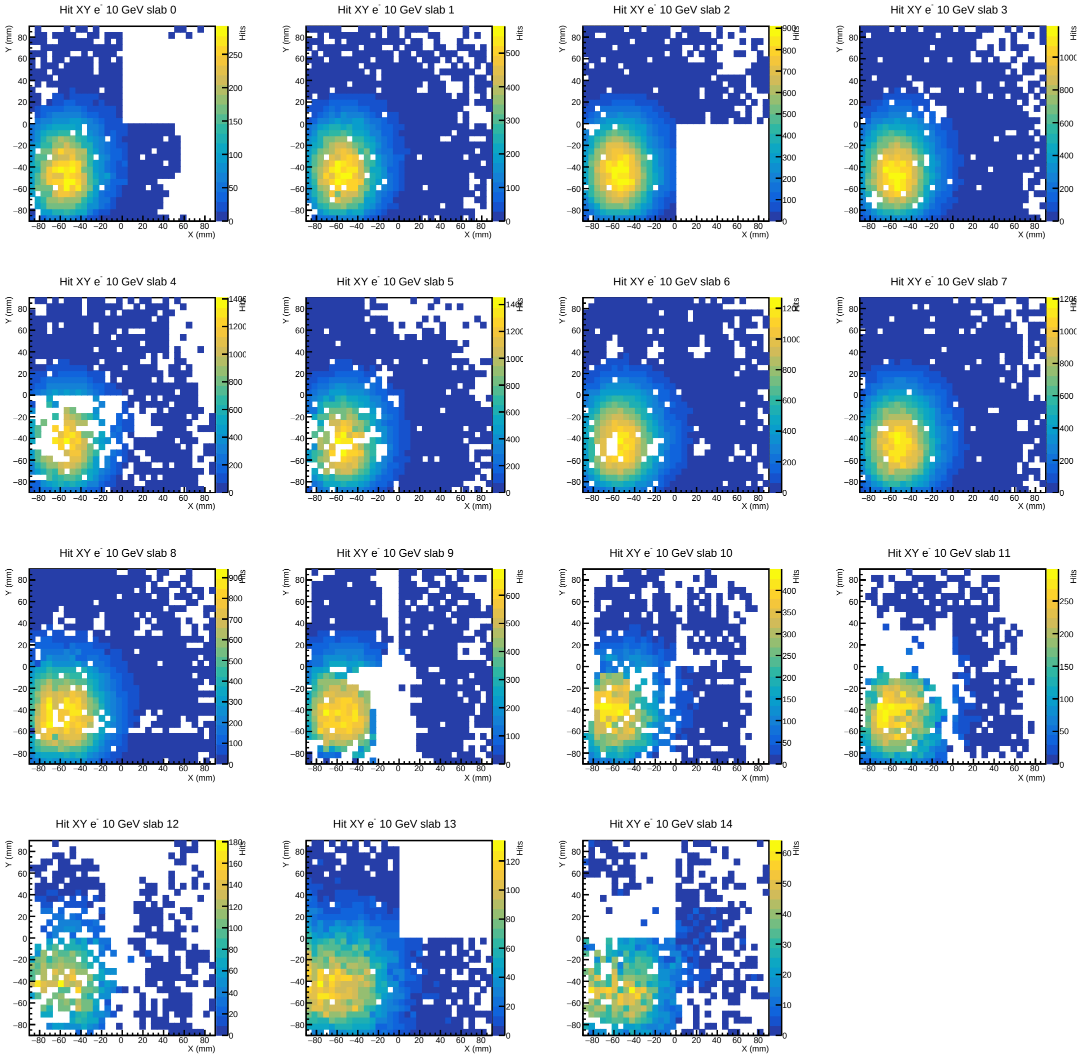

FIGURE 4.33: Reconstructed XY positions of the hits are displayed for all 15 layers for 10 GeV electron beam. The color in the map corresponds to the number of hits. White cells represents unhit or masked channels.

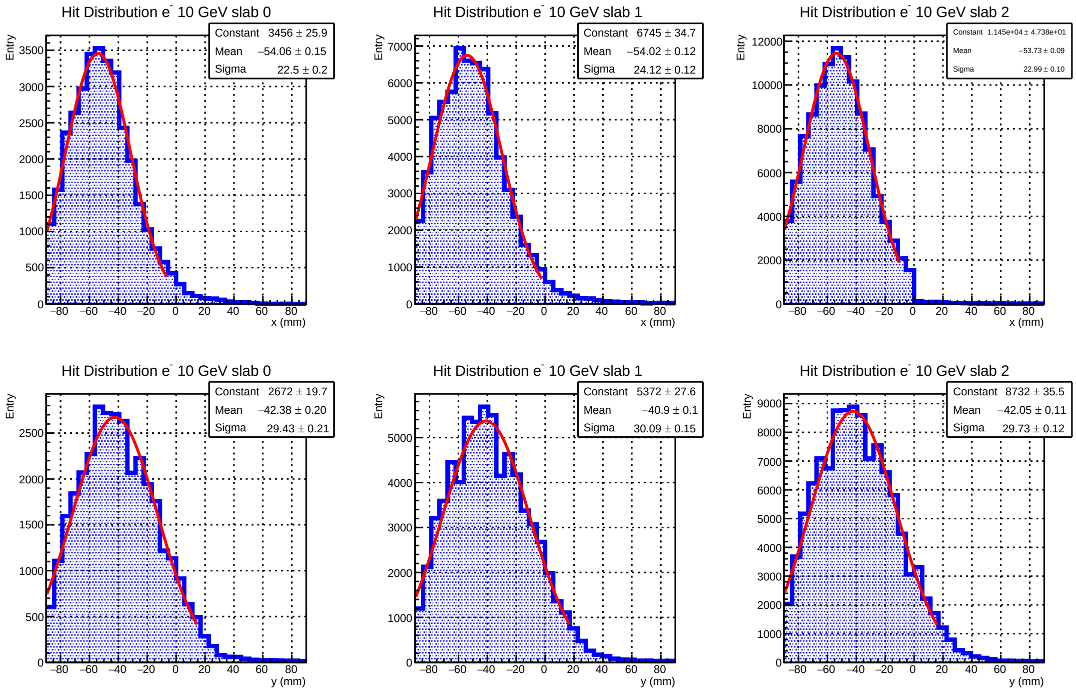

FIGURE 4.34: From the left to right, the hit map for the first three layers are projected onto the x (top) and y (bottom) axes. The red curve represents the Gaussian fit function, and the fit parameters are displayed in the top right of each histogram.

First, without any application of masking, 5,000 electron beam events with varying energies from 10 GeV–150 GeV were generated, in order to verify that the electromagnetic showers can be contained inside the SiW-ECAL prototype with 20.4 X_0. The longitudinal shower profile for several beam energies is illustrated in Figure 4.35. Each distribution was fitted with the function of [55]:

$$f(X_0) = E_0 \cdot t^{\alpha} \cdot e^{-\gamma t} \tag{4.5}$$

where E_0 is constant, $t = X_0 - \beta$, α is the shower maximum position, and β is the measure of the radiation length in front of the calorimeter. The simulation's shower profile reveals the shower maximum at $X_0 = 6$ to 8, corresponding to layers 4 to 6 in the SiW-ECAL prototype. Furthermore, for all beam energies, the showers reach a minimum before 20.4 X_0, indicating that all electromagnetic showers are contained well within the detector.

To align the simulation with the actual beam test conditions, the identical mask setting was implemented. The resulting hit map for the 10 GeV electron simulation is shown in Figure 4.36.

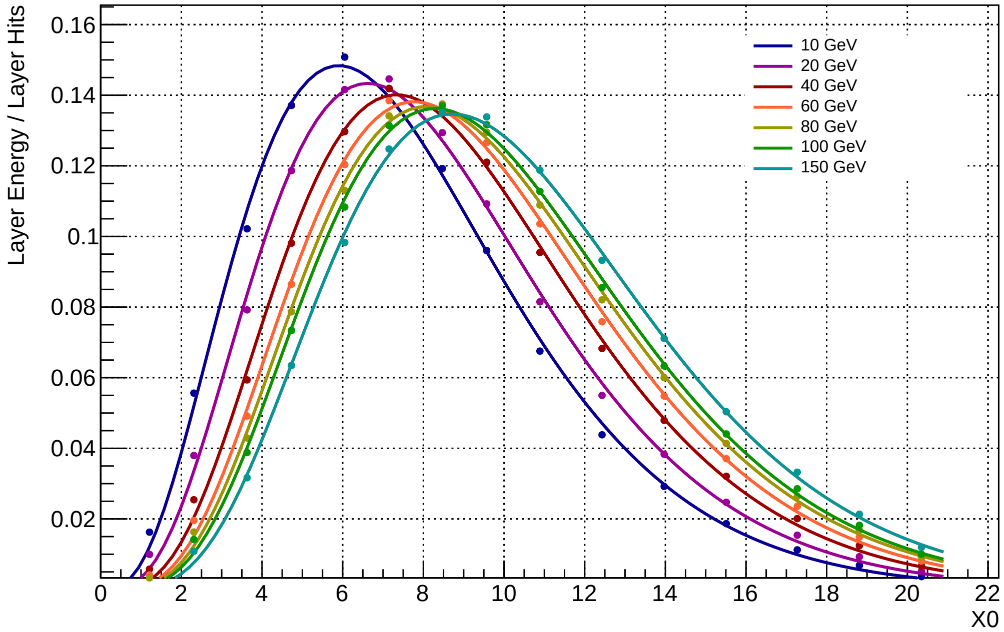

FIGURE 4.35: Simulated shower profiles resulting from e^- beams before masking, at seven distinct energies, depicted as a function of X_0. Each simulated data points were fitted with shower profile function described in (4.5).

4.10 Analysis

As described in Section 4.3, we will concentrate on one of the electron beam runs conducted at an energy of 10 GeV. During this run, the detector was subjected to an electron beam exposure during 30 min. Over all, 23,980 events were reconstructed.

4.10.1 Event Selection

A series of selections were applied before processing the events to the analysis.

- **Coincidence**:

  In order to avoid the event reconstructed from the noise hits, a minimum of 13 layer coincidence was required.

- **Low SCA**:

  In absence of noise, one expects the physics hits at low SCA values. Therefore it is intuitive to restrict also the selected hits to the low SCA values.

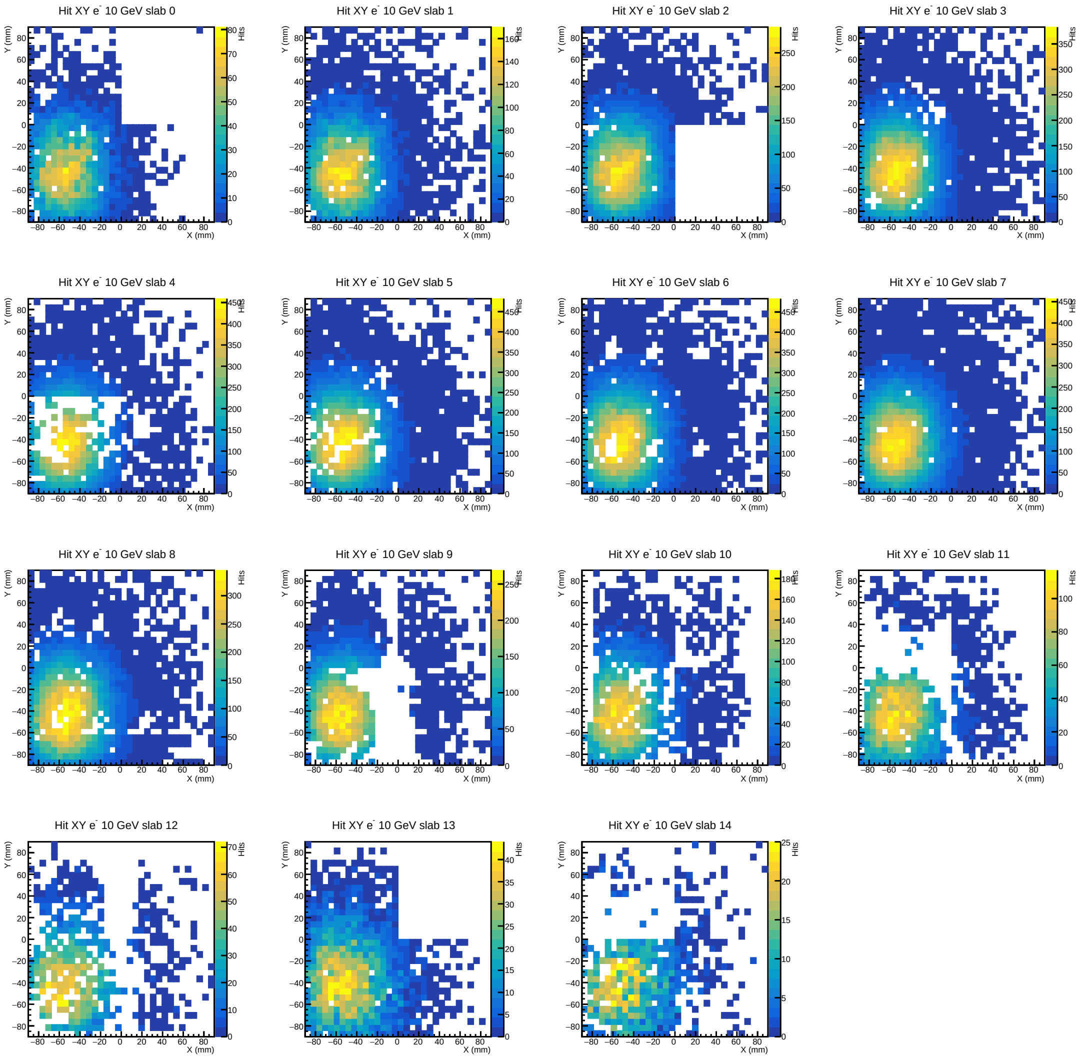

FIGURE 4.36: Simulated XY positions of the hits are displayed for all 15 layers for 10 GeV electron beam. The color in the map corresponds to the number of hits. White cells represents unhit or masked channels.

- **Total number of hits**:

  In the presence of a 13-layer coincidence originating from noise sources such as electronic cross-talks, fewer number of hits is expected compared to the signal. The minimum total number of hits required for analysis was determined based on the count obtained from simulation results, shown in Figure 4.37. For 10 GeV analysis, at least 30 hits were required.

- **Hits in each layer**:

  The analysis anticipates the generation of at least one hit in each layer from 0 to 7. In addition, more than three hits in layers 6 to 8 are required, corresponding to the region where the shower maximum is anticipated to occur.

- **Minimum energy**

  A minimum hit energy requirement of 1 MIP is required for each hit.

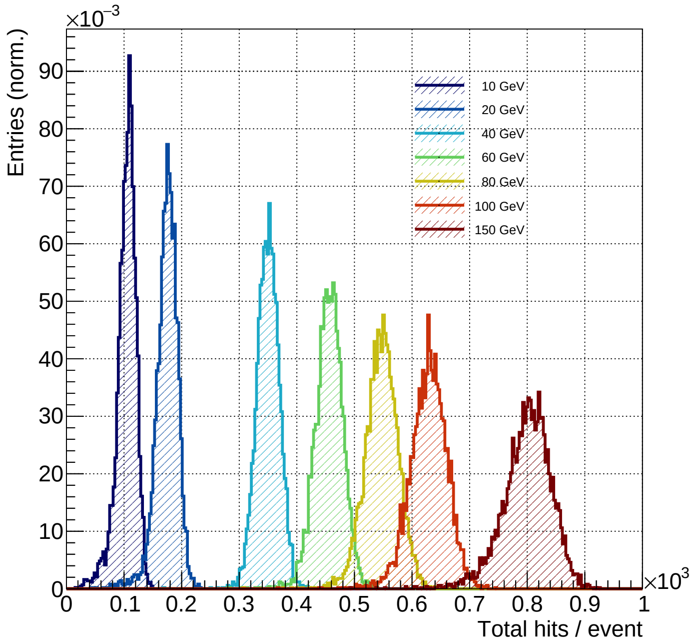

FIGURE 4.37: Total number of hits recorded for each simulated event, varied across different beam energies.

After the series of event selections, the reconstructed events were left with 11,053 events, while 4,347 events remained for the simulation. As a result, data and simulation yields the selection efficiencies of 48.1% and 86.9%, respectively. A typical event shape is visualized in form of event display, presented in Figure 4.38 for a reconstructed event, and in Figure 4.39 for a simulated event.

4.10.2 Data & Simulation Comparison

In this analysis, data and Monte Carlo simulation were compared. Figure 4.40a illustrates the number of hits registered in each layer. Both the data and simulated distributions have general agreement, with the shower maximum between layers 6 and 7, while Data indicates the slightly early development of the shower, as there are more hits in data over the simulation in the front than in the rear. This is likely due to the fact that the material content of the detector in the simulation differs from the one from the test beam, which requires further revision. In addition, the simulation also reproduces the drop between layers 4-6 attributed to masked cells in the core of the shower.

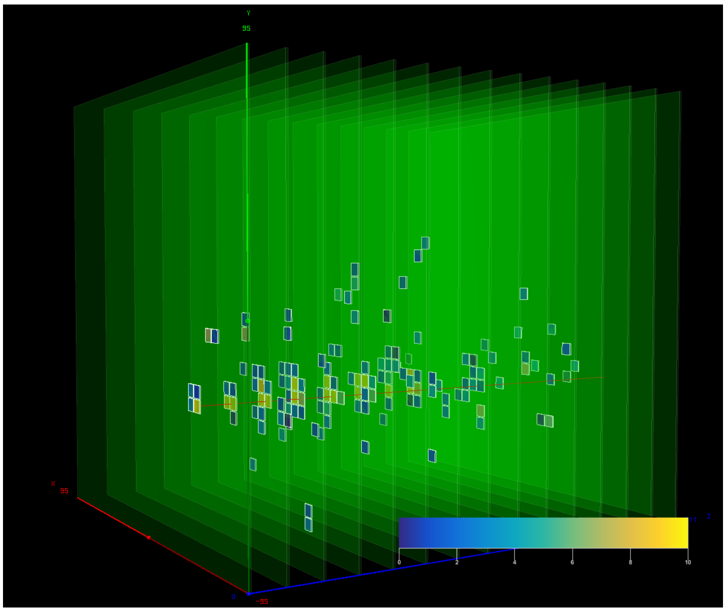

FIGURE 4.38: An image of an event display from one of the reconstructed events after the selection. The green planes represent the layers, and each box represents a hit. The coloring of the hit boxes is determined by the charge measurement readout from those hits in ADC units. The red line connects the center of gravity positions of the hits on each layer, which represents the beam axis.

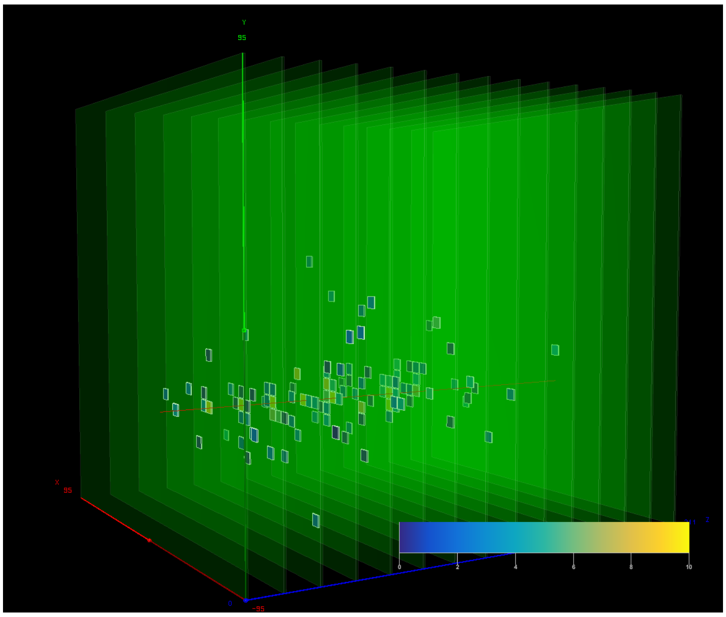

FIGURE 4.39: An image of an event display from one of the simulated events after the selection. The green planes represent the layers, and each box represents a hit. The coloring of the hit boxes is determined by the charge measurement readout from those hits in ADC units. The red line connects the center of gravity positions of the hits on each layer, which represents the beam axis.

Figure 4.40b depicts the overall number of hits. The mean number of hits agrees between data and simulation with 110 hits. Data exceeds the entries of simulation for higher number of hits, which is associated with issues stemming from factors such as the abundance of hits with low ADC counts due to electronic noise, or double-hit events. In addition, a discrepancy is observed at the lower side of the distribution. This discrepancy may caused by an uncertainties related to the beam size and position in the simulation, which slightly differs from the simulation parameters. This discrepancy is also reflected in the number of hits in individual layers, which are presented in Appendix G.

Then the energy measurements are performed. Figure 4.41 displays the total energy deposition in 15 layers for both simulation and reconstruction. Both distributions were fitted with a Gaussian function with the fit range between 400 to 750 MIPs. Fit results are presented in the top right of the figure. The final observed energy resolutions for both simulation and reconstruction are:

$$\begin{aligned} \frac{\sigma_{E_{sim}}}{E_{sim}} &= 12.5 \pm 0.3\ (\text{stat.})\ \% \\ \frac{\sigma_{E_{reco}}}{E_{reco}} &= 13.6 \pm 0.2\ (\text{stat.})\ \% \end{aligned} \tag{4.6}$$

While the energy reconstruction reasonably agrees with the expectations from the simulation, the obtained energy resolutions have discrepancy between the proposed resolution in TDR [51]. In TDR, ECAL is proposed to have energy resolution of order $15\%/\sqrt{E}$. For 10 GeV electron beam, this corresponds to the resolution of 4.74%. One of the reasons for this discrepancy, is due to the difference in their sampling fractions. As outlined in Section 4.4, there will be total of 30 layers with higher sampling fraction in the proposed ILD ECAL thus the final energy resolution will be better. In order to estimate the reachable resolution by the current SiW-ECAL prototype, energy resolution was measured without any masking on the cells. The result is shown in Figure 4.42. The fitted curve shows higher MIP peak with narrower standard deviation.

$$\frac{\sigma_{E_{sim}}}{E_{sim}} = 7.67 \pm 0.085\ (\text{stat.})\ \% \tag{4.7}$$

which is closer to the proposed value. The rest of about 3% discrepancy originates from the maskings that we applied to our prototype, which is expected to be further improved in analysis in the future.

4.11 Conclusion & Outlook

In this section of the thesis, technical tests of the SiW-ECAL prototype were conducted. For the beam test, we assembled 15 layers of SiW-ECAL prototypes, that

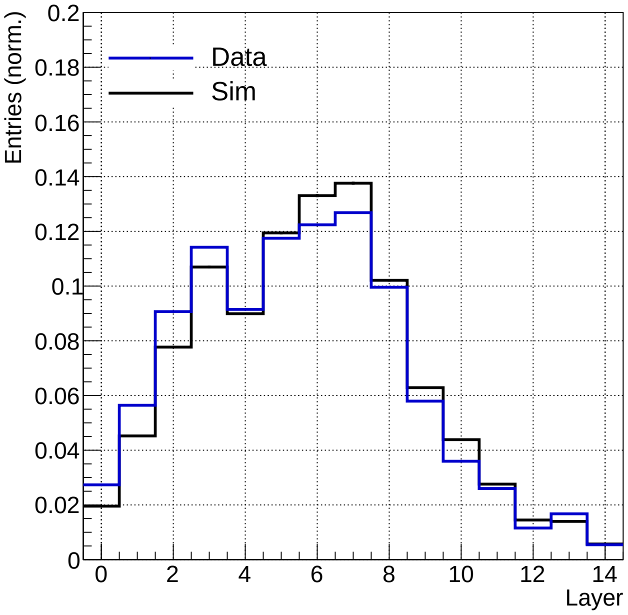

(a) Hits per layer

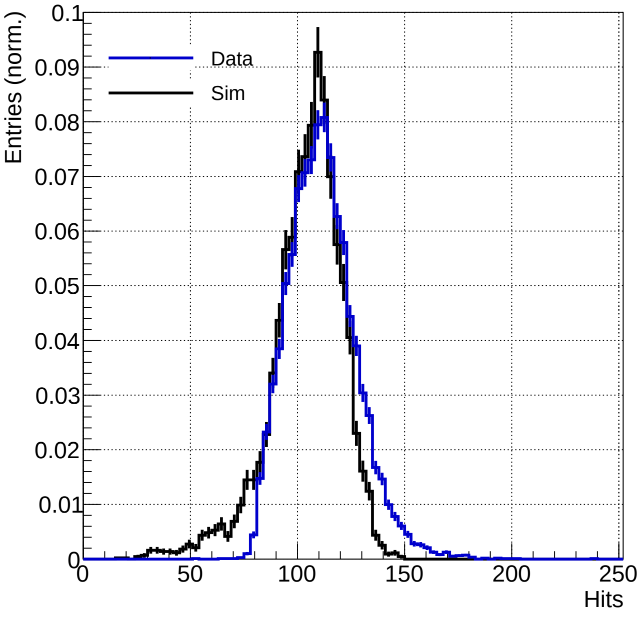

(b) Total number of hits

FIGURE 4.40: Comparison of data and simulated number of hits. (a) Total number of hits per layer. (b) Total number of hits throughout the 15 layers.

comprised several variants of PCBs and several sensor thicknesses. The test was conducted with various beam types including electron, muon and Pion with the beam energy 10 GeV–200 GeV, while this pilot analysis focused on one of the 10 GeV electron beam

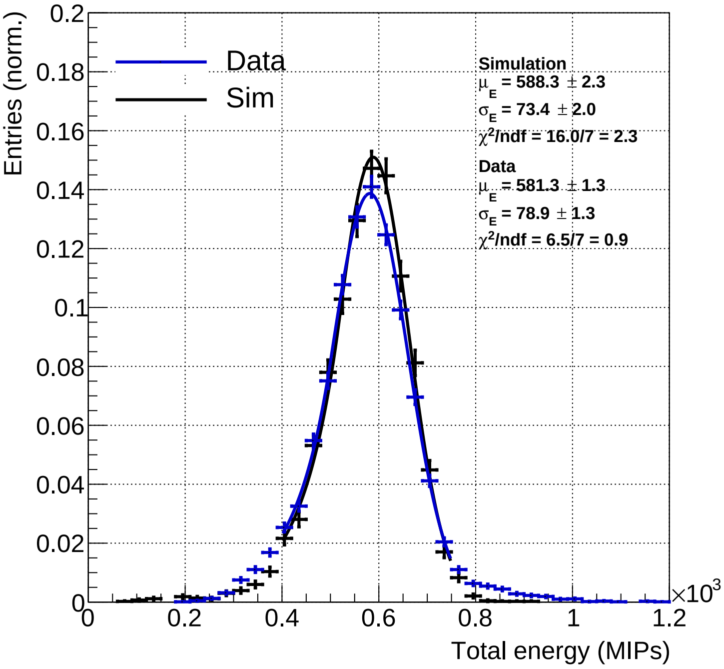

FIGURE 4.41: Comparison of simulated and reconstructed total energy deposition from the 15 layers. Both data and simulation distributions are normalized to 1. Top left shows the fitted result using the Gaussian function for with the fit range between 400 to 750 MIPs.

runs. To prepare for the beam test, a full chain of commissioning procedures was carried out. Despite issues with sensor delaminations, our masking result demonstrated that over 80% of cells could be used for measurements. The reconstruction results revealed that the energy resolution of electromagnetic showers can be measured up to 13.6% ± 0.2% (stat.). This value was compared to the GEANT4 simulation with the same detector setup, showing 12.5% ± 0.3% (stat.), demonstrating broad agreement with the reconstruction. The discrepancy between the proposed energy resolution in the IDR and our simulation was shown to be due to the difference in the sampling fraction, as the current prototype has a half the number of layers compared to the number proposed for ILD. Thus, the simulation was performed without masking setup used for this beam test, yielding a result of 7.67% ± 0.085% (stat.), which is closer to the proposed resolution for the ILD of order $15\%/\sqrt{E}$. To make the simulation closer to the actual beam test environment, the aluminum support of the detector frame needs to be taken into account, which was not considered in this analysis and the beam has to be simulated further upstream in order to take effects of the beam line into account.

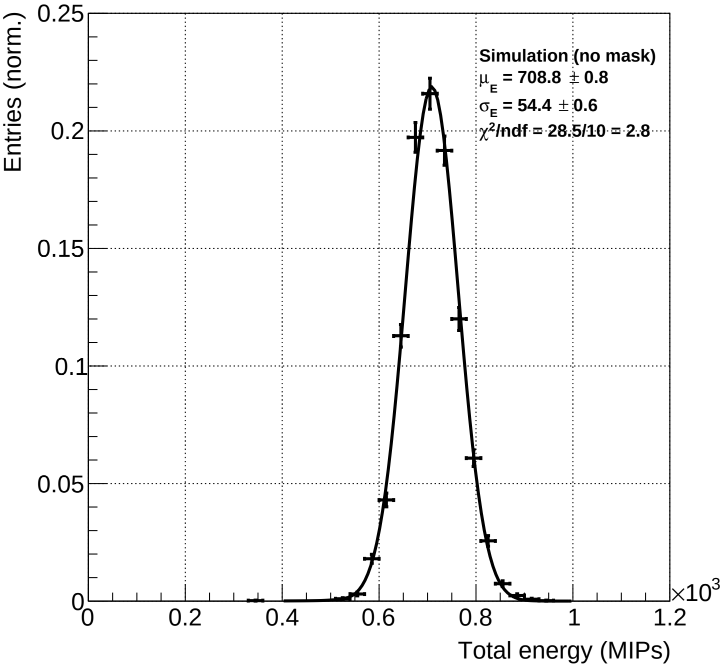

FIGURE 4.42: Simulated total energy deposition without any masking on the cells. Both data and simulation distributions are normalized to 1. Top left shows the fitted result using the Gaussian function for with the fit range between 400 to 1000 MIPs.

Chapter 5

Light Quark Pair Production at the ILC

5.1 Introduction

As discussed in Section 1.3.2, the electroweak coupling between the Z^0/γ bosons and quark pair serves as a robust test of the Standard Model, providing insights into theories beyond the Standard Model. In this study, we simulated $e^+e^- \to q\bar{q}$ events at the ILC with $\sqrt{s} = 250\,\mathrm{GeV}$, with specific focus given to the light quarks $q_L\bar{q_L}$, with $L = u, d, s$.

5.2 Observable

5.2.1 Cross Section

The extraction of the coupling between Z/γ and $q\bar{q}$ is done by measuring the $e^+e^- \to q\bar{q}$ cross section and calculation of forward-backward asymmetry A_{FB} (see Section 5.3). The definition of the measured cross section is:

$$\sigma \equiv \frac{N}{\epsilon \mathcal{L}_{int}} \tag{5.1}$$

where N is the accepted number of events, ϵ is the reconstruction efficiency, $\mathcal{L}_{int}$ is the integrated luminosity.

5.2.1.1 Beam Polarization

One of the key features of the ILC is its ability to polarize both electron and positron beams. Polarisation allows for suppression of background and increases the number of accessible observables. This in turn allows for the independent determination of form factors or coupling constants. The polarization at the ILC won't be at 100% for each beam. The maximum left and right-handed polarization that can be achieved for electron and positron beams are ±80% and ∓30%, respectively. The total cross section for any process including beam polarization can be written as following:

$$\sigma_{\mathcal{P}\mathcal{P}'} = \frac{1}{4}[(1-\mathcal{P}\mathcal{P}')(\sigma_{LR}+\sigma_{RL})+(\mathcal{P}-\mathcal{P}')(\sigma_{RL}-\sigma_{LR})] \tag{5.2}$$

where $\mathcal{P}$ ($\mathcal{P}'$) is the polarization of electron (positron) beam, and σ_{LR} is the cross section for 100% left and right-handed polarization, and vice versa. Equation (5.2) neglects σ_{LL} and σ_{RR} cases where both beams are fully polarized. This is due to the helicity conservation at electron vertex in high energy limit, where the mass of electron can be ignored ($m_e/E \mapsto 0$) at $E = 250\,\text{GeV}$.

5.3 Forward-Backward Asymmetry

In section 1.5, the total cross section of $e^+e^- \to Z^0/\gamma \to f\bar{f}$ was expressed in terms of the form factors for polarized beams $\mathcal{F}^I ij$, as in (1.49). By exploiting the relation between (1.43) and (1.44), coupling between Z boson and fermion pairs can be computed. Parity violation of electroweak interactions yields a term $\cos\theta$ in the differential cross section. Therefore, the forward-backward asymmetry A_{FB} is a classical observable to test the electroweak theory. It is defined as:

$$A_{FB} \equiv \frac{\sigma(\cos\theta > 0) - \sigma(\cos\theta < 0)}{\sigma(\cos\theta > 0) + \sigma(\cos\theta < 0)} \tag{5.3}$$

where $\sigma(\cos\theta > 0)$ ($\sigma(\cos\theta < 0)$) is the total cross section in which fermions are scattered towards forward (backward) direction. The statistical uncertainty of the A_{FB} is given by:

$$\delta A_{FB} = \sqrt{\frac{1-A_{FB}^2}{N}} \tag{5.4}$$

where N is the number of reconstructed events. Plugging the differential cross section defined in (1.47) into the A_{FB} (5.3) yields:

$$A^I_{FB} = \pm \mathcal{A} N_c \frac{3\beta \mathcal{F}^I_{1A}(\mathcal{F}^I_{1V} + \mathcal{F}^I_{2V})}{\sigma^I_{tot}} \tag{5.5}$$

5.4 Event Generation and Detector Simulation

Throughout this chapter, all results have been derived from an analysis based on Leading Order (LO) matrix elements computed using the Monte Carlo event generator implemented in the `WHIZARD` (version 2.8.5) [56]. Subsequently, the generated particles underwent parton showering and hadronization using the `PYTHIA` (version 6.4) framework [2], which has been tuned to the OPAL experiment conducted at the LEP [57]. Within the `WHIZARD` framework, generation of both signal and background processes were performed at a center-of-mass energy of $\sqrt{s} = 250\,\text{GeV}$ for the e^+e^- collision events, with integrated luminosities listed in Table 5.1.

	Integrated Luminosity [fb^{-1}]	
Process	$e^-_L e^+_R$	$e^-_R e^+_L$
$q\bar{q}$	4994	4994
$WW \to 4q$	4996	5116
$ZZ \to 4q$	5052	5109
$q\bar{q}H$	1457	2278

TABLE 5.1: List of integrated luminosities for each Standard Model process.

The cross sections for both signal and background process for this analysis are presented in Table 5.2. `WHIZARD` accounts for QED Initial State Radiation (ISR) and Final State Radiation (FSR). Moreover, the simulation supposed 100% beam polarization. These results will be scaled to the realistic scenario $(\mathcal{P}, \mathcal{P}') = (\mp 0.8, \pm 0.3)$. Generated events undergo full detector simulation of ILD using the `DD4HEP` framework [54], which provides geometrical parameters to the `Geant4` toolkit [53]. Background emerges from the beam-beam interactions, which produces incoherent e^+e^- pairs, are simulated via `Guinea-Pig` [58].

Signal $\sigma_{e^+e^-\to q\bar{q}}$ [fb]		
Process	$e^-_L e^+_R$	$e^-_R e^+_L$
$d\bar{d}$	4484.52	988.93
$u\bar{u}$	6548.26	2772.10
$s\bar{s}$	4442.36	979.51
$c\bar{c}$	6573.02	2782.64
$b\bar{b}$	4566.99	1007.46
Background $\sigma_{e^+e^-\to X}$ [fb]		
$WW \to 4q$	14867.8	136.8
$ZZ \to 4q$	1405.2	606.7
$q\bar{q}H$	343.0	219.5

TABLE 5.2: List of the production cross section for signal and background process, calculated using the generated number of each processes and integrated luminosities.

5.5 Parton Shower and Hadronization

After the hard process, higher order QCD processes are approximated by parton showering. This is a series of small angle low energy gluon radiation and $q\bar{q}$ pair production. This cycle continues until the momentum transfer to the following emission become small (typically $\sim 1\,\text{GeV}$) [59]. After the parton shower, these partons will start to form color neutral hadrons, which is called *hadronization*. In the experiment, particles will be detected only after the hadronization process. The entire process of parton shower, fragmentation and hadronization is illustrated in Figure 5.1.

Typically the final state hadrons form a collimated set of particles, called a jet (see Section 5.6.3). The secondary partons emitted from the gluons are predominantly soft, while primary partons inherit large fraction of the momentum from the hard process. Therefore, the reconstructed particle with the highest momentum in a jet will most likely contain the original quark from the hard process. This property is exploited in signal selection in Section 5.7.

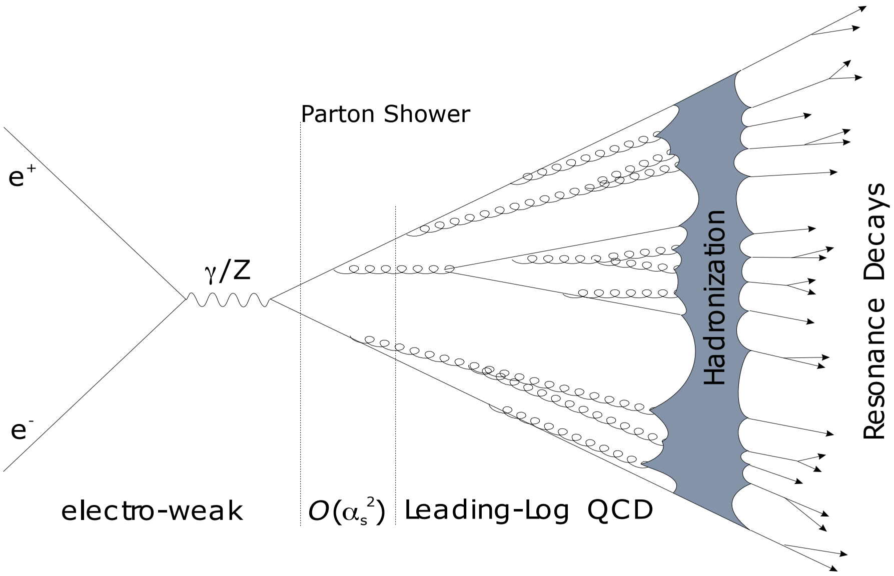

FIGURE 5.1: Illustration of parton shower and hadronization [11].

5.6 Reconstruction

After the full detector simulation of the ILD, reconstruction of the $e^+e^- \to q\bar{q}$ undergoes several steps before starting the event selection process. `ILCSOFT v02-02` was used for the reconstruction algorithm.

5.6.1 Reconstruction Tools

As stated in Section 3.2, PFA is utilized to create the Particle Flow Objects (PFO). This process is managed by the `PandoraPFA` package, which is responsible for the clusteriazation of the calorimeter hits, classification of the particles and track cluster matching. The jet clustering, vertex finding and flavor tagging are governed by the `LCFI+` package [60]. As will be described in Section 5.6.2, one of the distinct features of `LCFI+` is the fact that it identifies vertices prior to the jet reconstruction. This early identification of vertices enables the seeding of relevant information into the subsequent jet clustering software. The distinct characteristics and functionalities of these software packages are introduced in following sections.

5.6.2 Vertex Finding

Vertex finding is essential for identifying primary and secondary vertices (and tertary, if any). Primary vertex represents the e^+e^- collision point, which becomes the origin of the two jets. Moreover, in discriminating the flavor of heavy quarks, the secondary vertex identification becomes a crucial step, especially considering the significant lifetimes of hadrons containing bottom or charm quarks, which can be precisely measured within the detector. These hadrons exhibit characteristic flight lengths, measured in terms of the lifetime at rest (τ) multiplied by the speed of light (c), where $c\tau$ is approximately 400 µm–500 µm for bottom hadrons and 20 µm–300 µm for charm hadrons. The Vertex Finding processor plays a pivotal role in this context, encompassing functionalities such as vertex fitting, primary vertex identification, secondary vertex identification, and V^0 rejection.

5.6.2.1 Vertex Fitter

Within the `ILCSoft` framework, the vertex fitter operates on the identified set of reconstructed tracks in the tracker to compute the probable point of origin for these tracks. The 3D position of the vertices is determined based on several conditions.

- If the fit involves a point constraint, such as estimations of beam spot positions, the initial value is set to the center of the point of constraint.
- In cases without a point constraint, the initial value is established at the 2D crossing point of two circles projected from the helical trajectories of the tracks. The z-direction, perpendicular to the projected circle, is determined subsequent to the calculation of the 2D point by scanning along the helical trajectory.
- When the number of tracks is three or more, the initial value is selected from the two tracks providing the highest vertex probability.

The 3D vertex fit employs the Minuit algorithm, implemented through the `Minuit2Minimizer` class of ROOT. The constructed χ^2 incorporates contributions from every track to the fitted vertex point, with the objective of minimizing this quantity.

5.6.2.2 Primary Vertex Finder

Following the identification of vertices, the subsequent step involves classifying them as primary, secondary, or tertiary vertices. In `LCFI+`, the primary vertex finder employs a tear-down algorithm. The process is follow:

1. Compiling the minimized vertex χ^2 value using all tracks in the event.

2. The track with the highest contribution to the χ^2 value is iteratively removed, provided this contribution exceeds a specified threshold value, set to 25 for this analysis.
3. This iterative removal continues until the contribution of all remaining tracks in the vertex falls below the threshold.

The beam spot constraint is incorporated into the primary vertex finder. According to the ILC Technical Design Report [51], the expected beam sizes for the ILC are $\sigma_x = 639\,\text{nm}$, $\sigma_y = 5.7\,\text{nm}$, and $\sigma_z = 91.3\,\mu\text{m}$.

5.6.2.3 Secondary Vertex Finder

The secondary vertex (SV) finder identifies the decay vertices of b and c hadrons, typically embedded within jets. Its functionality extends beyond the identification of secondary vertices to include tertiary vertices. To enhance efficiency in secondary vertex finding, particularly in scenarios with numerous vertices, the finder discards vertices inconsistent with the jet direction. The first step involves considering tracks not part of the primary vertex, and all possible track pairs are generated as seeds for the secondary vertex finder. The χ^2 value is computed for each track pair using the vertex fitter. Selection criteria are then applied to improve the quality of two-track vertices. They are:

1. Invariant mass of the track pairs (M_{ij}) lower than 10 GeV.
2. M_{ij} lower than the energy of both tracks.
3. Requiring the reconstructed vertex position with respect to the primary vertex to be on the same side as the sum of the track momentum.
4. χ^2 value of the vertex below a designated threshold (9 for our case).

Additional tracks are associated with track pairs to create vertices with three or more tracks. This process iterates until no further tracks can be combined based on the established criteria.

An example of SV reconstruction is illustrated in Figure 5.2. The orange point signifies the Primary Vertex (PV) position, while the red point indicates the Secondary Vertex (SV) location, following the procedures outlined in Section 5.6.2.2 and Section 5.6.2.3. The small points along the dotted lines denote the Impact Parameter (IP) positions,

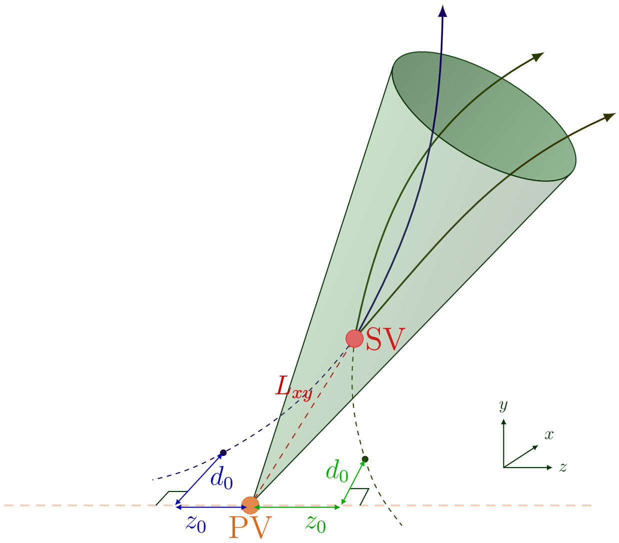

FIGURE 5.2: Illustration of SV reconstruction for a jet [12]. Green cone is represents the jet cone and arrows are the tracks of the associate PFOs. Black dot on the dotted lines are the IP position along the extension of track line. d_0 and z_0 are the transverse and longitudinal distance of the IP, respectively. Orange and Red dot represent PV and SV positions, respectively. L_{xy} is the distance between PV and SV.

representing the closest approach of respective tracks to the beam axis. Their transverse and longitudinal displacements are defined as d_0 and z_0, respectively, and will contribute to the flavor tagging discussed in Section 5.6.4.

5.6.3 Jet Clustering

The second step in the reconstruction process is jet clustering. The *Valencia vertex algorithm* [61, 62] was chosen as the jet clustering algorithm. The Valencia algorithm, designed for lepton colliders, represents a combination of the natural distance criterion relevant for e^+e^- colliders with the increased resilience against backgrounds found in algorithms traditionally adapted for hadron colliders. In the distinctive setting of lepton colliders, where QCD backgrounds are essentially negligible compared to hadron collider experiments, the impact of $\gamma\gamma \to$ hadrons backgrounds on jet reconstruction performance has been shown to be non-negligible. Therefore historically, the `Durham` algorithm [63] was extensively used at LEP and SLC experiments for the jet clustering. This algorithm utilized the distance between any pair of particles i and j, determined by their respective energy (E_i and E_j) and their separation angle (θ_{ij}) as following:

$$d_{ij} = 2\min(E_i^2, E_j^2)(1 - \cos\theta_{ij}) \tag{5.6}$$

The Valencia algorithm, also adopting a Durham-like approach, maintains the distance criterion based on energy and polar angle. In contrast to the anti-k_t algorithm [64], which is widely employed in hadron colliders and relies on transverse momentum and rapidity criteria, the Valencia algorithm employs a distance metric determined by the jet energy squared of the softer of the two particles relative to the harder one with the power of β.

$$d_{ij} = \min(E_i^{2\beta}, E_j^{2\beta}) \frac{(1 - \cos\theta_{ij})}{R^2} \tag{5.7}$$

The radius parameter (R) is a key factor governing the final size of the reconstructed jets. The beam distance in the Valencia algorithm is defined as:

$$d_{iB} = p_T^{2\beta} \tag{5.8}$$

where p_T is the transverse momentum of the selected particle i.

5.6.4 Flavor Tagging

The flavor tagging process employs a multivariate classifier implemented in the Toolkit for MultiVariate data Analysis (TMVA) package. Applied individually to each jet, this procedure avoids considering interactions between jets beyond the current implementation. Jets are categorized based on the number of reconstructed vertices. Categorization considers events with zero, one, or two reconstructed vertices per jet. Additionally, jets can have a single-track pseudo vertex. For each category, specific input variables are defined and passed to the multivariate classifier. Boosted Decision Trees (BDTs) are employed as the multivariate classifier, utilizing gradient boosting and operating in multi-class mode for simultaneous training of multiple event classes. Three classes are defined: b-jets, c-jets, and light-flavor jets. Flavor input variables are constructed from jet constituents, including charged tracks and secondary vertices. Jet momentum is utilized to examine jet constituents in terms of jet direction. To account for particle boost dependence, many input variables are normalized using the jet energy. However, complete elimination of jet energy dependence is challenging due to non-invariant acceptance cuts and detector effects relative to jet energy. Finally, each jet is assigned with likelihood to be originated from b-quark and c-quark, with b-tag and c-tag values, respectively. For the light quark pair production analysis, events with high b-tag and c-tag values were discarded (see Section 5.10.1).

5.6.5 Charged Particle Identification

The measurement of the differential cross section as relevant for this analysis relies heavily on the correct particle identification. In ILD the TPC allows for particle identification via dE/dx and the Bethe-Bloch formula. As outlined in Section 4.2.2, each particle type follows a distinct curve in the Bethe-Bloch formula when plotting its energy loss within the medium (dE/dx) against its momentum. This can be used to distinguish the particles passing through the detector. Figure 5.3a shows the dE/dx distribution vs. track momentum, with each color corresponding to a particle type as indicated in the legend. Distributions in each bin depict the number of entries in individual momentum ranges, with Kaon, Pion, and proton dominating the majority of the distribution. This separation and dominance become more pronounced when projected onto the dE/dx axis, as shown in Figure 5.3b.

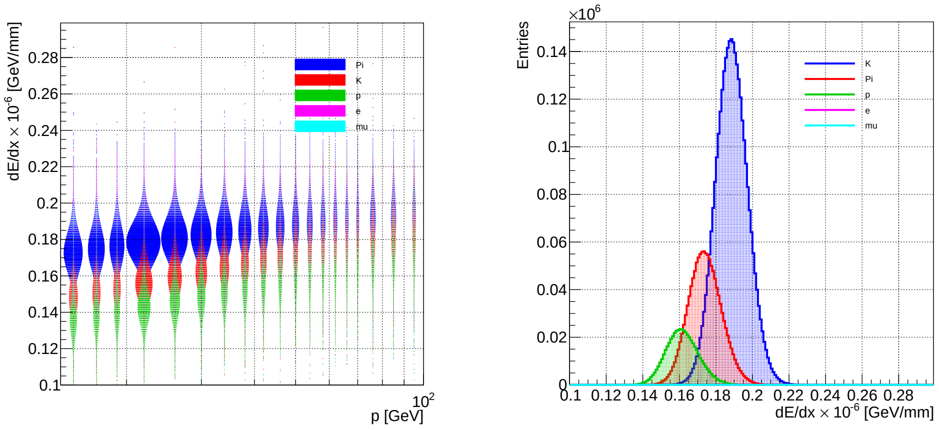

(a)

(b)

FIGURE 5.3: dE/dx distribution for individual tracks in $q_L\bar{q}_L$ samples. (a) dE/dx vs. track momentum and (b) its projection to dE/dx.

One can quantify the separation power $\eta_{A,B}$ for distinguishing two particle types, A and B, by fitting a Gaussian distribution to each phase-space region and obtaining the mean $\mu(p)$ and standard deviation $\sigma(p)$ as follows [40]:

$$\eta_{A,B}(p) = \frac{|\mu_A - \mu_B|}{\sqrt{\frac{1}{2}(\sigma_A^2 - \sigma_B^2)}} \tag{5.9}$$

The $\eta_{A,B}$ serves as a quantitative measure of particle separation, with higher values indicating better separation. Figure 5.4 illustrates the separation between Pion/Kaon and Pion/Proton. The observed low separation power in the 1 GeV region signifies the crossing of dE/dx values between the three particles. Above, the separation power

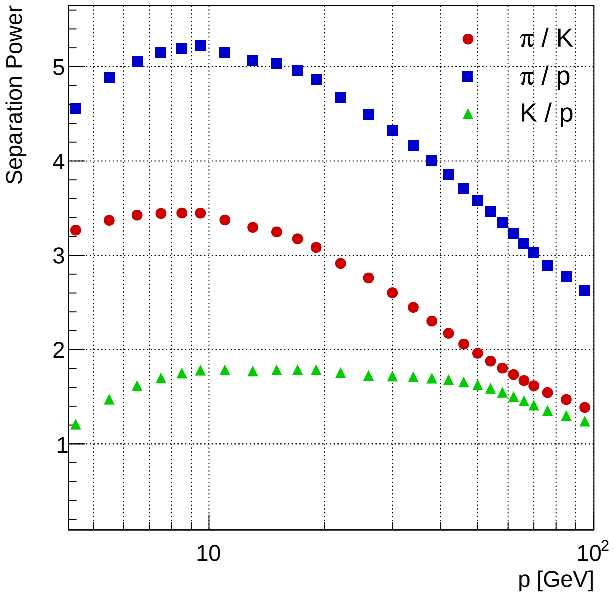

FIGURE 5.4: Separation power for distinguishing π/K, π/p and K/p.

for both Pion/Kaon and Pion/Proton reaches its maximum around 10 GeV. At higher energies, all types of particles become relativistic, resulting in a lower separation power.

Moreover, a thorough examination of dE/dx consistency as a function of the polar angle was carried out for Pion, Kaon and proton. Figure 5.5 presents the dE/dx values vs the $\cos\theta$ of each track for three different types of particles. Each bin in $\cos\theta$ was subject to a Gaussian distribution fit, and the error bars were computed based on the standard deviations of this fit. The plot confirms that each particle forms distinct peak in its dE/dx value.

Figure 5.6a depicts Pion selection purity (green) and efficiency (blue) vs track angle. Flat green curve shows one can select Pions from any given polar angle with constant purity. However, the selection efficiency exhibits a distinct pattern across the polar angle, particularly in regions (a) $|\cos\theta| < 0.2$ (near TPC plate), (b) $0.2 < |\cos\theta| < 0.8$ (barrel region), and (c) $0.8 < |\cos\theta|$ (forward region). The efficiency decrease in the $0.8 < |\cos\theta|$ region is likely due to the decreasing number of TPC hits with increasing polar angle. In particular, the dE/dx resolution ($\sigma_{dE/dx}$) follows a formula:

$$\sigma_{dE/dx} \propto L^{-0.34} \times N^{-0.13} \tag{5.10}$$

where L represents the total sampled length, and N is the number of samples. In the $0.2 < |\cos\theta| < 0.8$ polar angle region, corresponding to the TPC barrel region, a change

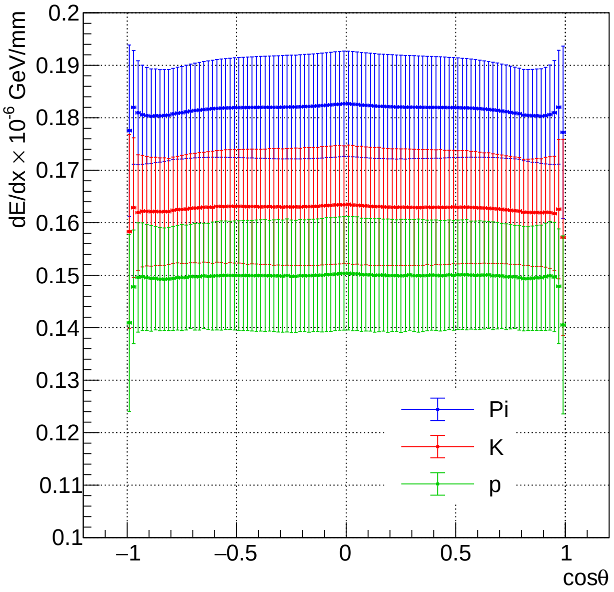

FIGURE 5.5: dE/dx distribution plotted against $\cos\theta$ for individual track. Mean and RMS values for Gaussian fits in individual bin is shown for each particle type.

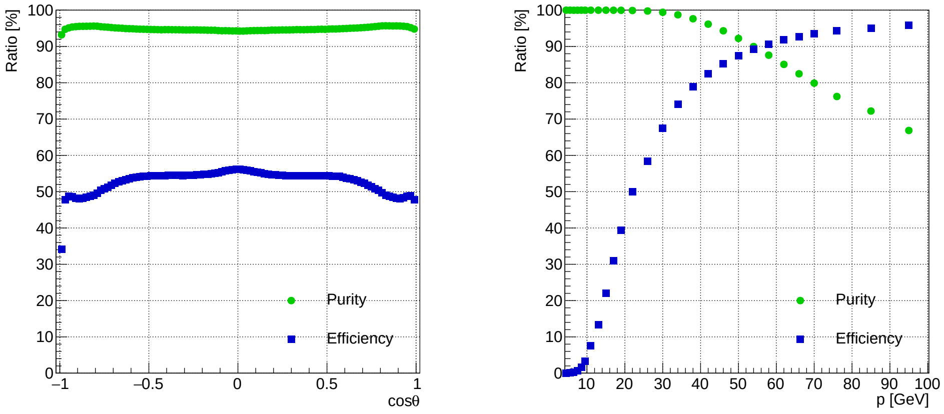

(a)

(b)

FIGURE 5.6: Pion selection purity and efficiency plotted for (a) dE/dx vs. track angle. (b) dE/dx vs. track momentum and

in N is proportional to the same change in L. Given this coupling, $\sigma_{dE/dx}$ becomes proportional to an exponent of -0.47. For tracks passing through the forward region $0.8 < |\cos\theta|$ with full TPC hits, a change in L is proportional to $1/\sin\theta$, leading to a reduction in $\sigma_{dE/dx}$ with a proportionality of $\sin\theta^{-0.34}$. Consequently, the selection efficiency decreases toward the forward region. Figure 5.6b illustrates the purity and efficiency of the Pion selection plotted as a function of track momentum. The purity decreases with increasing momentum, as observed in Figure 5.4, where the separation power decreases. Based on our observations, we have opted for a Pion selection criterion at $dE/dx > 0.178 \times 10^3\,\mathrm{GeV\,mm^{-1}}$, resulting in an efficiency of 52.8%, while maintaining an average purity of 94.9% across the entire polar angle range in $q_L\bar{q}_L$ samples.

For charged Kaon identification, different selection approach was taken. In case of Pion identification, it can benefit from the fact that there is a background free region in upper part of dE/dx distribution, whereas for Kaons, it is contaminated from both upper and lower bounds from Pion and proton, respectively. In order to optimize the Kaon selection, dE/dx distance $\Delta_{dE/dx-i}$ is defined as follows [20]:

$$\Delta_{dE/dx-i} = \left(\frac{dE/dx_{exp} - dE/dx_{i,BB}}{\Delta dE/dx_{exp}}\right) \tag{5.11}$$

where dE/dx_{exp} is the measured dE/dx value, $dE/d_{i,BB}$ is the theoretical dE/dx value expected from the Bethe-Bloch formula of the particle i, and $\Delta dE/dx_{exp}$ is the expected experimental uncertainty for dE/dx measurement. $\Delta_{dE/dx-K}$ for the $s\bar{s}$ process is shown in Figure 5.7a. One can clearly identify a region that is dominated by Kaons at the center of the distribution, while large fraction is still being contaminated by Pions. Therefore, Kaons were selected such that:

$$min(\Delta_{dE/dx-\pi}, \Delta_{dE/dx-K}, \Delta_{dE/dx-p}) = \Delta_{dE/dx-K} \tag{5.12}$$

The resulting distribution is shown in Figure 5.7b.

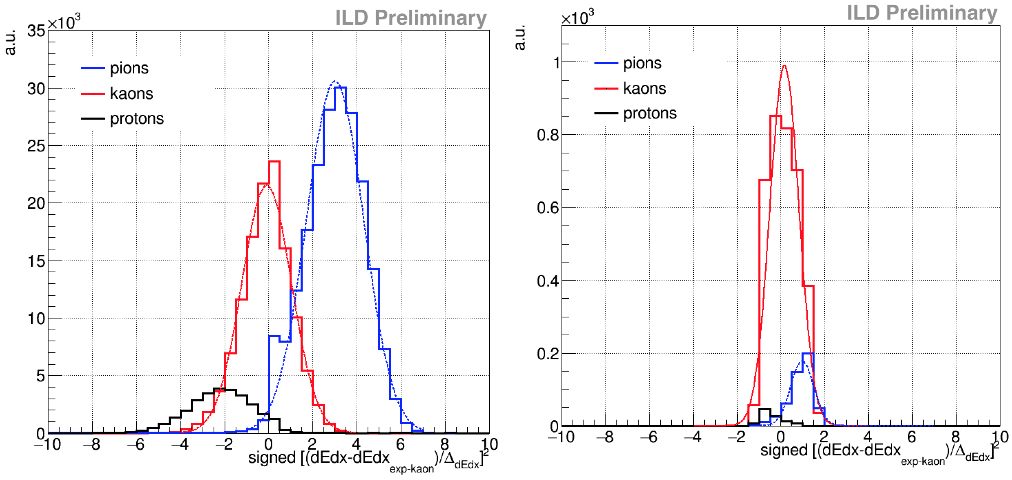

(a) (b)

FIGURE 5.7: (a) dE/dx distances from kaon Bethe-Bloch formula for $s\bar{s}$ process, and (b) after the minimizing particle dE/dx distance to kaon Bethe-Bloch formula

5.7 Signal Process

The $e^+e^- \to q\bar{q}$ processes at 250 GeV result in two jet final states. The precise measurement of the observable A_{FB} as described in (5.3) necessitates the accurate identification of both the charge and the angular properties of these two jets. In order to distinguish q from $\bar{q}$, charges carried by jet or PFO need to be compared for both hemispheres. Each final state with different flavor has unique property:

- $b\bar{b}$: Bottom quark, the second heaviest flavor, mainly hadronizes to B^- and B^0 mesons, both with 40.4% probabilities [5], which have a lifetime of τ =1.6 ps. This corresponds to a $c\tau$ of 450 µm giving rise to secondary vertices (see Section 5.6.2).
- $c\bar{c}$: Charm hadronizes to D meson among others, with a lifetime of about τ =1 ps.
- $s\bar{s}$: Strange quark predominantly hadronized into Kaon with 23.9% probability [19]. Therefore, Kaons can be used as an imprint of the hard process.
- $u\bar{u}$: Unlike strange quark, u-quark will predominantly hadronize into Pions with probability of 38.3%, with a minor probability of 12.2% hadronizing into Kaons [19]. Therefore Pions can be used as an imprint of the hard process.
- $d\bar{d}$: Similarly to the u-quark, d quark will also predominantly hadronize into Pions with 38.7% [19]. Thus Pions can also be used as an imprint of the hard process. Note that it can also hadronize into Kaon (6.17%), via $d \to K^{*0} \to K^+\pi^-$ while the charge appears to be flipped compared to the original quark.

Illustrations of jets which originate from the aforementioned quarks are shown in Figure 5.8. This analysis focuses on the cross section measurement of the light quark pair production, namely the $e^+e^- \to q_L\bar{q}_L$ process. As introduced in Section 5.5, all of the momentum from the hard process is carried by the primary parton, which form hard hadrons. Therefore, for calculating the differential cross section from the hard process, we use the PFOs with the highest momentum in each jet, called Leading PFO (LPFO).

As explained in Section 5.3, the ultimate objective of this analysis is to measure the A_{FB} from the $e^+e^- \to q_L\bar{q}_L$ using the polar angle of the charged LPFO track. Both u and d quark predominantly hadronizes into Pion, which makes it difficult to disentangle each event. On the other hand, the s-quark predominantly hadronizes into Kaons, allowing for it to distinguish from u and d events. Therefore, we have chosen to calculate A_{FB} for combined u/d spectra and individually only for the s quark. Moreover, since u and d also hadronize to Kaon, one needs to estimate the background contribution from these processes. Therefore, the strategy is follows:

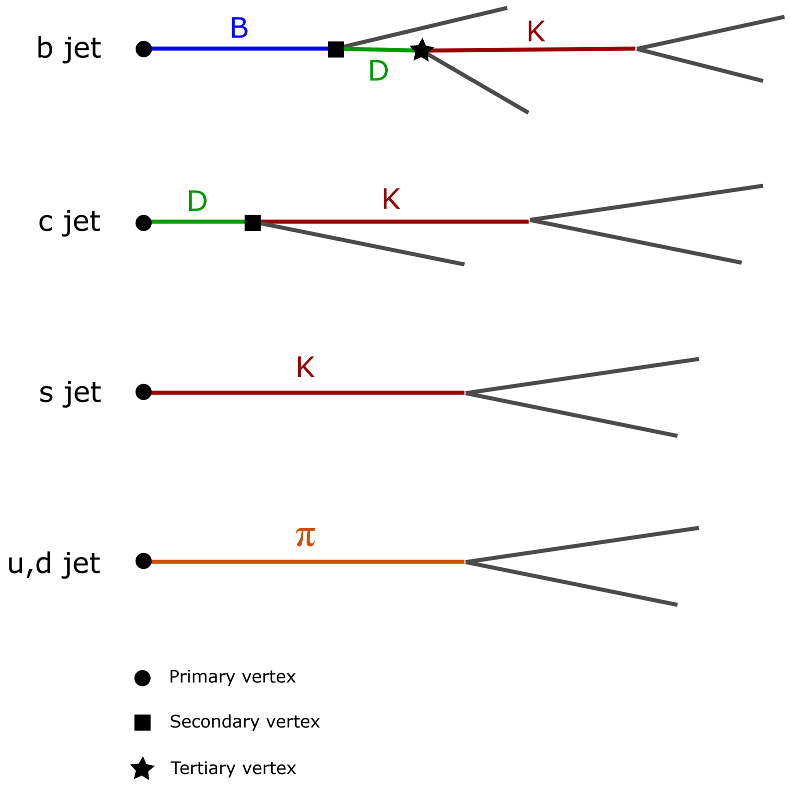

FIGURE 5.8: Graphical representation of jets from various flavors.

1. Reconstruct the $q\bar{q}$ events using Pion as a signature. This distribution will be interpreted as the imprint of the hard processes $e^+e^- \to u\bar{u}/d\bar{d}$.
2. Measure the differential cross section and compare the result with the MC.
3. Reconstruct the $q\bar{q}$ events using Kaon as a signature.
4. Assuming that the Kaons from the $u\bar{u}$ and $d\bar{d}$ processes follows the SM, subtract its distribution from the total events.
5. Calculate the cross section and A_{FB} after the background subtraction. This distribution will be the imprint of hard process from $s\bar{s}$ processes.

5.8 Migration by Charge Flipping

The measurement of the forward-backward asymmetry necessitates precise charge of particles in both hemispheres. When the charges of the two LPFO from both sides are consistent, while conflicting with the corresponding charges in the parton level, the event is considered to be a "migration" (see Figure 5.9), which dilutes the polar angle spectrum and therefore the measurement of A_{FB}. The most of this kind of migrations

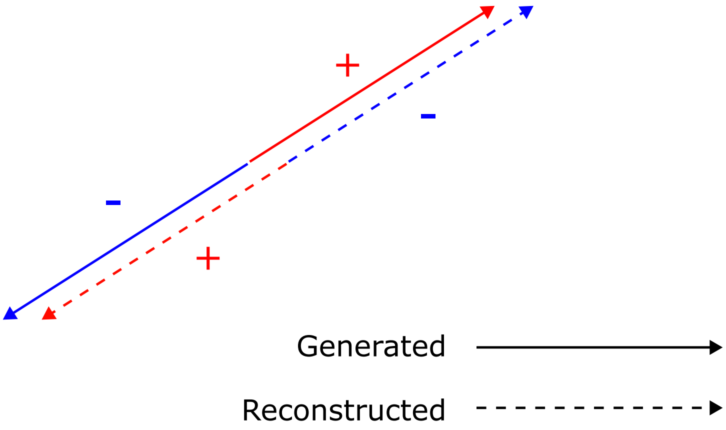

FIGURE 5.9: Illustration of the migration.

are caused by the particle mis-identifications. In order to mitigate the migrations, we applied a series of selection and corrections, which are introduced in Section 5.10.6 and Section 5.11.1.1.

5.9 Preselection and Background Processes

Having defined the signal process, one must now consider the background contributions to this analysis. In $e^+e^- \to q\bar{q}$ analysis, there are two sources of backgrounds: ISR/FSR and di-boson production backgrounds. The ISR and FSR processes are represented as the Feynman diagrams in Figure 5.10. ISR and FSR are the corrections of order α to the leading order electroweak process. Both affect the measurement of final observables. Thus one must separate the phase-space region, depending on the ISR/FSR photon, region where signal events are not affected by much.

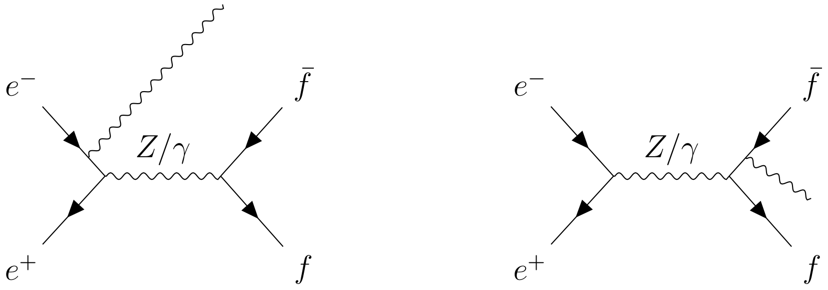

(a) ISR process (b) FSR process

FIGURE 5.10: Feynman diagrams of ISR and FSR.

Additionally, we consider e^+e^- to WW, ZZ, and HZ processes as the di-boson backgrounds, as the jet clustering algorithm can group constituents from these events into two jets. The Feynman diagrams for these processes are illustrated in Figure 5.11. The cuts were, therefore, carefully chosen in order to reject the background as much as possible, while retaining the majority of signal events. In the following sections, each rejection step is introduced.

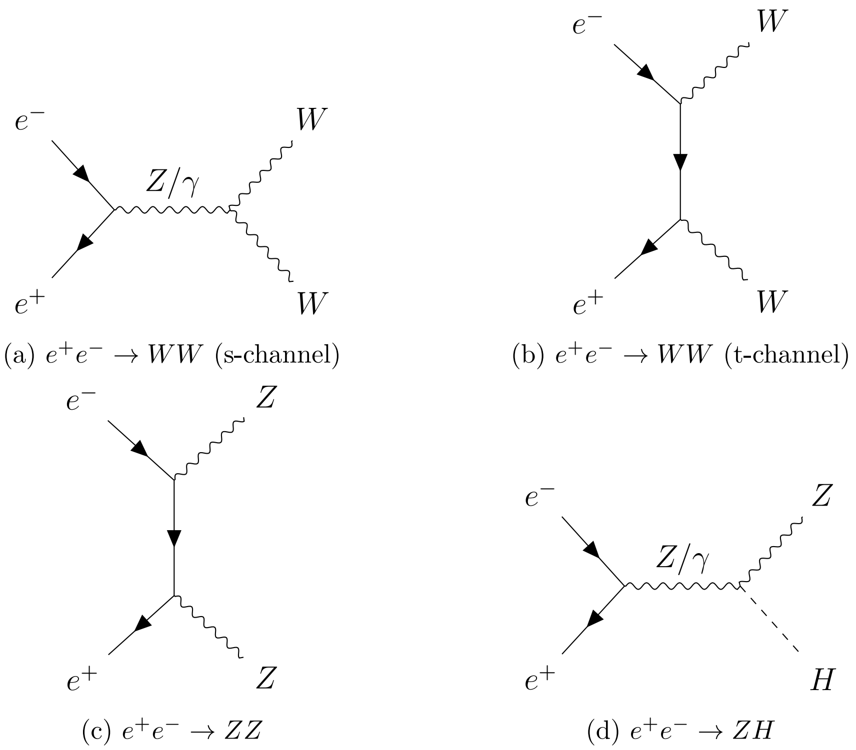

(a) $e^+e^- \to WW$ (s-channel)

(b) $e^+e^- \to WW$ (t-channel)

(c) $e^+e^- \to ZZ$

(d) $e^+e^- \to ZH$

FIGURE 5.11: Feynman diagrams of major Standard Model backgrounds.

5.9.1 Energetic Photon Removal

Most of ISR is collinear to the beam direction. In order to remove events, which are contaminated by such photons, the neutral cluster (γ_{clus}) was defined. A neutral cluster is a sub-group of the reconstructed jet, that consists of neutral PFOs. The neutral energy and polar angle were defined for each γ_{clus} as $E_{\gamma_{clus}}$ and $\theta_{\gamma_{clus}}$, respectively, and they are depicted in Figure 5.12. Figure 5.12c describes that most of jets which embed the ISR will have number of PFOs less than two. In addition, Figure 5.12f tells that one can separate ISR contaminated events from the signal events using γ_{clus} variables since there is a phase-space region dominated by the ISR event. Based on this information, we reject events with $E_{\gamma_{clus}} > 115\,\text{GeV}$ or $|\cos\theta_{\gamma_{clus}}| > 0.97$.

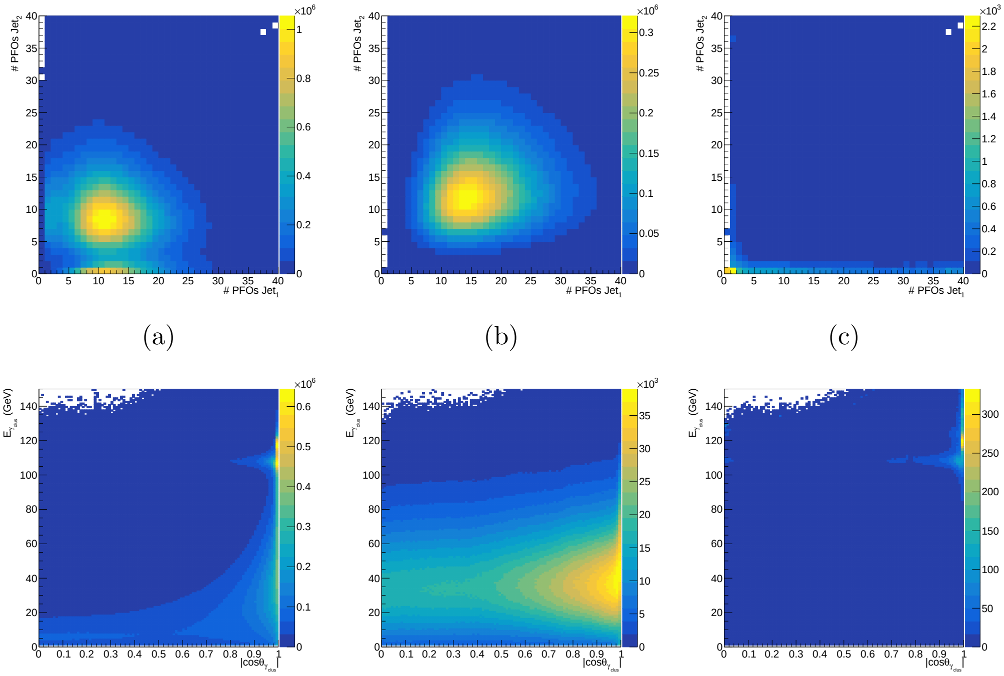

(a) (b) (c)

(d) (e) (f)

FIGURE 5.12: Two-dimensional distributions of neutral cluster variables are presented. The number of PFO constituents inside each jet is plotted for (a) ISR and (b) signal events. (c) represents the ISR/signal ratio of the two distributions. Similarly, (d), (e), and (f) depict the ISR, signal, and their ratio for the two-dimensional distribution of $E_{\gamma_{clus}}$ and $|\cos\theta_{\gamma_{clus}}|$, respectively.

5.9.2 Jet Acollinearity

Jet acollinearity is defined as:

$$\begin{aligned} \sin\Psi_{acol} &= \frac{|\mathbf{p}_{j1} \times \mathbf{p}_{j2}|}{|\mathbf{p}_{j1}||\mathbf{p}_{j2}|} \\ \cos\Psi_{acol} &= \frac{\mathbf{p}_{j1} \cdot \mathbf{p}_{j2}}{|\mathbf{p}_{j1}||\mathbf{p}_{j2}|} \end{aligned} \tag{5.13}$$

where $\mathbf{p}_{j1,2}$ is the momentum direction of two jets. This variable is valuable for eliminating ISR and FSR. Therefore we reject events with the jet acollinearity $\sin\Psi_{acol} < 0.3$ when $\cos\Psi_{acol} < 0$.

5.9.3 Invariant Mass

The invariant mass threshold is primarily established to mitigate ISR-contaminated events. ISR yields a lower center-of-mass energy. Therefore, the invariant mass of the final state varies as a function of the energy of the ISR photon. In events unaffected by ISR, one would anticipate a distinct peak around 250 GeV, the nominal center of mass energy. To select the phase-space region near the nominal center of mass energy, we reject events with jet invariant mass $m_{j1j2} < 140\,\text{GeV}$ to differentiate between these scenarios.

5.9.4 Jet Distance

Productions of heavy boson pairs such as $e^+e^- \rightarrow WW$ and ZZ is a background to the analysis. In particular, WW cross section is very high (see Table 5.2) in case of a left handed polarized beam. Both processes yield a final state with four quarks. Since the jet clustering algorithm mandates the clustering of PFOs into two jets, their cone angles become larger than those in the signal events. Therefore, a jet parameter, y_{23}, is introduced. y_{23} is the jet distance at which a two-jet system would be reconstructed as a three-jet system, as defined in the Valencia jet clustering algorithm. We have chosen $y_{23} < 0.02$ as a rejection criterion for di-boson events. Moreover, this cut aids in eliminating ISR backgrounds that might have been missed by the invariant mass threshold, owing to their softness in the scattering process.

5.9.5 Performance

The cuts against background processes are summarized in Table 5.3. Figure 5.13 illustrates the distribution of jet acollinearity ($\sin\Psi_{acol}$) after the removal of photons. Each color in the legend corresponds to different signal and background processes, where $r\bar{r}$ denotes radiative return events associated with ISR-contaminated events. The radiative return events exhibit a peak at $\sin\Psi_{acol} = 1$, indicating 90° opening of the two jets. Figure 5.14 shows the distribution of the invariant mass m_{j1j2} after photon rejection and $\sin\Psi_{acol}$ cut. As described in Section 5.9.3, the radiative return events peak at the Z boson mass of $m_{j1j2} = 91.2\,\text{GeV}$, which can be efficiently removed by our cut. Figure

#	**Name**	**Quantity**
1	Photon Removal	Events which include any γ_{clus} with $E_{\gamma_{clus}} > 115\,\text{GeV}$ & $\lvert\cos\theta_{\gamma_{clus}}\rvert > 0.97$
2	Jet Acollinearity	Events with two jets with $\sin\Psi_{acol} < 0.3$ when $\cos\Psi_{acol} < 0$
3	Invariant Mass	Events with $m_{j1j2} < 140\,\text{GeV}$
4	Jet Distance	Events with $y_{23} < 0.02$

Table 5.3: Summary of cuts against background processes.

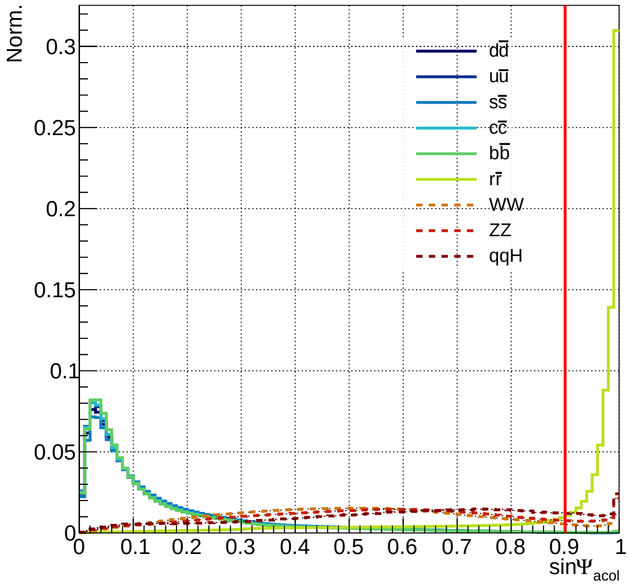

FIGURE 5.13: Acollinearity ($\sin\Psi_{acol}$) distribution with mixture of left and right-handed fully polarized electron beams. Each histogram successively refined by applying a cut on the energetic photon cut. Red line shows the cut.

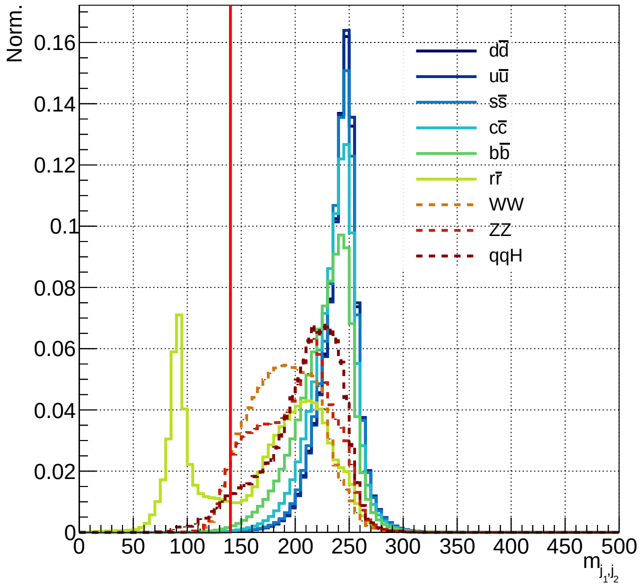

FIGURE 5.14: y_{23} distribution of two jets with mixture of left and right-handed fully polarized electron beams. Each histogram successively refined by applying a cut on the acollinearity cut. Red line shows the cut.

5.15 depicts the y_{23} parameter for the jets after the previous three cuts. As mentioned in Section 5.9.4, Standard Model backgrounds tend to have a larger y_{23} parameter since the jet clustering algorithms force four-quark final states to be clustered into two jets,

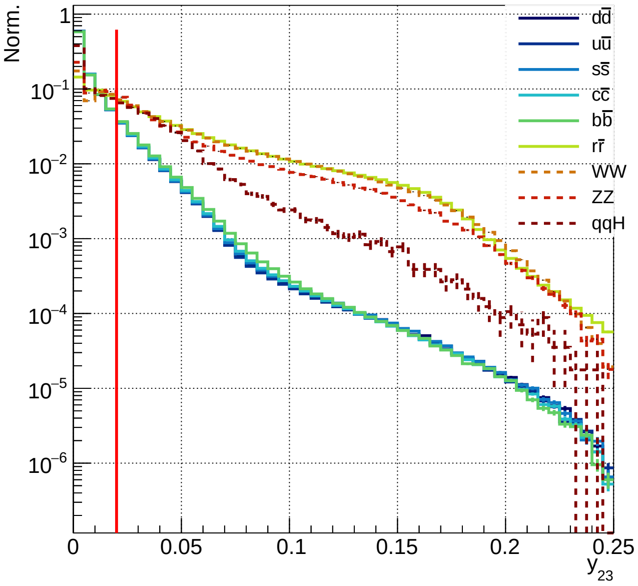

FIGURE 5.15: Invariant mass (m_{j_1,j_2}) distribution with mixture of left and right-handed fully polarized electron beams. Each histogram successively refined by applying a cut on the invariant mass cut. Red line shows the cut.

which is consistent with the distribution.

After applying all the cuts listed in 5.3, selection efficiencies were calculated for every signal and background process (see Table 5.4). About 70% of signal event are retained on average for both left and right-handed electron beam polarizations. For the backgrounds, firstly, the radiative return events are attenuated down to 0.5% level, which is significantly lower compared to the signal events. For the Standard Model backgrounds, all processes are reduced down to 7-8% level.

	Signal					Background			
Cuts	$d\bar{d}$	$u\bar{u}$	$s\bar{s}$	$c\bar{c}$	$b\bar{b}$	Rad. Ret.	WW	ZZ	$q\bar{q}H$
None	100% (2.92e7)	100% (4.22e7)	100% (2.92e7)	100% (4.22e7)	100% (2.92e7)	100% (4.68e8)	100% (7.43e7)	100% (3.86e6)	100% (2.04e5)
Cut 1	92.7%	93.1%	92.3%	93.3%	93.3%	54.9%	89.6%	91.1%	93.1%
+ Cut 2	78.1%	78.9%	77.2%	79.4%	79.9%	2.0%	18.6%	16.0%	14.7%
+ Cut 3	78.0%	78.9%	77.2%	79.3%	79.5%	1.3%	17.7%	15.0%	13.7%
+ Cut 4	69.0%	69.8%	68.2%	69.7%	69.5%	0.5%	7.4%	7.5%	8.7%

TABLE 5.4: Percentage of remaining events after the entire background removal with left-handed electron beam polarization. The number after "Cut" corresponds to the number in Table 5.3.

	Signal					**Background**			
Cuts	$d\bar{d}$	$u\bar{u}$	$s\bar{s}$	$c\bar{c}$	$b\bar{b}$	Rad. Ret.	WW	ZZ	$q\bar{q}H$
None	100% (6.44e6)	100% (1.78e7)	100% (6.44e6)	100% (1.78e7)	100% (6.44e6)	100% (2.96e8)	100% (7.00e5)	100% (1.66e6)	100% (2.10e5)
Cut 1	92.7%	93.2%	92.3%	93.4%	93.2%	52.6%	94.0%	89.5%	93.0%
+ Cut 2	78.0%	79.0%	77.1%	79.5%	79.8%	1.9%	14.9%	16.6%	14.8%
+ Cut 3	77.9%	79.0%	77.0%	79.4%	79.4%	1.2%	13.2%	15.7%	13.7%
+ Cut 4	68.9%	69.8%	68.1%	69.8%	69.4%	0.5%	3.3%	8.1%	8.8%

TABLE 5.5: Percentage of remaining events after the entire background removal with right-handed electron beam polarization. The number after "Cut" corresponds to the number in Table 5.3.

5.10 Event Selection

As introduced in Section 5.7, identification of LPFO plays the central role in this analysis. After the background rejection, series of selection criteria were applied to efficiently single out the light quark process. In the following sections, these criteria are introduced.

5.10.1 Rejection of Heavy Flavor Events

After the flavor tagging of the jets, c and b-tag variables are assigned to each jet to indicate its likelihood to be originate from respective quarks. Figure 5.16 depicts the flavor tagging results for jets from each $q\bar{q}$ process. Each distribution is normalized to its cross section. Figure 5.16a highlights the clear separation of $b\bar{b}$ events from other process. Specifically, choosing a selection criterion of 0.3 results in a 98.94% reduction in $b\bar{b}$ events while retaining over 93% of light quark events. While the c-tagging result

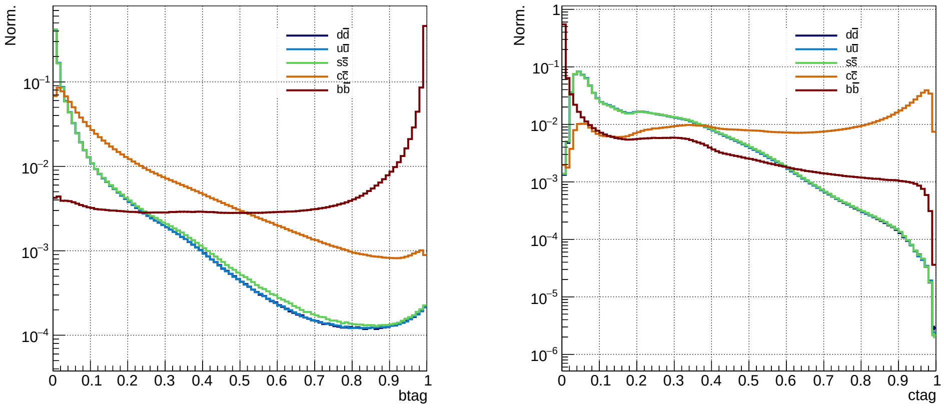

(a) (b)

FIGURE 5.16: (Left) b and (Right) c-tag distributions of two jets in $q\bar{q}$ events before any event selection.

also exhibits separation of $c\bar{c}$ from other processes, the peak is not as distinct as in the b-tagging result. This is primarily due to the tagging performance being dependent on the impact parameter resolution, and c hadrons (i.e. D mesons) have a shorter lifetime compared to B hadrons.

5.10.2 Number of Vertices

One characteristic of light quark events is that they do not produce either secondary or tertiary vertices, as all u, d, and s quarks predominantly hadronize immediately into Pions or Kaons. While the b and c-tag cuts introduced in Section 5.10.1 provide strong suppression against heavy quark events, the number of vertices is also a valuable parameter for distinguishing light quark events from heavy ones. Figure 5.17 reveals

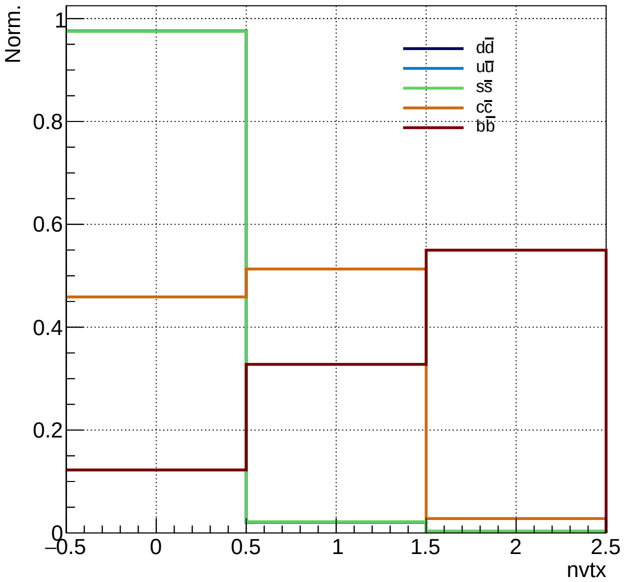

FIGURE 5.17: The number of reconstructed vertices for different $q\bar{q}$ processes prior to any selection is presented, where $nvtx = 0$ indicates the presence of only a primary vertex, 1 corresponds to events with a secondary vertex, and 2 represents those with a tertiary vertex.

that over 97% of light quark events reconstruct only the primary vertex, while 54.1% of $c\bar{c}$ events and 87.8% of $b\bar{b}$ events reconstruct a secondary vertex or higher. Therefore, we decided to reject the events with any vertices other than a primary vertex.

5.10.3 LPFO Selection

As it was discussed in Section 5.7, light quark pair production process often results in production of hard PFO, which can be used as an imprint of the hard process. Therefore, one needs to choose a PFO with the highest momentum in each jet. Moreover, there needs to be a cutoff value for those momentum, since:

- LPFO lower than 10 GeV will suffer from low separation power in terms of PID. (see Figure 5.4)
- Constituents inside the soft jets with higher multiplicities tend to share energy and momentum among the constituents, which will lead to soft LPFO. Such LPFO is not suitable to be used as an imprint of the hard process, since they are no longer back-to-back.

Figure 5.18 displays track momentum for LPFO and the rest of PFOs (non-LPFO) inside the jet without any selections applied. The distribution reveals that the LPFO peaks at

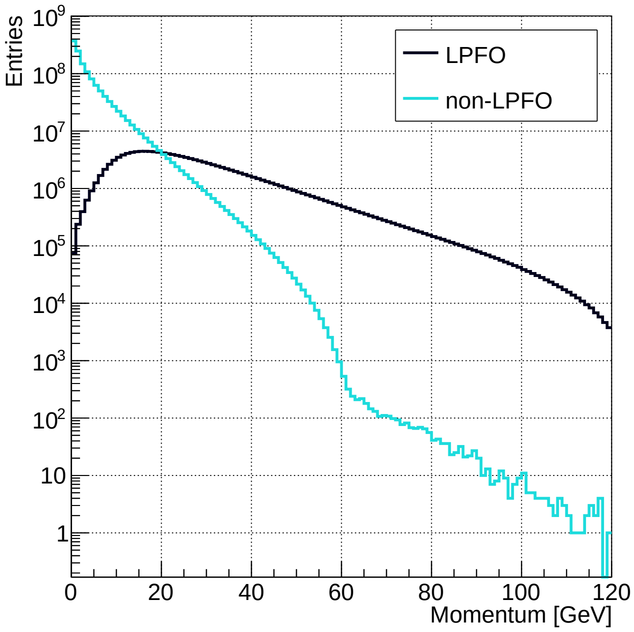

FIGURE 5.18: Momentum distributions of PFOs for the $e^+e^- \to q_L\bar{q}_L$ Black and blue line are the distribution for LPFO and non-LPFO, respectively.

around 20 GeV which is distinct from the rest of PFOs. As it will be discussed in Section 5.11, the momentum cut plays an important role for suppressing Kaon contamination by $s\bar{s}$ events to the $u\bar{u}$ and $d\bar{d}$ samples.

5.10.4 Long-Lived Hadron Rejection

The quark pair production process not only results in Pions, Kaons, or protons but also produces long-lived light hadrons, such as K_s^0 ($d\bar{s}$) and Λ (uds). In K_s^0 fragmentation, $K_s^0 \rightarrow \pi^+\pi^-$ dominates with a 69.2% branching ratio [65], while $\Lambda \rightarrow p\pi^-$ occurs with a 64.6% probability [66]. While both K_s^0 and Λ can be used as indicators of the hard process, similar to Pions, this analysis focuses on directly produced Pions as the indicator, and products from such long-lived hadrons are considered here as background. Therefore, the decision was made to suppress the effects from long-lived hadrons. Most of these hadrons create a V^0 vertex within the tracker with large offsets from both the PV and SV, due to their long mean lifetimes, which are $\tau_{K_s^0} = 89.54 \pm 0.04\,\mathrm{ps}$ ($c\tau = 26.86\,\mathrm{mm}$) [67] and $\tau_\Lambda = 263.2 \pm 2.0\,\mathrm{ps}$ ($c\tau = 78.95\,\mathrm{mm}$) [68]. Therefore, the offset was calculated to set a threshold against the V^0. The offset is defined as:

$$\text{Offset} = \sqrt{d_0^2 + z_0^2} \tag{5.14}$$

where d_0 and z_0 are the transverse and longitudinal displacements of the track origin. To separate PV-originated events from those from SV and V^0, an offset cut was chosen to be 1 mm.

5.10.5 Particle Identification

As explained in Section 5.6.5, PID is performed by choosing a distinct region in dE/dx distribution where it is dominated by the particle of interest. In this section, PID performance after the aforementioned selections are introduced. Figure 5.19 depicts the migration matrix for the PID for $K^\pm$, $\pi^\pm$ and p ($\bar{p}$) for all quark pair production process after the series of following selections: b-tag, c-tag, number of vertices, LPFO acollinearity, and offset cut. Diagonal element of this matrix corresponds to the number of correctly identified PFO. On top of Pions being the lightest of all hadrons, all the $q_L\bar{q}_L$ process involves either in direct or indirect (e.g. $K^{*\pm} \rightarrow \pi^\pm\pi^0$ with B.R. 20.7% [69]) Pion production thus its multiplicity is the highest among three particles. Table 5.6 summarizes the performance of PID assignments, again after the same selections. Each row represents the identification purity for each particle and they are normalized to 1. For Pions assignment, it reaches excellent purity and efficiency of 96.5%, after the selections of b/c-tag, number of vertex, LPFO momentum and offset. The high performance in the Pion identification purity comes from the fact that it has the largest mean dE/dx among the three, and is well separated from the other two, as we saw in Figure 5.4. Moreover, Pions are not constrained in the upper bound for its dE/dx

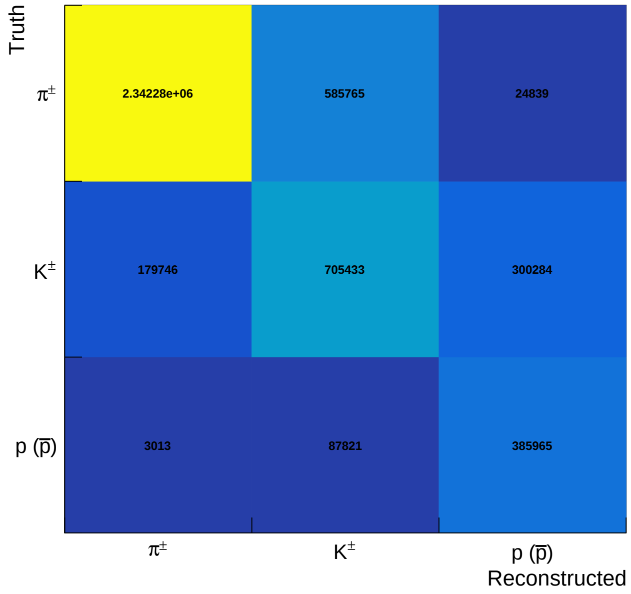

FIGURE 5.19: Migration matrix for $K^{\pm}$, $\pi^{\pm}$ and p ($\bar{p}$).

value, which leads to higher efficiency. Kaons, on the other hand, suffers from low performance, with purity being 51.0% while the efficiency is at 51.2%, since the dE/dx value of Kaons resides between those of Pions and protons, which becomes prone to the misidentification. Proton also suffers from the low purity of 50.3% and efficiency of 54.3%, due to its low separation power between Kaon, as seen in Figure 5.4. The contamination from the leptons towards any particles here is considered negligible.

	Truth PID			
Reco. PID	$\pi^{\pm}$	$K^{\pm}$	p ($\bar{p}$)	$e^{\pm}$, $\mu^{\pm}$
$\pi^{\pm}$	0.968	0.031	0.000	0.001
$K^{\pm}$	0.363	0.574	0.062	0.001
p ($\bar{p}$)	0.015	0.363	0.579	0.043
Efficiency	0.968	0.575	0.605	-

TABLE 5.6: PID fraction for different particle type after dE/dx PID process. Diagonal elements are the identification purity for each particle, and rest is the fraction of the confusion. Elements in each row is normalized to unity. The last row is the reconstruction efficiency for individual particle type. Efficiency is not calculated for the lepton entry, since other particles are not tagged.

5.10.6 Secondary PFOs

Neutral hadrons, i.e. K^{*0} turns into a pair of charge Pion and Kaon with 93% branching ratio, which becomes background to this analysis [70], since both of these hadron momenta is competitive enough to become a LPFO. In such case, it becomes a source of migration. For convenience, sub-leading PFOs with momentum greater than 10 GeV is referred to as Secondary PFO (SPFO). In order to suppress this effect, following condition is applied:

1. Search for the LPFO and SPFOs.
2. For each SPFO, check if its charge is consistent with the LPFO charge.
3. If the charge is opposite, discard the event.

This ensures that there are no SPFOs with opposite charge in the phase-space near the LPFO.

5.10.7 Selection Summary

The selection criteria mentioned in this section are summarized in Table 5.7.

#	**Name**	**Quantity**	**Description**
1	b-tag	$btag < 0.3$	Reject events with b-like jets
2	c-tag	$ctag < 0.65$	Reject events with c-like jets
3	nvtx	$nvtx = 1$	Jets should have only PV as vertex
4	Leading momentum	$p_{LPFO} > 15\,\mathrm{GeV}$	Leading momentum cut
5	LPFO acollinearity	$\cos\theta_{LPFO_{1,2}} > 0.97$	LPFOs should be back-to-back
6	Offset	$V_0 = \sqrt{d_0^2 + z_0^2} < 1\,\mathrm{mm}$	Offset cut to reject Λ_0 contribution
7a	dE/dx PID (π)	$dE/dx > 0.178 \times 10^{-6}\,\mathrm{GeV\,mm^{-1}}$	$\pi^{\pm}$ identification
7b	dE/dx PID (K)	$min(\Delta_{dE/dx-(K,\pi,p)})$ for $\Delta_{dE/dx-K}$	$K^{\pm}$ identification
8	SPFO	Veto $p_{SPFO} > 10\,\mathrm{GeV}$ and charge opposite to LPFO.	Attenuate the charge migration by rejecting oppositely charge LPFO competitor
9	Charge	$Q_{LPFO1} \times Q_{LPFO2} < 0$ opposite charge.	Charge of LPFOs from both sides has

TABLE 5.7: Summary of selection criteria for this analysis.

The retained fraction of reconstructed events after each cut for $e^-_L e^+_R$ sample is shown in Table 5.8 and Table 5.9, and for $e^-_R e^+_L$ sample in Table 5.10 and Table 5.11. There are two modes for reconstructing $q_L\bar{q}_L$: PID with Kaon and Pion. As discussed in Section 5.7, Pion mode will dominated by the $u\bar{u}$ and $d\bar{d}$ events with $s\bar{s}$ process as background, while Kaon mode will be dominated by the $s\bar{s}$ events. Therefore, the selection efficiency results for both are shown. First, selection efficiency result for Pion identification is presented in Table 5.8, with $e^-_L e^+_R$ polarization for 4.9 ab^{-1}. The efficiencies were calculated for different flavor samples, which is represented in each column. The first row shows the number of events before any cut. First three cuts are mainly for the heavy quark background rejection. One can see significant decrease in both both $c\bar{c}$ and $b\bar{b}$ events, which leads to 11.4% and 0.423%, respectively. General selection criteria for the LPFO selection is preformed in cut 4-6. Among the light quark samples, all flavors retain over 40% of the original events at this point. The drastic reduction in the efficiency is observed for the Pion PID selection (Cut 7a). For $u\bar{u}$ and $d\bar{d}$, the reduction about 1/3 of number before PID. This is due to the fact that the LPFO from the both hemisphere needs to be tagged as Pion. The double tagging requirement reduces the efficiency with the square of Pion production probability for each flavor, which is determined by the fragmentation function from the OPAL tune. Moreover, while the PID efficiency for the pion recorded over 92% of the efficiency, double tagging will reduce it down to 15%. For $s\bar{s}$ events, the production probability of Pion is low and expected to show reduction in events upon PID. SPFO selection (Cut 8) is another criteria which significantly reduces the event fraction. This reduction reflects the production of neutral hadrons, as mentioned in Section 5.10.6, and serves to improve the overall purity for selecting LPFO from the hard process.

Table 5.9 displays the selection efficiencies with Kaon PID. Cut 1-6 are identical to one in Table 5.8, thus omitted. Cut 7b shows the selection efficiencies after the Kaon PID selection. Kaon PID also displays significant reduction in efficiencies for all flavors, while retaining more events for $s\bar{s}$ as we expect. For $u\bar{u}$ and $d\bar{d}$,

5.11 Results

In Section 5.10, we have introduced the methods to select the LPFOs which represent the hard process. In this section, the result of polar angle reconstruction of those LPFOs is shown. The charge of light quark is determined by measuring the charge of selected LPFO.

Cuts	**Fraction of events after cut (Number of events)**				
	$d\bar{d}$	$u\bar{u}$	$s\bar{s}$	$c\bar{c}$	$b\bar{b}$
None	100% (2.01e7)	100% (2.94e7)	100% (1.99e7)	100% (2.94e7)	100% (2.03e7)
Cut 1	94.1%	94.1%	93.2%	69.4%	1.06%
+ Cut 2	91.8%	91.8%	90.9%	12.3%	0.494%
+ Cut 3	89.7%	89.7%	88.8%	11.4%	0.423%
+ Cut 4	51.2%	56.1%	48.4%	4.17%	0.069%
+ Cut 5	46.5%	50.8%	43.9%	3.76%	0.058%
+ Cut 6	44.9%	49.1%	41.7%	3.48%	0.050%
+ Cut 7a	13.7%	13.7%	5.92%	0.438%	0.007%
+ Cut 8	1.75%	2.04%	0.889%	0.102%	0.003%

TABLE 5.8: The list of selection efficiencies after each cut for $e^-_L e^+_R$ polarization, selecting the $e^+e^- \to u\bar{u}/d\bar{d}$ using Pions. Number after "Cut" corresponds to the number in Table 5.7. Each number represents the fraction of remaining number of events respect to the number before the selection, but after the preselection.

Cuts	**Fraction of events after cut (Number of events)**				
	$d\bar{d}$	$u\bar{u}$	$s\bar{s}$	$c\bar{c}$	$b\bar{b}$
None	100% (2.01e7)	100% (2.94e7)	100% (1.99e7)	100% (2.94e7)	100% (2.03e7)
Cut 1-6	44.9%	49.1%	41.7%	3.48%	0.050%
+ Cut 7b	1.61%	1.94%	4.91%	0.276%	0.003%
+ Cut 8	0.198%	0.296%	0.625%	0.056%	0.000%

TABLE 5.9: The list of selection efficiencies after each cut for $e^-_L e^+_R$ polarization, selecting the $e^+e^- \to s\bar{s}$ using Kaons. Fractions before the PID is identical to Table 5.8 thus they are omitted and only the relevant efficiencies are listed.

5.11.1 Corrections

5.11.1.1 Charge Flip Correction

In order to correct for the charge flip, probabilities on double charge measurements for light quark pair production process were calculated. Suppose we have a probability of correctly identifying the generated quark charge by measuring the reconstructed LPFO charge, denoted as p. Then we define the probability of getting it wrong to be $q = 1 - p$. Assuming that each LPFO charge measurements are independent and symmetric

Cuts	**Fraction of events after cut (Number of events)**				
	$d\bar{d}$	$u\bar{u}$	$s\bar{s}$	$c\bar{c}$	$b\bar{b}$
None	100% (4.43e6)	100% (1.25e7)	100% (4.39e6)	100% (1.25e7)	100% (4.47e6)
Cut 1	94%	94.1%	93.3%	69.4%	1.06%
+ Cut 2	91.8%	91.8%	90.9%	12.3%	0.497%
+ Cut 3	89.7%	89.7%	88.8%	11.4%	0.427%
+ Cut 4	51.2%	56.2%	48.4%	4.17%	0.070%
+ Cut 5	46.4%	50.9%	43.9%	3.76%	0.060%
+ Cut 6	44.8%	49.1%	41.7%	3.48%	0.051%
+ Cut 7a	13.7%	13.7%	5.95%	0.440%	0.007%
+ Cut 8	1.75%	2.05%	0.896%	0.102%	0.003%

TABLE 5.10: The list of selection efficiencies after each cut for $e^-_R e^+_L$ polarization, when identifying Pions. Number after "Cut" corresponds to the number in Table 5.7. Each number represents the fraction of remaining number of events respect to the number before the selection, but after the preselection.

Cuts	**Fraction of events after cut (Number of events)**				
	$d\bar{d}$	$u\bar{u}$	$s\bar{s}$	$c\bar{c}$	$b\bar{b}$
None	100% (4.43e6)	100% (1.25e7)	100% (4.39e6)	100% (1.25e7)	100% (4.47e6)
Cut 1-6	44.8%	49.1%	41.7%	3.48%	0.051%
+ Cut 7b	1.59%	1.93%	4.89%	0.275%	0.003%
+ Cut 8	0.192%	0.293%	0.635%	0.055%	0.001%

TABLE 5.11: The list of selection efficiencies after each cut for $e^-_R e^+_L$ polarization, when identifying Kaons. Fractions before the PID is identical to Table 5.10 thus they are omitted and only the relevant efficiencies are listed.

throughout at the entire polar angle, one can construct following simultaneous equations:

$$\left.\begin{aligned} N_{acc} &= Np^2 + Nq^2 \\ N_{rej} &= 2Npq \end{aligned}\right\} \quad p = \frac{1}{2}\left(1 + \sqrt{1 - \frac{2N_{rej}}{N}}\right) \tag{5.15}$$

where N_{acc} (N_{rej}) is the number of accepted (rejected) events and N is the total number of events. The first line in the left hand side of the equation represents two cases where the events are accepted: when reconstructing the charges of the both hemispheres correct, thus probability p^2, and getting it doubly wrong, hence probability q^2. The second line represents the rejected events, when one of the charges is mis-identified, thus $2Npq$. The right hand side of (5.15) is the result after solving the second equation for p. Since the Np^2 reflects the intrinsic number of pure signal events, one can use p-value to apply correction to the N_{acc} to extract this number. Based on (5.15), the corrected number of events N_{corr} is calculated for each bin in $\cos\theta$ distribution as following:

$$N_{corr} = \frac{N_{acc}}{p^2 - q^2} \tag{5.16}$$

5.11.1.2 Acceptance Correction

Since this is the analysis on the differential cross section measurement, it is crucial that each selection criteria yields same amount of efficiency throughout the entire polar angle. Therefore, the efficiency dependence to the polar angle was investigated. Figure 5.20 shows the selection efficiency for each cut plotted against the polar angle. The efficiencies in each histogram are:

$$\epsilon_i = \frac{N_i}{N_{i-1}} \tag{5.17}$$

where N_i and ϵ_i are the number and selection efficiency after Cut i, respectively. N_0 corresponds to the number before any selection. The collection of efficiency histograms signifies that the polar angle dependence of efficiencies for each selection is constant except at the extreme forward region, particularly in $|\cos\theta| > 0.8$. This dependence emerges primarily due to the loss in the acceptance in ILD. According to Figure 3.1, TPC extends its length up to 2.35 m on one side, with maximum radius of 1.808 m. The calorimeter barrel and endcap connects at $\theta = 37.6°$, which corresponds to $\cos\theta = 0.8$. Beyond this region,

1. dE/dx resolution degrades due to lowering number of hits in the TPC (see Section 5.6.5).
2. b and c tagging efficiency will be reduced due to the lack of acceptance of the central vertex detector and poor forward tracking.

Therefore, for the final polar angle distribution, the correction of $\prod_1^9 1/\epsilon_i$ was applied for each bin in throughout the polar angle.

5.11.1.3 Correction for dE/dx resolution

As outlined in Section 5.6.5, Pions can benefit from a background free region in upper part of dE/dx distribution, whereas for Kaons, it is contaminated from both upper and lower bounds from Pion and proton. Due to this nature, Kaons are more vulnerable

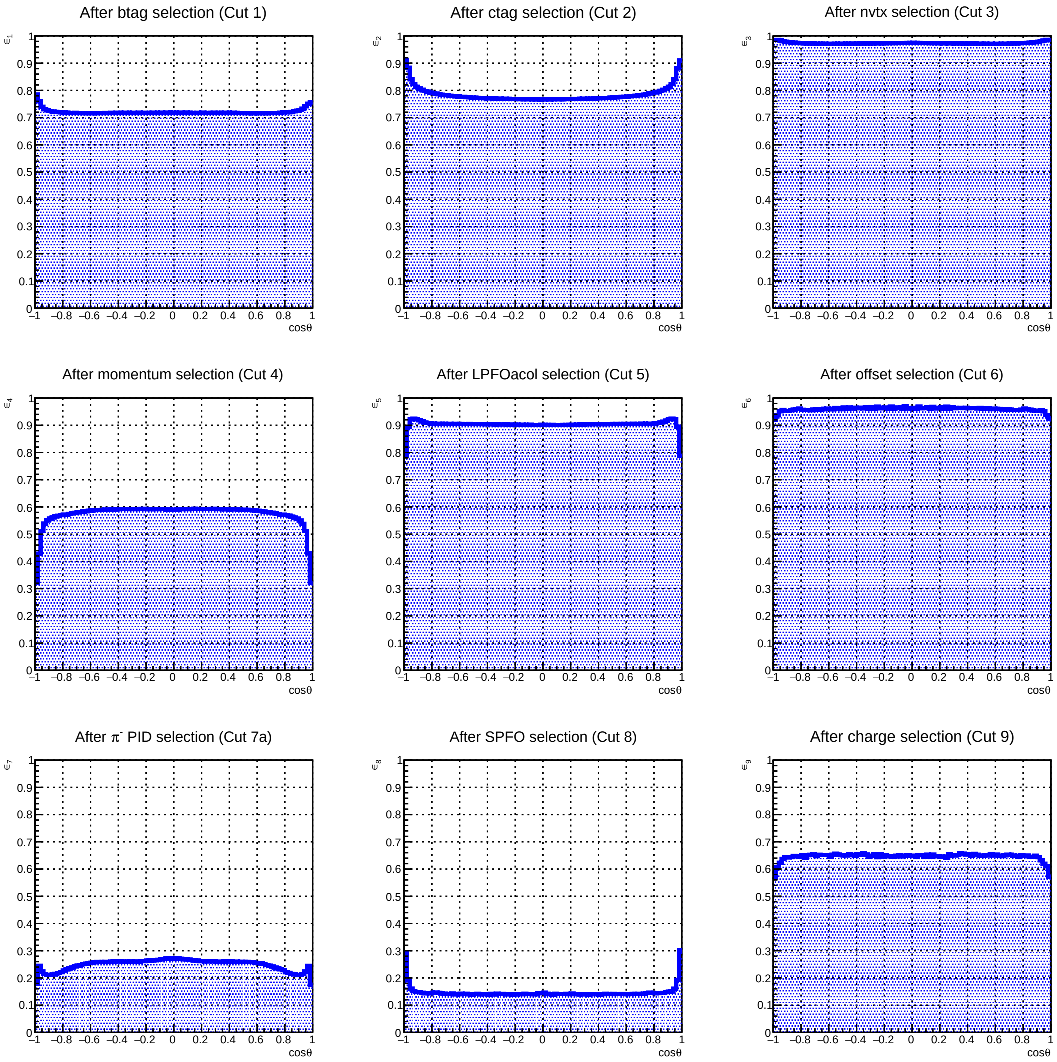
After btag selection (Cut 1)

After ctag selection (Cut 2)

After nvtx selection (Cut 3)

After momentum selection (Cut 4)

After LPFOacol selection (Cut 5)

After offset selection (Cut 6)

After π^- PID selection (Cut 7a)

After SPFO selection (Cut 8)

After charge selection (Cut 9)

FIGURE 5.20: Selection efficiency vs. polar angle following the applied cut as compared to before, using the $e^-_L e^+_R$ sample. Each efficiency was calculated using the entire sample of $e^-e^+ \to q\bar{q}$ process, including heavy quark process. Pion PID (Cut 7a) was performed to produced this efficiency analysis. The result using the Kaon PID (Cut 7b) is shown in Figure 5.21.

to the Pion contamination. This effect is pronounced in the extreme forward region ($|\cos\theta| > 0.8$) where the number of TPC hits is reduced, resulting in a degradation of the dE/dx resolution. In order take this into account, stability and purity for Kaon reconstruction and generation are calculated. Stability and purity are defined as follows:

$$\begin{aligned} \text{Stability} &= \frac{N_{rec} \cap N_{gen}}{N_{gen}} \\ \text{Purity} &= \frac{N_{rec} \cap N_{gen}}{N_{rec}} \end{aligned} \tag{5.18}$$

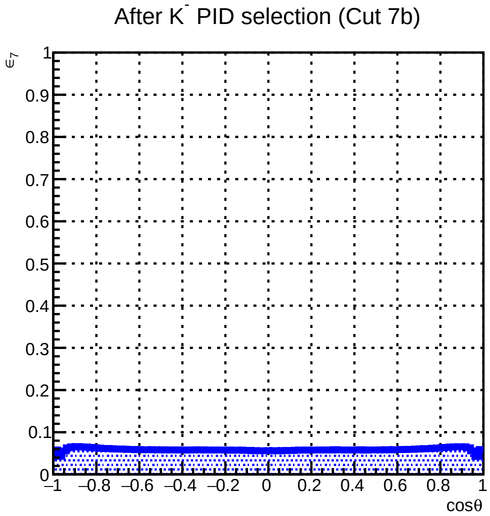

FIGURE 5.21: Selection efficiency vs. polar angle following the applied cut as compared to before, using the $e_L^- e_R^+$ sample, with Kaon PID (Cut 7b). Each efficiency was calculated using the entire sample of $e^- e^+ \to q\bar{q}$ process, including heavy quark process.

where N_{rec} and N_{gen} are number of reconstructed and generated Kaons, respectively. The $N_{rec} \cap N_{gen}$ represents the number of Kaons being reconstructed and generated in the same direction. The number of reconstructed and generated Kaons vs polar angle is shown in Figure 5.22. The black line shows the N_{gen} while the blue line represents

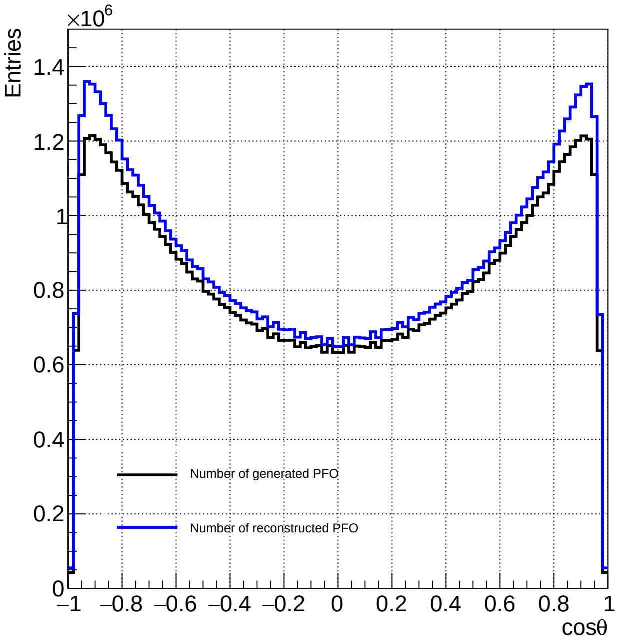

FIGURE 5.22: Distribution for number of Kaons generated and reconstructed throughout the polar angle from the combined samples of $e_L^- e_R^+$ and $e_R^- e_L^+$.

the N_{reco} in a given polar angle bin. Given that there is low abundance of protons, the discrepancy in two lines shows that there are Pion contamination upon Kaon ID, which is pronounced in extreme forward region, as expected. Thus the correction was applied with stability divided by the purity.

5.11.2 Polar Angle Distribution

In this section, the results from the differential cross section measurements for $e^+e^- \to s\bar{s}$ sample, and the combined sample of $u\bar{u}$ and $d\bar{d}$ are presented. As described in Section 5.7, the $s\bar{s}$ process is background to $u\bar{u}$ and $d\bar{d}$ measurement. Conversely, $u\bar{u}$ and $d\bar{d}$ process are the background for the $s\bar{s}$ process. There are two methods to PID the LPFO: using K^- as signature particle (Kaon mode) and using π^- as signature (Pion mode).

5.11.2.1 Pion mode

Firstly, polar angle distributions for $u\bar{u}$ and $d\bar{d}$ generated samples using the integrated luminosity of $\mathcal{L}_{int} = 4.2$ ab^{-1} were analyzed. $u\bar{u}$ and $d\bar{d}$ predominantly hadronize into Pions, with the reported fraction of 38.6% by the OPAL experiment [19], thus Pion mode was used to analyze these samples. Figure 5.23 shows the distribution for reconstructed π^- (blue), and combined generated polar angle distribution from generated (green). The error bars on the reconstructed points are the statistical uncertainties. For the barrel region ($|\cos\theta| < 0.8$) excellent agreement between the reconstruction and the parton level distributions is obtained for both polarization modes. The slight discrepancy in the backward region of Figure 5.23a arises from the over-correction introduced by the efficiency correction. Nonetheless, the discrepancy is as small as 4.5% of the parton level at $\cos\theta = -0.8$. The total number of entries in the right-handed sample is half as much as the entries in the left-handed sample, which is expected from the difference in their cross-sections.

The same distribution is then plotted along with the background processes, i.e. $s\bar{s}$, heavy quark and di-boson processes, to identify the polar angle region where it is contaminated by the background sources (Figure 5.24). All processes are normalized to their integrated luminosity. For the left-handed sample in Figure 5.24a, we observed that the contributions from ZZ, $q\bar{q}H$ backgrounds and heavy quark events are negligible. Residual WW contribution is observed at large $\cos\theta$. Overall contribution in the barrel region is still less than 4% compared to the combined sample of $u\bar{u}$ and $d\bar{d}$. For light flavor quarks, we observed a clean separation in peaks between up and down type quark events. Note that since we select Pions, the original quark corresponds to d and

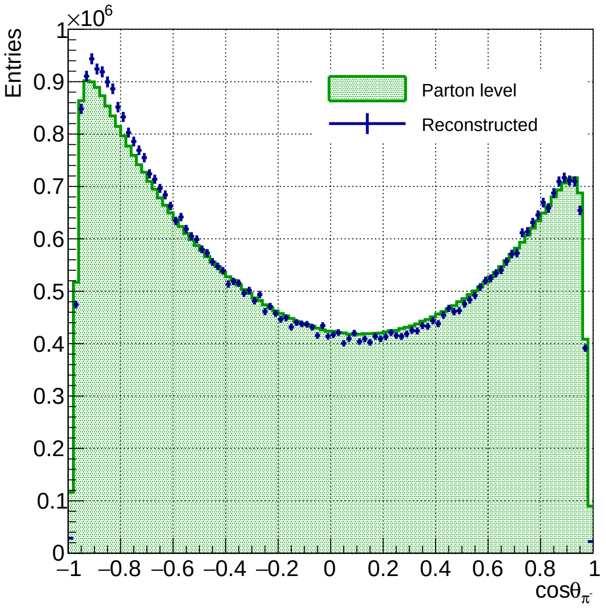

(a)

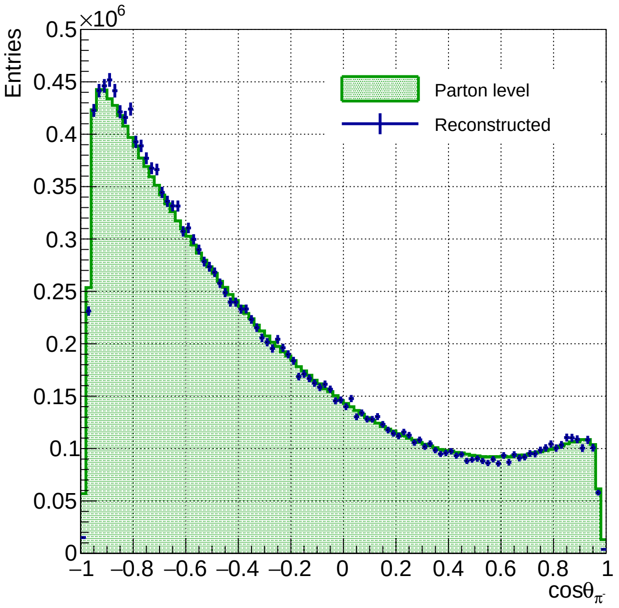

(b)

FIGURE 5.23: Polar angle distributions for reconstructed π^- (blue), and combined polar angle distribution from generated $\bar{u}$ and d-quark (green) with: (a) $e^-_L e^+_R$ and (b) $e^-_R e^+_L$ polarization samples. Pion mode was used for the PID for the LPFOs. Due to the difference in the reconstruction efficiencies between $u\bar{u}$ and $d\bar{d}$, both distributions are scaled to the respective reconstruction efficiency.

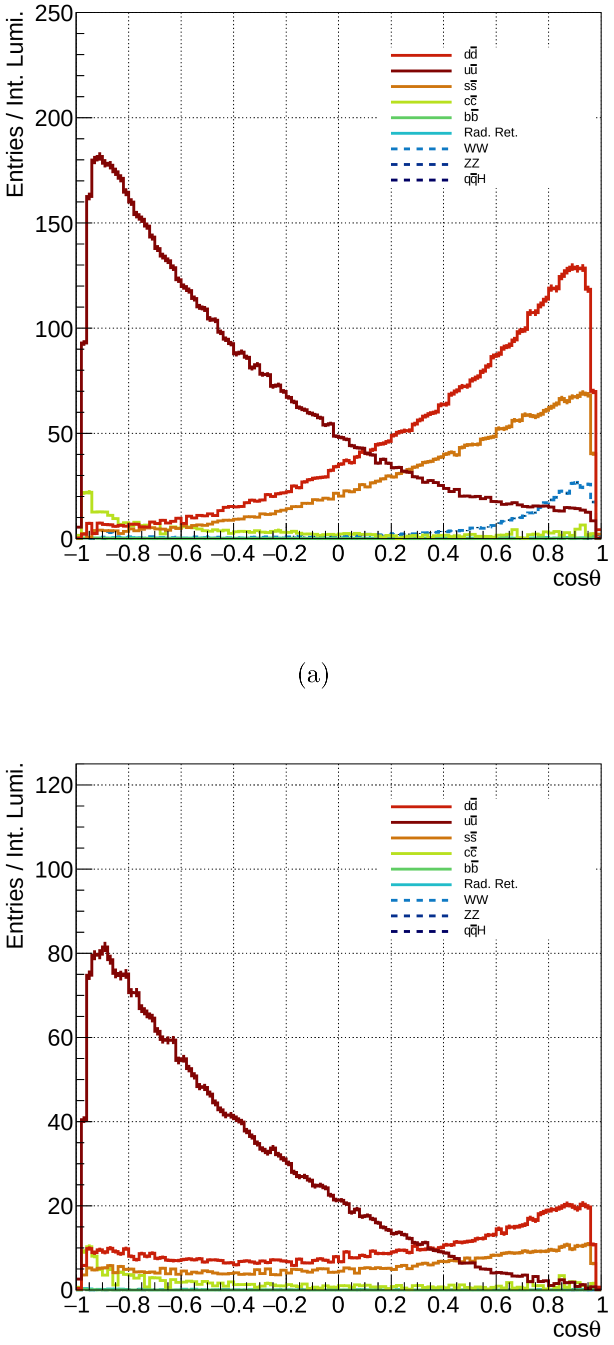

(a)

(b)

FIGURE 5.24: Polar angle distributions of background processes ($s\bar{s}$ and diboson process) are overlaid on top of signal process ($u\bar{u}$, $d\bar{d}$) for (a) $e^-_L e^+_R$ and (b) $e^-_R e^+_L$ polarization samples. Pion mode was used for the PID for the LPFOs.

$\bar{u}$. Hence, $u\bar{u}$ events peak in the backward region, clearly being separated by the rest of flavors. The signal to noise ratio in the backward region ($\cos\theta < 0$) is over 84.3%.

The $d\bar{d}$ events peak in the forward region. Here, the $s\bar{s}$ process is a visible background. This is partially due to the fact that $s\bar{s}$ process can hadronize into $\pi^{\pm}$ through the decay of K^{*0} and Λ^0. Table 5.12 lists the number of events recorded for which s-quark hadronize into $K^{\pm}$ and Λ^0 in a SLAC experiment. Another reason is simply that with a certain probability a Pion produced in the hadronization process has more momentum than than the Kaon that is issue of the original strange quark. We attempt to improves the signal over background ratio by an increase of the momentum cut on the LPFO. The results are shown in Figure 5.25. While this selection will greatly attenuate the $s\bar{s}$ contamination, it will drastically reduce the selection efficiency, which is already low from both PID and SPFO selection as seen in table 5.8 and 5.10.

Mode	Data Events	MC prediction
K^+K^-	1290	1312.2
$K^+\Lambda^0, K^-\bar{\Lambda}^0$	219	213.5
$\Lambda^0\bar{\Lambda}^0$	17	13.7
$K^{\pm}K_s^0$	1580	1617.3
$\Lambda^0 K_s^0, \bar{\Lambda}^0 K_s^0$	193	194.1
Total	3299	3350.8

TABLE 5.12: Summary of the selected event sample for 5 tagging modes in data and simulation at SLAC experiment [14].

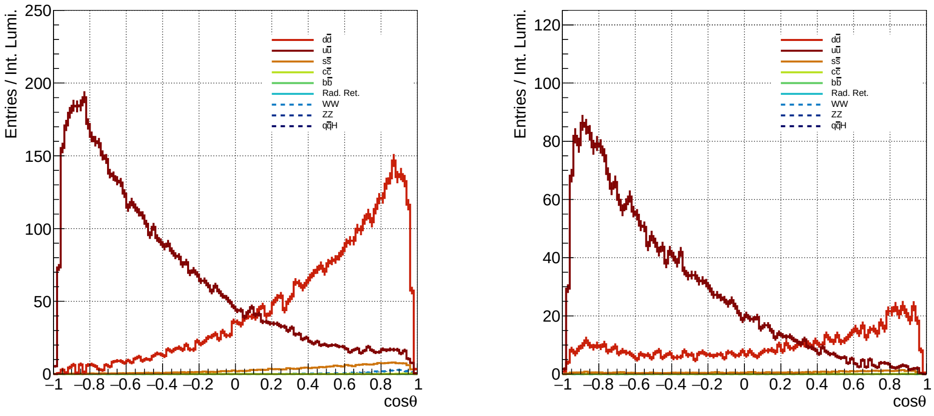

(a)

(b)

FIGURE 5.25: Polar angle distributions of background processes ($s\bar{s}$ and di-boson process) are overlaid on top of signal process ($u\bar{u}$, $d\bar{d}$) for (a) $e_L^- e_R^+$ and (b) $e_R^- e_L^+$ polarization samples, with LPFO momentum selection above 40 GeV.

Polar angle distribution from background processes are then subtracted from the total distribution, depicted in Figure 5.26. Uncertainty on each data point now includes systematic and statistical error. The mean uncertainty for both polarizations are measured to be as small as 1.46%, comparable to the statistical uncertainty of 1.27%. Based on the obtained distributions, the differential cross section was fitted with the following function:

$$\frac{d\sigma}{d\cos\theta} = S(1+\cos^2\theta) + A\cos\theta \tag{5.19}$$

The S and A are the fit parameters, which corresponds to the terms associated with $\cos^2\theta$ and $\cos\theta$ in (1.47). Given that the γ factor is large for the quarks in the pair production, $\sin^2\theta$ term was omitted for the simplicity. The fit curve for the parton level is represented by the green dotted line, while the reconstruction is plotted with red solid line. The fit region is restricted to be $|\cos\theta| < 0.8$ in order to capture the barrel region. From the two curves, fitted result from the parton level and reconstructed distributions have excellent agreement for both polarizations. This is quantitatively confirmed by the fit results, which are summarized in Table 5.13. For the left-handed samples, reconstruction fit result shows that both S and A values can be measured up to 0.205% and 2.11%, respectively, for the right-handed case, they can be measured up to 0.301% and 0.680%. The precision achieved from the fits, coupled with the remarkable agreement with the parton level, and provided that the present discrepancy in A can be resolved in the future, it enables MC subtraction from the Kaon mode result, as detailed in Section 5.11.2.2, under the assumption that the polar angle spectrum from $u\bar{u}$ and $d\bar{d}$ will be consistent with the Standard Model.

		S	$\sigma_\mathbf{S}$	**A**	$\sigma_\mathbf{A}$
$\mathbf{e^-_L e^+_R}$	**Gen**	85.7	0.026	-20.2	0.073
	Reco	85.4	0.175	-23.4	0.495
$\mathbf{e^-_R e^+_L}$	**Gen**	29.2	0.015	-35.5	0.040
	Reco	29.2	0.088	-36.2	0.246

TABLE 5.13: Fit result for the polar angle region $|\cos\theta| < 0.8$, with S and A parameters described in (5.19).

For the systematic uncertainties, one takes the ±5% error on the residual background event contribution. Therefore, the levels of backgrounds were varied by 5%, and fits were repeated to obtain systematic uncertainties of S and A. The result is shown in Table 5.14.

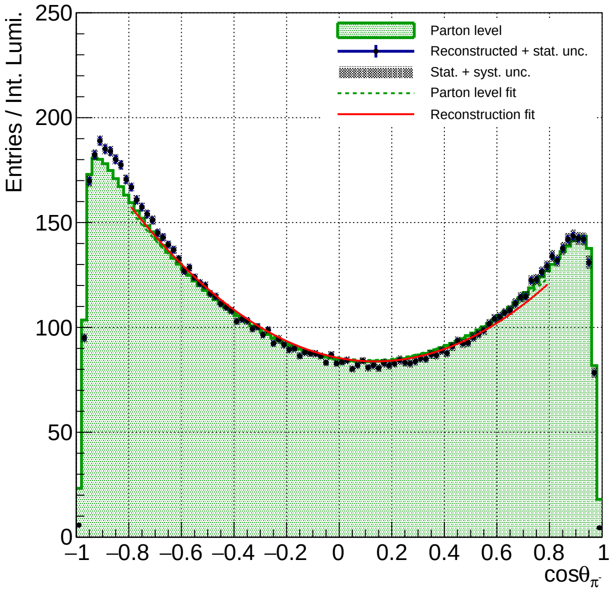

(a)

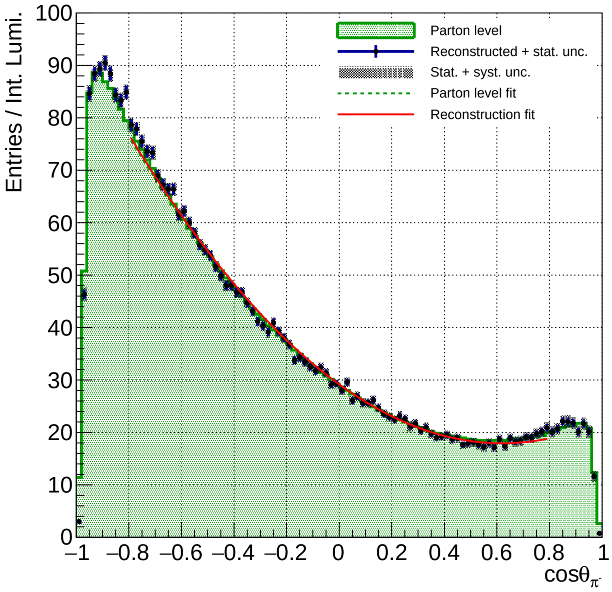

(b)

FIGURE 5.26: Polar angle distributions of background processes ($s\bar{s}$ and diboson process) are subtracted from the signal process ($u\bar{u}$, $d\bar{d}$) in (a) $e^-_L e^+_R$ and (b) $e^-_R e^+_L$ polarization samples. Green dotted line represents the fit curve for the parton level distribution, while the red line shows the fit curve for the reconstruction.

	$\sigma_{\mathbf{S}_{\mathbf{sys.}}}$	$\sigma_{\mathbf{A}_{\mathbf{sys.}}}$
$\mathbf{e^-_L e^+_R}$	0.110	0.306
$\mathbf{e^-_R e^+_L}$	0.050	0.144

TABLE 5.14: Systematic uncertainties derived from statistical and background uncertainties.

5.11.2.2 Kaon mode

Secondly, the polar angle distribution of the $s\bar{s}$ generated samples is analyzed. Strange quarks predominantly hadronize into charged Kaons with the fraction of 23.9% according to the OPAL fragmentation results [19]. Therefore charged Kaons are used to measure the $e^+e^- \to s\bar{s}$ cross section. Figure 5.27 shows the distributions for reconstructed K^- (blue) and generated s-quark angle (green), for an integrated luminosity of $\mathcal{L}_{int} = 4.2$ ab^{-1}. Each distribution is normalized to 1, and the error bars are the statistical uncertainties. For left-handed polar angle in Figure 5.27a, excellent agreement between the reconstruction and parton level is observed. The reason for the efficiency drop efficiency at $\cos\theta > 0.8$ region is the acceptance drop in the TPC. Nonetheless, the distribution shows the capability of Kaon to be used as an imprint of the hard process. For right-handed polar angle in Figure 5.27b, one sees the statistical uncertainty increases due to both lower cross section and Kaon selection efficiency. Nevertheless reconstructed distribution agrees with the parton level distribution within statistical errors.

The reconstructed polar angle distribution for the signal process $s\bar{s}$ is then overlayed along with the $u\bar{u}$, $d\bar{d}$ and di-boson production processes. Figure 5.28a and Figure 5.28b depict the those polar angle plots for left-handed and right-handed polarization, respectively. The distributions are scaled with the individual integrated luminosity. From the left-handed plot, small contribution from the WW process is seen at the forward region, similarly to the Pion result. An additional background to be taken into account here is $e^+e^- \to c\bar{c}$. This is due to the fact that $c\bar{c}$ process undergoes the hadronization of $c \to D^+$, which also creates K^- with a branching ratio of 25.7% [71]. Both contributions together add 8.6% to the signal process. For the right-handed distribution, WW contribution disappears, which further purifies the sample. Both $u\bar{u}$ and $d\bar{d}$ polar angle distributions with Kaon mode retain the same shape observed in Pion mode, which facilitates the background subtraction from the total cross section using the parameters presented in Table 5.13, given that they both follow the Standard Model fit with excellent precision.

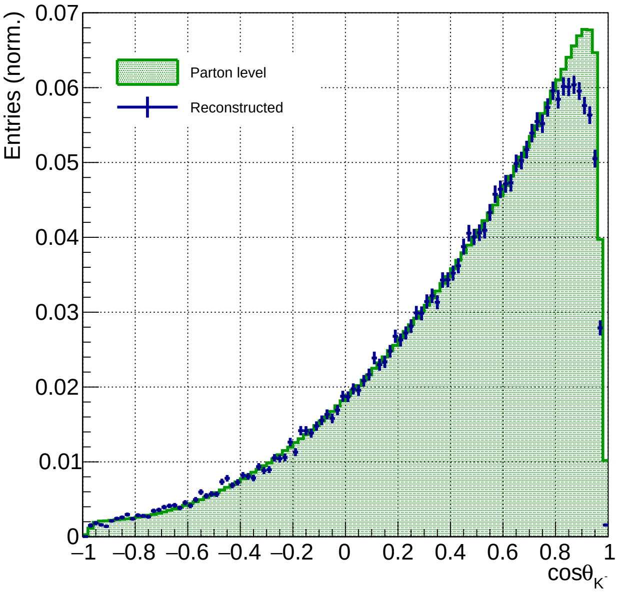

(a)

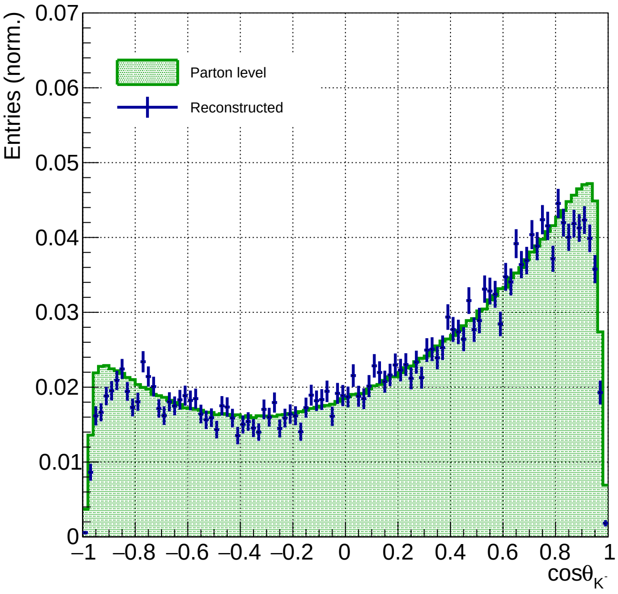

(b)

FIGURE 5.27: Polar angle distributions for reconstructed K^- (blue), and combined polar angle distribution from generated $\bar{u}$ and d-quark (green) with: (a) $e^-_L e^+_R$ and (b) $e^-_R e^+_L$ polarization samples. Pion mode was used for the PID for the LPFOs. Due to the difference in the reconstruction efficiencies between $u\bar{u}$ and $d\bar{d}$, both distributions are scaled to the respective reconstruction efficiency.

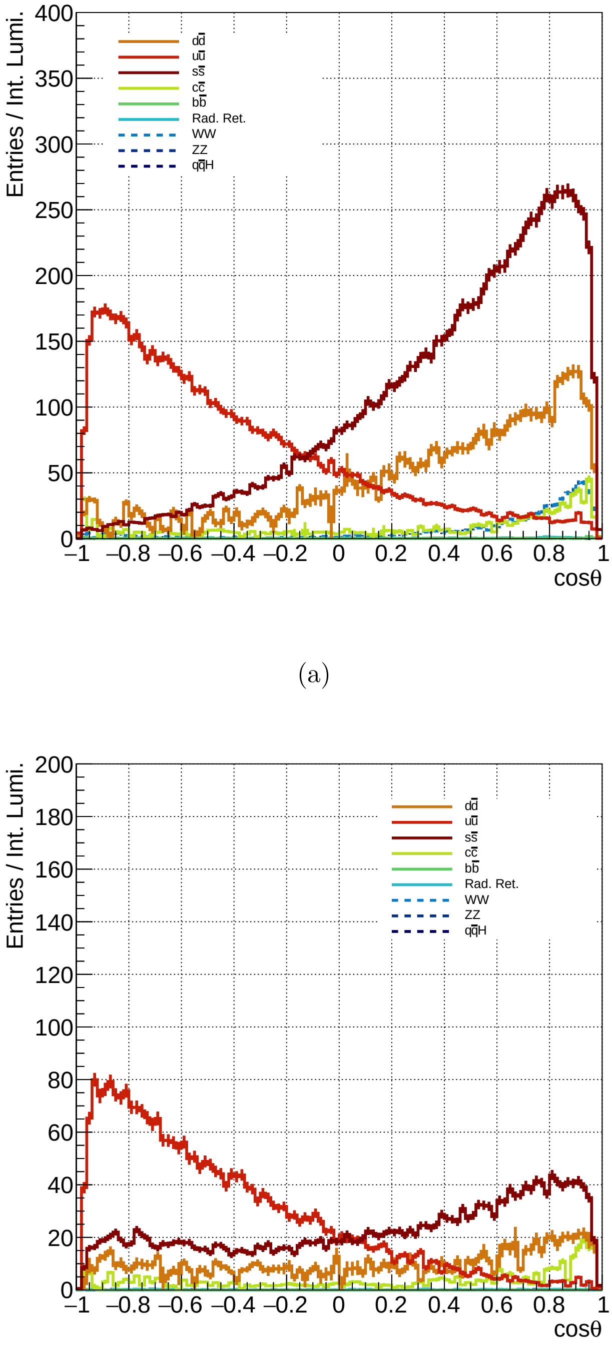

(a)

(b)

FIGURE 5.28: Polar angle distributions of background processes ($u\bar{u}$, $d\bar{d}$ and di-boson process) are overlaid on top of signal process ($s\bar{s}$) for (a) $e_L^- e_R^+$ and (b) $e_R^- e_L^+$ polarization samples. Kaon mode was used for the PID for the LPFOs.

Finally, result for the background subtraction from the total processes is performed, which is illustrated in Figure 5.29. Similarly to Figure 5.27, green distribution is the parton level, and blue points are the reconstructed K^-. The uncertainties on the reconstructed distribution include the systematic errors. Both distributions are fitted with (5.19) shown in red and green lines. The parameters obtained from the fit is presented with combined statistical and systematic uncertainties in 5.15. A discrepancy in A parameter is most likely due to the imperfect efficiency correction. On the other hand, both left and right-handed polarization results have excellent agreement between the parton level and reconstructed S parameter within their errors. Similarly to the Pion mode case, systematic uncertainties are evaluated by varying the background contribution, with repeating S and A fits. The result is shown in Table 5.16.

		S	$\sigma_{\mathbf{S}}$	**A**	$\sigma_{\mathbf{A}}$
$\mathbf{e^-_L e^+_R}$	**Gen**	1.86e-2	1.54e-5	3.51e-2	4.35e-5
	Reco	1.85e-2	1.06e-4	3.48e-2	2.89e-4
$\mathbf{e^-_R e^+_L}$	**Gen**	1.86e-2	4.00e-5	1.35e-2	1.10e-4
	Reco	1.86e-2	2.20e-4	1.37e-2	6.16e-4

TABLE 5.15: Result of fits to the polar angle distribution in $s\bar{s}$ sample for both polarization is summarized in this table. Fit region was taken for $|\cos\theta| < 0.8$ in order disregard the acceptance effect.

	$\sigma_{\mathbf{S_{sys.}}}$	$\sigma_{\mathbf{A_{sys.}}}$
$\mathbf{e^-_L e^+_R}$	5.08e-5	8.68e-5
$\mathbf{e^-_R e^+_L}$	1.24e-4	2.08e-4

TABLE 5.16: Systematic uncertainties derived from statistical and background uncertainties.

5.11.3 Observables and Uncertainties

As detailed in Section 5.7, cross section and forward-backward asymmetry for $s\bar{s}$ process are calculated, along with their statistical uncertainties.

5.11.3.1 Cross Section Result

The definition of cross section was described in (5.1). Through the error propagation, one can obtain statistical uncertainty (σ_{stat}) for the measured cross section σ as:

$$\frac{\sigma_{stat}}{\sigma} = \sqrt{\left(\frac{\delta N}{N}\right)^2 + \left(\frac{\delta \mathcal{L}_{int}}{\mathcal{L}_{int}}\right)^2} \tag{5.20}$$

where N is the number of reconstructed events, δN is the statistical uncertainty for the event count, with $\delta N/N = 1/\sqrt{N}$. $\mathcal{L}_{int}$ and $\delta\mathcal{L}_{int}$ the integrated luminosity and its uncertainty, respectively. At the ILC, the uncertainty for the measured luminosity can be achieved up to 0.1% at 250 GeV [72]. As a result, cross section for $s\bar{s}$ events was measured with statistical uncertainty of 0.340% for $e^-_L e^+_R$ and 0.694% for $e^-_R e^+_L$ polarization.

5.11.3.2 Forward-Backward Asymmetry Result

From the fit function described in (5.19), A_{FB} can be extracted using the fit parameters as:

$$A_{FB} = \frac{3A}{8S} \tag{5.21}$$

A_{FB} values are calculated along with its systematic and statistical uncertainties, using the fits obtained from u/d polar angle (Table 5.14), and s polar angle (Table 5.16). Firstly, the results from the $u\bar{u}$ and $d\bar{d}$ polar angle distributions are summarized in Table 5.17. The systematic uncertainty for both left and right-handed polarization are significantly large due to the contribution from the background, mainly from the $s\bar{s}$ process. Overall generated and reconstructed A_{FB} values agree within the calculated uncertainties.

Polarization	A^{gen}_{FB}	A^{reco}_{FB}	δA^{stat}_{FB}	δA^{sys}_{FB}	$\delta A_{FB}/A^{reco}_{FB}$ [%]
$e^-_L e^+_R$	-8.75e-2	-9.94e-2	1.18e-4	9.48e-3	$0.12 \oplus 9.52$
$e^-_R e^+_L$	-4.56e-1	-4.64e-1	1.76e-4	1.45e-2	$0.03 \oplus 3.12$

Table 5.17: Summary of calculated A_{FB} values extracted from combined events of $u\bar{u}$ and $d\bar{d}$, along with statistical and systematic uncertainty δA_{FB}. Right most column shows the precision respect to each uncertainty.

Secondly, A_{FB} and its uncertainties for $s\bar{s}$ process is summarized in Table 5.18. Due to

Polarization	A_{FB}^{gen}	A_{FB}^{reco}	δA_{FB}^{stat}	δA_{FB}^{sys}	$\delta A_{FB}/A_{FB}^{reco}$ [%]
$e_L^- e_R^+$	0.709	0.702	1.00e-4	1.67e-3	$0.01 \oplus 0.23$
$e_R^- e_L^+$	0.272	0.275	2.85e-4	4.10e-3	$0.10 \oplus 1.49$

TABLE 5.18: Summary of calculated A_{FB} values for generated and reconstructed $s\bar{s}$ events, along with statistical and systematic uncertainty δA_{FB}. Right most column shows the precision for the A_{FB} reconstruction.

low contamination from the background $u\bar{u}$ and $d\bar{d}$ events, both statistical and systematic uncertainties reach down to few permille level.

5.12 Conclusion and Outlook

This analysis performed first measurement of cross section and A_{FB} of the Z^0/γ to the light quark pair at ILC with center of mass energy $\sqrt{s} = 250\,\text{GeV}$, using the full detector simulation of the ILD. To measure the differential cross section of light quark pair production process, LPFOs were used as an imprint of the hard process. In order to distinguish light quark events, Pion and Kaon identifications were performed for LPFOs. For the PID, we used dE/dx information from the TPC. We used conservative cut on dE/dx value for Pion identification, in order to maximize the final purity. For Kaon identification, dE/dx distance was defined to counter contamination from Pions and protons. Pions were used for $u\bar{u}$ and $d\bar{d}$ identification, while Kaons were used for $s\bar{s}$ identification. The final cross section measurement result for $s\bar{s}$ events has shown the precision of 0.340% for left-handed and 0.694% for right-handed polarization. For $u\bar{u}$ and $d\bar{d}$ events, A_{FB} measurement result showed agreement with generated and reconstructed values within its precision for both polarizations, while they still suffer from the systematic uncertainties. For $s\bar{s}$ events, A_{FB} measurement not only presented its agreement between generation and reconstruction, but also has shown it can achieve its precision down to few permille level. The analysis mainly suffered from significant loss of efficiency upon PID, as dE/dx identification method reduced the efficiency by 70% for Pions and by 88% for Kaons. While this analysis was carried out using the conventional dE/dx measurement technique, recent R&D [3] has revealed that migrating to the Cluster Counting method will further improve the separation with dE/dx resolution up to 3.5%.

The overall analysis was conducted using the cut based approach, in order to reveal the observables relevant to the final polar angle measurements. With the event reconstruction method we have established in this study, one can optimize the the event selection criteria using the machine learning and multivariate techniques.

A fraction of systematic uncertainty is given by the fragmentation, which has been tuned to the OPAL experiment for this analysis. This uncertainty can be minimized by measuring the fragmentation function at the Z-pole with large statistics at ILC.

The precision measurement of A_{FB} translates into the precision of the coupling between Z/γ and fermion pair. Previous studies [20] on coupling measurements for heavy quark pairs ($b\bar{b}$, $c\bar{c}$) revealed that A_{FB} can be measured with statistical and systematic uncertainties of ∼0.2% at the ILC with $\sqrt{s}$ =250 GeV and an integrated luminosity of 2000 fb^{-1}. This, in turn, implies sensitivity to new Z' boson masses, indicating that the ILC can reach sensitivities up to mass scales of 10 TeV, which are beyond what is achievable by LHC experiments (around 9 TeV) [73]. Given the A_{FB} results presented in Section 5.11.3.2, we anticipate reaching a similar level of sensitivity with the light quark pair production process.

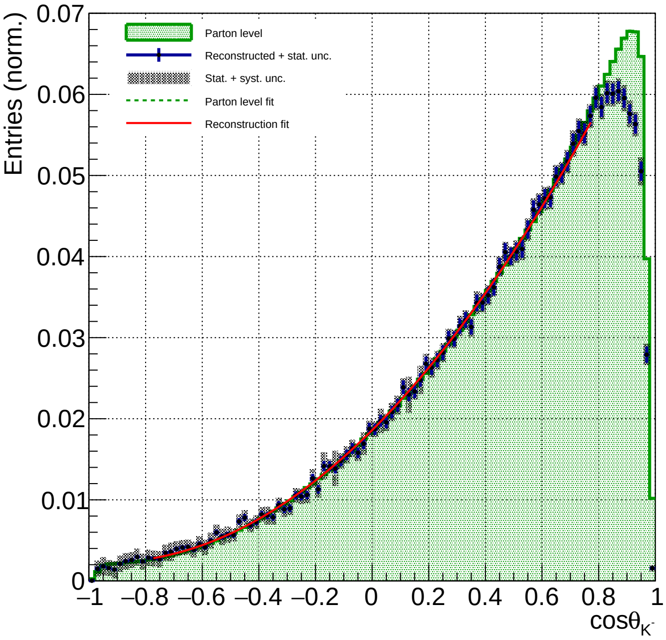

(a)

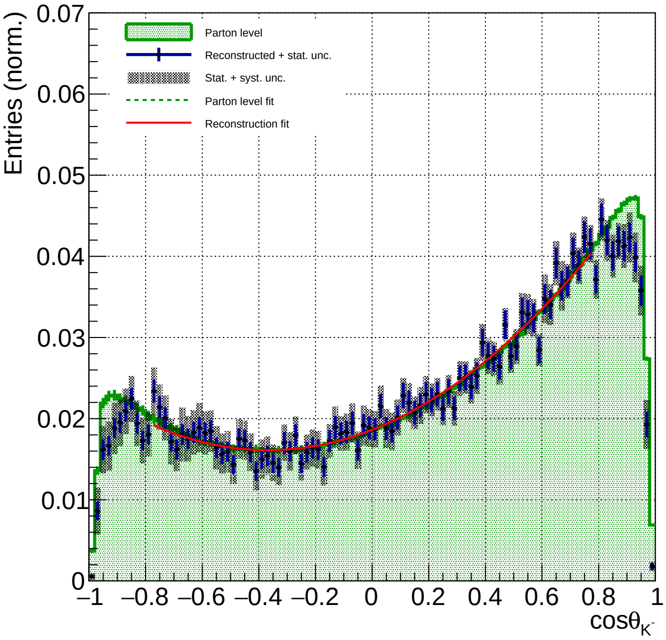

(b)

FIGURE 5.29: Polar angle distributions of background processes ($u\bar{u}$, $d\bar{d}$ and di-boson process) are subtracted from the signal process ($s\bar{s}$) in (a) $e_L^- e_R^+$ and (b) $e_R^- e_L^+$ polarization samples. Green dotted line represents the fit curve for the parton level distribution, while the red line shows the fit curve for the reconstruction.

Appendix A

SKIROC Mapping

Mapping of SKIROC channel numbers are provided for FEV in Figure A.1a and for COB in Figure A.1b. Each ASIC has 64 channels numbered from 0-63. Colored tiles in figures represent ASICs. For both figures, the SL Board is inserted to the right side of the PCB. Differences in channel positions exist between FEV and COB models, primarily arising from variations in circuit wiring.

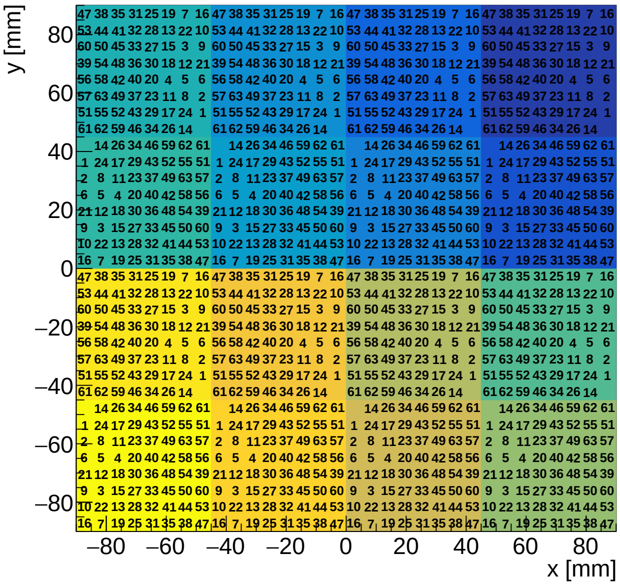

47	38	35	31	25	19	7	16	47	38	35	31	25	19	7	16	47	38	35	31	25	19	7	16	47	38	35	31	25	19	7	16
53	44	41	32	28	13	22	10	53	44	41	32	28	13	22	10	53	44	41	32	28	13	22	10	53	44	41	32	28	13	22	10
60	50	45	33	27	15	3	9	60	50	45	33	27	15	3	9	60	50	45	33	27	15	3	9	60	50	45	33	27	15	3	9
39	54	48	36	30	18	12	21	39	54	48	36	30	18	12	21	39	54	48	36	30	18	12	21	39	54	48	36	30	18	12	21
56	58	42	40	20	4	5	6	56	58	42	40	20	4	5	6	56	58	42	40	20	4	5	6	56	58	42	40	20	4	5	6
57	63	49	37	23	11	8	2	57	63	49	37	23	11	8	2	57	63	49	37	23	11	8	2	57	63	49	37	23	11	8	2
51	55	52	43	29	17	24	1	51	55	52	43	29	17	24	1	51	55	52	43	29	17	24	1	51	55	52	43	29	17	24	1
61	62	59	46	34	26	14		61	62	59	46	34	26	14		61	62	59	46	34	26	14		61	62	59	46	34	26	14	
	14	26	34	46	59	62	61		14	26	34	46	59	62	61		14	26	34	46	59	62	61		14	26	34	46	59	62	61
1	24	17	29	43	52	55	51	1	24	17	29	43	52	55	51	1	24	17	29	43	52	55	51	1	24	17	29	43	52	55	51
2	8	11	23	37	49	63	57	2	8	11	23	37	49	63	57	2	8	11	23	37	49	63	57	2	8	11	23	37	49	63	57
6	5	4	20	40	42	58	56	6	5	4	20	40	42	58	56	6	5	4	20	40	42	58	56	6	5	4	20	40	42	58	56
21	12	18	30	36	48	54	39	21	12	18	30	36	48	54	39	21	12	18	30	36	48	54	39	21	12	18	30	36	48	54	39
9	3	15	27	33	45	50	60	9	3	15	27	33	45	50	60	9	3	15	27	33	45	50	60	9	3	15	27	33	45	50	60
10	22	13	28	32	41	44	53	10	22	13	28	32	41	44	53	10	22	13	28	32	41	44	53	10	22	13	28	32	41	44	53
16	7	19	25	31	35	38	47	16	7	19	25	31	35	38	47	16	7	19	25	31	35	38	47	16	7	19	25	31	35	38	47
47	38	35	31	25	19	7	16	47	38	35	31	25	19	7	16	47	38	35	31	25	19	7	16	47	38	35	31	25	19	7	16
53	44	41	32	28	13	22	10	53	44	41	32	28	13	22	10	53	44	41	32	28	13	22	10	53	44	41	32	28	13	22	10
60	50	45	33	27	15	3	9	60	50	45	33	27	15	3	9	60	50	45	33	27	15	3	9	60	50	45	33	27	15	3	9
39	54	48	36	30	18	12	21	39	54	48	36	30	18	12	21	39	54	48	36	30	18	12	21	39	54	48	36	30	18	12	21
56	58	42	40	20	4	5	6	56	58	42	40	20	4	5	6	56	58	42	40	20	4	5	6	56	58	42	40	20	4	5	6
57	63	49	37	23	11	8	2	57	63	49	37	23	11	8	2	57	63	49	37	23	11	8	2	57	63	49	37	23	11	8	2
51	55	52	43	29	17	24	1	51	55	52	43	29	17	24	1	51	55	52	43	29	17	24	1	51	55	52	43	29	17	24	1
61	62	59	46	34	26	14		61	62	59	46	34	26	14		61	62	59	46	34	26	14		61	62	59	46	34	26	14	
	14	26	34	46	59	62	61		14	26	34	46	59	62	61		14	26	34	46	59	62	61		14	26	34	46	59	62	61
1	24	17	29	43	52	55	51	1	24	17	29	43	52	55	51	1	24	17	29	43	52	55	51	1	24	17	29	43	52	55	51
2	8	11	23	37	49	63	57	2	8	11	23	37	49	63	57	2	8	11	23	37	49	63	57	2	8	11	23	37	49	63	57
6	5	4	20	40	42	58	56	6	5	4	20	40	42	58	56	6	5	4	20	40	42	58	56	6	5	4	20	40	42	58	56
21	12	18	30	36	48	54	39	21	12	18	30	36	48	54	39	21	12	18	30	36	48	54	39	21	12	18	30	36	48	54	39
9	3	15	27	33	45	50	60	9	3	15	27	33	45	50	60	9	3	15	27	33	45	50	60	9	3	15	27	33	45	50	60
10	22	13	28	32	41	44	53	10	22	13	28	32	41	44	53	10	22	13	28	32	41	44	53	10	22	13	28	32	41	44	53
16	7	19	25	31	35	38	47	16	7	19	25	31	35	38	47	16	7	19	25	31	35	38	47	16	7	19	25	31	35	38	47

(a) Channel map for FEV 10-12

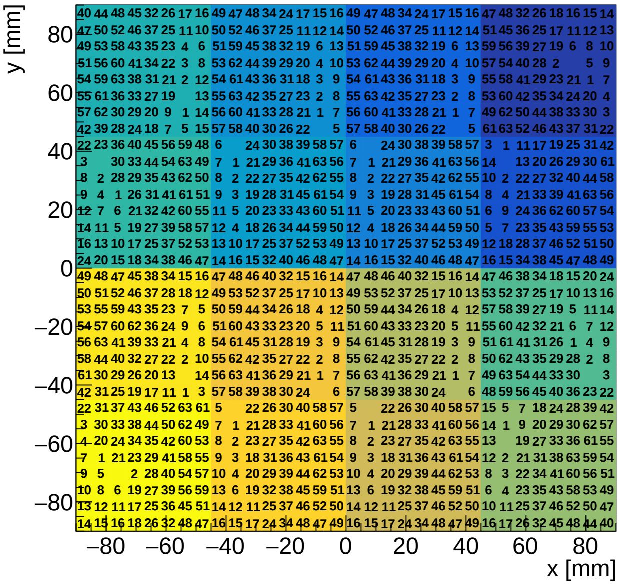

40	44	48	45	32	26	17	16	49	47	48	34	24	17	15	16	49	47	48	34	24	17	15	16	47	48	32	26	18	16	15	14
47	50	52	46	37	25	11	10	50	52	46	37	25	11	12	14	50	52	46	37	25	11	12	14	51	45	36	25	17	11	12	13
49	53	58	43	35	23	4	6	51	59	45	38	32	19	6	13	51	59	45	38	32	19	6	13	59	56	39	27	19	6	8	10
51	56	60	41	34	22	3	8	53	62	44	39	29	20	4	10	53	62	44	39	29	20	4	10	57	54	40	28	2		5	9
54	59	63	38	31	21	2	12	54	61	43	36	31	18	3	9	54	61	43	36	31	18	3	9	55	58	41	29	23	21	1	7
55	61	36	33	27	19		13	55	63	42	35	27	23	2	8	55	63	42	35	27	23	2	8	53	60	42	35	34	24	20	4
57	62	30	29	20	9	1	14	56	60	41	33	28	21	1	7	56	60	41	33	28	21	1	7	49	62	50	44	38	33	30	3
42	39	28	24	18	7	5	15	57	58	40	30	26	22		5	57	58	40	30	26	22		5	61	63	52	46	43	37	31	22
22	23	36	40	45	56	59	48	6		24	30	38	39	58	57	6		24	30	38	39	58	57	3	1	11	17	19	25	31	42
3		30	33	44	54	63	49	7	1	21	29	36	41	63	56	7	1	21	29	36	41	63	56	14		13	20	26	29	30	61
8	2	28	29	35	43	62	50	8	2	22	27	35	42	62	55	8	2	22	27	35	42	62	55	10	2	22	27	32	40	44	58
9	4	1	26	31	41	61	51	9	3	19	28	31	45	61	54	9	3	19	28	31	45	61	54	8	4	21	33	39	41	63	56
12	7	6	21	32	42	60	55	11	5	20	23	33	43	60	51	11	5	20	23	33	43	60	51	6	9	24	36	62	60	57	54
14	11	5	19	27	39	58	57	12	4	18	26	34	44	59	50	12	4	18	26	34	44	59	50	5	7	23	35	43	59	55	53
16	13	10	17	25	37	52	53	13	10	17	25	37	52	53	49	13	10	17	25	37	52	53	49	12	18	28	37	46	52	51	50
24	20	15	18	34	38	46	47	14	16	15	32	40	46	48	47	14	16	15	32	40	46	48	47	16	15	34	38	45	47	48	49
49	48	47	45	38	34	15	16	47	48	46	40	32	15	16	14	47	48	46	40	32	15	16	14	47	46	38	34	18	15	20	24
50	51	52	46	37	28	18	12	49	53	52	37	25	17	10	13	49	53	52	37	25	17	10	13	53	52	37	25	17	10	13	16
53	55	59	43	35	23	7	5	50	59	44	34	26	18	4	12	50	59	44	34	26	18	4	12	57	58	39	27	19	5	11	14
54	57	60	62	36	24	9	6	51	60	43	33	23	20	5	11	51	60	43	33	23	20	5	11	55	60	42	32	21	6	7	12
56	63	41	39	33	21	4	8	54	61	45	31	28	19	3	9	54	61	45	31	28	19	3	9	51	61	41	31	26	1	4	9
58	44	40	32	27	22	2	10	55	62	42	35	27	22	2	8	55	62	42	35	27	22	2	8	50	62	43	35	29	28	2	8
61	30	29	26	20	13		14	56	63	41	36	29	21	1	7	56	63	41	36	29	21	1	7	49	63	54	44	33	30		3
42	31	25	19	17	11	1	3	57	58	39	38	30	24		6	57	58	39	38	30	24		6	48	59	56	45	40	36	23	22
22	31	37	43	46	52	63	61	5		22	26	30	40	58	57	5		22	26	30	40	58	57	15	5	7	18	24	28	39	42
3	30	33	38	44	50	62	49	7	1	21	28	33	41	60	56	7	1	21	28	33	41	60	56	14	1	9	20	29	30	62	57
4	20	24	34	35	42	60	53	8	2	23	27	35	42	63	55	8	2	23	27	35	42	63	55	13		19	27	33	36	61	55
7	1	21	23	29	41	58	55	9	3	18	31	36	43	61	54	9	3	18	31	36	43	61	54	12	2	21	31	38	63	59	54
9	5		2	28	40	54	57	10	4	20	29	39	44	62	53	10	4	20	29	39	44	62	53	8	3	22	34	41	60	56	51
10	8	6	19	27	39	56	59	13	6	19	32	38	45	59	51	13	6	19	32	38	45	59	51	6	4	23	35	43	58	53	49
13	12	11	17	25	36	45	51	14	12	11	25	37	46	52	50	14	12	11	25	37	46	52	50	10	11	25	37	46	52	50	47
14	15	16	18	26	32	48	47	16	15	17	24	34	48	47	49	16	15	17	24	34	48	47	49	16	17	26	32	45	48	44	40

(b) Channel map for COBs

Figure A.1: Channel ID numbers for (a) FEVs and for (b) COBs.

Appendix B

Masked Cells

Mask distribution for the entire 15 layer is presented in this section. Black spots represent masked channels. Each layer is presented with two mask maps: channel vs chip and X vs Y position.

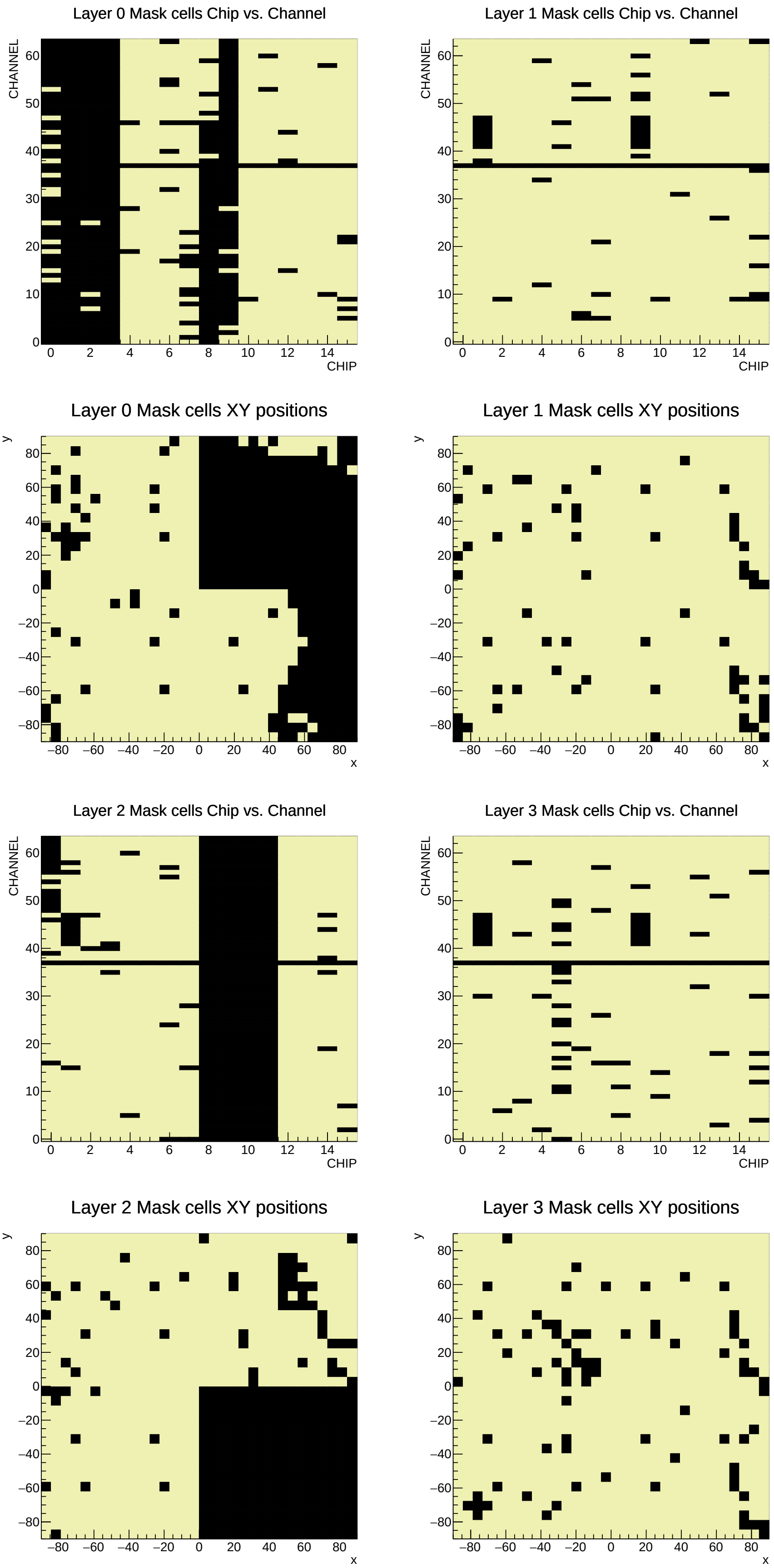

FIGURE B.1: Masked cell distributions from layer 0 to 3

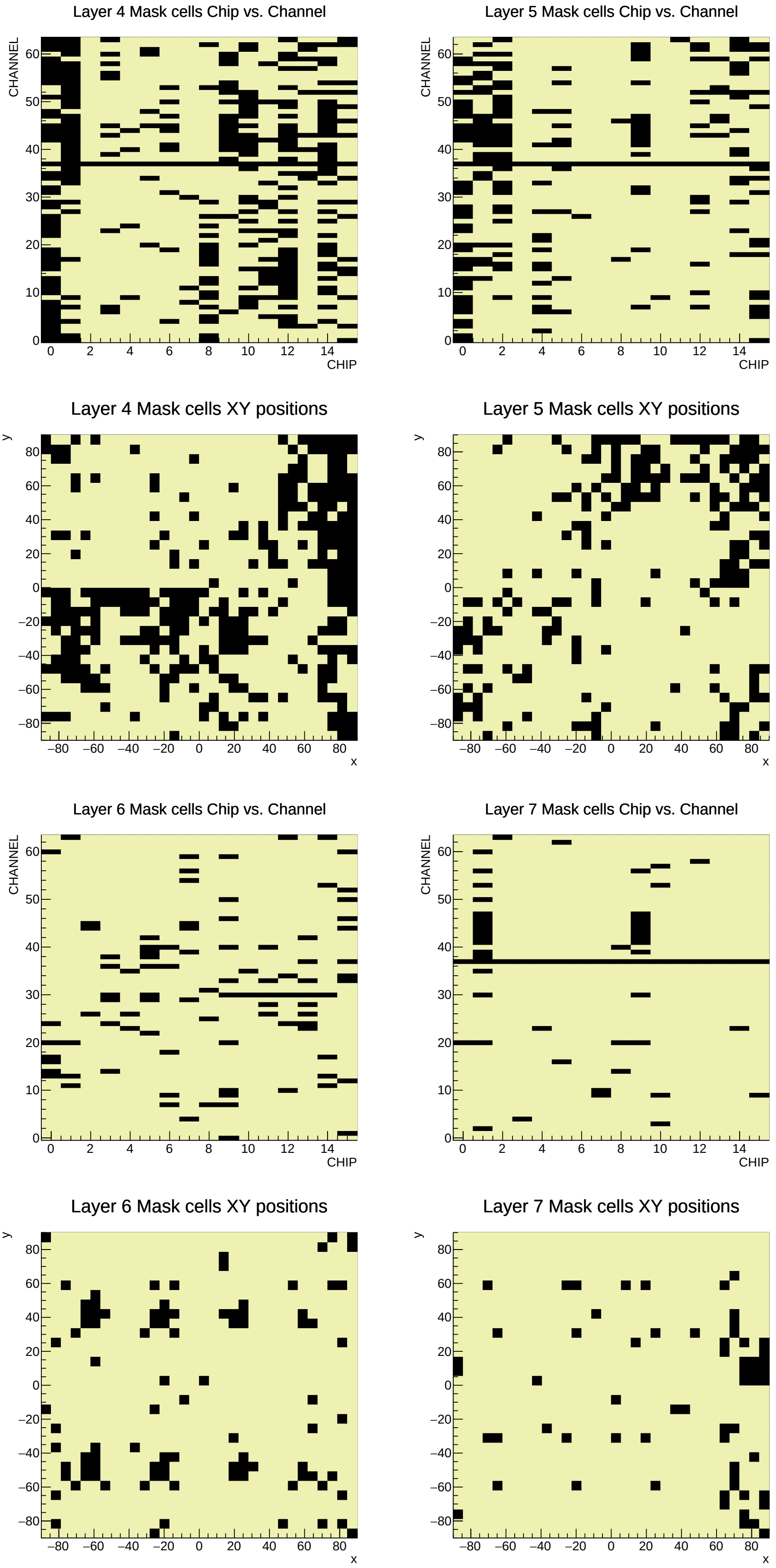

Figure B.2: Masked cell distributions from layer 4 to 7

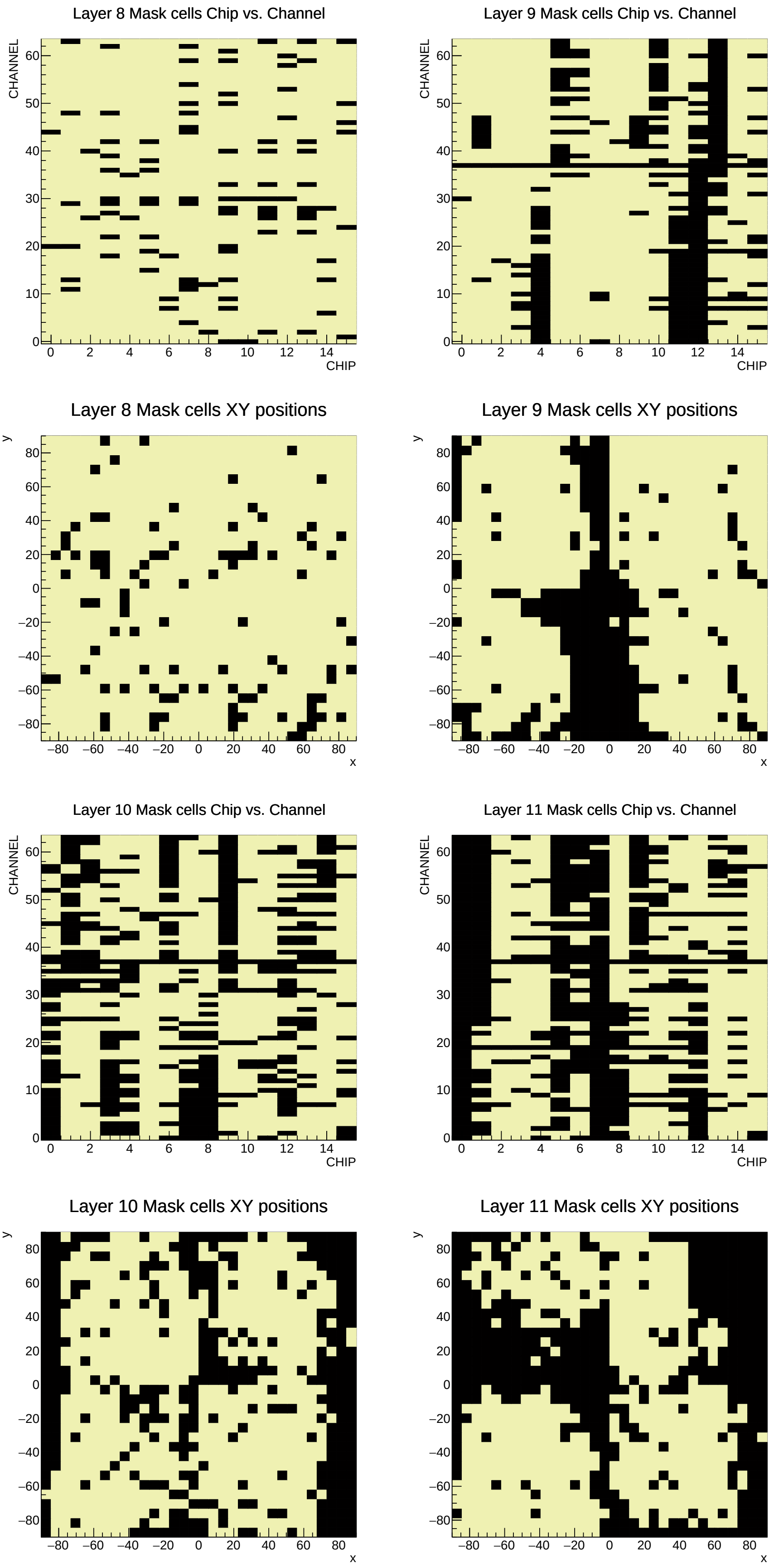

Figure B.3: Masked cell distributions from layer 8 to 11

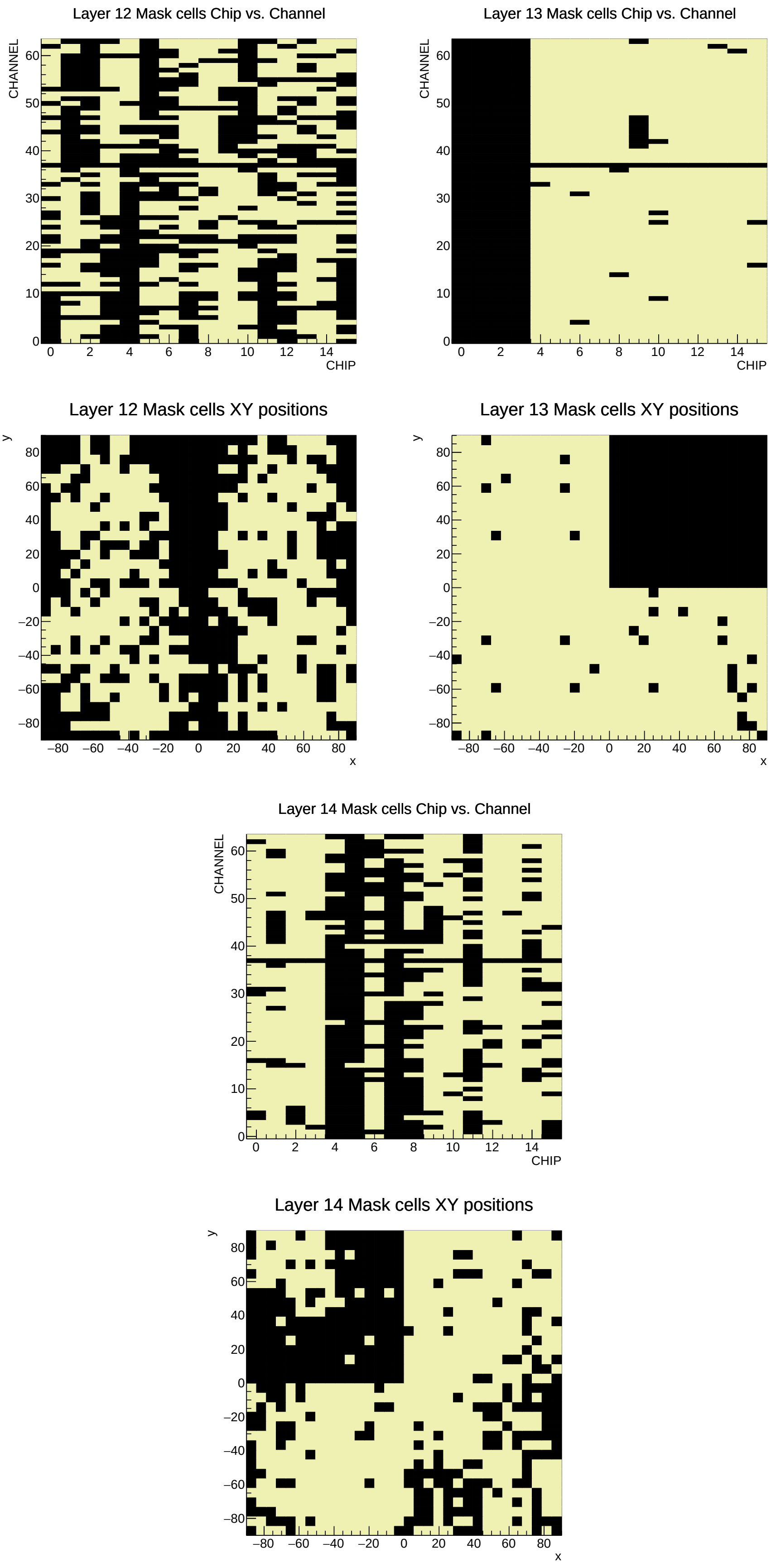

Figure B.4: Masked cell distributions from layer 12 to 14

Appendix C

Thresholds

In this section, threshold values for all cells are displayed. For each layer, the top plot shows the channel vs. chip with the global threshold on the z-axis, and the added channel threshold is indicated by the number text. The bottom plot displays the x and y positions of the cells with the global threshold on the z-axis, and the added channel threshold is represented in the number text. Layers without the number texts are those with SKIROC2, which cannot adjust the channel thresholds. Blank cells are masked channels.

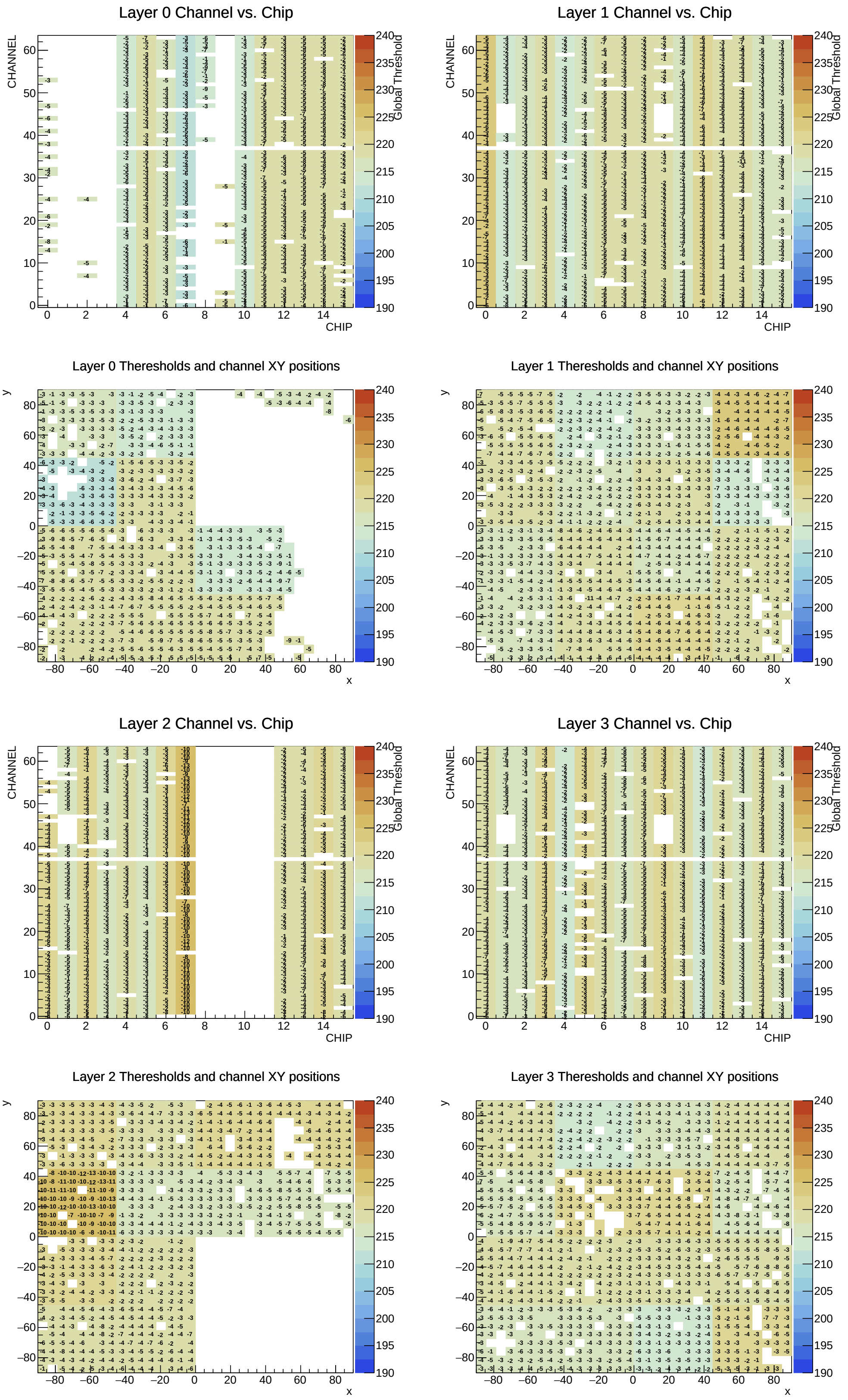

Figure C.1: Channel thresholds from layer 0 to 3

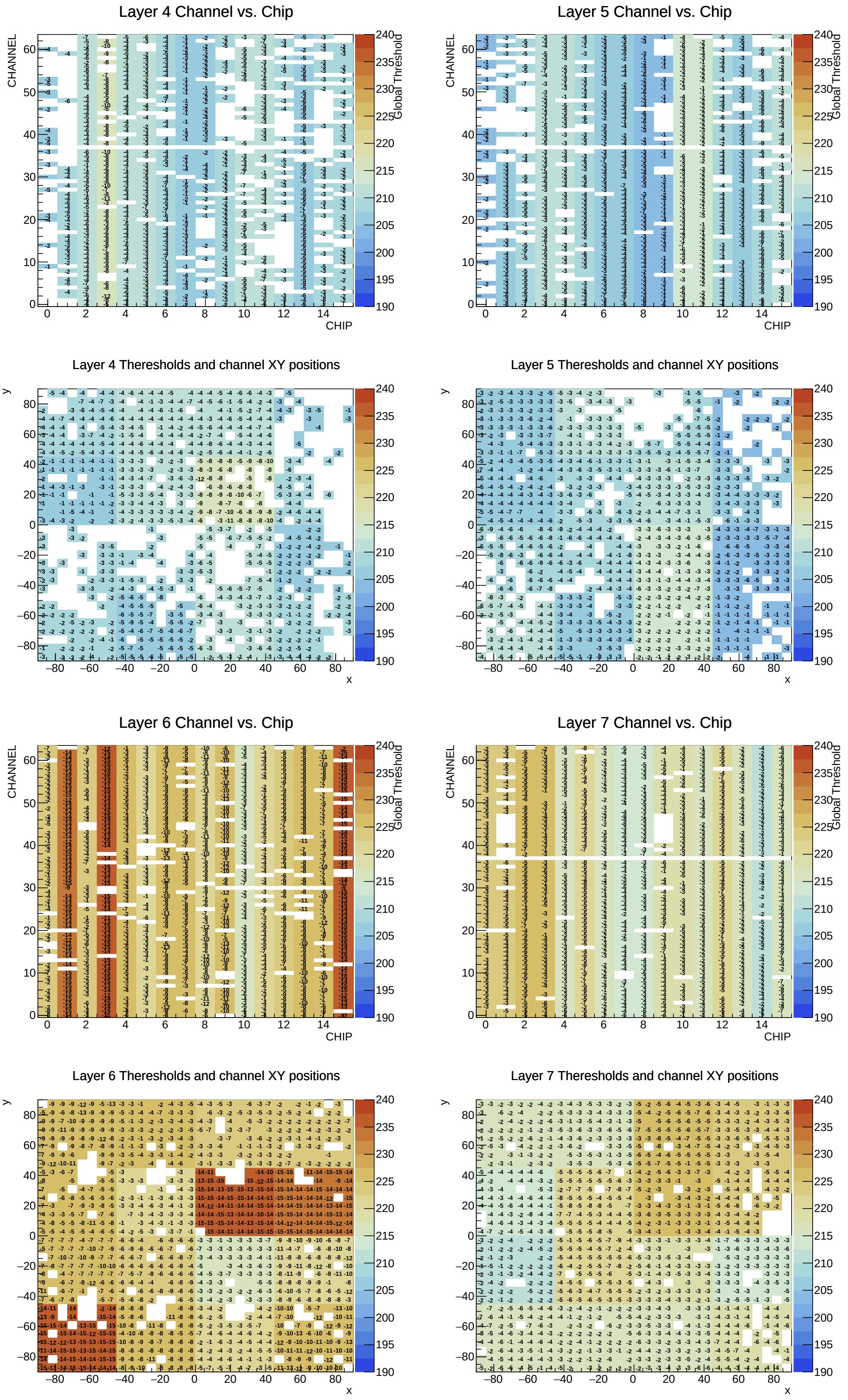

Layer 4 Channel vs. Chip

Layer 5 Channel vs. Chip

Layer 4 Theresholds and channel XY positions

Layer 5 Theresholds and channel XY positions

Layer 6 Channel vs. Chip

Layer 7 Channel vs. Chip

Layer 6 Thresholds and channel XY positions

Layer 7 Thresholds and channel XY positions

Figure C.1: Channel thresholds from layer 4 to 7

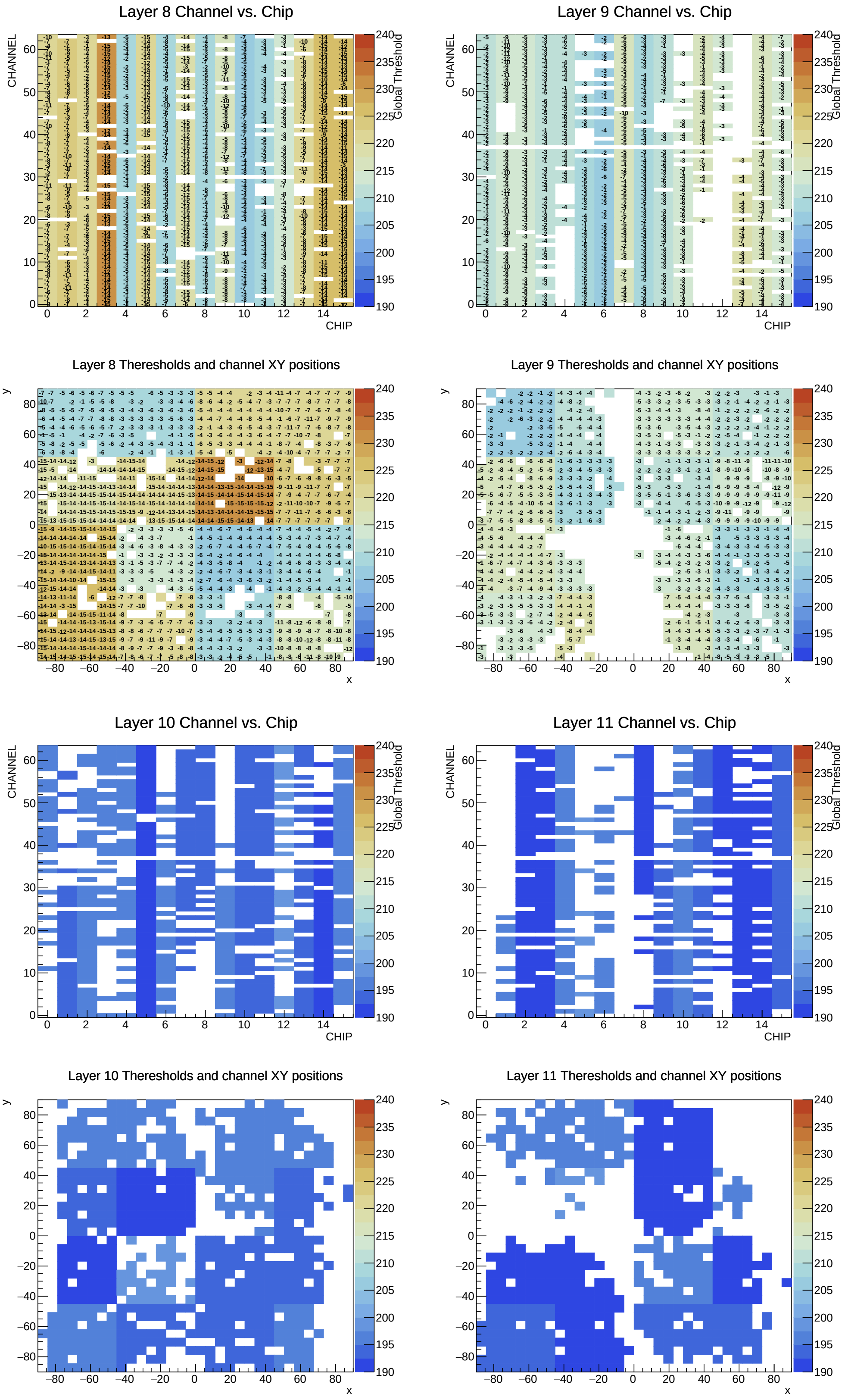

Figure C.1: Channel thresholds from layer 8 to 11

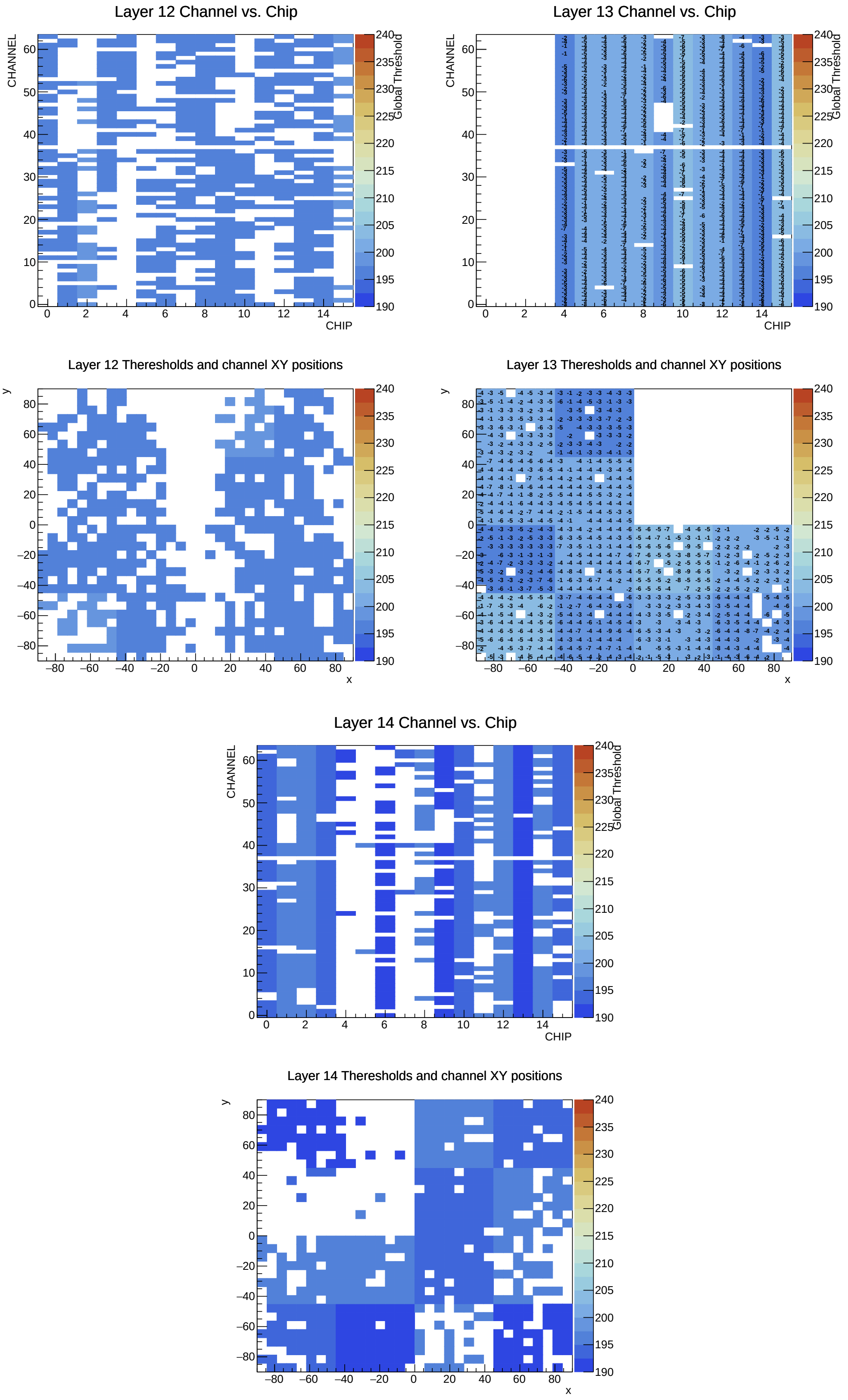

Figure C.1: Channel thresholds from layer 12 to 14

Appendix D

Summary of MIP and Pedestal Calibrations

The pedestal and noise for all SCAs are presented in Figure 4.25. In Figure D.1a, a stripe pattern can be seen throughout all layers. This suggests that the pedestal values for a chip in a layer are uniform across all channels and SCAs. Figure D.1b represents the noise for individual SCAs. The yellow spectrum in layers 6 and 8 is likely due to the high noise contribution from the COBs, which are relatively vulnerable to noise compared to the FEVs due to their design without the BGA, making them sensitive to the background. Moreover, the noise effect is position-dependent, indicating that noise from the pedestals is higher in certain regions on the PCB, a common pattern seen throughout all layers. This is attributed to the routing of the PCB, and this effect has been improved in the FEV13.

A comprehensive overview of the results for all 15 layers is provided in Figure D.2, where Figure D.2a represents the fitted mean, and Figure D.2b illustrates the width. Notably, the consistent coloring for both MIP value and width across all chips highlights the uniformity of these values within the chip set.

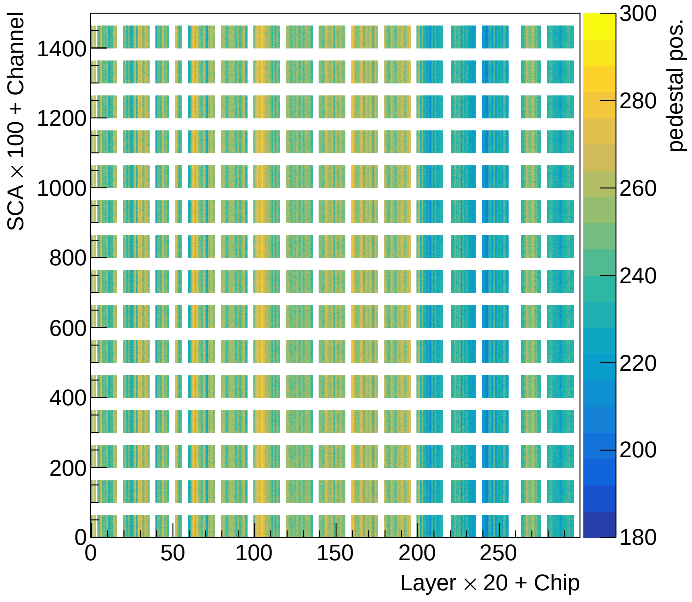

(a) Pedestals

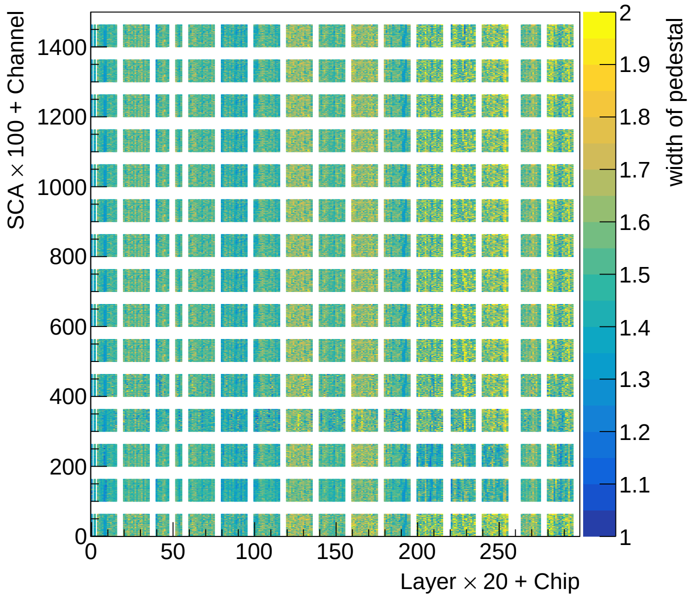

(b) Pedestal width

FIGURE D.1: Fitted pedestal information for high gain setting is condensed in the plots above. (a): Fitted pedestal value and (b): width of the pedestal fit for each channel in all 15 layers.

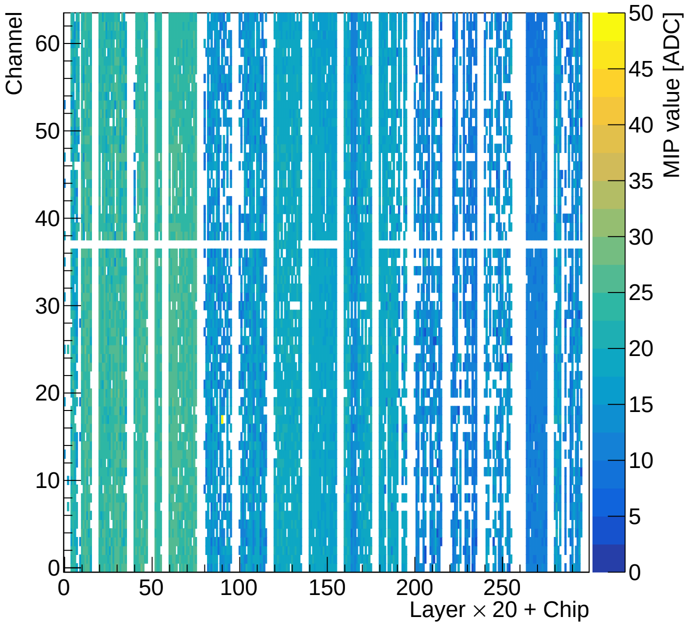

(a) Mean MIP values

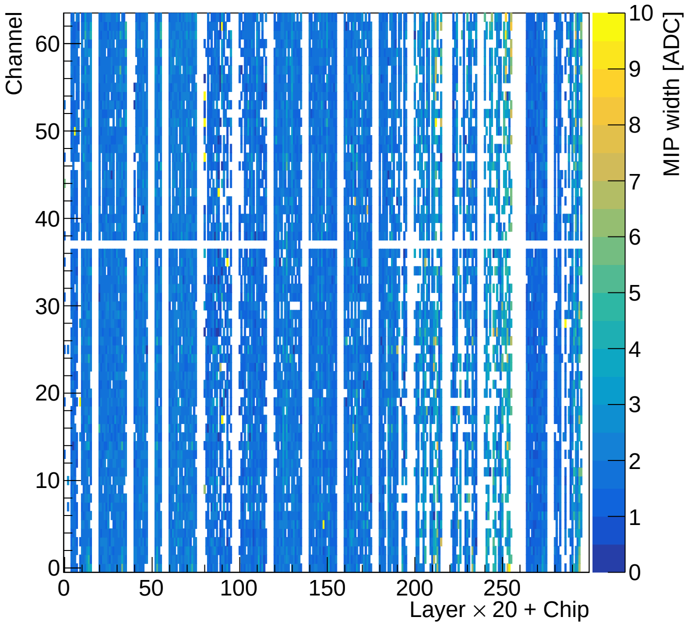

(b) MIP widths

FIGURE D.2: MIP value measurement results for all layer, chip and channel. To concisely contain all information, layer number was multiplied by 20 before adding the corresponding chip number. (a) MIP values and (b) MIP width are shown in the z-axis.

Appendix E

MIP Values

MIP values with high gain setting for 15 layers are shown in this section. For each ASIC, charge measurement results using the muon beam with 150 GeV were fitted with landau distribution. Fit was performed in a region between (mean - sigma) and (mean×1.3). Among these distributions there are ASICs without fits or entries. These are likely due to lack of hits or failed fits. In such case, two methods were taken:

- In case where there are hits but the fit fails, the mean ADC counts of the chip was taken.
- In case of no hits, negative MIP value was assigned to indicate anomaly of chip.

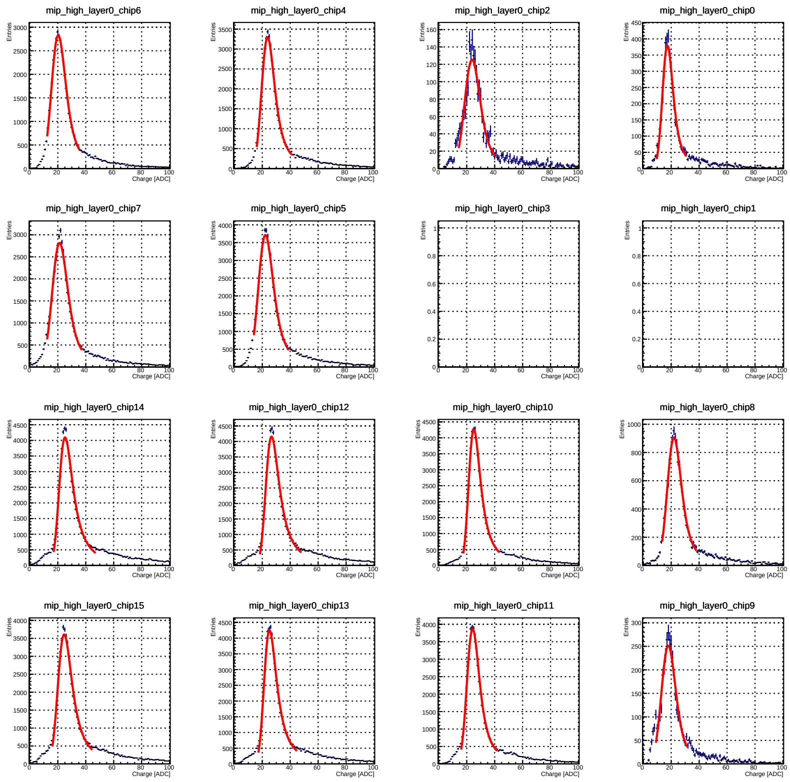

(a) Layer 0

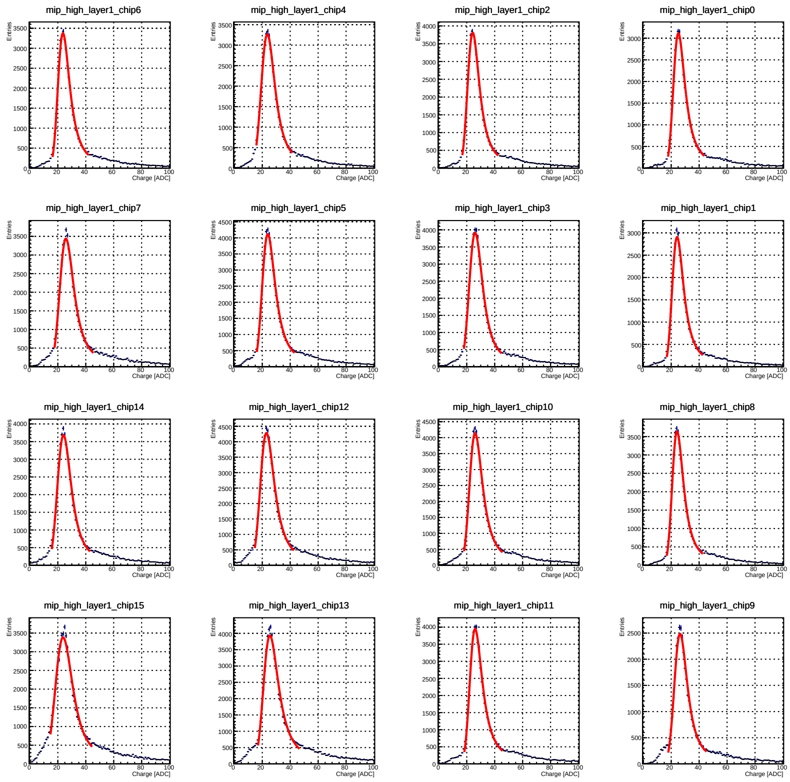

(b) Layer 1

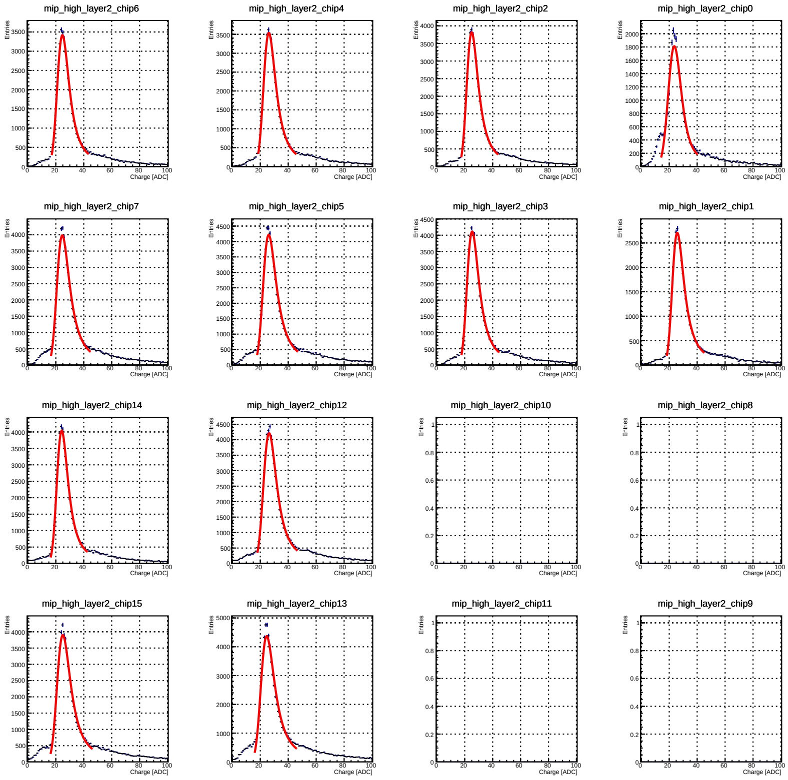

(c) Layer 2

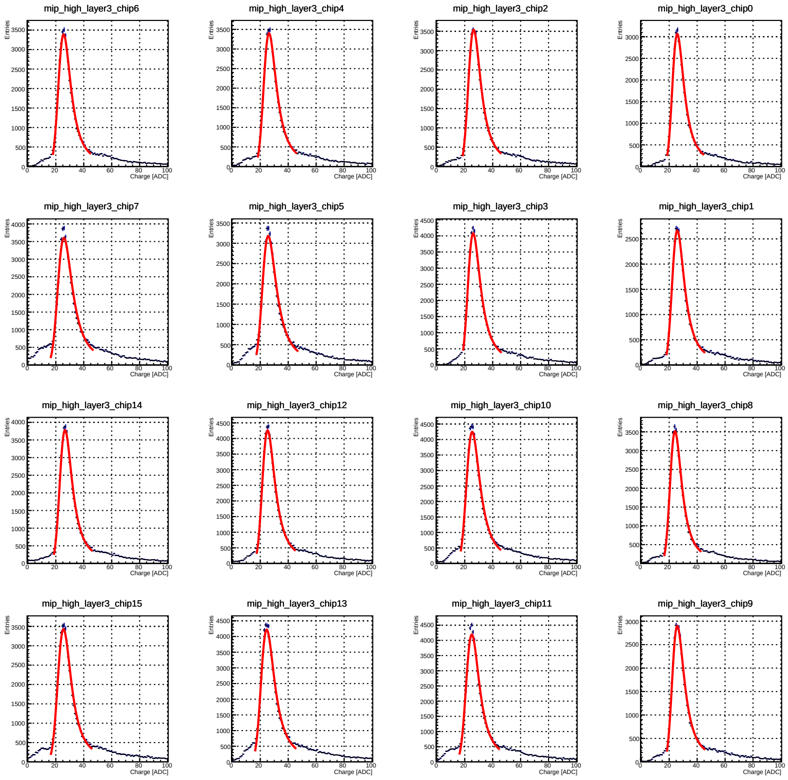

(d) Layer 3

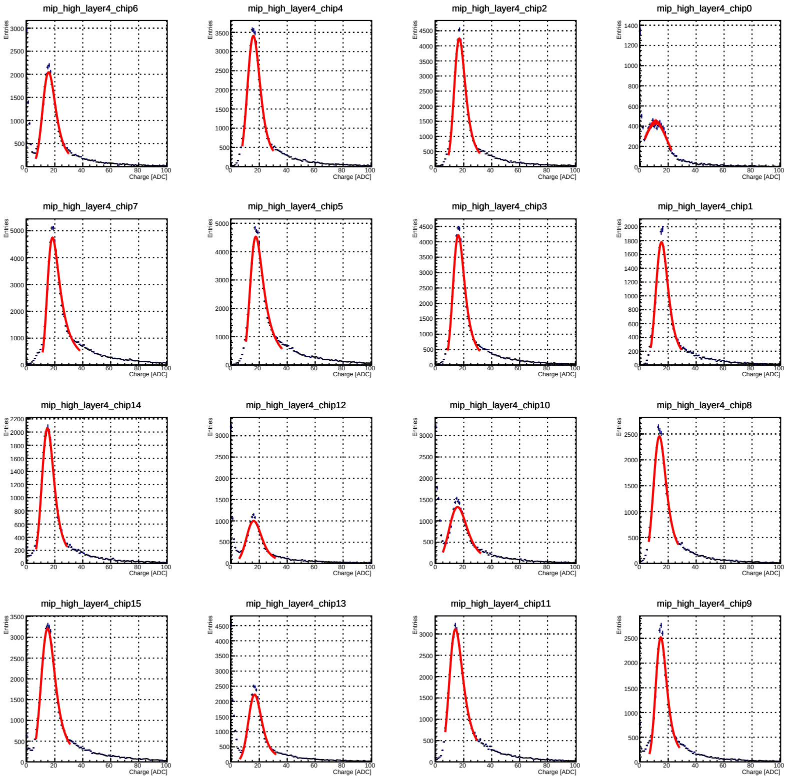

(e) Layer 4

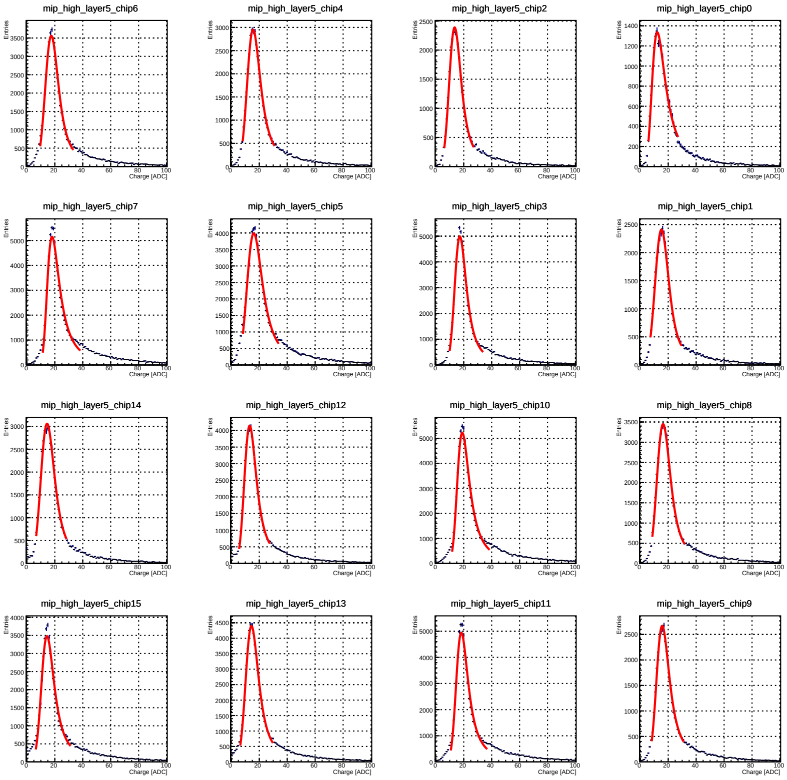

(f) Layer 5

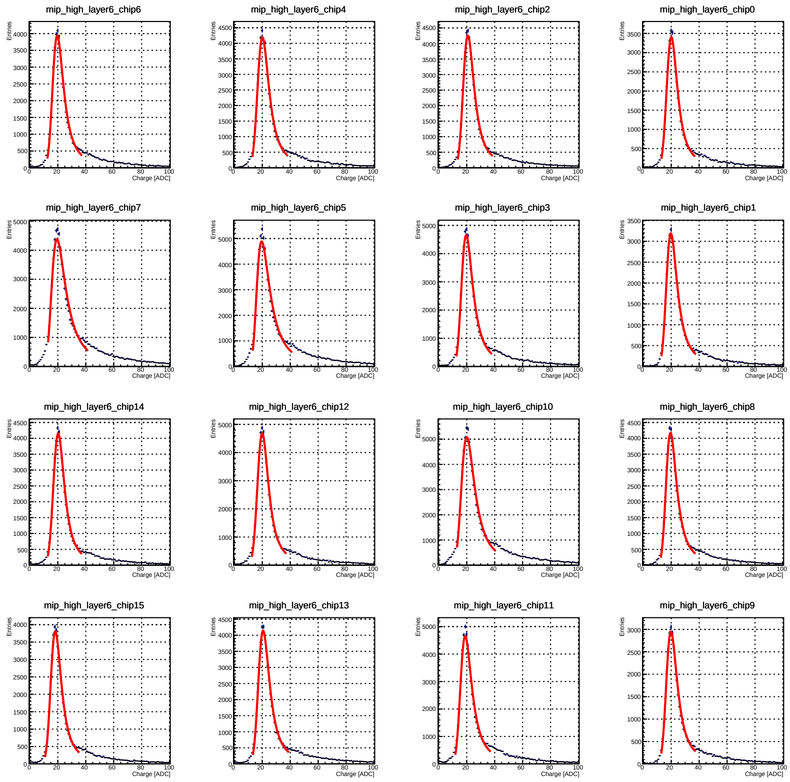

(g) Layer 6

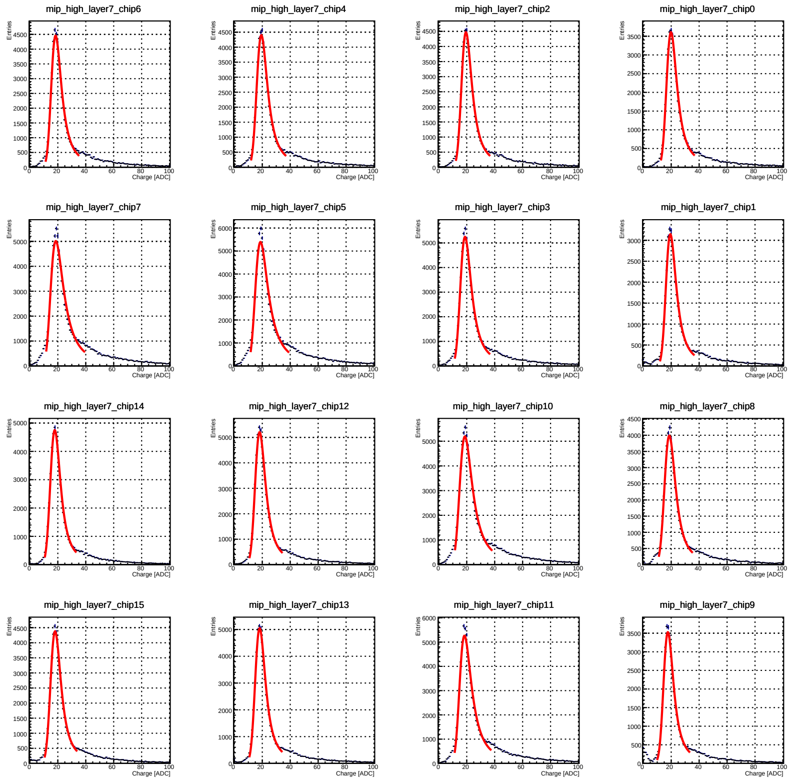

(h) Layer 7

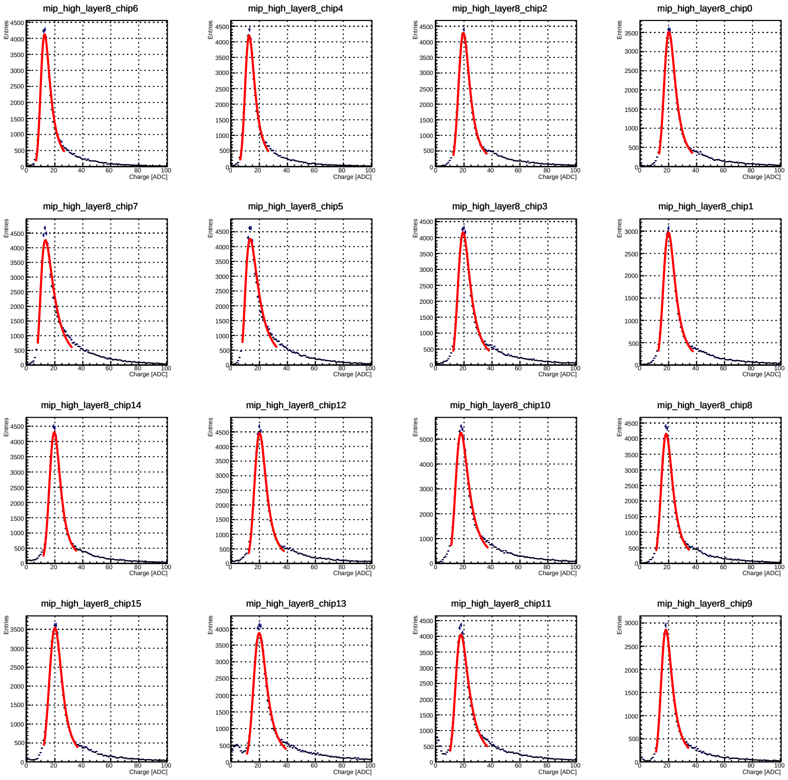

(i) Layer 8

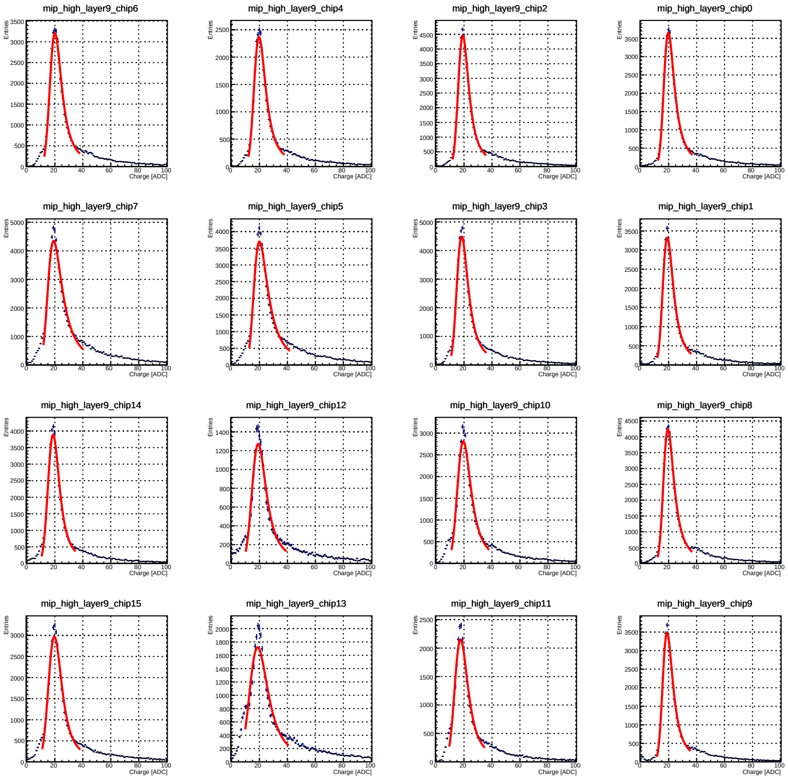

(j) Layer 9

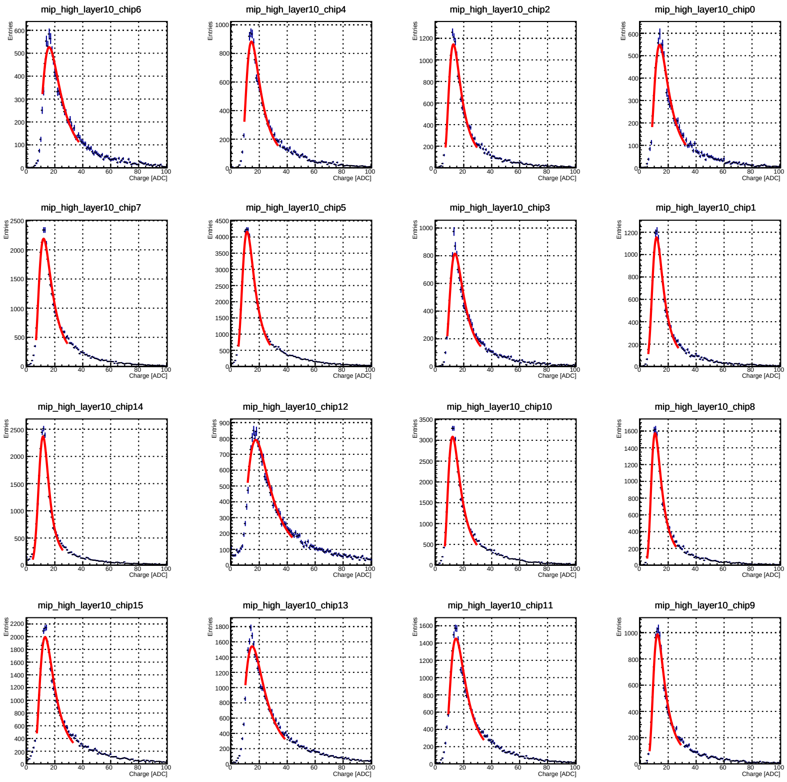

(k) Layer 10

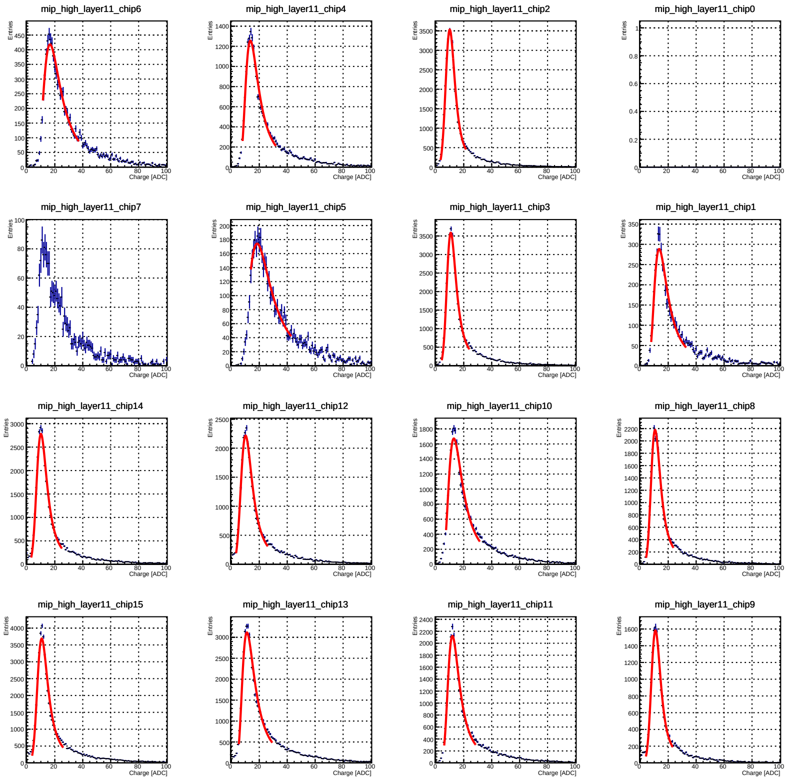

(l) Layer 11

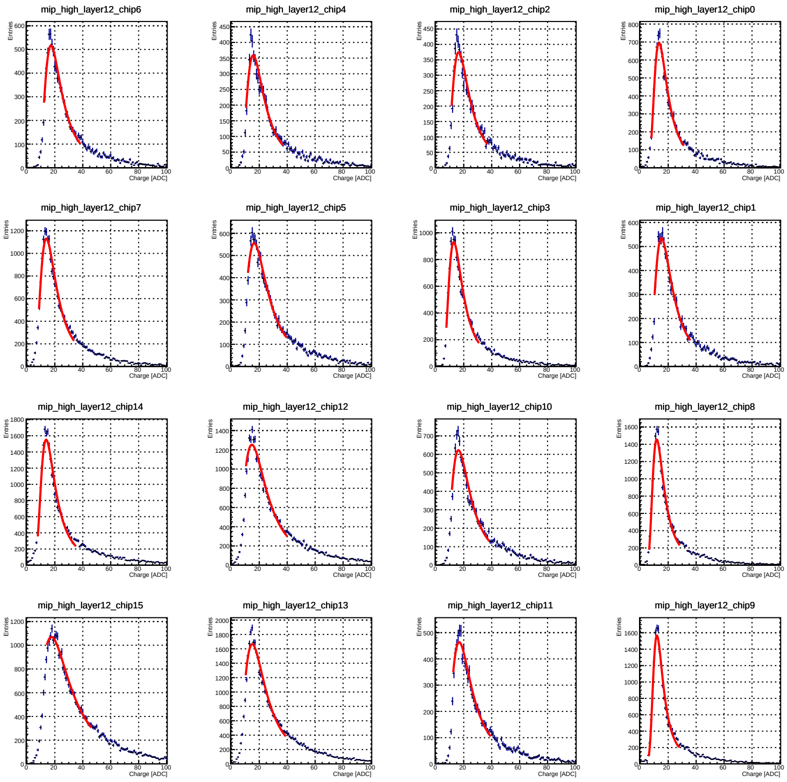

(m) Layer 12

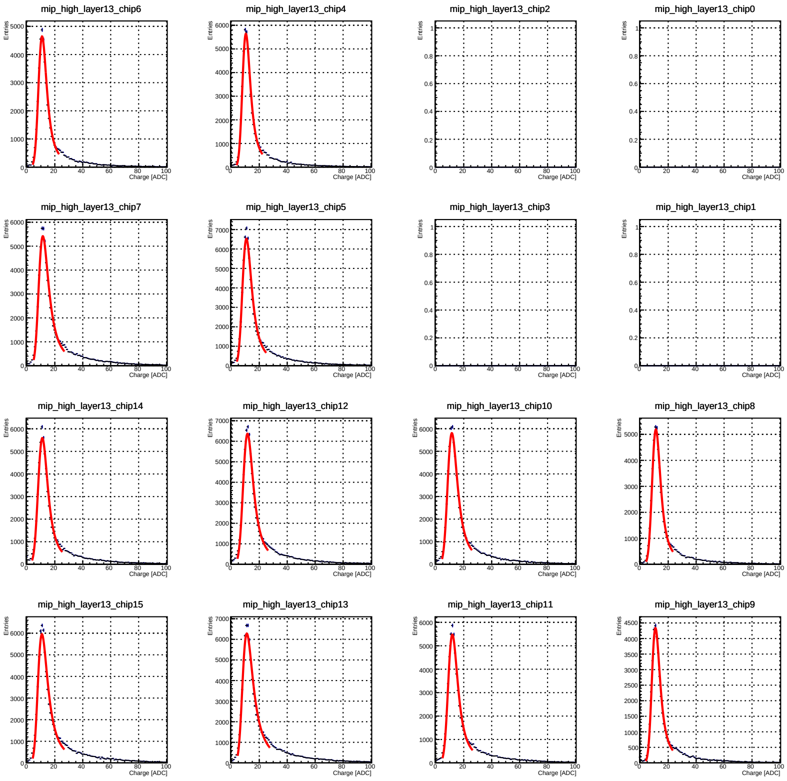

(n) Layer 13

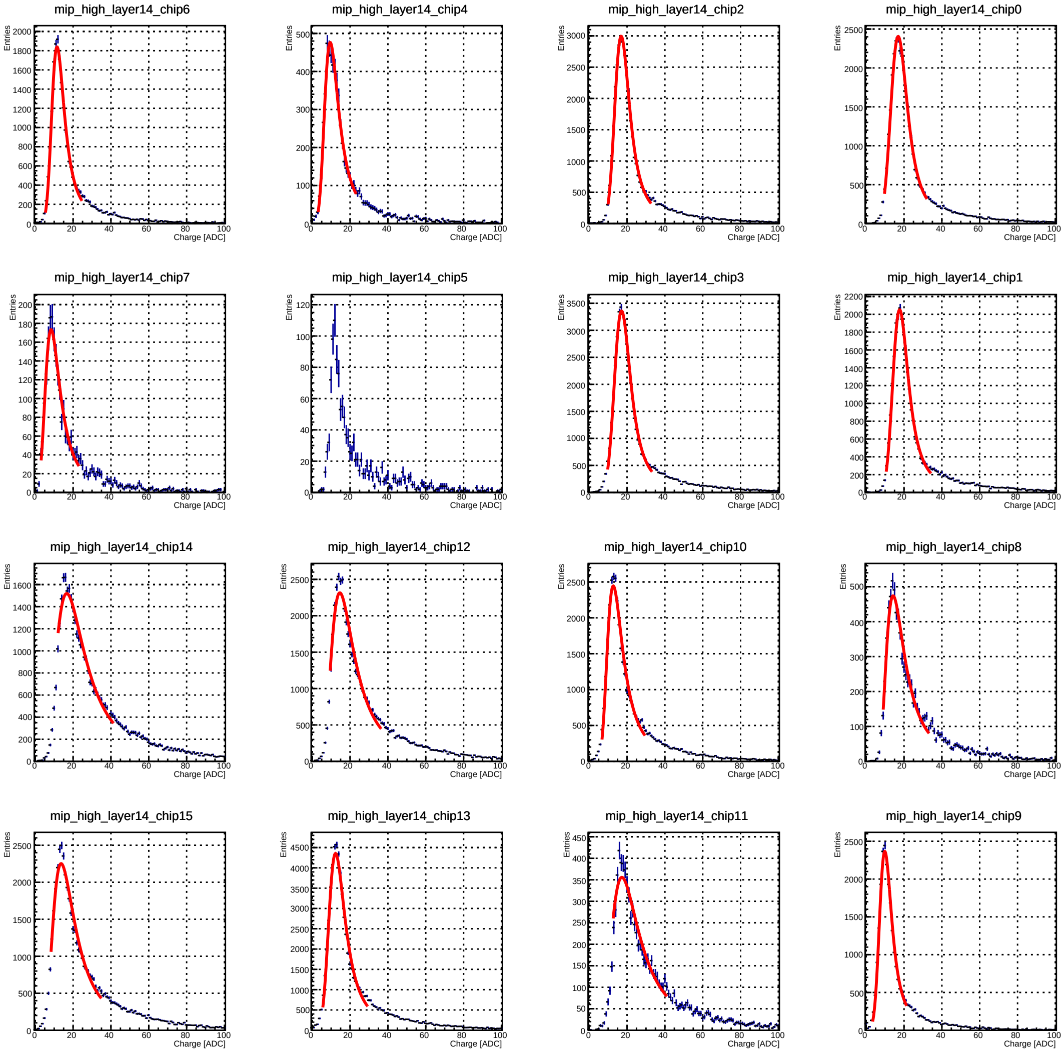

(o) Layer 14

Figure E.1: Charge measurements in ADC values.

Appendix F

MIP Thresholds

MIN injection test results for all layers are shown here.

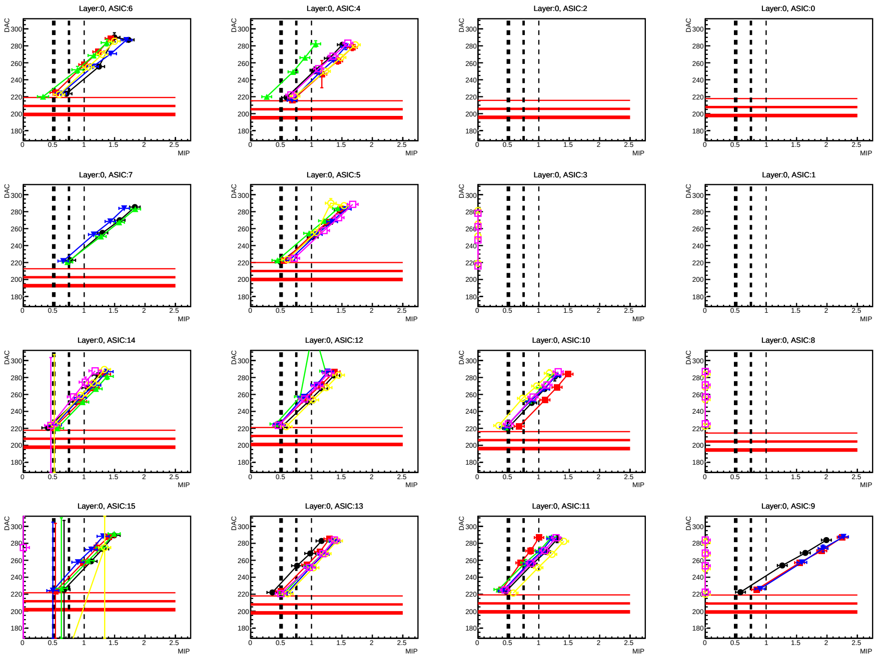

(a) Layer 0

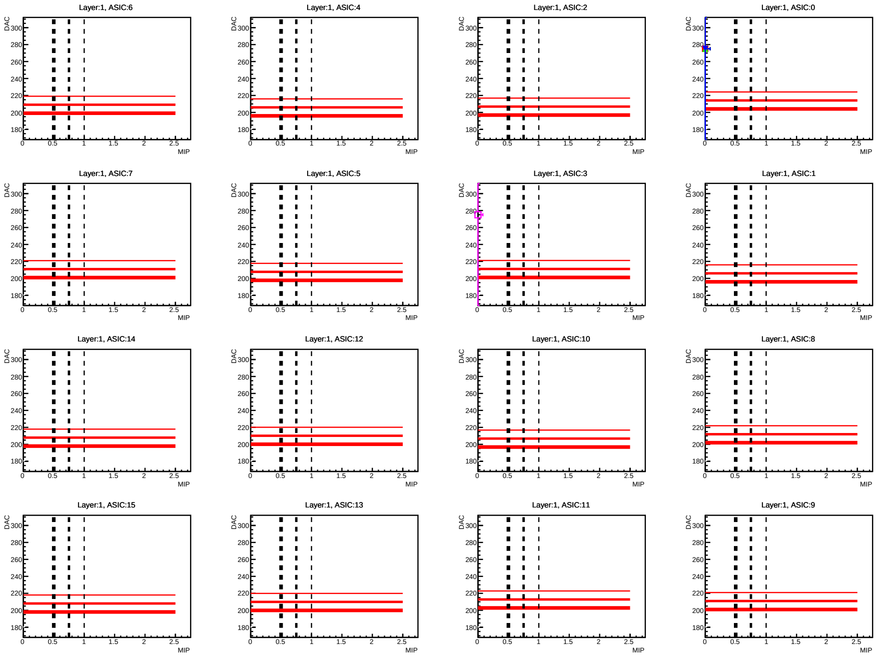

(b) Layer 1

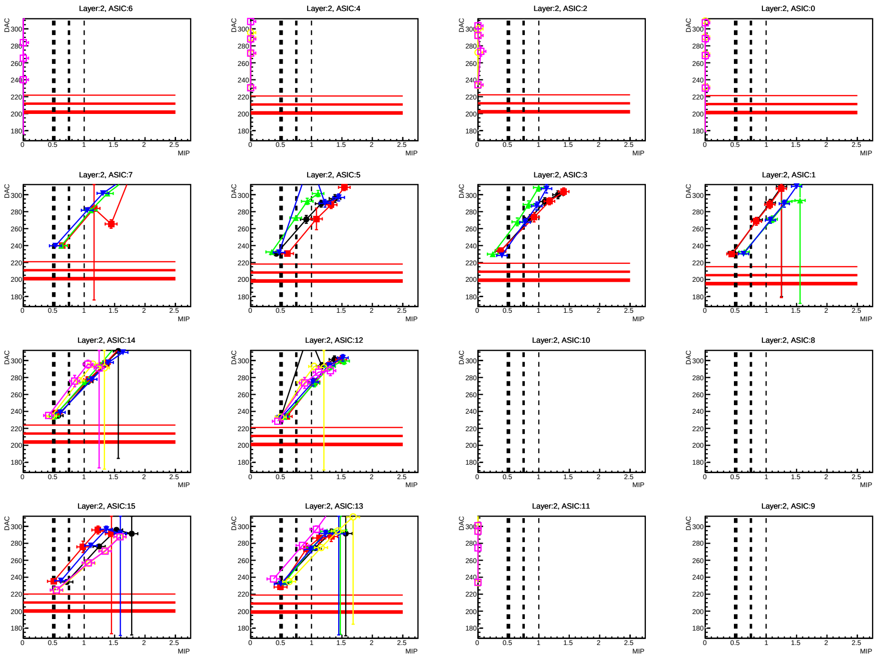

(c) Layer 2

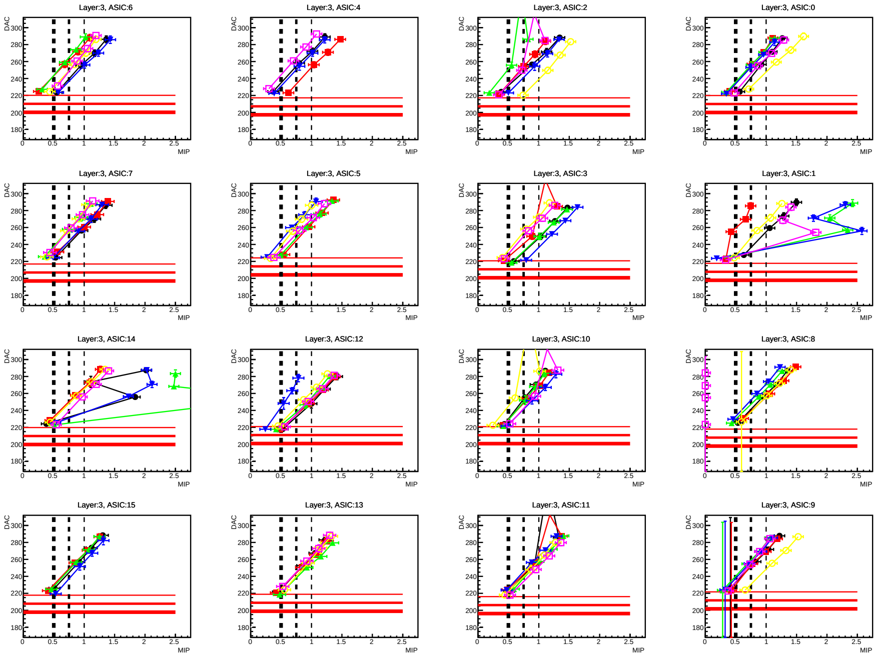

(d) Layer 3

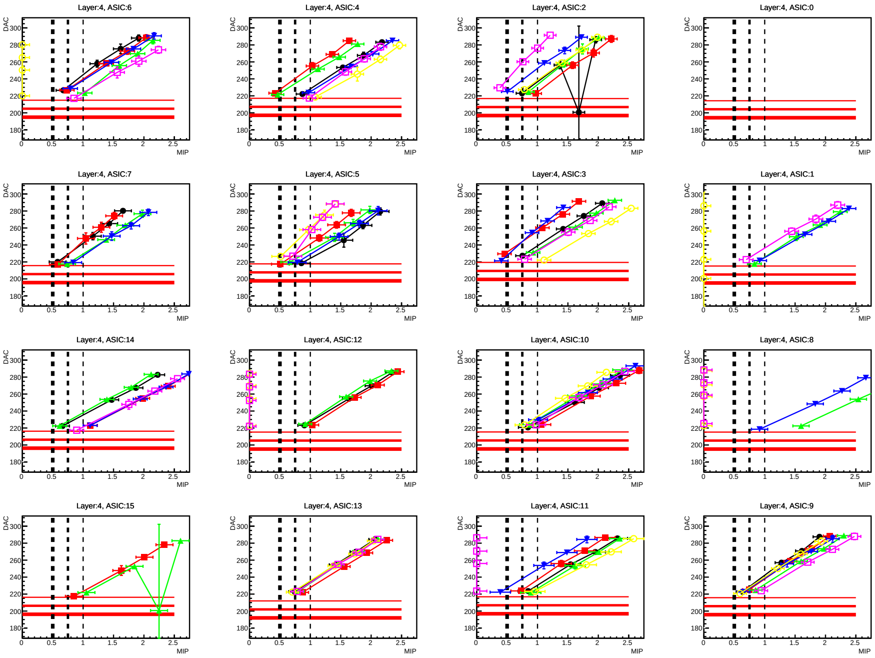

(e) Layer 4

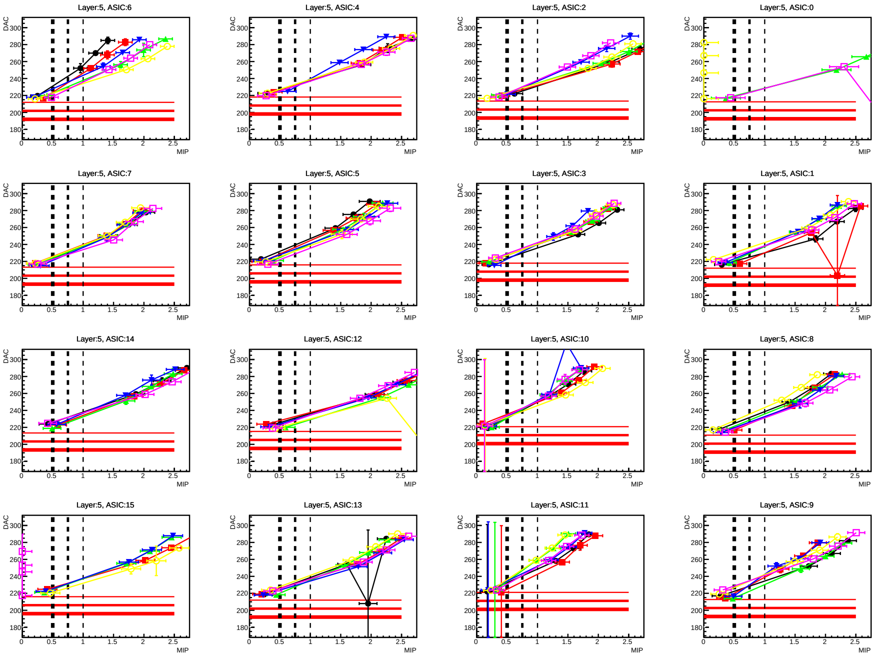

(f) Layer 5

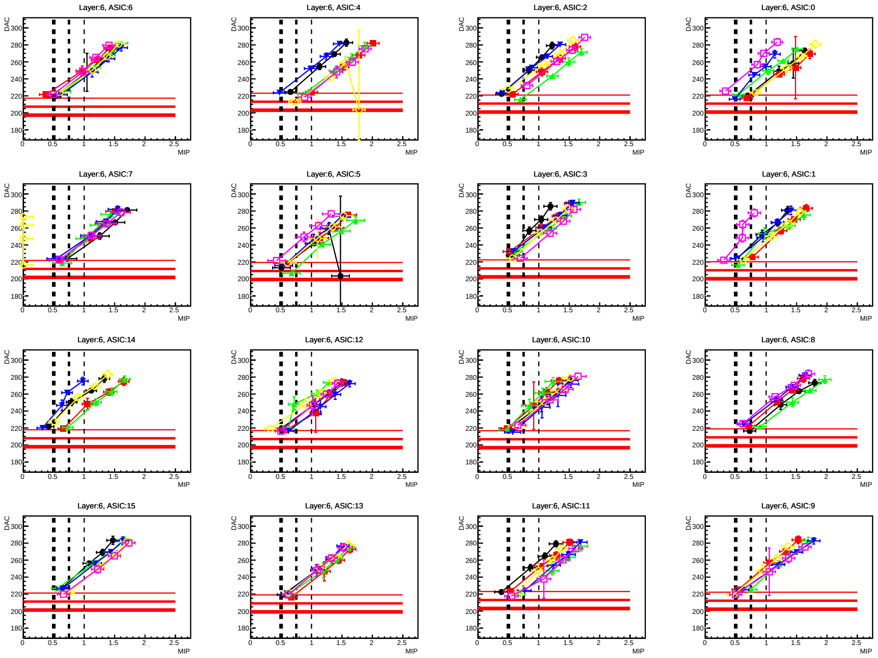

(g) Layer 6

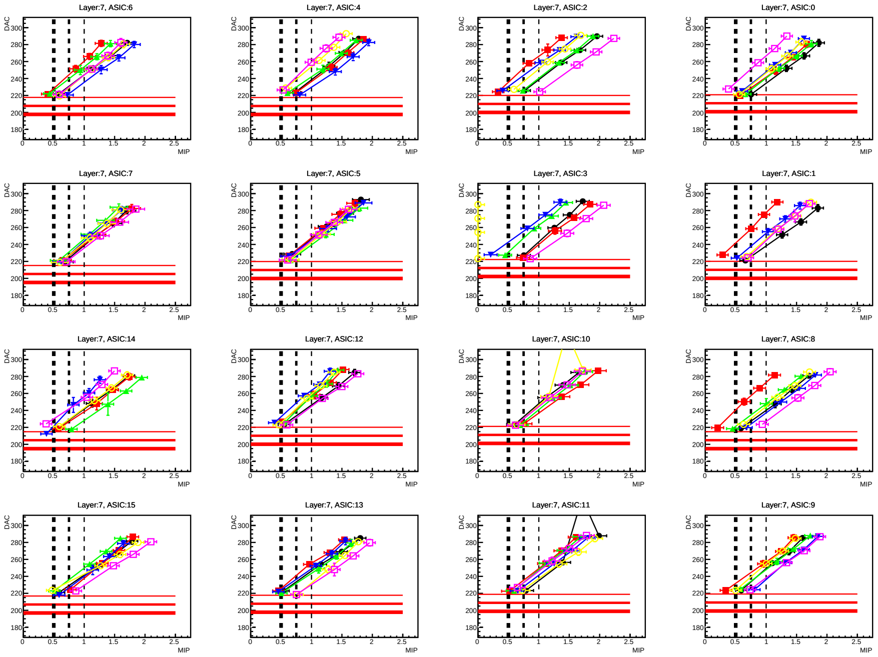

(h) Layer 7

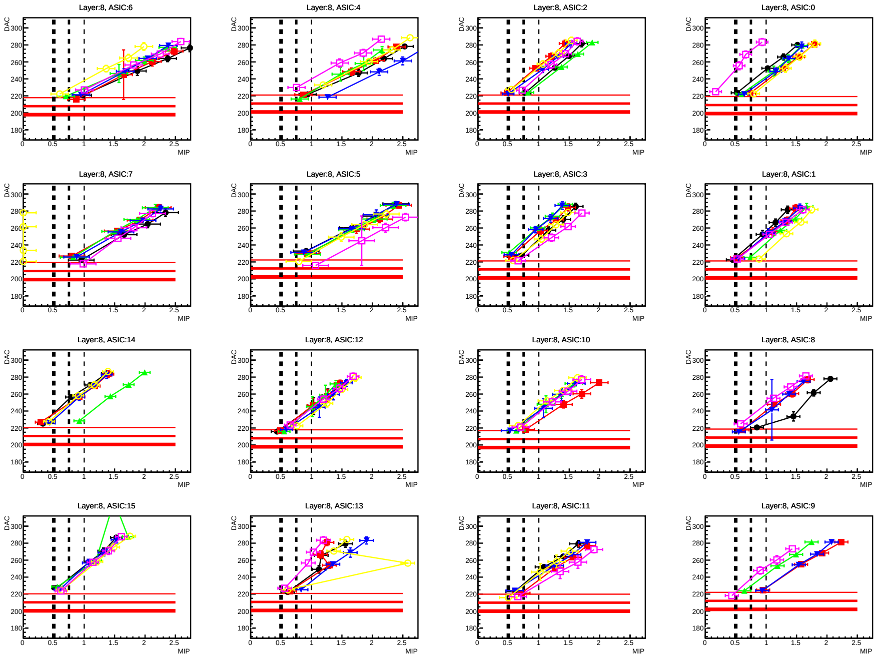

(i) Layer 8

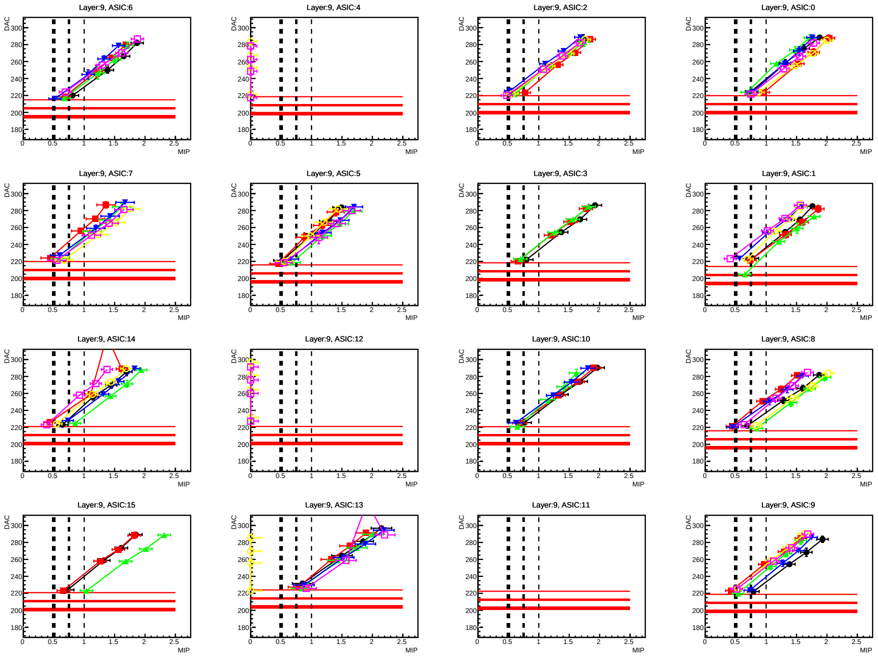

(j) Layer 9

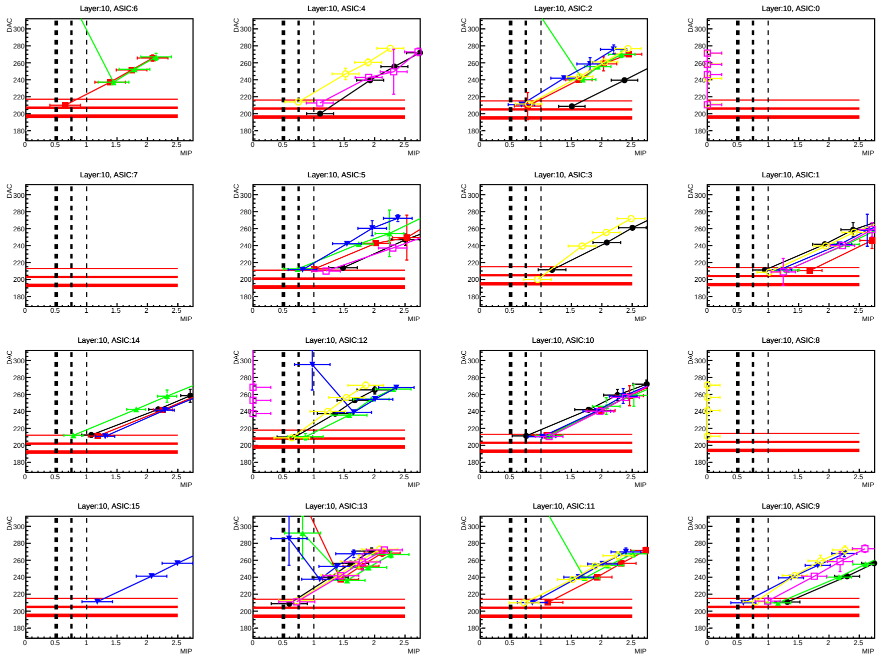

(k) Layer 10

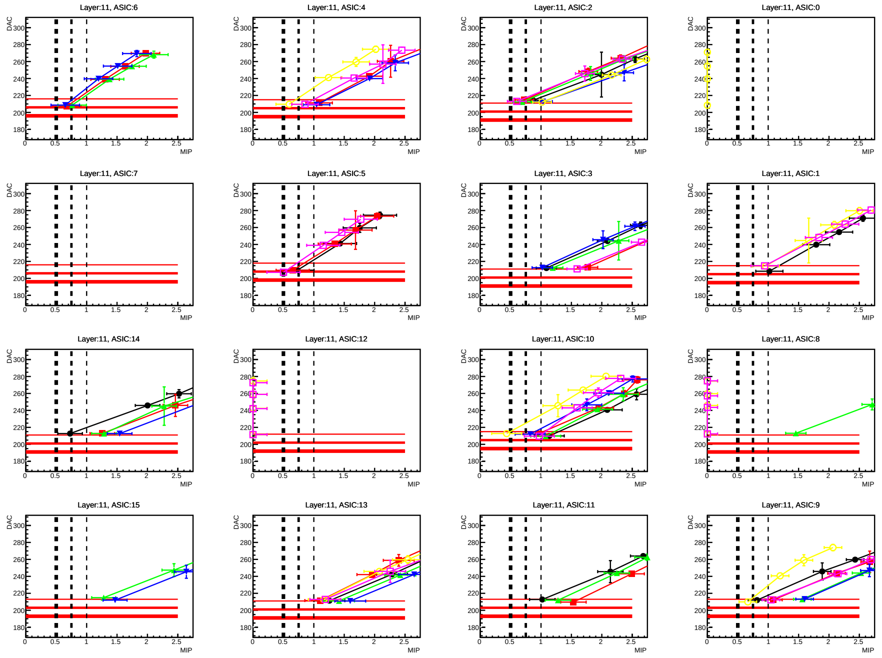

(l) Layer 11

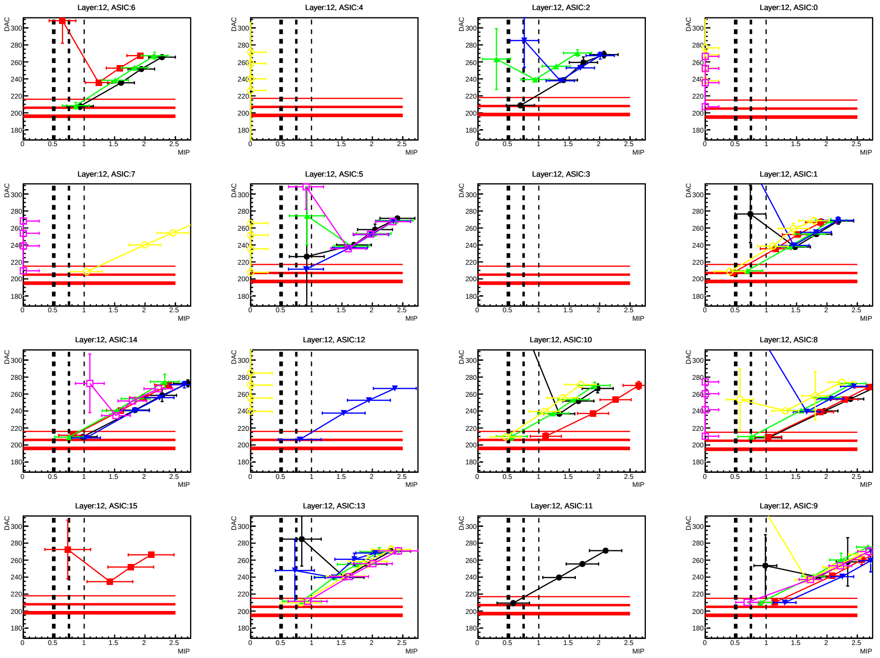

(m) Layer 12

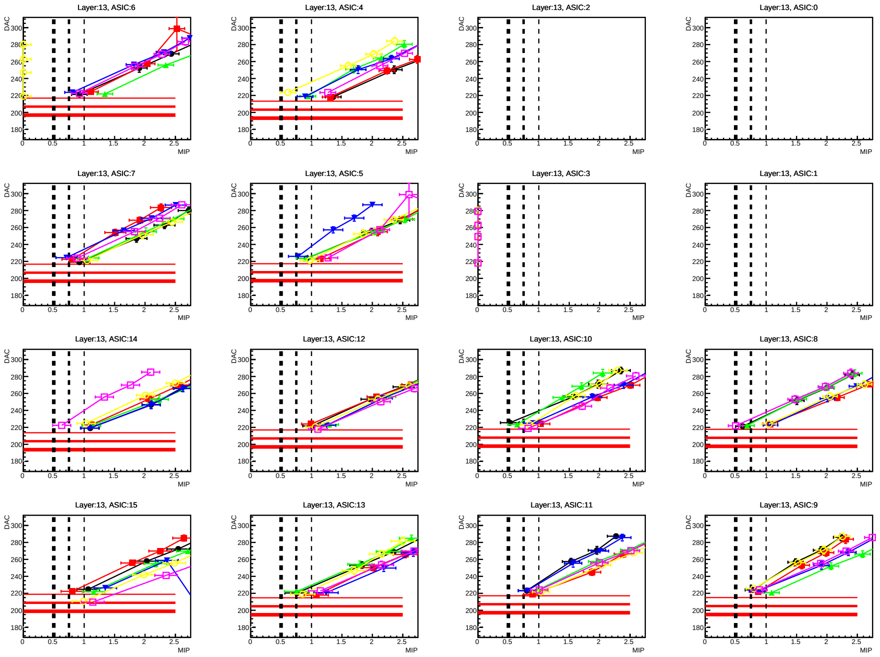

(n) Layer 13

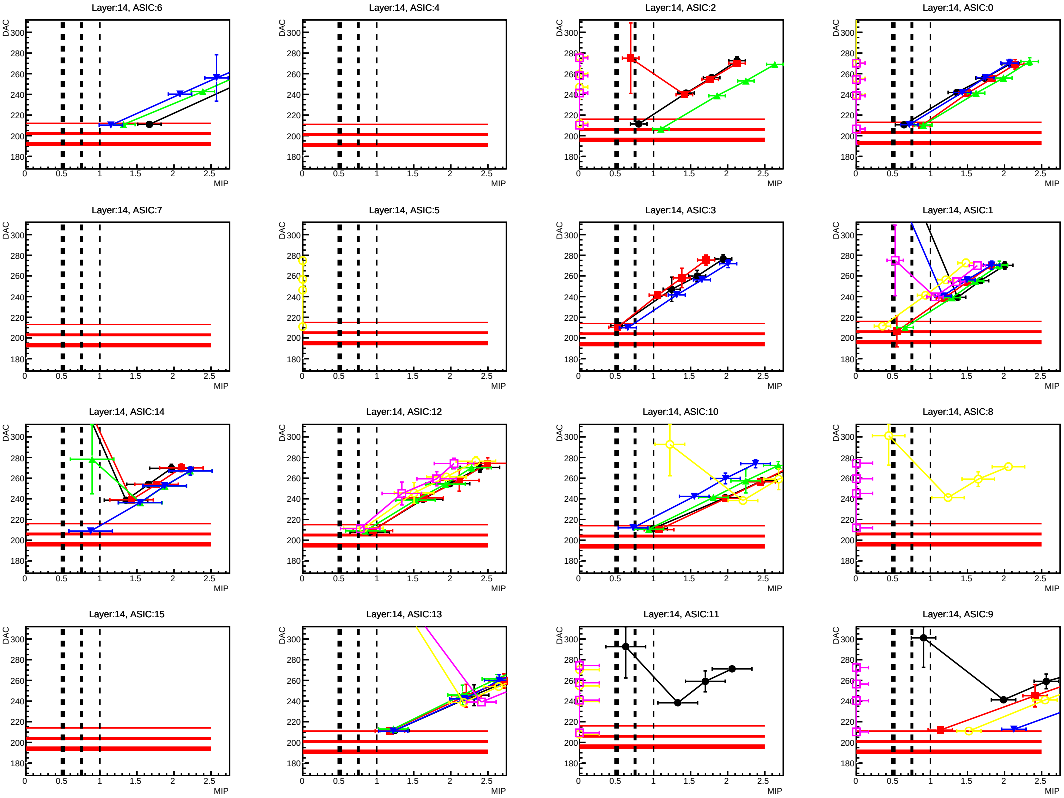

(o) Layer 14

Figure F.1: MIP injection results for every layer.

Appendix G

Data & Simulation Full Comparison

Comparison of data and simulation for total number of hits, total energy deposition and individual hit energy per layer.

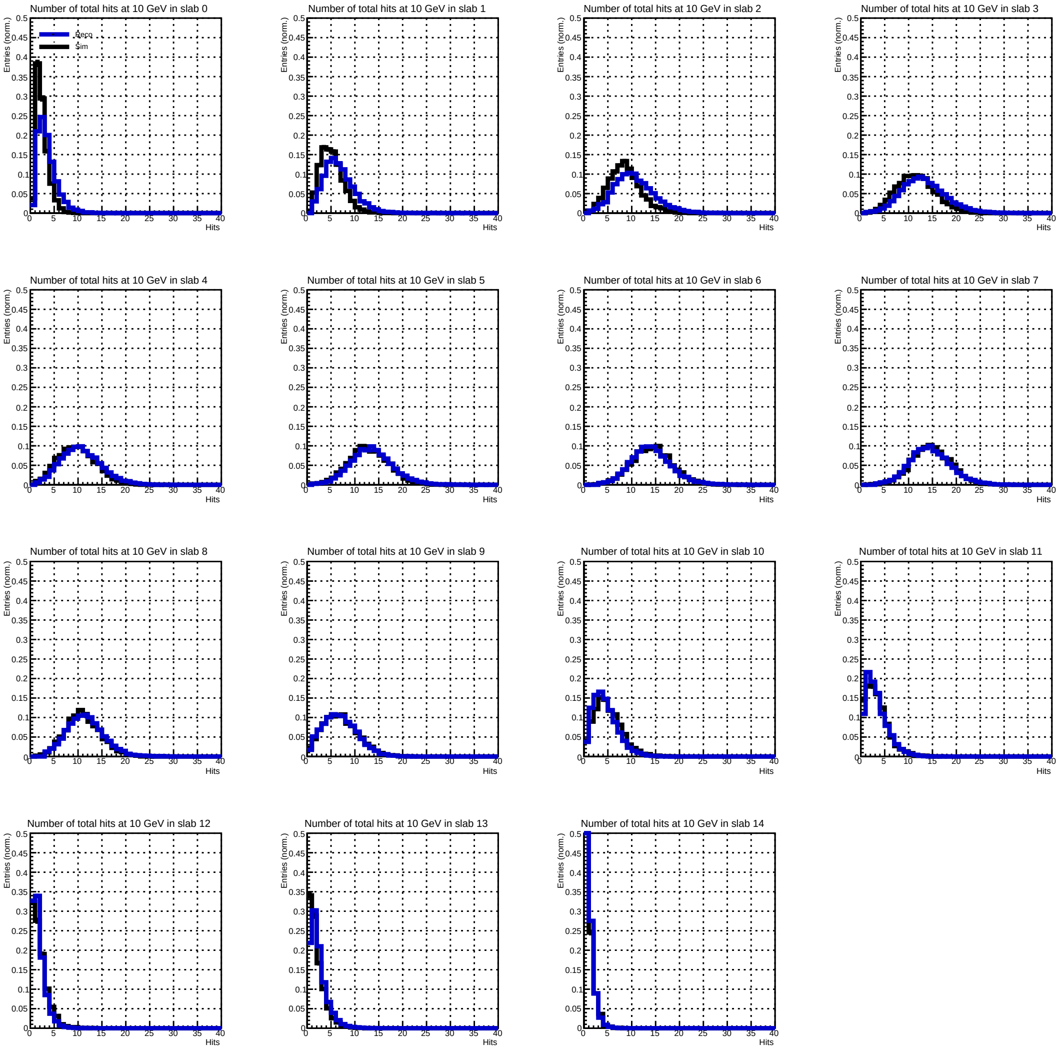

Figure G.1: Total number of hits in each layer.

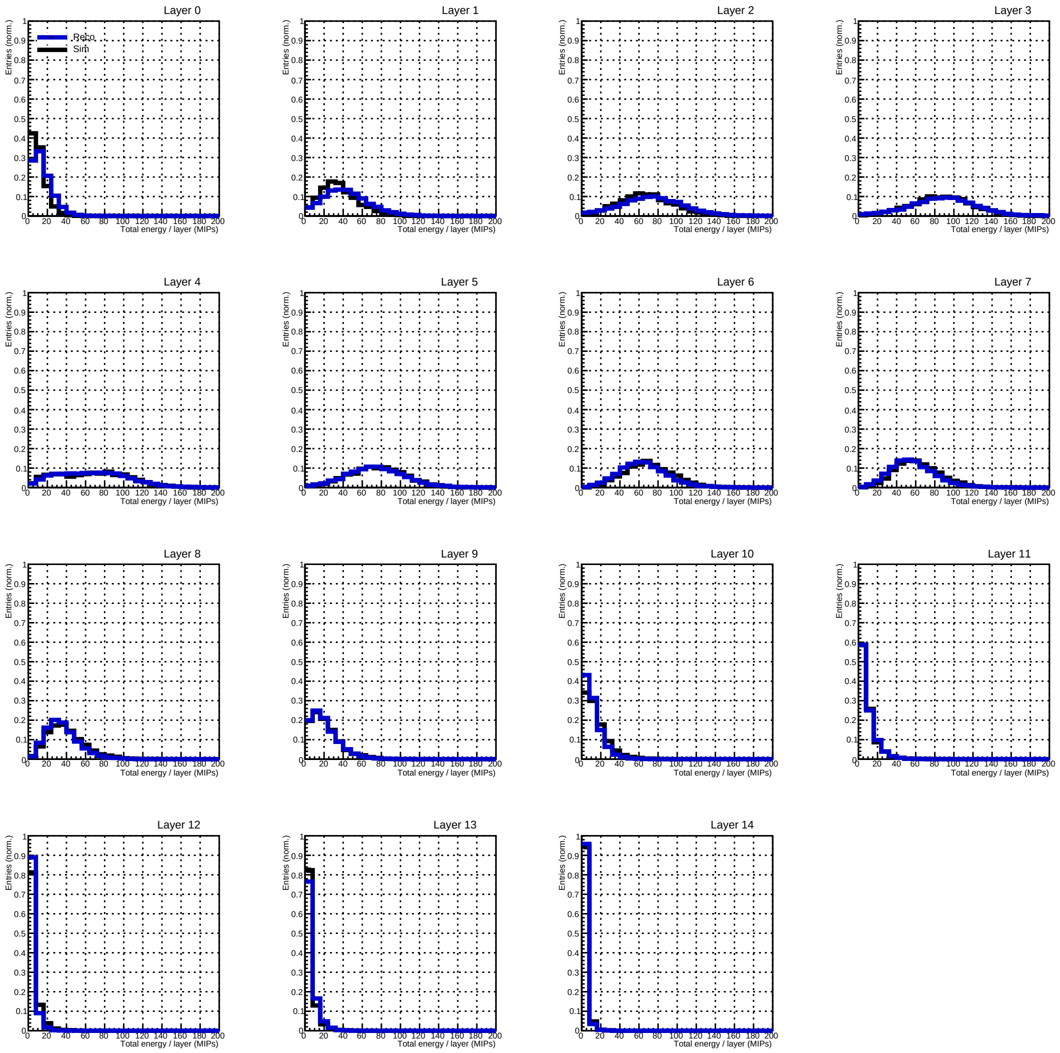

Figure G.2: Total deposited energy in each layer.

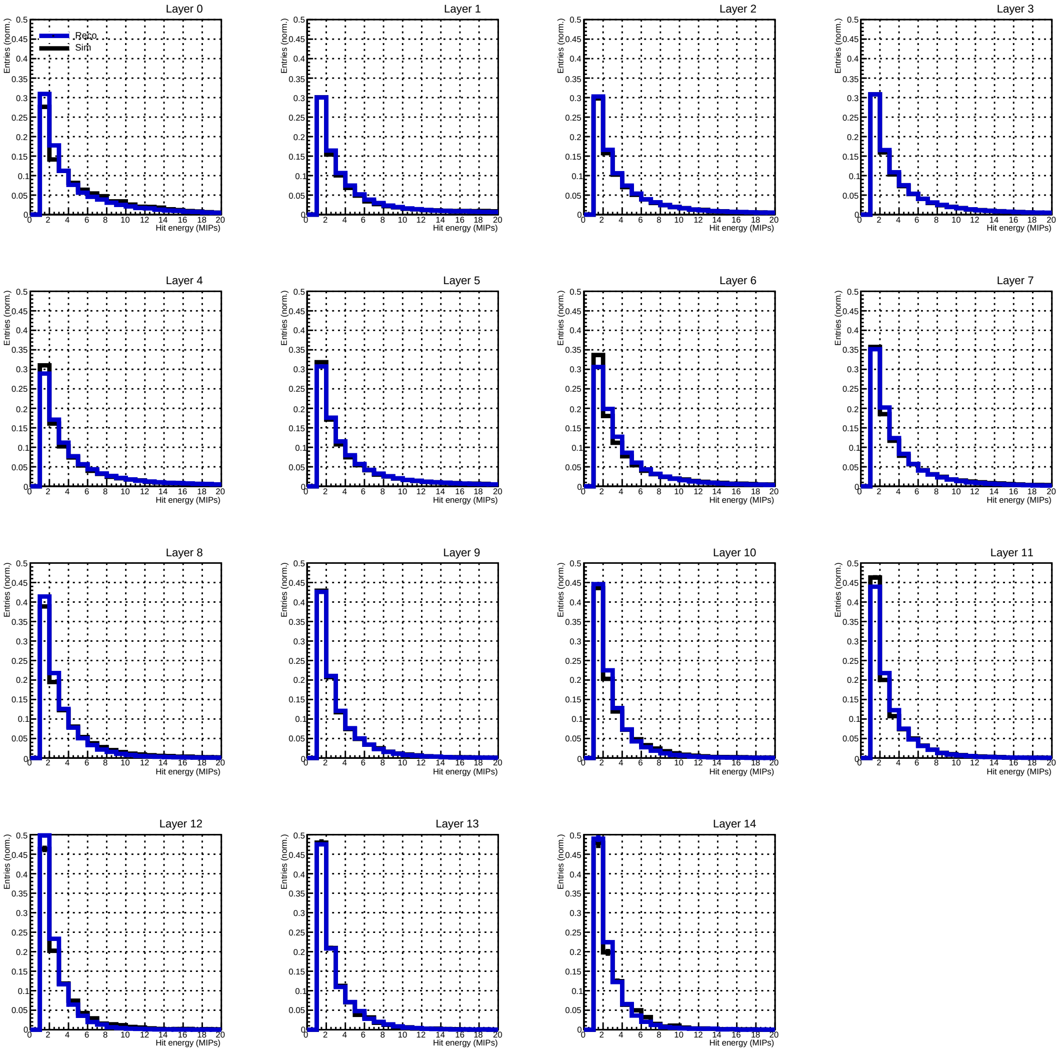

Figure G.3: Individual hit energy in each layer.

Bibliography

[1] M. Thomson, *Particle flow calorimetry and the pandorapfa algorithm*, *Nuclear Instruments and Methods in Physics Research Section A: Accelerators, Spectrometers, Detectors and Associated Equipment* **611** (2009) 25.

[2] "A time projection chamber for a future linear collider." `https://www.lctpc.org/e8/e57671`.

[3] U. Einhaus, U. Krämer and P. Malek, *Studies on Particle Identification with dE/dx for the ILD TPC*, in *International Workshop on Future Linear Colliders*, 2, 2019, `1902.05519`.

[4] F. Sauli, *Interaction of photons and neutrons with matter*, p. 4649. Cambridge Monographs on Particle Physics, Nuclear Physics and Cosmology. Cambridge University Press, 2014. 10.1017/CBO9781107337701.005.

[5] Particle Data Group collaboration, *Review of Particle Physics*, *PTEP* **2022** (2022) 083C01.

[6] S. Callier, F. Dulucq, C. de La Taille, G. Martin-Chassard and N. Seguin-Moreau, *Skiroc2, front end chip designed to readout the electromagnetic calorimeter at the ilc*, *Journal of Instrumentation* **6** (2011) C12040.

[7] CALICESiWECALgroupswithintheCALICE collaboration, *CALICE SiW ECAL - Development and performance of a highly compact digital readout system*, *JINST* **15** (2020) C05074 [`2002.09556`].

[8] Y. Kato, "Status on siw-ecal technological prototype." 2020.

[9] "The cern accelerator complex, layout in 2022." `https://cds.cern.ch/images/CERN-GRAPHICS-2022-001-1`.

[10] S. Callier, "Skiroc2e & skiroc2a measurements." 2016.

[11] D. Buskulic, D. Casper, I. Bonis, D. Decamp, P. Ghez, C. Goy et al., *Measurement of α_s from scaling violations in fragmentation functions in e^+e^- annihilation*, .

[12] I. Neutelings, "B tagging jets." `https://tikz.net/jet_btag/`.

[13] S. Funatsu, H. Hatanaka, Y. Hosotani, Y. Orikasa and N. Yamatsu, *Fermion pair production at e^-e^+ linear collider experiments in GUT inspired gauge-Higgs unification*, *Phys. Rev. D* **102** (2020) 015029 [`2006.02157`].

[14] H. Stängle, *Measurement of the $Z^0 \to s\bar{s}$ coupling at the SLD*, Ph.D. thesis, Stanford U., 1999.

[15] N. Yamatsu, S. Funatsu, H. Hatanaka, Y. Hosotani and Y. Orikasa, *W and Z Boson Pair Production at Electron-Positron Colliders in Gauge-Higgs Unification*, `2309.01132`.

[16] S. Funatsu, H. Hatanaka, Y. Hosotani, Y. Orikasa and N. Yamatsu, *GUT inspired $SO(5) \times U(1) \times SU(3)$ gauge-Higgs unification*, *Phys. Rev. D* **99** (2019) 095010 [`1902.01603`].

[17] ATLAS Collaboration collaboration, *Search for a heavy charged boson in events with a charged lepton and missing transverse momentum from pp collisions at $\sqrt{s} = 13$ TeV with the atlas detector*, *Phys. Rev. D* **100** (2019) 052013.

[18] K. Jonas, *A direct measurement of Higgs boson branching ratios in electron-positron collisions at 250 GeV*, theses, Institut polytechnique de Paris, Oct., 2022.

[19] OPAL collaboration, *Leading particle production in light flavor jets*, *Eur. Phys. J. C* **16** (2000) 407 [`hep-ex/0001054`].

[20] A. Irles, R. Pöschl and F. Richard, *Experimental methods and prospects on the measurement of electroweak b and c-quark observables at the ILC operating at 250 GeV*, `2306.11413`.

[21] K. Hentschel, *Atomic models, j.j. thomson's plum pudding model*, .

[22] P. E. R. F.R.S., *Lxxix. the scattering of α and β particles by matter and the structure of the atom*, *The London, Edinburgh, and Dublin Philosophical Magazine and Journal of Science* **21** (1911) 669.

[23] D. Hanneke, S. Fogwell and G. Gabrielse, *New measurement of the electron magnetic moment and the fine structure constant*, *Phys. Rev. Lett.* **100** (2008) 120801.

[24] C. S. Wu, E. Ambler, R. W. Hayward, D. D. Hoppes and R. P. Hudson, *Experimental test of parity conservation in beta decay*, *Phys. Rev.* **105** (1957) 1413.

[25] S. L. Glashow, *Partial-symmetries of weak interactions*, *Nuclear Physics* **22** (1961) 579.

[26] A. Salam, *Weak and Electromagnetic Interactions*, *Conf. Proc. C* **680519** (1968) 367.

[27] S. Weinberg, *A model of leptons*, *Phys. Rev. Lett.* **19** (1967) 1264.

[28] UA1 collaboration, *Experimental Observation of Lepton Pairs of Invariant Mass Around 95-GeV/c**2 at the CERN SPS Collider*, *Phys. Lett. B* **126** (1983) 398.

[29] TEVATRON ELECTROWEAK WORKING GROUP collaboration, *Combination of CDF and D0 Results on the Width of the W boson*, `1003.2826`.

[30] T. Behnke, J. E. Brau, B. Foster, J. Fuster, M. Harrison, J. M. Paterson et al., *The International Linear Collider Technical Design Report - Volume 1: Executive Summary*, `1306.6327`.

[31] LHCB collaboration, *Measurements of the B^+, B^0, B_s^0 meson and Λ_b^0 baryon lifetimes*, *JHEP* **04** (2014) 114 [`1402.2554`].

[32] BELLE-II collaboration, *Precise measurement of the D^0 and D^+ lifetimes at Belle II*, *Phys. Rev. Lett.* **127** (2021) 211801 [`2108.03216`].

[33] S. Murai, A. Ishikawa, T. Sanuki, A. Miyamoto, Y. Sugimoto, C. Constantino et al., *Recent status of FPCCD vertex detector R&D*, in *International Workshop on Future Linear Colliders*, 2, 2016, `1603.00009`.

[34] T. Radermacher, *Measurements and simulation of drift gas properties for the time projection chambers of the T2K experiment and for future neutrino experiments*, Ph.D. thesis, RWTH Aachen U., 2019. 10.18154/RWTH-2019-08019.

[35] Y. Giomataris, P. Rebourgeard, J. Robert and G. Charpak, *Micromegas: a high-granularity position-sensitive gaseous detector for high particle-flux environments*, *Nuclear Instruments and Methods in Physics Research Section A: Accelerators, Spectrometers, Detectors and Associated Equipment* **376** (1996) 29.

[36] F. Sauli, *The gas electron multiplier (gem): Operating principles and applications*, *Nuclear Instruments and Methods in Physics Research Section A: Accelerators, Spectrometers, Detectors and Associated Equipment* **805** (2016) 2.

[37] D. Attié, S. Aune, E. Berthoumieux, F. Bossù, P. Colas, A. Delbart et al., *Current status and future developments of micromegas detectors for physics and applications*, *Applied Sciences* **11** (2021) .

[38] K. Black et al., *MPGDs for tracking and Muon detection at future high energy physics colliders*, in *Snowmass 2021*, 3, 2022, `2203.06525`.

[39] LCTPC Asia Group collaboration, *Performance evaluation of a GEM-based readout module for the ILC TPC with a large aperture GEM-like gating device by a beam test*, in *International Workshop on Future Linear Colliders*, 2019, `2002.10779`.

[40] ILD Concept Group collaboration, *International Large Detector: Interim Design Report*, `2003.01116`.

[41] Linear Collider ILD Concept Group - collaboration, *The International Large Detector: Letter of Intent*, `1006.3396`.

[42] R. Cornat and (on behalf ofthe CALICE collaboration), *Semiconductor sensors for the calice siw emc and study of the cross-talk between guard rings and pixels in the calice siw prototype*, *Journal of Physics: Conference Series* **160** (2009) 012067.

[43] T. C. collaboration, J. Repond, J. Yu, C. M. Hawkes, Y. Mikami, O. Miller et al., *Design and electronics commissioning of the physics prototype of a si-w electromagnetic calorimeter for the international linear collider*, *Journal of Instrumentation* **3** (2008) P08001.

[44] C. Adloff et al., *Study of the interactions of pions in the CALICE silicon-tungsten calorimeter prototype*, *JINST* **5** (2010) P05007 [`1004.4996`].

[45] CALICE collaboration, *Testing hadronic interaction models using a highly granular silicon–tungsten calorimeter*, *Nucl. Instrum. Meth. A* **794** (2015) 240 [`1411.7215`].

[46] J. Rouëné, *A Highly Granular Silicon-Tungsten Electromagnetic Calorimeter and Top Quark Production at the International Linear Collider*, theses, Université Paris Sud - Paris XI, June, 2014.

[47] CALICE collaboration, *The CALICE SiW ECAL Technological Prototype—Status and Outlook*, *Instruments* **6** (2022) 75 [`2211.07457`].

[48] M. Anduze, D. Bailey, R. Cornat, P. Cornebise, A. Falou, J. Fleury et al., *Jra3 electromagnetic calorimeter technical design report*, .

[49] I. Corporation, *Cycloneő iv device handbook*, Tech. Rep. CYIV-5V1-2.2, Intel Corporation, 2016.

[50] F. Gastaldi, R. Cornat, F. Magniette and V. Boudry, *A scalable gigabit data acquisition system for calorimeters for linear collider*, *PoS* **TIPP2014** (2015) 193.

[51] H. Abramowicz et al., *The International Linear Collider Technical Design Report - Volume 4: Detectors*, `1306.6329`.

[52] CALICE collaboration, *New results of the technological prototype of the CALICE highly granular silicon tungsten calorimeter*, *Nucl. Instrum. Meth. A* **1051** (2023) 168185 [`2211.05614`].

[53] GEANT4 collaboration, *GEANT4–a simulation toolkit*, *Nucl. Instrum. Meth. A* **506** (2003) 250.

[54] M. Frank, F. Gaede, C. Grefe and P. Mato, *Dd4hep: A detector description toolkit for high energy physics experiments*, *Journal of Physics: Conference Series* **513** (2014) 022010.

[55] E. Longo and I. Sestili, *Monte carlo calculation of photon-initiated electromagnetic showers in lead glass*, *Nuclear Instruments and Methods* **128** (1975) 283.

[56] W. Kilian, T. Ohl and J. Reuter, *WHIZARD: Simulating Multi-Particle Processes at LHC and ILC*, *Eur. Phys. J. C* **71** (2011) 1742 [`0708.4233`].

[57] P. Acton, G. Alexander, J. Allison, P. Allport, K. Anderson, S. Arcelli et al., *An improved measuremebts of s (mz0) using energy correlations with the opal detector at lep*, *Physics Letters B* **276** (1992) 547.

[58] D. Schulte, *Beam-Beam Simulations with GUINEA-PIG*, .

[59] I. G. Knowles and G. D. Lafferty, *Hadronization in Z^0 decay*, *J. Phys. G* **23** (1997) 731 [`hep-ph/9705217`].

[60] T. Suehara and T. Tanabe, *LCFIPlus: A Framework for Jet Analysis in Linear Collider Studies*, *Nucl. Instrum. Meth. A* **808** (2016) 109 [`1506.08371`].

[61] M. Boronat, J. Fuster, I. Garcia, E. Ros and M. Vos, *A robust jet reconstruction algorithm for high-energy lepton colliders*, *Phys. Lett. B* **750** (2015) 95 [`1404.4294`].

[62] M. Boronat, J. Fuster, I. Garcia, P. Roloff, R. Simoniello and M. Vos, *Jet reconstruction at high-energy electron–positron colliders*, *Eur. Phys. J. C* **78** (2018) 144 [`1607.05039`].

[63] Y. L. Dokshitzer, G. D. Leder, S. Moretti and B. R. Webber, *Better jet clustering algorithms*, *JHEP* **08** (1997) 001 [`hep-ph/9707323`].

[64] M. Cacciari, G. P. Salam and G. Soyez, *The anti-k_t jet clustering algorithm*, *JHEP* **04** (2008) 063 [`0802.1189`].

[65] J. C. Doyle, *Study of pisup$-$ + p yields lambda + ksup0 from 944 mev/c to 1170 mev/c.*, .

[66] C. Baltay, A. Bridgewater, W. A. Cooper, M. Habibi and N. Yeh, *Precision measurement of the lifetime and decay branching ratio of the lambda0 hyperon*, *Phys. Rev. D* **4** (1971) 670.

[67] KTeV collaboration, *Precise Measurements of Direct CP Violation, CPT Symmetry, and Other Parameters in the Neutral Kaon System*, *Phys. Rev. D* **83** (2011) 092001 [`1011.0127`].

[68] G. Zech, F. Dydak, F. L. Navarria, O. E. Overseth, P. Steffen, H. Wahl et al., *A Measurement of the Lifetimes of xi0 and Lambda Hyperons*, *Nucl. Phys. B* **124** (1977) 413.

[69] KLOE collaboration, *Measurement of the absolute branching ratio of the $K^+ \to \pi^+\pi^0(\gamma)$ decay with the KLOE detector*, *Phys. Lett. B* **666** (2008) 305 [`0804.4577`].

[70] D. Aston et al., *A Study of K- pi+ Scattering in the Reaction K- p —> K- pi+ n at 11-GeV/c*, *Nucl. Phys. B* **296** (1988) 493.

[71] ACCMOR collaboration, *A Reanalysis of branching fractions of charmed mesons D0, D+ and D(s)+.*, *Z. Phys. C* **55** (1992) 383.

[72] I. Bozovic-Jelisavcic, S. Lukic, M. Pandurovic and I. Smiljanic, *Precision luminosity measurement at ILC*, in *International Workshop on Future Linear Colliders*, 3, 2014, `1403.7348`.

[73] S. Funatsu, H. Hatanaka, Y. Hosotani and Y. Orikasa, *Distinct signals of the gauge-higgs unification in e+e collider experiments*, *Physics Letters B* **775** (2017) 297.